UNIVERSITY OF CALIFORNIA

Los Angeles

Next Generation Liquefaction Database and Probabilistic Liquefaction Model Development

A dissertation submitted in partial satisfaction of the requirements for the degree Doctor of Philosophy in Civil Engineering

by

Kenneth Stewart Hudson

2023

ABSTRACT OF THE DISSERTATION

Next Generation Liquefaction Database and

Probabilistic Liquefaction Model Development

by

Kenneth Stewart Hudson

Doctor of Philosophy in Civil Engineering

University of California, Los Angeles, 2023

Professor Scott J. Brandenberg, Co-Chair

Professor Jonathan P. Stewart, Co-Chair

Soil liquefaction and resulting ground failure due to earthquakes present a significant hazard to infrastructure around the world. On a site-specific basis, liquefaction evaluations are performed by first evaluating whether a given soil material exhibits a type of soil behavior in which large pore pressure generation and strength loss is possible (susceptibility analysis), followed by assessing whether the state of the soil and the potential future ground shaking at the site are likely to lead to such strength loss (triggering analysis), and finally by considering the potential consequences if

liquefaction were to be triggered. The research presented in this thesis, which was conducted as part of the Next Generation Liquefaction (NGL) Project, aimed to improve all three steps in this modeling framework, but with an emphasis on the latter two. The NGL Project has database and modeling components, with my contributions mainly in connection with modeling.

NGL modeling was undertaken by a supported modeling team (SMT), of which I was a member. The susceptibility model solely considers soil type and behavior considerations and expresses results in a probabilistic manner instead of binary "yes" or "no" determinations common in previous models. The triggering model was developed in two phases. Initially, a Bayesian prior model was derived from a large inventory of laboratory data that was compiled by another SMT member. This prior model provides a probability density function for liquefaction triggering conditional on the relative density of granular soils. That model is later adjusted through a Bayesian inference process, as described further below.

My major contribution to SMT modeling was to evaluate the probability that individual layers within a site profile, and ultimately the profile as a whole, express the effects of liquefaction triggering at the ground surface. Referred to as a manifestation problem, my approach is to evaluate triggering and susceptibility probabilities for each layer at a site, and to combine such results with information on liquefied layer depths, layer thicknesses, and soil type characteristics to predict manifestation probabilities. This analysis is empirical, using the NGL database within a Bayesian inference process. Outcomes of Bayesian inference are referred to as posterior distributions, and include both models for layer and profile manifestation, as well as updates to the triggering prior.

The most significant original contributions of this research relative to prior work are the separation of liquefaction triggering from manifestation in model development. In particular, the triggering analysis reflects fundamental understanding of soil behavior as derived from laboratory testing, while the manifestation model was empirically derived from case histories and uses physically meaningful parameters related to the full profile. A number of other innovations were introduced to make this modeling effort possible, including development of machine learning algorithms to layer site profiles, development of improved models for predicting fines contents from CPT sounding data, and improved routines for ground motion prediction at liquefaction sites from past earthquakes.

The dissertation of Kenneth Stewart Hudson is approved.

Steven L. Kramer

Paolo Zimmaro

Timu W. Gallien

Scott J. Brandenberg, Committee Co-chair

Jonathan P. Stewart, Committee Co-chair

University of California, Los Angeles

2023

Table of Contents

List of Figures

List of Tables

Acknowledgements

This thesis was prepared to document work performed for the Geoscience and Engineering Department (GED) at Southwest Research Institute® and its contractors for the U.S. Nuclear Regulatory Commission (NRC) under Contract No. 31310018D0002 and through an interagency agreement with the U.S. Bureau of Reclamation (Agreement Number R20PG00126). The activities reported here were performed on behalf of the NRC Office of Nuclear Regulatory Research.

I wish to acknowledge members of the Next-Generation Liquefaction (NGL) community for their contributions to the aims of NGL that have supported this work, including:

- NGL Supported Modeling Team (SMT) members for their guidance in model development
- NGL Database Working Group (DWG) members for their work on the NGL database;
- NGL Executive Advisor Prof. I.M Idriss and NGL Advisory Board members (Profs. Misko Cubrinovski, Jonathan Bray, and Ross Boulanger) for their suggestions and insight;
- Dr. Brian Carlton, Dr. Kristin Ulmer, and Prof. Armin Stuedlein for their work on NGL supporting studies; and
- members of other NGL Modeling Teams for fruitful discussions.

Vita

Professional qualifications/registrations:

Registered Professional Geologist (PG), CA, License Number: 9991

Education:

Doctor of Philosophy, Geotechnical Engineering, University of California, Los Angeles, 2023 (projected)

Master of Science, Geotechnical Engineering, University of California, Los Angeles, June 2020

Master of Science, Earth Science, University of California Santa Barbara, June 2017

Bachelor of Science, Earth Science, University of California Santa Barbara, June 2016

Employment history:

Graduate Student Researcher – University of California, Los Angeles 2019 to present

Staff Geologist – WSP (formerly Wood E&IS and Amec Foster Wheeler), Los Angeles, CA, 2017 to present

Teaching Assistant for UCSB Earth Science Department (2016-2017)

Student Intern - Earth Research Institute, University of California, Santa Barbara, CA, 2014 to 2017

Student Intern - GEOVision Geophysical Services, Inc., Corona, CA, 2015

Student Intern - Northrop Grumman Corporation, Redondo Beach, CA, 2012 to 2014

Recent Publications:

Hudson, K.S., S.J. Brandenberg, P. Zimmaro, K.J. Ulmer, S.L. Kramer, and J.P. Stewart. (2023) Relationship Between Fines Content and Soil Behavior Type Index at Liquefaction Sites. Journal of *Geotechnical and Geoenvironmental Engineering*. Accepted for Publication.

Hudson, K.S., Ulmer, K.J., Zimmaro, P., Kramer, S.L., Stewart, J.P., Brandenberg, S.J. (2023) Unsupervised Machine Learning for Detecting Soil Layer Boundaries from Cone Penetration Test Data, *Earthquake Engineering & Structural Dynamics*. DOI: 10.1002/eqe.3961.

Hudson, K.S., Brandenberg, S.J., Zimmaro, P., Ulmer, K.J., Kramer, S.L., Stewart, J.P. (2023) Kriging Interpolation of Ground Motion Residuals at Liquefaction Case History Sites, *Proceedings of the 2023 Geocongress*, p. 365-372, DOI: 10.1061/9780784484654.037.

Hudson, K. S., Zimmaro, P., Ulmer, K., Carlton, B., Stuedlein, A., Jana, A., Dadashiserej, A., Brandenberg, S. J., Stamatakos, J., Kramer, S. L., & Stewart, J. P. (2022). Laboratory Component of Next-Generation Liquefaction Project Database. In L. Wang, J.-M. Zhang, & R. Wang (Eds.), *Proceedings of the 4th International Conference on Performance Based Design in Earthquake Geotechnical Engineering (Beijing 2022)* (pp. 1865–1874). Springer International Publishing. DOI: 10.1007/978-3-031-11898-2_170.

Nweke, C. C., Davis, C. A., Hudson, K.S., Hudnut, K.W., Brandenberg, S. J., & Stewart, J. P. (2022). Performance of Water Pipelines at Fault Crossings from the 2019 Ridgecrest Earthquakes. *Lifelines 2022*. American Society of Civil Engineers. DOI: 10.1061/9780784484449.031

Lee, Y., Z. Hu, J. Hu, A. Harounian, M.B. Hudson, K.S. Hudson, and R.T. Eguchi. (2022) Probabilistic Seismic Risk Evaluation of the City of Los Angeles Water System Pipeline Network, *Lifelines 2022*, ASCE, p. 819-832, DOI: 10.1061/9780784484432.073.

Hudson, K.S., Hudson, M.B., Hu, J., Harounian, A., & Lew, M. (2022) Quantifying Earthquake Hazards to Lifeline Systems at a Regional Scale with a Study of the Los Angeles Water System Pipeline Network, *Proceedings of the ASCE-UCLA Lifelines Conference 2021-2022*, DOI: 10.1061/9780784484432.038.

Hudson, M. B., Choi, S. H. J., Hansmire, W. H., & Hudson, K.S. (2022). Seismic Design of Los Angeles Underground Transit Stations. *Lifelines 2022*. ASCE. DOI: 10.1061/9780784484432.027.

Christine A. Goulet, Yongfei Wang, Chukwuebuka C. Nweke, Bo-xiang Tang, Pengfei Wang, Kenneth S. Hudson, Sean K. Ahdi, Xiaofeng Meng, Martin B. Hudson, Andrea Donnellan, Gregory A. Lyzenga, Scott J. Brandenberg, Jonathan P. Stewart, Timu W. Gallien, Maria A. Winters; Comparison of Near-Fault Displacement Interpretations from Field and Aerial Data for the M 6.5 and 7.1 Ridgecrest Earthquake Sequence Ruptures. *Bulletin of the Seismological Society of America* 2021; doi: https://doi.org/10.1785/0120200222

Yong, A., E. Cochran, J. Andrews, A. Martin, K.S. Hudson, Y. Ellen, J. Herrick, and J. Dozal. (2020) "V_{S30} and f_d As Station M_L Adjustments (dM_L) in California" Bulletin of the Seismological Society of America. https://doi.org/10.1785/0120200130

1. Introduction

1.1 Soil Liquefaction Overview and Mechanics

Liquefaction in its most general definition is “the act or process of transforming any substance into a liquid” (Lange and Forker 1967). Therefore, soil liquefaction (referred to simply as liquefaction for the rest of this document) was originally defined as the transformation of soil from a solid state to a liquid state. In reality, a soil temporarily behaves like a liquid rather than transforming into a liquid. This was similarly stated by Youd: “Liquefaction is defined as the transformation of a granular material from a solid state into a liquefied state as a consequence of increased pore-water pressures” (Youd 1973). Many definitions of soil liquefaction have been published emphasizing different aspects of the causes or effects of liquefaction such as “the sudden drop of shear strength under undrained conditions from the yield strength to substantially smaller critical state strength” (Terzaghi et al. 1996) or “The sudden large decrease of shearing resistance of a cohesionless soil, caused by a collapse of the structure by shock or strain, and associated with a sudden but temporary increase of the pore fluid pressure” (American Society of Civil Engineers 1958). In summary, liquefaction is characterized by a substantial loss of soil stiffness and shear strength that results from increased pore-water pressures.

The basic cause of liquefaction can be understood qualitatively as an attempt to decrease volume in a contractive soil during undrained conditions leading to an increase in pore water pressure to the point at which the representative Mohr circle for the state of stress intersects the Mohr-Coulomb failure envelope. The effective stress path for such a failure is shown in Figure 1-1b for a monotonic stress path. Figure 1-1a shows the stress-strain response, Figure 1-1c shows how

excess pore pressure builds, and Figure 1-1d shows the stress path relative to the critical state line all for the monotonic undrained liquefaction triggering.

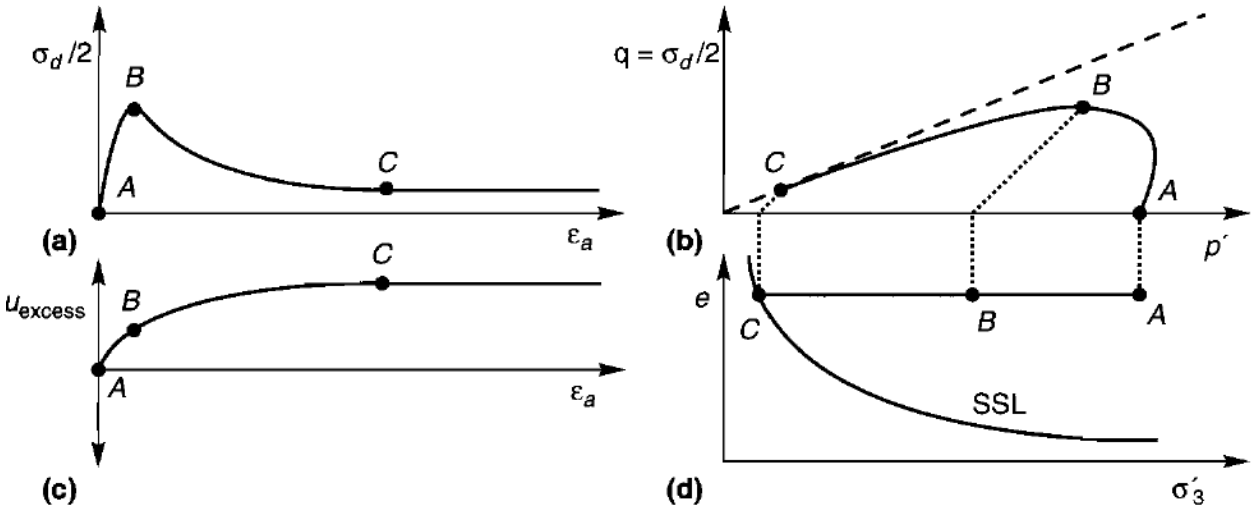

Figure 1-1 Schematic liquefaction-triggering mechanism by monotonic undrained stress path: (a) stress-strain curve; (b) effective stress path; (c) excess pore pressure; (d) effective confining pressure (Kramer 1996). Point A represents the state of the soil following consolidation but prior to undrained shear. Point B represents the condition at peak shear resistance, which defines the flow liquefaction surface. Point C represents the condition where the soil has been sheared to large strain and the rate of change in pore pressure and shear resistance with increasing shear strain change is zero, which is at steady state.

Soils that contain inherent cohesion due to inter-particle attraction (i.e., clays and some silts) do not lose strength to the same degree as granular soils (gravels, sands, non-plastic silts). As a result, only granular media are considered as potentially susceptible to liquefaction. Such soils also tend to have a large hydraulic conductivity. With a large hydraulic conductivity, pore fluids can move quickly through the soil and therefore, sands behave in a drained manner during most loading time scales. However, if a shear stress is applied faster than the pore fluid can drain, normal stresses

will be transferred from inter-particle forces to pore fluid pressure in an undrained manner. When the stress transferred to the pore fluid causes the pore pressure to equal the total effective stress, a state of *initial liquefaction* (Seed and Lee 1966) is reached. Alternative definitions of liquefaction have been based on granular soil reaching certain levels of cyclic shear strains, which may occur at different times than initial liquefaction. To generate pore fluid pressure in response to volume change, the soil needs to be fully saturated (S=1) or nearly so. If a soil is not fully saturated (even if S = 0.95), the compressibility of the air in the voids allows volumetric strain to occur without generating appreciable pore pressure. Therefore, dry (S = 0) soils cannot experience liquefaction and partially saturated soils have an increased liquefaction resistance (O'Donnell et al. 2017; Zhang et al. 2016).

A fully saturated, cohesionless sand's potential for liquefaction is governed by two main characteristics: (1) the soil's response to shear deformation is contractive, even if only temporarily during cyclic loading (this characteristic is related to soil state, being more common for loose materials and large confining pressures); and (2) the shear loading must occur sufficiently rapidly for positive pore fluid pressures to develop, which can only occur if excess water pressures cannot dissipate during the time interval of shearing (i.e., undrained conditions are present).

When soil experiences drained shear, its volume changes as the void ratio moves towards the critical void ratio (Figure 1-1d) where continuous deformation occurs with no change in principal stress difference (Casagrande 1936). A soil must either decrease or increase in void ratio or effective confining stress to approach the critical void ratio; if a soil begins with a void ratio larger than the critical void ratio, it will contract as the void ratio or effective confining pressure decreases. A decrease in void ratio in a fully saturated soil means that pore fluids will have to displace and if

they cannot, the pore fluid will generate excess pore pressure because water is almost incompressible (it experiences negligible volume change at the scale of soil particles). In a case where the pore fluid cannot displace (i.e., undrained shear) and enough shear deformation is applied, pore pressure can be generated to a sufficiently high value to equal the total stress (reducing the effective stress to zero) and cause initial liquefaction. Therefore, liquefaction risk is greatest in loose soils because loose soils are typically contractive and can generate a positive pore pressure. Although Terzaghi et al. (1996) indicated that clean sands with a relative density less than approximately 40 to 60% are loose enough to have liquefaction triggered, it is now understood that dilatant materials can also generate large pore pressures for relatively small-strain deformations and thereby achieve a condition of temporary strength loss (e.g., Seed 1979).

In order for a positive pore pressure to be maintained in a contractive soil, the pore fluid cannot diffuse from the soil over the time interval of the shear loading. For this to occur, the ratio of the loading time to some metric of drainage time (e.g., time to 15% consolidation) must be sufficiently large that the pore fluid can generate pressure before it has time to drain. Therefore, as the hydraulic conductivity of a soil decreases (increasing drainage time), or drainage is impeded by bounding low-permeability layers above and beneath, the likelihood of that soil experiencing liquefaction increases.

Additionally, aging effects influence a soil's liquefaction potential as well. Aging effects include decreasing the void ratio and increasing the cohesion. Therefore, the resistance to liquefaction of a soil decreases as the age of the soil increases. Generally, soils that are Pleistocene (11.7 ka) or older are more resistant to liquefaction (Andrus et al. 2009; Seed 1979).

When a soil crosses a line in effective stress space known as the flow liquefaction surface (FLS) it becomes unstable and the shear strength reduces to a steady-state strength. The FLS is defined as the line that runs through the peak point in the stress paths from the same soil tested at the same void ratio (density) under different initial effective confining pressures as shown in Figure 1-2 (Vaid and Chern 1985). The FLS is approximately two-thirds the slope of the drained failure envelope for clean sands (Kramer 1996).

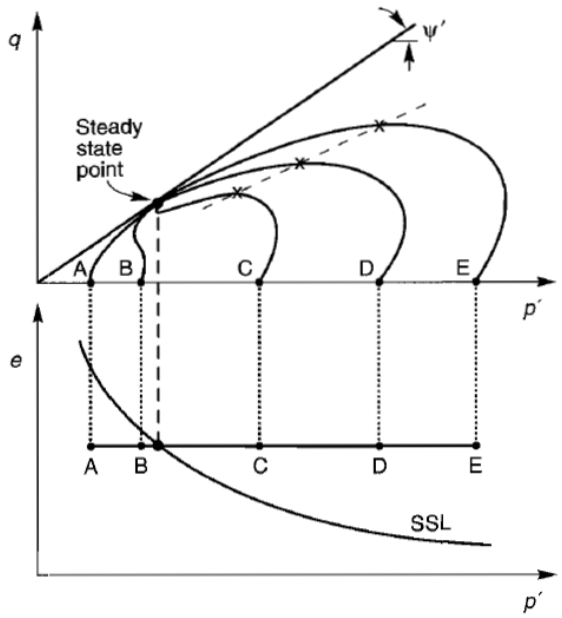

Figure 1-2. Response of five specimens isotropically consolidated to the same initial void ratio at different initial effective confining pressures. Liquefaction is initiated in specimens C, D, and E at the point marked with an x which has a straight line that fits through all these points and the origin, known as the flow liquefaction surface (FLS) (Kramer 1996).

Liquefaction can occur during cyclic loading as well as monotonic loading (Vaid and Chern 1983). Consider the response of two anisotropically consolidated, identical, triaxial specimens of loose,

saturated sand in Figure 1-3. The specimens both begin at point A under a static shear stress that is greater than the steady-state strength (meaning that flow liquefaction is possible). One specimen is loaded monotonically under undrained conditions and follows the stress path drawn to point B where it intersects the FLS, becomes unstable, and rapidly strains toward the steady state at point C. The other specimen is loaded cyclically in undrained conditions so that the effective stress decreases and permanent strains accumulate until it reaches point D at the FLS where it also becomes unstable and strains to the steady state at point C.

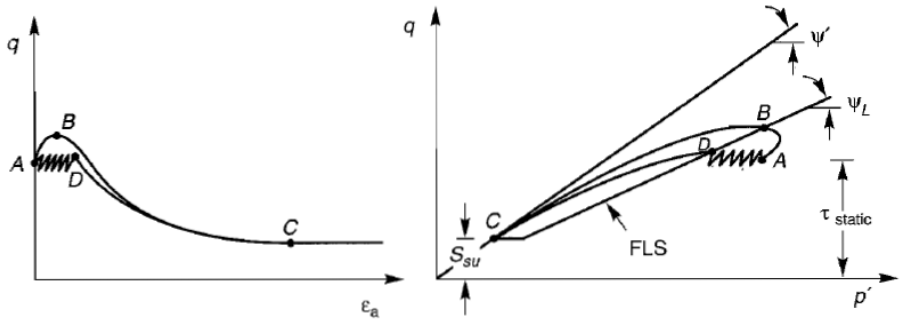

Figure 1-3. Initiation of liquefaction by cyclic and monotonic loading of two identical specimens.

1.2 Liquefaction Susceptibility, Triggering, and Consequences

To understand liquefaction phenomena as a whole, it is useful to compartmentalize the causes and effects of liquefaction so that each phase can be analyzed successively. The steps for performing a liquefaction analysis can be broken into three categories: susceptibility, triggering, and consequences.

1.2.1 Liquefaction Susceptibility

Within the geotechnical engineering community, different engineers have different understandings of the word "susceptibility" as applied to liquefaction problems (Chapter 3 of Steudlein et al., 2023). However, as used here, *liquefaction susceptibility* is related to fundamental material characteristics of the soil that control the level of pore pressure generation and strength loss that is possible if the soil were to be cyclically sheared under undrained conditions. Susceptibility is unrelated to the density and current saturation level of the soil; while both of these factors affect the potential for triggering, they do not control the fundamental susceptibility of a soil. The susceptibility of a soil addresses the question of whether a soil *can* liquefy in some condition (not necessarily its in situ condition) – whether it *will* liquefy or not is an issue of triggering.

The two end members can be simply summarized as "sand-like" behavior – liquefiable – and "clay-like" behavior – non-liquefiable. Fine-grained soils can either exhibit clay-like or sand-like behavior depending on whether the controlling fines are plastic (e.g., clay) or non-plastic (e.g., coarse silt). Non-plastic silt particles are sand-like in that they exhibit the same mechanical properties as sands (gravitational forces) whereas clay is mechanically different because it is controlled by plasticity (Hydrogen and van der Waals bond forces). The soil characteristics that indicate whether a soil will behave in a sand-like or clay-like manner are the similarity of slope between the critical state line (CSL) and the isotropic consolidation line (ICL) and its cyclic response (shape of the stress-strain loops) and corresponding pore pressure generation. These soil properties are often correlated to index properties such as grain size distribution (median grain size diameter (D_{50}), percent clay content ($\%CC$), etc.) and Atterberg limits (LL, PL, and PI). Therefore, index properties are frequently used as a predictor of soil susceptibility. Susceptibility is not

controlled by those index properties, rather it is correlated to them. Often distinguishing clay-like versus sand-like behavior is difficult in the field because clay can undergo cyclic softening which can be misinterpreted as liquefaction.

Environmental conditions contribute to liquefaction being able to occur or not. For instance, a clean sand that has a degree of saturation (S) of 50% will not liquefy because excess pore pressure will not generate. This is not a property of the soil itself but is a consequence of environmental conditions that led to the soil being saturated or not. A clean sand is susceptible to liquefaction, but it will not liquefy if not fully or nearly fully saturated; therefore, S is not a property that controls susceptibility. Other properties that affect liquefaction resistance but are not considered to be fundamental contributors to susceptibility are state and drainage conditions. State (characterized by the state parameter) reflects the position of a soil in void ratio and effective stress space relative to the CSL which is controlled by the effective stress the soil is experiencing (σ'_{v0}) and the density (i.e. void ratio (e) which can be related to other density measures such as relative density (D_R) and water content (w)). Many studies have used environmental variables in models for liquefaction "susceptibility." For instance, the Chinese criteria uses $w/LL > 0.9$ as a criterion (Seed and Idriss 1982; Wang 1979) and Bray and Sancio (2006) use $w/LL > 0.8$ as a criterion.

1.2.1.1 Susceptibility of Fine-Grained Soils

Earthquake-induced ground shaking and resultant pore pressure accumulation can lead to ground failure under two mechanisms: cyclic softening or liquefaction. Cyclic softening and liquefaction produce different effects and therefore properly identifying whether a soil is at risk to one or the

other is critical for performing analysis and then engineering design of mitigation strategies for those effects. Cohesionless soils are susceptible to liquefaction because during undrained loading they can experience conditions during rapid shearing (earthquake loading) that cause high levels of pore-water pressure to develop that can approach the total stress, thereby lowering the effective stress (even only temporarily) to near zero, which in turn dramatically reduces shear resistance. Uncemented sands and silts are susceptible to liquefaction. Due to inter-particle attraction stresses that remain following pore pressure generation, clays with plasticity do not experience the same degree of strength and stiffness degradation and are not considered to be susceptible to liquefaction. However, these materials can experience strength loss and contribute to ground failure, which is referred to as cyclic softening. Fine-grained soils can either be cohesionless (coarse silts) or cohesive (finer silts and clay) and can be susceptible to liquefaction or cyclic softening, respectively. Therefore, Boulanger and Idriss (2006) recommended that evaluation of potential hazards involving fine-grained soils must be separated into procedures applicable for "sand-like" fine-grained soils that can liquefy and "clay-like" fine-grained soils that can experience cyclic softening, requiring a liquefaction susceptibility criteria to determine whether a soil is sand-like or clay-like. However, currently there is no consensus in liquefaction susceptibility criteria of fine-grained soils.

Two general procedures have been used to develop liquefaction susceptibility criteria: (1) criteria based on field case histories of ground failure or non-ground failure (Seed and Idriss 1982; Seed et al. 2003); (2) criteria based on observed laboratory responses (Boulanger and Idriss 2006; Bray and Sancio 2006; Stuedlein et al. 2023). These two types of models are discussed in the following

subsections. Table 1-1 summarizes the current susceptibility models that are described in those sections.

Table 1-1. Comparison of liquefaction susceptibility criteria. *%CC*: percent clay content, w_C/LL: water content over liquid limit, *USCS*: Unified Soil Classification System, *LL*: liquid limit, *PI*: plasticity index, I_L: liquidity index, D_{50}: median grain size diameter.

Name of Criterion	Basis for Study	Susceptible to Liquefaction if:
"Chinese Criteria" (Wang 1979)	Case histories in China	Composition and state: *%CC* and w_C/LL
Modified Chinese Criteria, (Seed and Idriss 1982)	Case histories in China	Composition and State: *%CC*, *LL*, and w_C/LL
Youd (1998)	Review of Chinese criteria, Koester (1992), and physical considerations	Composition: *USCS*, *LL*, and *PI*
Martin et al. (1999)	Modified Chinese Criteria	Composition and State: *%CC*, *LL*, and w_C/LL
Polito (1999)	Laboratory tests on synthetic soil	Composition: *PI* and *LL*
Andrews and Martin (2000)	Case histories in California, China, Japan	Composition: *%CC* and *LL*
Polito and Martin (2001)	Laboratory tests on synthetic soil	Composition: *PI* and *LL*
Seed et al. (2003)	Case histories in Turkey and Taiwan	Composition: *PI* and *LL*
Sancio (2003); (Bray et al. 2004b; a)	Case histories in Adapazari, Turkey	Composition and State: *PI* and w_C/LL
Bray and Sancio (2006)	Laboratory tests on specimens from Adapazari, Turkey	Composition and State: *PI* and w_C/LL
Boulanger and Idriss (2006)	Laboratory tests on natural soil, soil mixtures, and mine tailings	Composition: *PI*
Bol et al. (2010)	Case histories in Adapazari, Turkey	Composition : *%CC*, *LL*, I_L, D_{50}

1.2.1.1.1 Susceptibility criteria based on field performance data

Challenges to establishing susceptibility criteria from field case histories are as follows:

- Ground failure can occur without liquefaction and be misidentified as liquefaction. One such example is provided by bearing capacity failures of foundations on softened clays, such as occurred in Wufeng, Taiwan during the 1999 Chi-Chi earthquake (Sections 3.5.1 and 7.1). The culprit in that case was strong inertial demands on the building foundations and strength loss from cyclic softening of the clays (Chu et al. 2008).
- False negatives occur when soils at a site are susceptible to liquefaction and liquefaction is triggered but its effects are not manifested at the ground surface. This situation can occur if a thick non-liquefiable layer overlies a liquefiable layer (Ishihara 1985). Similarly, liquefaction can also occur in individual disconnected layers and not produce surface manifestations, as observed in Christchurch after the 2010-2011 Canterbury earthquake sequence (Cubrinovski et al. 2019).
- It is possible that a soil is in fact susceptible to liquefaction but has not been shaken strongly enough to trigger during past earthquakes.

Figure 1-4. Punched footings and intermediate slab heaving due to cyclic softening of high-plasticity clay in Wufang, Taiwan. Photo by R. Seed (1999).

For many years, the Chinese criteria were used to evaluate liquefaction susceptibility of silts and clays, based on observations of liquefaction during earthquakes at various sites in China (Wang 1979). Following the major events in 1999 in Turkey and Taiwan, more research was conducted with varying definitions of "liquefaction susceptibility" of fine-grained soils as shown in Table 1-1 (Andrews and Martin 2000; Boulanger and Idriss 2006; Bray and Sancio 2006; Polito 2001; Seed et al. 2003; Youd 1998). One issue lies in the definition of liquefaction: clays can undergo cyclic softening, which has not had a widely understood or accepted definition, therefore many researchers have classified certain soils that experience cyclic softening as liquefying while others

have not. Another issue lies in the definition of susceptibility, with some models for its prediction using parameters that do not control susceptibility in the manner used here.

Due to the aforementioned difficulties of relating surface effects of liquefaction to susceptibility, most recent susceptibility models have adopted the approach of assessing susceptibility from material behavior characteristics. Such methods are the subject of the next sub-section.

1.2.1.1.2 Susceptibility criteria based on laboratory test data

As a result of these false negatives, false positives, and intermediate soil issues, susceptibility is poorly suited to analysis based solely on case history data. Laboratory test data provides a good alternative, with the potential to investigate pore pressures responses, stress-strain responses, and strength normalization behavior that is indicative of the fundamental behavior of a soil as being principally governed by granular particle interactions (i.e., sand-like) or by a cohesive soil matrix (i.e., clay-like).

While the models in Table 1-1 are all based on laboratory test data, they do not always use consistent testing procedures nor consistent test data interpretations. Differences between models include the soils tested (i.e., natural or synthetically blended soils, source location of soils, soil types, and *PI* ranges), how the soils are tested (i.e., *CSR* and strain ranges, triaxial or direct simple shear, etc.), and how the authors of the study decided to differentiate susceptible versus non-susceptible (i.e., whether a soil does or does not surpass a threshold r_u during cyclic shear, the shape of the stress-strain loops, or the similarity of the critical state line (CSL) and the isotropic consolidation line). To illustrate some of these differences, Figure 1-5 presents ranges of *CSR* and

PI parameters used in the development of Polito (1999), Polito and Martin (2001), Bray and Sancio (2006), and Boulanger and Idriss (2006) liquefaction susceptibility criteria for fine grained soils. Each study has different ranges of plasticity indices and cyclic stress ratios (*CSR*s) along with testing different soils with different mineralogies which possibly explains why they have different criteria. *CSR* is defined in Equation 1.1 where τ_{cyc} is the cyclic shear stress and $\sigma'_{v,0}$ is the initial effective vertical stress.

$$CSR = \frac{\tau_{cyc}}{\sigma'_{v,0}} \tag{1.1}$$

Among the susceptibility models listed in Table 1-1 and for which parametric ranges are shown in Figure 1-5, the Boulanger and Idriss (2006) and Bray and Sancio (2006) criteria are relatively widely used and will be emphasized in subsequent discussion in this section.

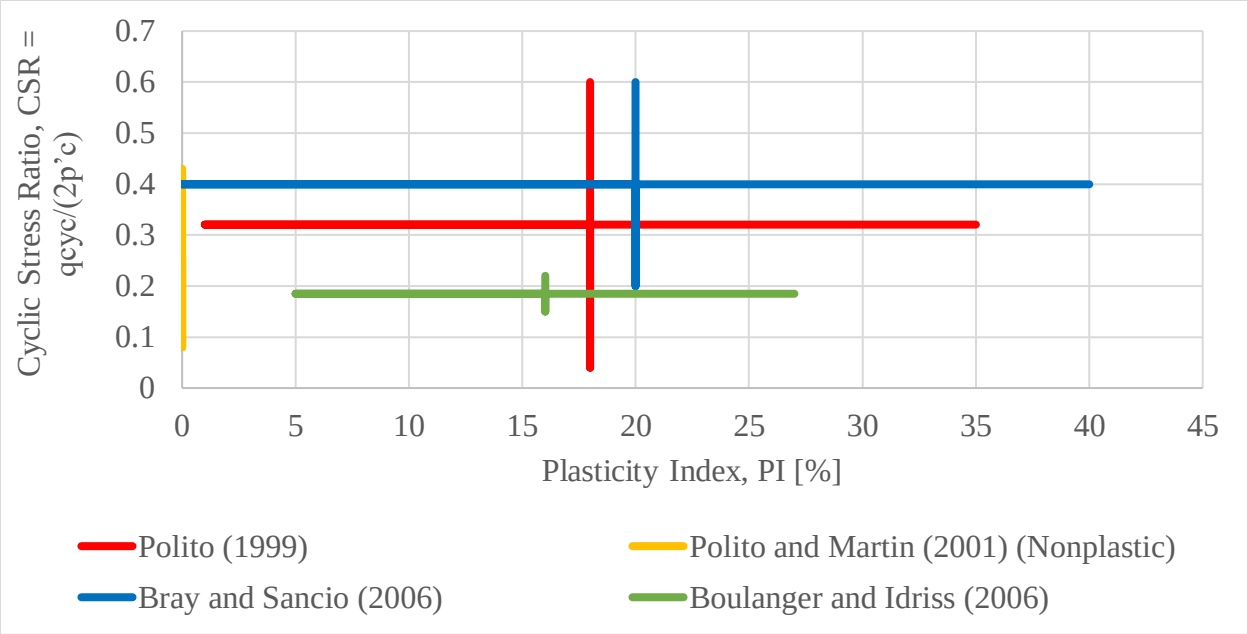

Figure 1-5. Ranges of PI and *CSR* for soils that were used to develop Boulanger and Idriss (2006), Bray and Sancio (2006), Polito (1999), and Polito and Martin (2001) liquefaction susceptibility criteria for fine grained soils.

Boulanger and Idriss (2006) present a transition zone between sand-like and clay-like behavior. They suggest that soils with PI < 3 behave as sand-like whereas soils with PI > 8.2 behave as clay-like, with an intermediate transition zone where the behavior is unclear (a hard threshold of clay-like behavior at PI > 7 was recommended by Boulanger and Idriss (2006)). The transition zone can be represented as shown in Figure 1-6a (Huang 2008). Then by dividing the red-shaded area in Figure 1-6a for a given PI by the total area of the transition zone (the cross-hatched area), it can be interpreted as a cumulative distribution function (CDF) as shown in Figure 1-6b. This CDF represents the probability of clay-like behavior, whereas its complement is the probability of sand-like behavior. A simple function can be written to approximate the numerical curve as

$$F_{ln\,(PI^*)}\big(ln(PI)\big) = 1 - \frac{1}{\left[1 + \left(\frac{\ln(PI)}{1.843}\right)^{11.483}\right]^2} \quad 1.2$$

where PI is the measured PI of the soil of interest (Huang 2008).

This function can be differentiated to obtain a probability density function (PDF) with an approximate mean ($\mu_{ln(PI^*)}$) and variance ($\sigma_{ln(PI^*)}$) of $\sigma_{ln(PI^*)}$ yielding $\mu_{ln(PI^*)}$ of 1.704 and $\sigma_{ln(PI^*)}$ of 0.218. Adding in uncertainty in PI values based on tests from Phoon and Kulhawy (1999) yields the following susceptibility PDF:

$$S_{BI}\big(ln(PI)\big) = \frac{1}{\left[1 + \left(\frac{\ln(PI)}{1.938}\right)^{6.767}\right]^2} \quad 1.3$$

where S_{BI} is the Boulanger and Idriss based susceptibility function.

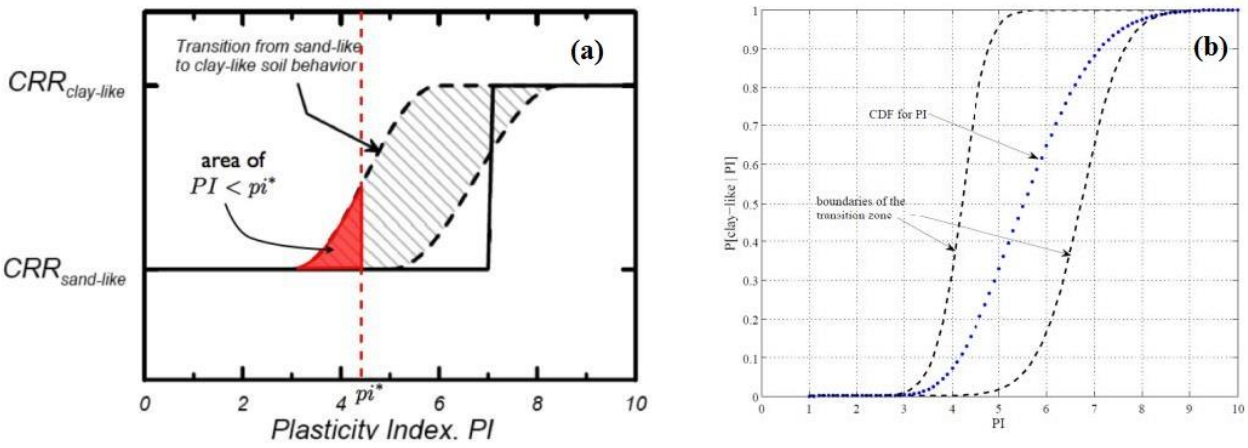

Figure 1-6. (a) Integration of Idriss & Boulanger (2006) transition zone between sand-like and clay-like behavior based on PI. (b) cumulative distribution function for PI based on the transition zone (Huang 2008).

The Bray and Sancio (2006) model examined the response of silty soils of varying plasticity and evaluated their responses in terms of excess pore water pressure ratios (r_u) and shapes of cyclic shear stress vs. cyclic shear strain loops. On this basis they classified materials as susceptible, not susceptible, or intermediate susceptibility, as shown in Figure 1-7. As with Boulanger and Idriss, the intermediate zone (in terms of *PI*) could be used to define probability criteria for liquefaction susceptibility, although this has not been done to my knowledge.

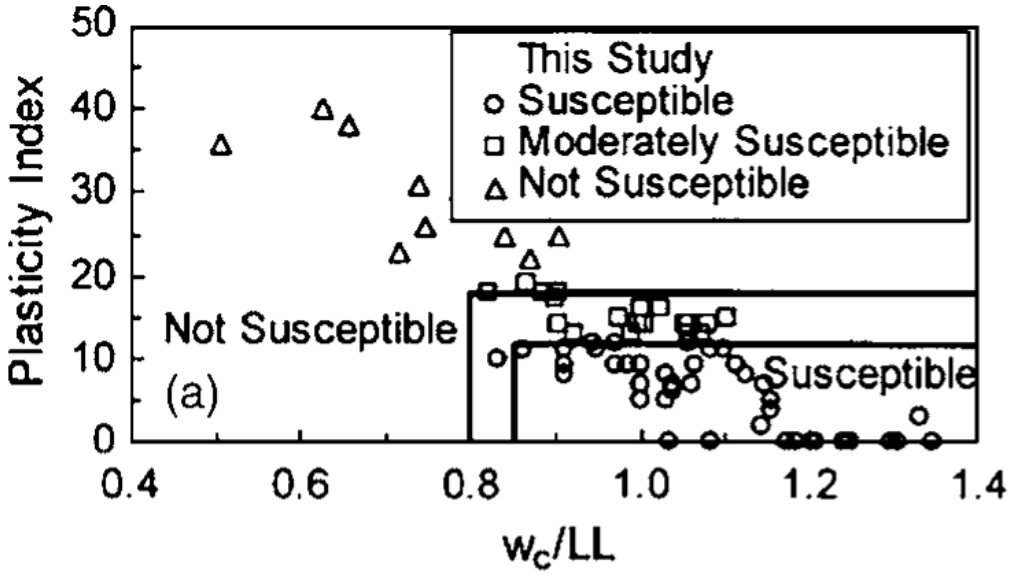

Figure 1-7. Partial illustration of susceptibility criteria by Bray and Sancio (2006), emphasizing the *PI* component.

PI-based susceptibility criteria can be translated to I_c criteria using a dataset that contains collocated borings and CPTs in which the borings had samples with Atterberg limit testing for depth intervals in which I_c is available from collocated CPTs. Maurer et al. (2017) evaluated this correlation between *PI* and I_c using a dataset from Christchurch, New Zealand (NZGD 2016). Receiver operating characteristics (ROC) curve analyses were performed to determine how well I_c correlated to liquefaction susceptibility based on four criteria: Boulanger and Idriss (2006), Bray and Sancio (2006), Polito and Martin (2001), and Polito (1999). I_c was found to correlate well, so Maurer et al. (2017) proceeded to develop a probabilistic correlation function with the form presented in Equation 1.4.

$$F_{not\ susceptible}(I_c) = \Phi\left[\frac{\ln\left(I_c/x_m\right)}{\sigma_m}\right] \quad 1.4$$

where Φ is the Gaussian cumulative distribution function, x_m is the median *PI* value of the distribution, and σ_m is the logarithmic standard deviation. Maurer et al. (2017) produced values for x_m and σ_m based on four susceptibility criteria: Boulanger and Idriss (2006), Bray and Sancio (2006), Polito and Martin (2001), and Polito (1999) as presented in Table 1-2. The relationships are plotted in Figure 1-8.

Table 1-2. Criteria-specific coefficients for use in the Maurer et al. (2017) probability of susceptibility estimated from I_c equation

Criteria	σ_m	x_m
Polito (2001)	0.0988	2.5474
Seed et al. (2003)	0.1348	2.6214
Bray & Sancio (2006)	0.1275	2.7315
Boulanger & Idriss (2006)/Idriss & Boulanger (2006)	0.0851	2.5031

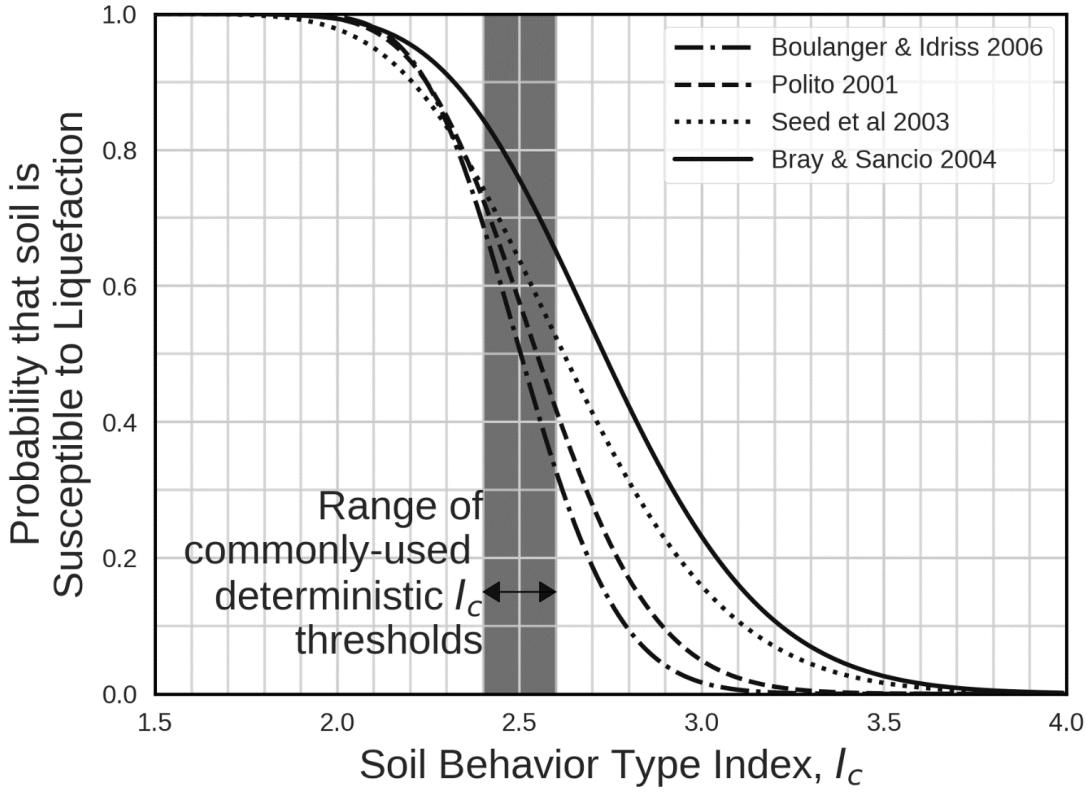

Figure 1-8. The probability of liquefaction susceptibility as a function of measured I_c. Susceptibility is as defined by four criteria (Boulanger and Idriss 2006; Bray and Sancio 2006; Polito 1999, 2001; Seed et al. 2003). The range of deterministic I_c thresholds commonly used in practice is also highlighted (Maurer et al. 2017).

1.2.2 Liquefaction Triggering

For liquefaction to trigger, shaking must exceed the cyclic resistance of the soil to generate sufficient pore water pressures that causes the soil to lose shear strength as effective stress decreases (e.g., Figure 1-9). This increase is often expressed as a ratio of the excess pore water pressure (u_{exc}) to $\sigma'_{v,0}$, which is the excess pore pressure ratio (r_u),

$$r_u = \frac{u_{exc}}{\sigma'_{v,0}} \quad (1.5)$$

Prior to cyclic loading, r_u = 0. A between-cycle increase in r_u indicates the soil may be advancing towards liquefaction. Initial liquefaction is defined as having occurred at the first cycle number where r_u = 1.0 is achieved (Seed 1979). In Figure 1-9, initial liquefaction occurs at 21 cycles because the effective stress (labeled normal stress in Figure 1-9) becomes 0 in the 21st cycle, corresponding to an increase in pore pressure equal to the total stress. An alternative definition of liquefaction is when a certain level of cyclic shear strain (e.g., +/- 3%) is first exceeded. Based on that definition, liquefaction occurs at 22 cycles in Figure 1-9.

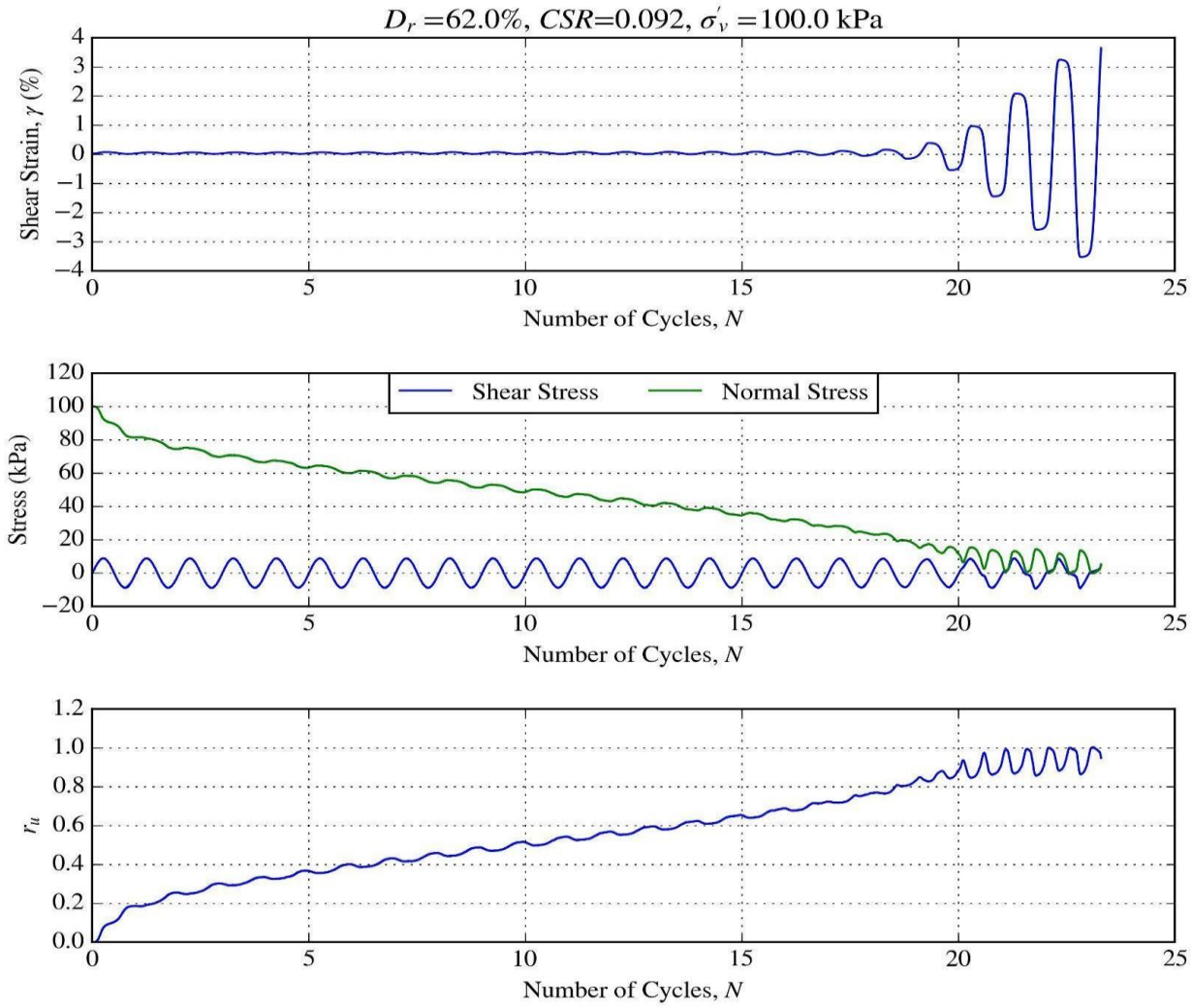

Figure 1-9. Shear strain, shear stress, normal effective stress, and ru vs number of cycles of loading during a cyclic test performed on a specimen of Monterey 0/30 sand (Ulmer 2019)

Tests such as that shown in Figure 1-9 can be used to evaluate the resistance of a given soil to liquefaction. The resistance is typically expressed as *CSR* required to liquefy granular soils in a standard number of cycles, typically 15 to 20, corresponding approximately to the duration of shaking from a reference moment magnitude (**M**) **M**7.5 earthquake. This resistance is taken as a cyclic resistance ratio, *CRR*. The demand on a given soil element from a given earthquake is the

ratio of a representative *CSR* (typically derived using 65% of the peak stress amplitude) to the initial vertical effective stress and is denoted cyclic stress ratio, *CSR*. Thus, liquefaction triggering occurs when the demand exceeds the capacity, or when *CSR* > *CRR*. This stress-based analysis is one of three general options, the others being strain-based (e.g., Dobry et al., 1982) or energy-based (e.g., Kayen and Mitchell (1997), Ulmer et al. (2023a)). There also exist alternative methods for assessing liquefaction triggering such as regional map-based assessments, laboratory and physical model tests, field measurement of pore-pressure generation under dynamic loading, and computational mechanics approaches.

The stress-based approach is the most commonly used framework (NASEM 2021; Seed and Idriss 1971; Seed et al. 1985; Whitman 1971). This framework is chosen for the approach presented herein because (i) of its common utilization in practice, which provides a strong precedent for the eventual NGL models and (ii) it provides a direct and simple way to estimate seismic demands at the NGL case history sites and in forward applications.

The use of liquefaction case histories was initiated in the late 1960s (Seed & Idriss, 1970, 1971; Seed & Peacock, 1970; Whitman, 1971). Seed & Idriss (1970) and Whitman (1971) estimated peak shear stress at depth *z* as the product of peak ground acceleration (*PGA*) and total stress (σ_v) at depth *z*. This product represents the stress if the soil profile were behaving as a rigid body. Seed & Idriss (1971) included a depth-dependent shear stress reduction coefficient, r_d, to account for the flexibility of the soil. Using this and modifying Equation 1.1 produces the following:

$$CSR_{\boldsymbol{M}=m}(z) = \frac{0.65 \cdot \tau_{cyc,max}(z)}{\sigma'_{v,0}(z)} = \frac{0.65 \cdot {PGA}/{g} \cdot \sigma_v(z) \cdot r_d(z)}{\sigma'_{v,0}(z)} \quad 1.6$$

Where $\tau_{cyc,max}$ is the maximum cyclic shear stress at depth z, $\sigma'_{v,0}$ is the initial vertical effective stress at depth *z*, *PGA* is the horizontal peak ground acceleration at the ground surface, g is the acceleration of gravity, σ_v is the total vertical stress, and r_d is a depth-dependent shear stress reduction coefficient that accounts for the nonrigid response of the soil deposit. The 0.65 coefficient reduces the *CSR* from the peak value of the shear stress to a more representative value that occurs multiple times during strong shaking. r_d is 1.0 at the ground surface and decreases with depth. Liquefaction triggering not only depends on the *CSR* but also on how many cycles occur and the confining stress and therefore the *CSR* can be adjusted using a magnitude scaling factor (MSF) and effective stress parameter (K_σ) to compute an equivalent *CSR* (*CSR**) for a reference **M** = 7.5 and $\sigma_v{}'$ = 1atm.

$$CSR_{\boldsymbol{M}=7.5,\sigma_v{}'=1atm}(z) = CSR^*(z) = CSR_{\boldsymbol{M}=m}(z) \cdot \frac{1}{MSF} \cdot \frac{1}{K_\sigma} \qquad 1.7$$

Commonly used relationships for MSF are Boulanger and Idriss (2014), Cetin et al. (2004), Cetin and Bilge (2014), and Youd et al. (2001). MSF has also been made dependent on soil density as well as magnitude in Boulanger and Idriss (2014) and Kishida and Tsai (2014) to account for decreasing density decreasing the slope of the *CSR*-N relationship (where N is the number of cycles). Others have found that this density-dependence of slope is not supported by all available data (Ulmer et al. 2018, 2022). Lack of case histories with magnitudes outside the range of 6.9 to 7.6 leads to large uncertainty in MSFs outside that range.

CRR is frequently correlated with penetration resistance such as SPT blow counts (N) or CPT tip resistance (q_c) and sometimes with small strain shear wave velocity (V_s) derived by comparing

liquefaction triggering observations and measured soil properties in case histories. The relationships predict *CRR* for reference $\sigma'_{v,0}$= 1 atmosphere, **M** = 7.5, clean sand (less than 5% soil grains less than 0.075mm by mass) and no initial static shear stress (i.e. a relatively flat site and no finite loads aka free-field). Adjustment factors for *CRR* are applied in situations where those reference conditions do not exist. Common relationships for predicting *CRR* from SPT *N* are Boulanger and Idriss (2014), Cetin et al. (2004), Cetin and Bilge (2014), and Youd et al. (2001). Relationships for *CRR* from CPT q_t are Boulanger and Idriss (2016), Moss et al. (2006), and Robertson and Wride (1998).

In liquefaction resistance analyses, different adjustments are applied to the measured in situ penetration resistance and to the computed *CRR* for reference conditions. Fines corrections are typically applied to the measured in situ parameter to modify it to an equivalent clean sand value such as clean sand corrected SPT *N* or CPT q_c. The effective stress adjustments are applied to both the in situ parameter to remove the effects of density of the soil (known as the C_N term) and the *CRR* to account for the suppression of dilatancy with increasing effective stress (known as the K_σ term). Shear stress adjustment (K_α) modifies the *CRR* to adjust for effects of static shear stress on the horizontal plane. Some of these adjustment factors in *CRR* relationships are based on field case history data which are lacking in a wide range of $\sigma'_{v,0}$ and initial static shear stress which means they are not applicable to those factors outside the dataset they were derived from. Therefore, using soil mechanics principles and experimental laboratory data (such as is done in Boulanger and Idriss 2014) to constrain these factors beyond the range existing in case histories is considered to be a sounder approach than regressing from case history data.

There are other adjustments that can be made to the in-situ measurements or *CRR* but are not accounted for in any commonly used relationships. These include system effects caused by interlayering of more and less resistant soils, drainage effects due to impeded drainage boundaries on the borders of susceptible layers and partial saturation in soil beneath the water table that may not be full saturated.

Triggering relationships can be developed within a probabilistic framework (Cetin et al. 2004; Liao et al. 1988; Moss et al. 2006; Youd and Noble 1997) so that they allow estimation of a probability of liquefaction based on a stress- and magnitude-adjusted *CSR* (CSR^*) and penetration resistance. Using a probabilistic approach provides advantages over a binary "yes" or "no" evaluation typically used in the simplified triggering procedures because it provides a result that reflects the natural variability in the data from the models were developed.

As described further in Chapter 3, these traditional case history methods for developing liquefaction triggering models require assumptions regarding identification of the layer causing the ground failure when it has occurred, or the layer mostly likely to have caused ground failure when it did not occur. The fundamental problem is that the field data of yes/no manifestation is non-uniquely related to layer performance. For these reasons, I apply an alternative approach using cyclic testing performed in the laboratory to develop an initial estimate (or "prior") for *CRR*.

Once the *CRR* and *CSR* are established, the factor of safety against liquefaction (FS_L) is computed as the ratio of *CRR* to *CSR*. Alternatively, in probabilistic models, the probability of liquefaction (P_L) can be computed as a function of CSR^* and penetration resistance.

1.2.3 Liquefaction Manifestation

Once liquefaction triggers in a soil layer, the type and magnitude of consequences can vary significantly. Potential consequences include settlement and lateral displacement, sediment ejecta (e.g., sand boils), slumping and failure of embankments, loss of foundation support, increased lateral loads on and reduced lateral resistance of earth retaining structures and their foundations, buoyancy uplift of buried structures, and modification of free-field ground motions. Some of these effects (e.g., slope, foundation, retaining structure movements) are stress-deformation problems and as such their potential for occurring is derived using equilibrium calculations with reduced strengths in liquefied strata. Others can occur in flat or nearly flat ground (sand boils, ground oscillation) and the likelihood of occurrence is determined using a liquefaction manifestation analysis that considers the thickness and depth of liquefied strata and the properties of other (non-liquefied) strata in a profile. Manifestation analyses for level-ground conditions was a major focus of my dissertation research. Manifestation apart from triggering is an important phenomenon to model because it impacts engineering design of systems that are supported above liquefiable layers, such as lightly-loaded foundations (e.g., for 1-2 story wood frame structures), paved roadways, and pipelines. The following subsections describe three methods for manifestation analysis from the literature: relative layer thickness criteria, severity index criteria, and hydraulic profile analysis criteria.

1.2.3.1 Relative Layer Thickness Criteria

Ishihara (1985) proposed bounding curves of the thickness of a non-liquefiable surficial soil layer (H_1) vs the thickness of an underlying liquefiable sand layer (H_2) to predict the occurrence of surficial manifestation of liquefaction-induced ground damage. This is illustrated in Figure 1-10. This method is widely used to essentially indicate whether a non-liquefiable crust can suppress surficial manifestation of liquefaction that triggers below the crust. Rateria and Maurer (2022) revisited this relationship and provided updated H_1-H_2 models. However, they noted that the two-layer H_1 and H_2 idealization is not necessarily entirely efficient nor sufficient to predict manifestation, and they recommended that new manifestation models are needed to explicitly account for other influential factors (e.g., effects of strata permeability, sequencing of layers, depth, and thickness on pore pressure gradients and transmission).

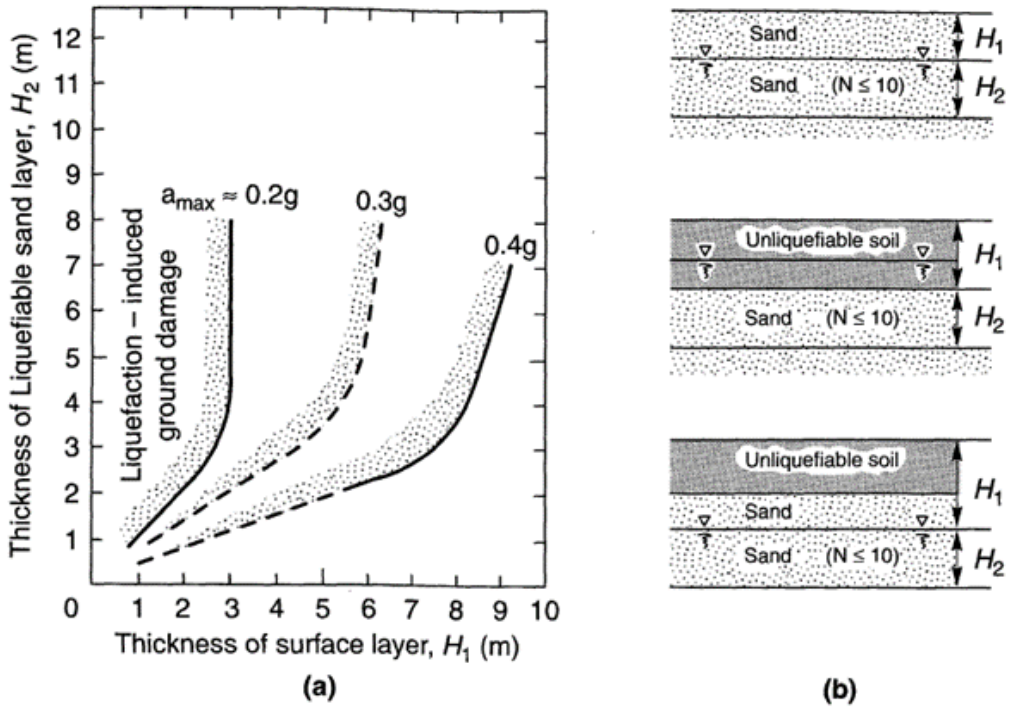

Figure 1-10. (a) Relationship between thickness of liquefiable layer and thickness of overlying layer at sites for which surface manifestation of level-ground liquefaction has been observed and (b) guides to evaluation of respective layer thicknesses (Ishihara 1985).

1.2.3.2 Severity Index Criteria

Liquefaction manifestation severity indices (MSI) estimate the severity of surface manifestations based on the cumulative liquefaction response of a profile. These models are useful because they provide indices of cumulative soil profile response, which can then be related to surface manifestations empirically. These methods do not require the identification of a critical layer as triggering models do.

Examples of common liquefaction severity indices include: the Liquefaction Potential Index (*LPI*) (Iwasaki et al. 1978), the Ishihara-inspired Liquefaction Potential Index (LPI_{ISH}) (Maurer et al., 2015), and the liquefaction severity number (*LSN*) (Van Ballegooy et al. 2014).

The *LPI* provides a depth-weighted integrated index of the potential for triggering of liquefaction at a site using the following equation:

$$LPI = \int_0^{20\ m} F \cdot W(z) \cdot dz \qquad 1.8$$

where $F = 1 - FS_L$ for $FS_L \leq 1$ and $F = 0$ for $FS_L > 1$, W(z) is the linear depth weighting function, $W(z) = 10\text{-}0.5z$ for $z \leq 20$ m and $W(z) = 0$ for $z > 20$, and z is depth in meters.

LPI depends on FS_L within the upper 20 m and depth and can apply to profiles with multiple liquefiable layers rather than selecting one critical layer. *LPI* ranges from 0 to 100 and Iwasaki et al. (1978) found that among 45 sites that liquefied in the 1964 Niigata earthquake the *LPI* corresponds to the severity categories presented in Table 1-3. Iwasaki et al. (1982, 1984, 1978) found that among 45 sites that liquefied in the 1964 Niigata earthquake the *LPI* correlates to the severity categories presented in Table 1-3. Toprak and Holzer (2003) studied the predictive capability of *LPI* at liquefaction sites in California and found that liquefaction case histories in the Monterey Bay region with an *LPI* ~ 15 have a 93% probability of showing surface manifestations while locations with *LPI* ~ 5 have a 58% probability of manifestations.

Maurer et al. (2015b) modified the *LPI* framework to include a power-law depth weighting function instead of the linear function and to account for limiting thickness of non-liquefiable capping layer according to the H_1-H_2 chart developed by Ishihara (1985). This modified *LPI* is

called LPI_{ISH} and was found to improve the predictive capacity of the index when compared to 60 case histories from several earthquakes in different regions outside Japan (Maurer et al. 2015b).

LSN uses a power-law depth weighting factor to determine cumulative liquefaction response of a profile and includes contributions from layers that have $FS_L < 2$ with the following equation:

$$LSN = 1000 \int \frac{\varepsilon_v}{z} \cdot dz \qquad 1.9$$

where ε_v is the post-earthquake volumetric strain at depth z in decimal form and z is the depth in meters. ε_v can be computed using a method developed by Ishihara & Yoshimine (1992) and implemented by Zhang et al. (2004) with CPT data. This method computes profile-averaged post-liquefaction volumetric strain as a function of FS_L. Van Ballegooy et al. (2014) computed *LPI* and *LSN* at locations where liquefaction land damage assessments had been performed after the Canterbury earthquake sequence in Christchurch, New Zealand to correlate land and building damage to those indices. They found that both *LPI* and *LSN* correlated well with observed liquefaction-induced damage. The *LSN* index value generally corresponds to severity categories shown in Table 1-3.

Table 1-3. *LPI* and *LSN* severity categories and index values (Iwasaki et al. 1984; Van Ballegooy et al. 2014).

Severity	*LPI* Value	*LSN* Value
Low	NA	≤ 20
Moderate	≤ 5	20 to 40
High	5 to 15	> 40
Very High	> 15	NA

1.2.3.3 Hydraulic Profile Analysis Criteria

A method for estimating severity of sediment ejecta onto the ground surface has been presented by Hutabarat and Bray (2021) using effective stress and transient flow analyses. They have also presented a simplified method to estimate sediment ejecta using CPT data (Hutabarat and Bray 2022). They define a liquefaction ejecta demand parameter (L_D) that estimates the upward seepage pressure that could produce artesian flow due to elevated excess hydraulic head and a crust layer resistance parameter (C_R) that captures the strength and thickness of the non-liquefiable crust layer. The method is illustrated in Figure 1-11.

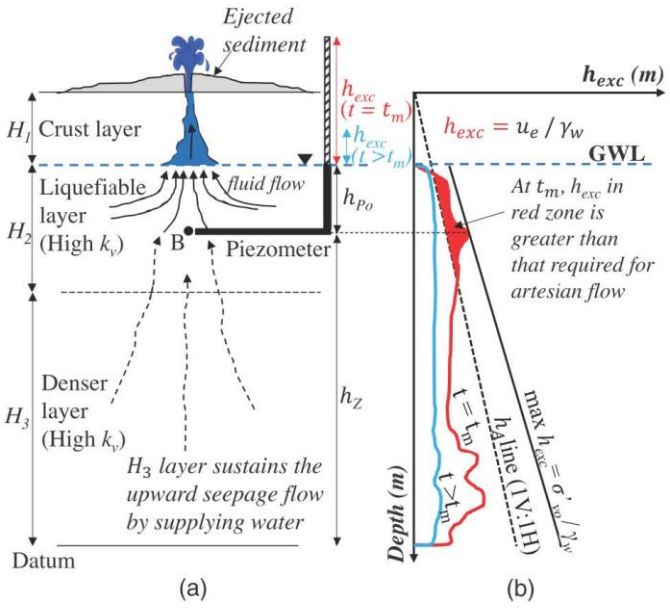

Figure 1-11. (a) Sediment ejecta mechanisms in a typical thick sand site and (b) Artesian Flow Potential concept (Hutabarat and Bray 2021).

The required parameters are calculated as follows:

$$C_R(kN/m) = \int_{0\ m}^{H_1} s_u \cdot dz \begin{cases} s_u = K_0 \cdot \sigma'_{v,0} \cdot \tan(\varphi_{cs}), if\ I_B > 22 \\ s_u = \dfrac{(q_t - \sigma_{v,0})}{N_{kt}}, if\ I_B \leq 22 \end{cases} \quad 1.10$$

where H_1 is the thickness of the non-liquefiable layer in meters as defined in Ishihara (1985), s_u is the shear strength of the crust layers in kN/m^2, K_o is the coefficient of lateral pressure (usually assumed to be 0.5), φ_{cs} is the critical state friction angle assumed to be 33 degrees (for quartz sand), and N_{kt} (i.e., the factor use to convert CPT tip resistance to shear strength) is between 14 and 20. To compute L_D, first the pore pressure ratio (r_u) needs to be estimated as a function of FS_L using a relationship proposed by Tokimatsu and Yoshimi (1983):

$$r_u = \begin{cases} 0.5 + \sin^{-1}\left(\dfrac{2 \cdot FS_L^{\left[\frac{1}{\alpha \cdot \beta}\right]} - 1}{\pi}\right), if\ 1 \leq FS_L \leq 3 \\ 1, if\ FS_L < 1 \end{cases} \quad 1.11$$

where α is 1.0 and β is -0.2. Next, the excess head (h_{exc}) is computed:

$$h_{exc} = \frac{r_u \cdot \sigma'_{v,0}}{\gamma_w} \quad 1.12$$

where γ_w is the unit weight of water (9.81 kN/m^3). The excess head can be used to estimate liquefaction ejecta demand. Another factor in ejecta demand is the vertical hydraulic conductivity (k_v) which can be estimated from CPT data using the Robertson and Cabal (2015) method:

$$k_v(m/s) = 10^{(0.952 - 3.04 \cdot I_c)} \quad 1.13$$

This correlation is only applicable when I_c is between 1 and 3.27. The k_v for a clean sand with I_c = 1.8 yields k_{cs} = 3.0E-5 m/s which is used to normalize the k_v in this method. Finally, L_D can be calculated as an integral of the normalized k_v and head with depth:

$$L_D(kN/m) = \begin{cases} \gamma_w \cdot \int_{z_A}^{z_B} \frac{k_v}{k_{cs}} \cdot (h_{exc} - h_A) \cdot dz, if\ h_{exc} \geq h_A \\ 0, if\ h_{exc} < h_A \end{cases} \quad 1.14$$

Where z_A is the depth below the groundwater table depth or the bottom depth of a crust layer that is at least 250 mm thick with $I_c \geq 2.6$, z_B is the top depth of a soil layer that is at least 250 mm thick after the first continuous sand-like layer with $I_c \geq 2.6$ between depths of z_A and 10 m (z_B will be 10 m if there is no such soil layer), and h_A is the initial hydraulic head (aka the depth in m).

Hutabarat and Bray (2022) computed the L_D and C_R at 176 field case histories and using observations of ejecta severity at those sites were able to create a chart with categories based on the L_D-C_R position as shown in Figure 1-12. This provides a useful approach for estimating manifestation severity in terms of ejecta at a site based on CPT that is applied in Section 7.2.

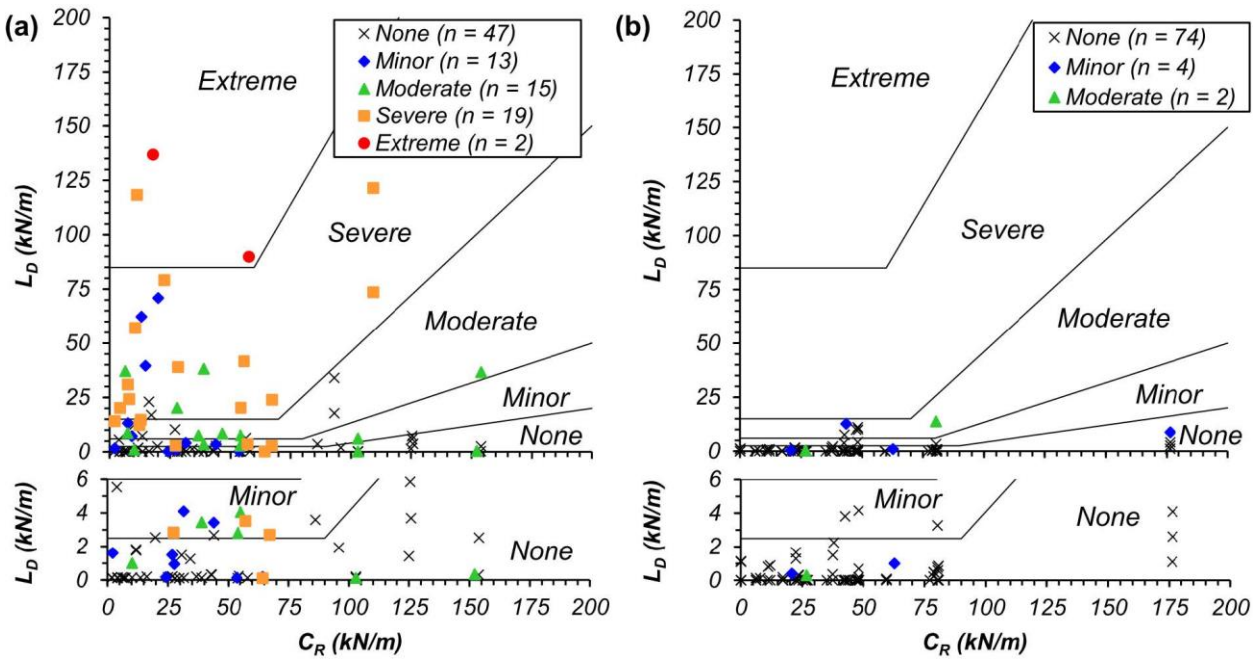

Figure 1-12. Ejecta severity using L_D and C_R parameters at: (a) thick sand sites and (b) stratified soil sites. The inserts below each plot clearly show data for L_D < 6 kN/m (Hutabarat and Bray 2021).

1.3 NGL Project Introduction

Quantifying liquefaction susceptibility, triggering, and manifestation requires datasets that span a wide parameter space, and a modeling framework that is founded in first principles known to control soil response to undrained shear. The combination of a physically meaningful modeling framework and a robust data set is required to develop robust semi-empirical models regressed from the data. One goal of the NGL project is to support this model building process by providing objective data to modeling teams, along with results of additional supporting studies to constrain effects that cannot be established solely from data. As such, a major component of the project has

been to provide a database of field case histories of liquefaction and its effects, as well as no-ground failure cases (Brandenberg et al. 2018, 2020c).

My roles in the project have had three main components. First, I have established and implemented the laboratory portion of the NGL database as described in Section 2.1. This involved designing the organization of the database structure and entering datasets into it. Second, interpolating ground motion intensity measures at liquefaction case history sites as described in Section . Third, I have assisted with the NGL supported modeling team (SMT) in its development of a new susceptibility, triggering, and manifestation framework (Chapter 4) and models (Chapter 6) using processed case histories (Chapter 5) and regression of model coefficients. The NGL SMT consists of Steve Kramer (chair), Scott Brandenberg, Kristin Ulmer, and Paolo Zimmaro (Jonathan Stewart also participates as an ex officio member).

I have also assisted NGL with case histories of special interest to the project, which are described in Sections 2.3.1 and 2.3.2.

2 Next Generation Liquefaction Database

This chapter describes my contributions to the NGL database. I was not a principal contributor to the schema design nor to the main effort to populate and review the case histories, which are described elsewhere (Brandenberg et al. 2020c). My contributions were in two main areas: (1) adding and populating a laboratory component of the database and (2) development of a few case histories of special interest. My work on (1) is presented in Section 2.2 and my work on (2) is summarized in Sections 2.4 and 2.5.

2.1 Laboratory Database Schema

While the NGL database will support model development over a certain parameter space, its contents are not sufficient to adequately constrain models over the parameter space required for application. As one example, liquefaction models need to be applicable over a wide range of vertical effective stresses (also known as K_σ affects), ranging from effectively zero up to perhaps 6 atm. The available case histories involve relatively shallow soils, and hence do not include high-overburden pressure cases. Extending models across broad parameters spaces requires additional information, which can often be provided by laboratory studies of soil behavior. As a result, the NGL database schema of (Brandenberg et al. 2020c) was expanded to allow for laboratory test information; this section describes this work. The contents of this section were previously published in a report to the US Geological Survey (Brandenberg et al. 2020a; Hudson et al. 2022).

There are many potential problem-solving capacities within NGL such as the issues with adjustment factors described in Section 1.2.2 (drainage effects (K_d), partial saturation, path

correction (K_P), 2-dimensional loading (K_{2D}), initial effective stress (K_σ), and initial static shear stress (K_α)) and the difficulty with liquefaction susceptibility criteria. The NGL database is also uniquely suited to addressing the issues with fine-grained soil susceptibility discussed in Section 1.2.1.1.

2.1.1 Database Structure

The laboratory component of the NGL database is built into the NGL relational database framework, which is a structured database that can be queried using structured query language (SQL). A relational database comprises tables linked to one another by means of identifiers called keys. Each table has a primary key that uniquely identifies table entries. If two tables are linked, the primary key of a table is used as a foreign key in another table. Primary-foreign key relationships produce the organized hierarchical structure of a database. Such organizational structure is called schema. The NGL laboratory component was developed in consultation with the NGL database working group (S.J. Brandenberg, K.O. Cetin, R.E.S. Moss, K.W. Franke, K. Ulmer, and P. Zimmaro). The schema presented here is mostly complete, but population of the database is ongoing and should continue indefinitely as more testing is done and researchers share data. The schema may have fields and/or tables added in the future if there is an interest in more types of datasets.

Twenty four tables were added to the NGL database for the laboratory component with a laboratory table at the top of the hierarchy. The field case history component is joined to the sample table via the sample-test table allowing samples to be associated with a test (under the field case history

schema) or not (under the laboratory component schema). The hierarchy of the laboratory component schema is shown in Figure 2-1. Table 2-1 contains descriptions for each table. There are 140 fields contained within the tables defined in Table 2-1 and shown in Appendix A. Appendix A also presents a dictionary with information for each new table's fields.

The table names in Table 2-1 below also correspond to the primary keys of those tables (for example, table SPEC has a primary key SPEC_ID). SPEC_ID is used as a foreign key in the following tables: TXG, DSSG, PLAS, RDEN, OTHR, INDX, GRAG, and CONG. The TXG table primary key, TXG_ID is used as a foreign key in the TXS table, which has a primary key TXS_ID that is used as a foreign key in the TXD table. Similarly, the DSSG table primary key, DSSG_ID, is used as the foreign key in DSSS which has a primary key DSSS_ID that is used as a foreign key in DSSD1D and DSSD2D. The FILE table with a primary key FILE_ID is used as a foreign key in the OTHR table, which therefore has two foreign keys, SPEC_ID and FILE_ID. GRAG_ID is used as a foreign key in the GRAT table. CONG_ID is used as a foreign key in the CON_STGE table which has its primary key (CON_STGE_ID) used in the COND table.

Table 2-1. List of Tables in the Laboratory Component of the NGL Database

Table Name	Table Description	Number of Fields
LAB	Laboratory information	5
LAB_PROGRAM	Testing Program information	3
LAB_PROGRAM_USER	Junction table between testing program and users	3
LAB_PROGRAM_SAMP	Junction table between testing program and sample	3
SAMP	General information for laboratory or field samples	10

SAMP_TEST	Junction table between sample and specimen	3
SPEC	General information for laboratory specimens taken from samples	7
INDX	Index tests include: dry and bulk density (ASTM D72863-09), water (moisture) content (ASTM D2216-10), and fines content (ASTM D1140-17). Standards recommended for each test are in parentheses.	9
RDEN	Relative density measurement	6
PLAS	Plasticity test (i.e., Liquid limit and plasticity limit) information (ASTM D4318-10e1)	6
GRAG	General information for particle size distribution analysis	4
GRAT	Test results (percent passing for a specific sieve) from particle size distribution analysis	4
OTHR	Other tests not specified above. Any format of test results can be uploaded.	6
FILE	Table storing supplemental files	5
DSSG	Direct simple shear test general information	7
DSSS	Information about each direct simple shear test stage	6
DSSD1D	One-dimensional direct simple shear test data	7
DSSD2D	Two-dimensional direct simple shear test data	9
TXG	Triaxial test general information	7
TXS	General information for triaxial test stages	6
TXD	Triaxial test data	8
CONG	Consolidation test general information	7
CON_STGE	Consolidation test stage information	5
COND	Consolidation test data	4

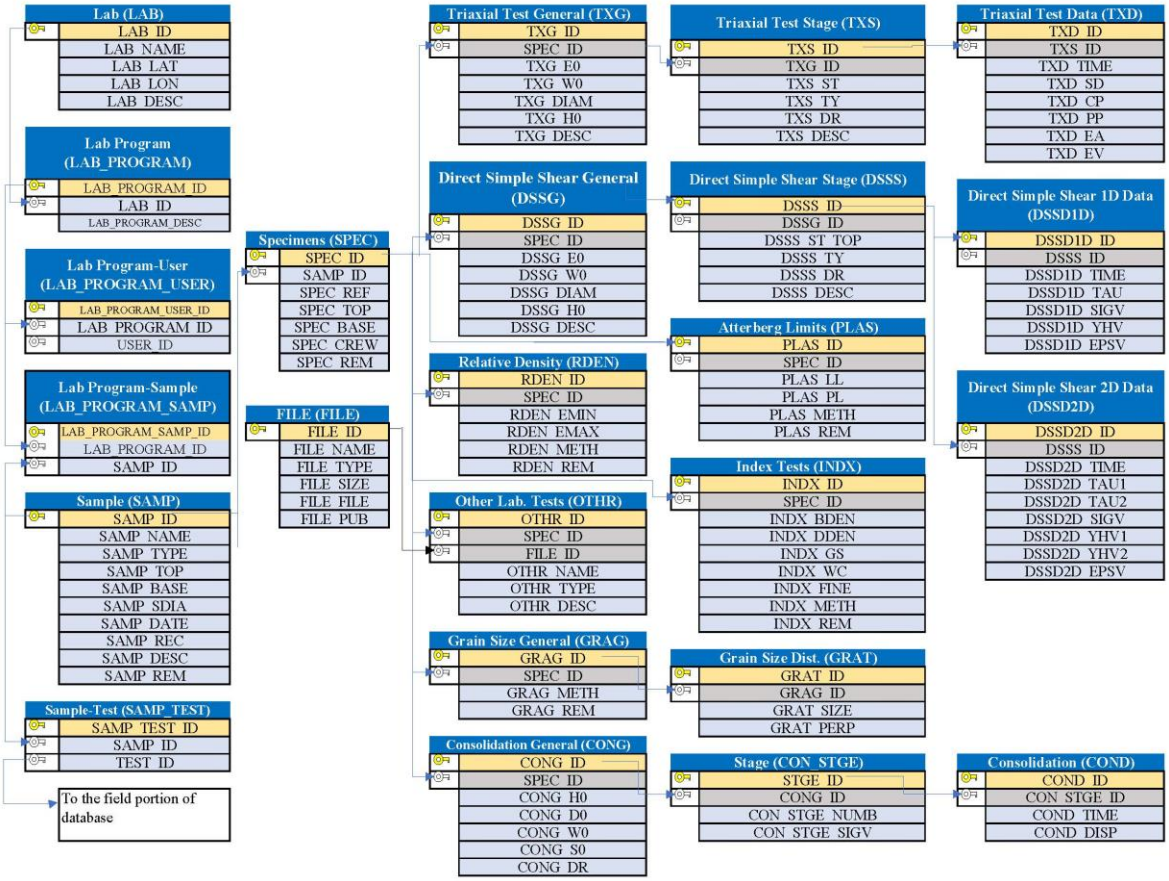

Figure 2-1. Laboratory Component Relational Database Schema Showing Relationships Between Tables Using Keys

To illustrate database functionality, consider the following example data entry for a triaxial cyclic shear test:

- First, the laboratory where the testing was performed needs to be created as an entry in the LAB table where information such as the lab name, location in latitude and longitude coordinates, and any description of the laboratory are entered. The specific testing program that the triaxial test was performed within also needs to have an entry created in the LAB_PROGRAM table and associated with the LAB entry using the LAB_ID foreign key

in the LAB_PROGRAM table. Any personnel who worked on the testing program and are to be associated with the testing program can be linked to it through the LAB_PROGRAM_USER junction table.

- The sample used in the testing is assigned an identifier (SAMP_ID) and its name (SAMP_NAME), sample type (SAMP_TYPE), depth to the top and base of the sample within a boring if associated with a boring (SAMP_TOP, SAMP_BASE) (these would be left blank if the material was a synthetic mixture created in the lab), the diameter of the sample (SAMP_SDIA), the date the sample was obtained (SAMP_DATE), the recovery rate for the sample (SAMP_REC), description of the sample (SAMP_DESC), and any remarks (SAMP_REM) are entered. This sample entry can be associated with the testing program via the LAB_PROGRAM_SAMP table and associated with a field test if it was not synthesized in the lab via the SAMP_TEST table.
- A specimen obtained from the sample (associated via the SAMP_ID foreign key) is assigned an ID (SPEC_ID), name (SPEC_NAME), and other metadata such as (1) the depth to the top and bottom of the specimen (SPEC_TOP, SPEC_BASE) if the specimen is from a boring (these would be left blank if the material was a synthetic mixture created in the lab), (2) name of the person or organization who did the testing (SPEC_CREW), and (3) other remarks about the specimen (SPEC_REM).
- Results of index testing, relative density measurements, grain size distribution analysis, or other testing is provided in tables INDX, RDEN, GRAG/GRAT, PLAS, and OTHR. That data is connected via the SPEC_ID foreign key to the SPEC table. If consolidation tests were performed separate from triaxial or direct simple shear tests, then metadata from each

stage of the consolidation tests such as final effective vertical stress and final height of the specimen (CONG_STGE_SIGV and CONG_HI, respectively) is entered into the CONG and CON_STGE tables and the consolidation data – time and displacement – are entered into the COND table. The COND table is linked via CON_STGE_ID as the foreign key which is linked to the CONG table using the CONG_ID foreign key.

- Triaxial data is entered by first entering the general metadata for the triaxial test (TXG table) such as initial void ratio, water content, specimen diameter, initial height, and any descriptive information (TXG_E0, TXG_W0, TXG_DIAM, TXG_H0, and TXG_DESC, respectively). The triaxial test stage table (TXS) contains a foreign key to the TXG table and also contains fields for the stage number, type of stage (i.e. consolidation, monotonic loading, or cyclic loading), drainage (i.e. drained, undrained, or neither), and a description of the stage (TXS_ST, TXS_TY, TXS_DR, and TXS_DESC, respectively). The triaxial test data (TXD) table has a foreign key connecting it to the TXS table (TXS_ID) and has fields for time, deviator stress, cell pressure, pore pressure, axial strain, radial strain, and volumetric strain vectors (TXD_TIME, TXD_SD, TXD_CP, TXD_PP, TXD_EA, TXD_ER, TXD_EV, respectively).

Direct simple shear tests are entered similarly to triaxial tests, however there is an option for entering 1 or 2-dimensional test data.

2.1.2 Data Querying and Visualization

Currently the laboratory component of the NGL database cannot be accessed in the same manner as the field case history component via the interactive website (https://nextgenerationliquefaction.org) because there has not been adequate time or budget to add that capability. However, the database is replicated daily to DesignSafe (Rathje et al., 2017a), where it can be queried by any user using Python scripts in Jupyter notebooks. A Jupyter notebook is a server-client application that allows editing and running notebook documents in a web browser and combines rich text elements and computer code executed by a Python kernel (Perez and Granger, 2007). Jupyter notebooks are published and available on DesignSafe in the NGL project partner data apps (Brandenberg et al. 2020c and references therein).

Users can create their own custom Jupyter notebooks to query and visualize data from the NGL database for use in model development. The published notebooks are a good starting place on which to base new custom notebooks and to learn how to write SQL queries in Python.

Figure 2-2 and Figure 2-3 present a Jupyter notebook for visualizing direct simple shear test data. The user can select a laboratory from the first dropdown menu and the tool populates the Program dropdown menu with all the testing programs at that particular lab. Based on the selection from the Program dropdown, the Sample dropdown is populated with all samples within that testing program. The user can then select a specimen from the Specimen dropdown menu and the tool populates the DSSG_ID dropdown menu with the direct simple shear general table IDs that are performed on that specimen (from the DSSG table). Based on the selection from that dropdown, the tool populates the DSSS_ID dropdown with the stages for that particular test. The tool plots

the data from the selected stage in nine separate plots to help visualize it. Figure 2-2 shows a view of the tool within a web browser. Figure 2-3 shows the consolidation stage and the cyclic loading stage of a randomly selected test.

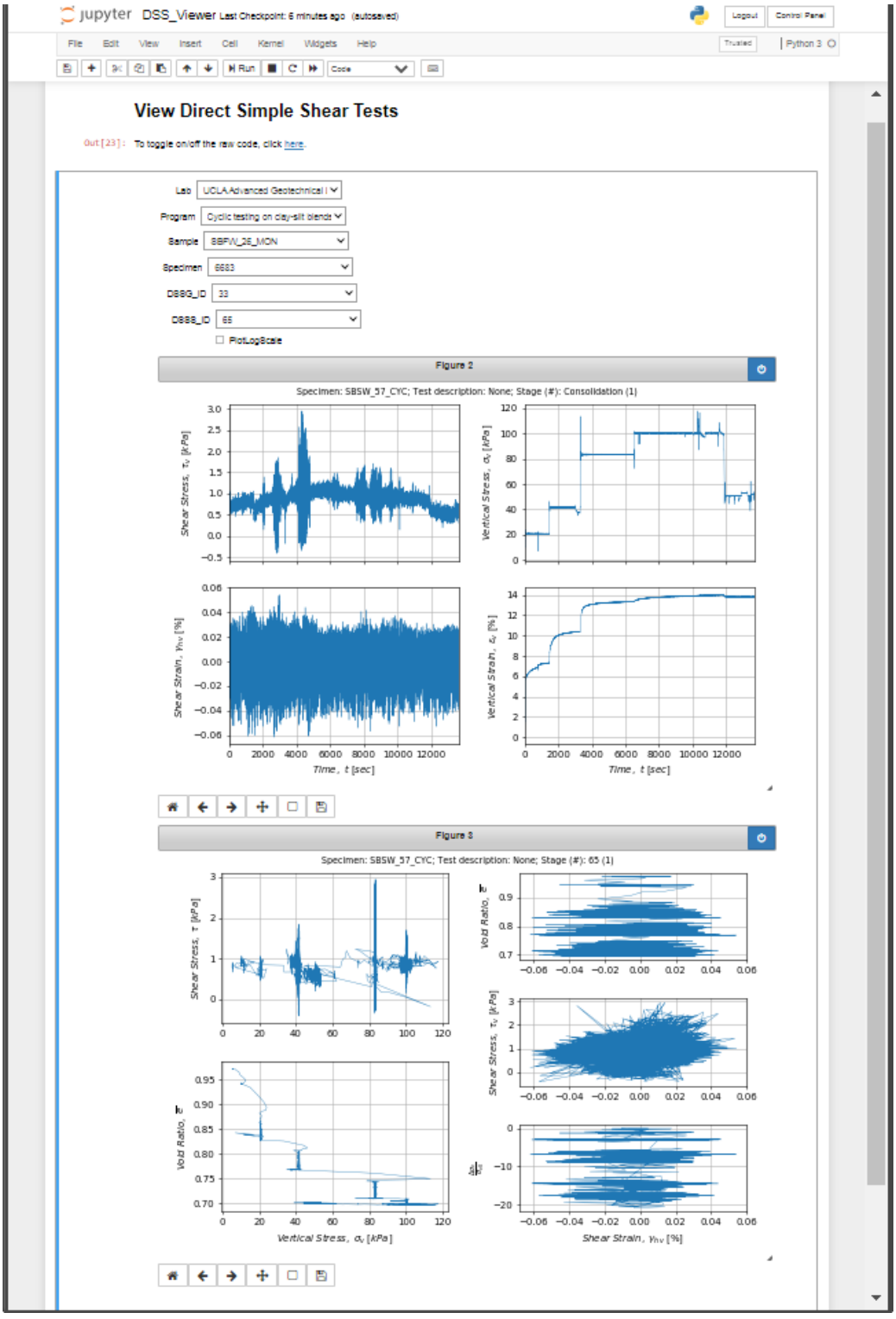

Figure 2-2. Direct Simple Shear Test Viewing Jupyter Notebook Tool in Web Browser

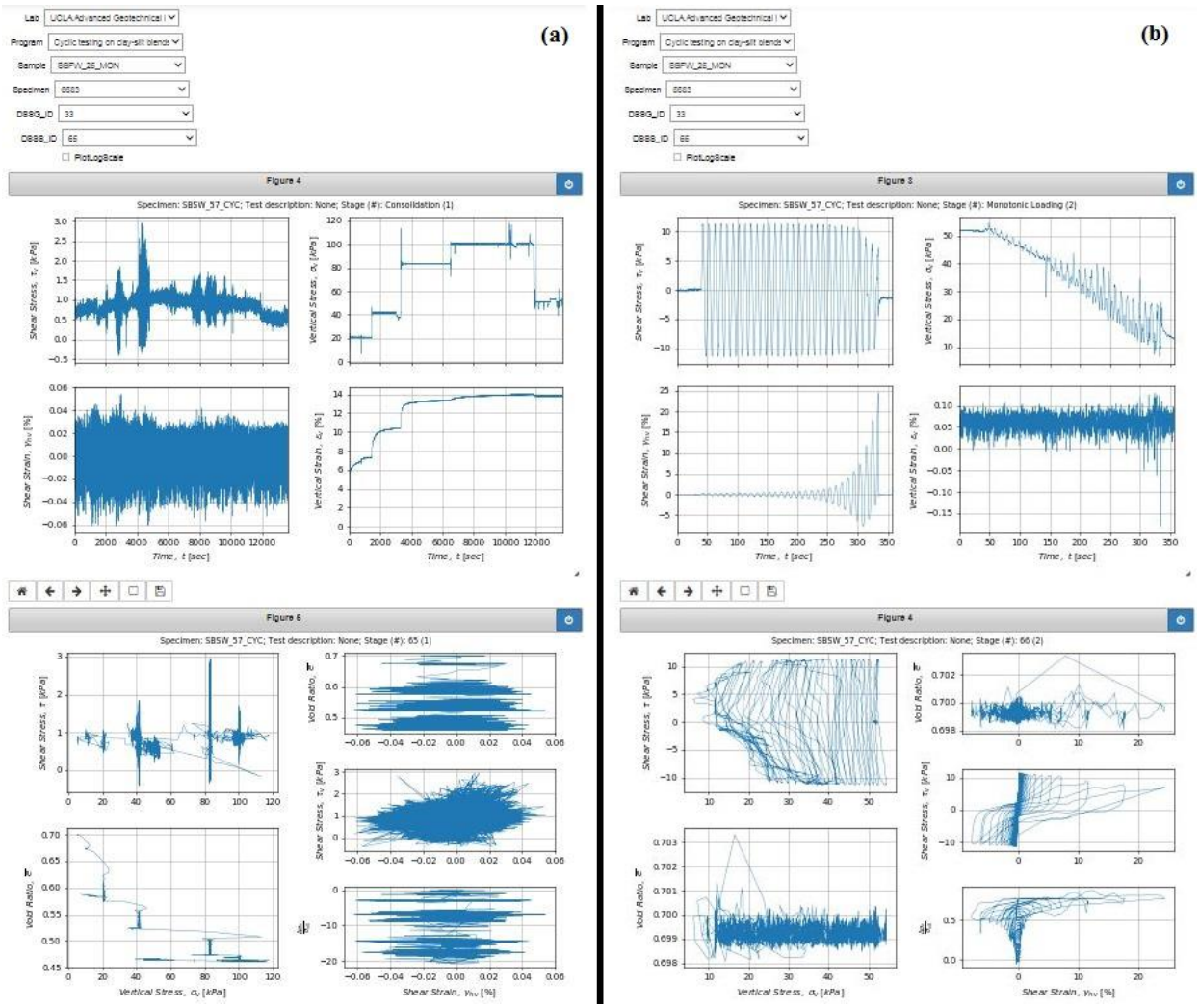

Figure 2-3. Direct Simple Shear Test Viewer Jupyter Notebook displaying consolidation stage (a) and cyclic stage (b) test data

2.2 Status of Database

The database consists of a case history portion (including sites with in situ tests, observations of liquefaction manifestations or no manifestations, and estimates of ground shaking intensity) and a

laboratory portion (consisting of tests performed on samples retrieved from sites and soils synthetically mixed in the laboratory). The following details the amount of data stored within each portion of the database.

As of this writing (December 2023), the NGL database has 347 sites, 147 of which have been fully reviewed (meaning reviewed twice) and 135 have been partially review (reviewed once). There are 843 cone penetration tests (CPTs), 696 boreholes with 7559 standard penetration test (SPT) measurements, 125 invasive shear wave velocity measurements (such as downhole), and 30 surface wave method tests (such as spectral analysis of surface waves, SASW).

There are 6 laboratories and 8 laboratory testing programs. The number of labs and testing programs are low because most tests outside of the direct simple shear and triaxial tests have not been linked with a laboratory and just with the field investigation. Table 2-2 shows the laboratory testing programs currently in the database. The counts for laboratory tests are shown in Table 2-3. Figure 2-4 displays a plot of all the plasticity tests in the database on a Casagrande chart to aide in visualizing of the data distribution.

Table 2-2. Lab testing programs currently in the NGL database

ID	Lab Program Description
1	Testing of samples from sites associated with the Canterbury Earthquake Sequence by Christine Beyzaei (Beyzaei 2017)
2	Cyclic and monotonic direct simple shear on Orange Co. Silica Sand by Mandro Eslami (Eslami 2017)
3	Testing on samples from Mihama Ward associated with 2011 Tohoku earthquake
4	Lab testing associated with Cetin et al. (2018)
5	Lab testing associated with Graded area east of New River at SW edge of Brawley
6	Lab testing associated with 1979-1981 with CPT retesting in 2003 (Moss et al. 2005). Additional site information and SPT descriptions given in Bennett et al. (1981) and Youd and Bennett (1983)
7	Cyclic testing on clay-silt blends for Mandro Elsami's dissertation (Eslami 2017)
8	Testing of remolded samples from Mihama Ward

Table 2-3. Counts of laboratory tests within the NGL database.

Test	**Total**
Index (specific gravity, water content, and/or percent passing number 200 sieve)	3847
Relative Density	77
Plasticity (Atterberg limits)	1385
Gradation	4495
Direct Simple Shear	53
Triaxial	63
Consolidation	4

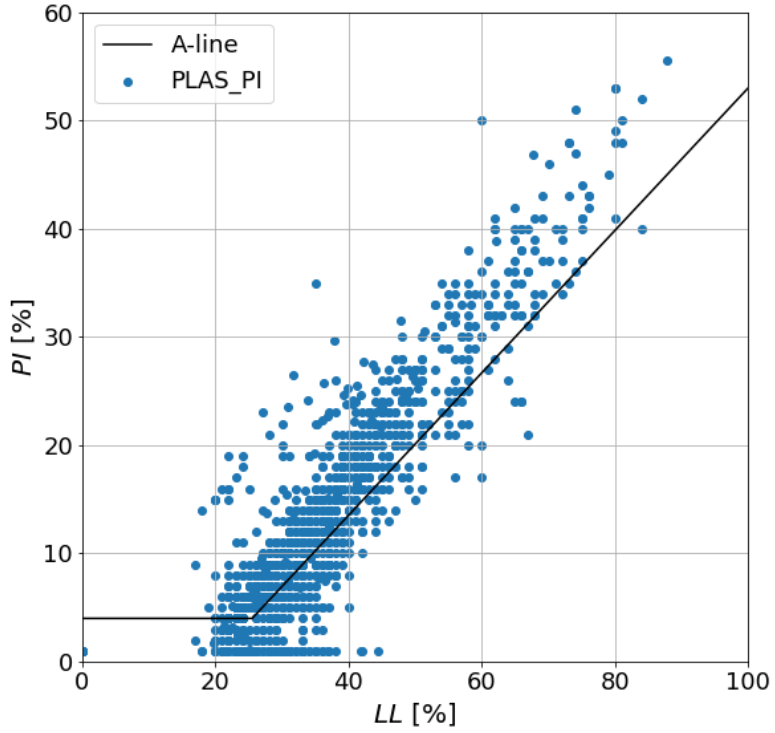

Figure 2-4. Collection of plasticity tests within the NGL database.

The field case histories in NGL are significantly larger than prior databases that have been used to develop liquefaction models. Figure 2-5 shows the number of liquefaction or non-liquefaction observations from earthquakes compared between prior databases and NGL.

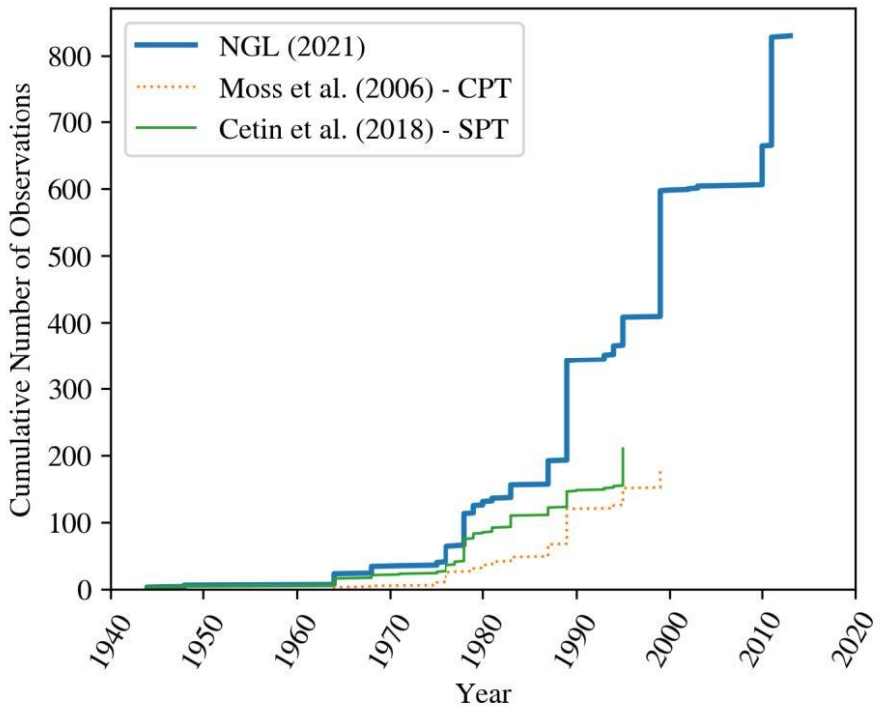

Figure 2-5. Cumulative Number of Liquefaction or Non-Liquefaction Observations from Earthquakes Since 1945 in the NGL Database Compared to Earlier Liquefaction Databases: Moss et al. (2006) and Cetin et al. (2018) (Ulmer et al., 2021)

2.3 Notable New Case Histories

I assisted in development of two notable case histories as part of this research project: Mihama-ward and Searles Lake. The former involved laboratory testing and populating the NGL database with information and the later involved post-earthquake reconnaissance and a series of truck mounted and handheld CPT soundings along with hand augers and sampling. A brief overview is provided in Sections 2.3.1 and 2.3.2 and some detailed analysis in Section 7.2.

2.3.1 Mihama-ward Case History Laboratory Tests

A moment magnitude (**M**) 9.1 earthquake (Duputel et al. 2012) occurred on March 11, 2011 near the northeast coast of Honshu, Japan approximately 129km east of Sendai resulting from shallow thrust faulting on the subduction zone plate boundary between the Pacific and North American plates. A region of the Mihama-ward district of Chiba has surficial soils consisting of hydraulic fill materials. Some of these soils are relatively granular and experienced liquefaction as evidenced by surface manifestations, while other areas are relatively cohesive and experienced no ground failure. This collection of different observations for essentially identical input motions and site geological conditions provides a unique case history for liquefaction susceptibility and triggering. Site investigations were performed in two phases. The first phase was conducted by a Chiba University team, who performed which conducted 9 CPT soundings (Nakai and Sekiguchi 2013). To obtain samples for laboratory testing, a subsequent investigation by a collaboration of UCLA and Chiba researchers drilled 3 borings and performed 3 SASW tests in areas with no ground failure, marginal ground failure, and severe ground failure. Samples from the borings were initially tested at Tokyo Soils Research.

Tokyo Soils sent some of these samples from the Mihama-ward borings after they had performed laboratory tests to the UCLA geotechnical laboratory for more testing. I performed several Atterberg limits tests, grain size distribution test, one consolidation test, minimum and maximum void ratio tests, and monotonic and cyclic direct simple shear tests on some of these samples. These laboratory tests were uploaded into the NGL database, but the efforts are not pertinent to the rest of this thesis and have not been included for brevity. Section 7.2 contains details on liquefaction

triggering and manifestation calculations from CPT data at Mihama-ward comparing prior and new models presented in this thesis.

2.3.2 2019 Ridgecrest Earthquake Sequence Reconnaissance

The 2019 Ridgecrest earthquake sequence provides unique and important case studies for liquefaction and surface fault rupture. The Ridgecrest earthquake sequence included a moment magnitude (**M**) 6.5 event on July 4 and **M** 7.1 event on July 5 on faults within the Salt Wells Valley Fault Zone and Paxton Ranch Fault Zone, respectively, approximately 10km northeast of Ridgecrest, California and approximately 15km west of Searles Lake.

Both the **M** 6.5 and 7.1 events caused widespread liquefaction within and along the margins of Searles Lake as well as some liquefaction within the Indian Wells and Salt Wells Valleys. The GEER Association deployed a team to collect perishable information in the area such as ground-failure features and damage to infrastructure and buildings. I assisted with the reconnaissance efforts and data processing (Stewart et al. 2019; Brandenberg et al. 2020b; Zimmaro et al. 2020b; Zimmaro and Hudson 2021; Goulet et al. 2021; Nweke et al. 2022). More recently, site characterization has been performed at several sites with and without manifestation of liquefaction in the Searles Lake lakebed area. That work will be presented in various reports and the dissertation of Timothy O'Donnell. This data is being input into the NGL database as case history data.

3 Legacy Models and Critical Layer Selection

The following Sections 3.1-3.4 were previously presented in an NGL SMT draft report (Ulmer et al. 2023b).

3.1 Past Approaches to Developing Triggering Models

The most common method used to obtain what has traditionally been considered a "triggering" model is to analyze case histories of observations of liquefaction manifestation or lack thereof in the field during past earthquake events. In principle, other information, including in situ pore pressure measurements, subsurface deformations, or ground motion recordings, could indicate the triggering of liquefaction within a subsurface layer at a site. However, such information has not been available nor used to any significant degree in the development of previous models. Thus, existing models tend to rely on observation of surface evidence of manifestation or no manifestation to indicate that triggering occurred or did not occur at some depth within any layer in the profile.

Efforts to document and process liquefaction case histories have been ongoing for decades (e.g., Andrus et al. 2003; Boulanger and Idriss 2014; Cetin et al. 2000, 2004, 2018; Kayen et al. 2013; Moss 2003; Seed et al. 1984; Seed and Idriss 1971), and have supported the development of multiple previous liquefaction models. These datasets provide information for each case history used in model development, such as:

- earthquake magnitude (**M**) and ground motion at the site (e.g., *PGA*),

- brief descriptions of observations at the ground surface (e.g., presence or absence of ground failure),
- depth to groundwater table,
- attributes of the soil layer considered by the model developers to indicate the single layer most likely to have liquefied (e.g., σ_v, $\sigma'_{v,0}$, in situ test measurements, *FC*) or of the layer that would have liquefied first if the ground shaking had been stronger.
- *CSR* as computed by the respective authors.

The triggering models developed from these case history datasets consist of a relationship between *CRR* and some indirect measure of soil relative density such as SPT blow counts (*N*), CPT tip resistance (q_c), or small strain shear wave velocity (V_s). These relationships were derived by plotting *CSR* vs the soil density parameter for "liquefaction" and "non-liquefaction" data points and drawing a boundary curve separating the two domains (e.g., Figure 3-1 from Seed et al., 1985). That curve, historically drawn to be conservative but more recently determined through regression, is assumed to represent *CRR*. The relationships predict *CRR* for reference conditions of $\sigma'_{v,0}$ = 1 atm., **M** = 7.5, clean sand (fines content less than 5%), complete saturation (*S* = 100%), and no initial static shear stress (i.e., a relatively flat site and no finite loads, also known as free-field sites).

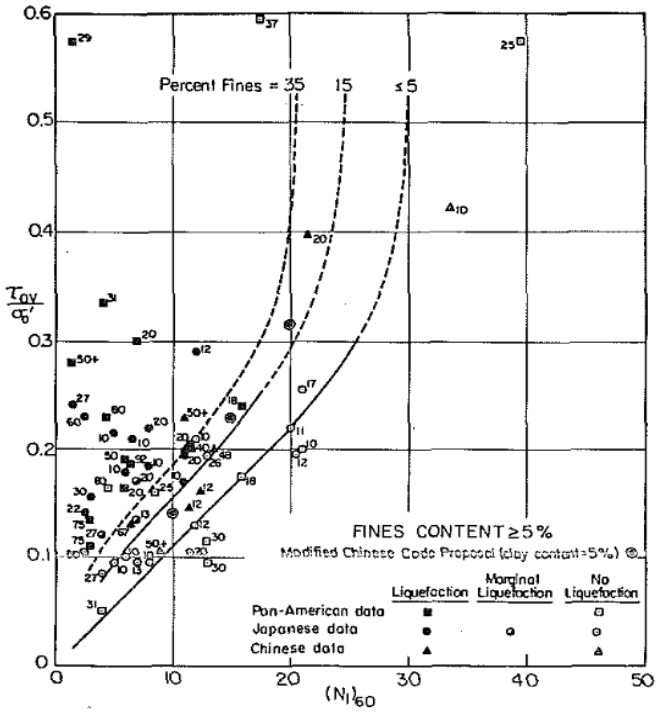

Figure 3-1. An example of a suite of *CRR* curves for different levels of fines content (from Seed et al., 1985)

As previously noted in Section 1.2.2, liquefaction "triggering" models also include adjustment factors to relate actual conditions to the assumed reference conditions. One group of factors is applied to the measured in situ parameter (i.e., N, q_c, or V_s) and the other is applied to the computed *CRR* or *CSR* (i.e., to compute the normalized value, $CSR_{\mathbf{M}7.5,1atm}$, which is commonly denoted CSR^*). The in-situ parameters are adjusted for the effects of overburden stress (through the C_N term) so that they apply for a common reference stress of 1 atm. The in-situ penetration resistance parameters are also corrected for non-zero fines contents to account for both the reduced penetration resistance of fine-grained soils at a common relative density, which is mainly a consequence of reduced moduli (Carraro et al. 2003; Cubrinovski and Ishihara 2002; Ecemis and

Karaman 2014; Jefferies and Been 2015), and changes in the cyclic strength of soils with fines (Park & Kim, 2013; Polito & Martin, 2001). The resulting overburden and clean-sand values are clean sand corrected SPT blow count ($N_{1,60cs}$) and CPT tip resistance (q_{c1Ncs}).

The *CRR* adjustments are applied to correct for systematic differences in the expected number of loading cycles for **M** ≠ 7.5 earthquakes, effective overburden stresses ≠ 1.0 atm, and static shear stresses ≠ zero. The magnitude correction (*MSF*) is used to account for reductions of resistance with increasing number of cycles. The overburden correction (via the K_σ term) accounts for the suppression of dilatancy with increasing effective stress. The shear stress adjustment factor (K_α) modifies the *CRR* to adjust for effects of initial static shear stress on the horizontal plane. More details about the K_σ and K_α correction factors are discussed in the NGL Task 5 report (Ulmer et al. 2022). The K_σ correction factor is typically obtained either through direct regression of the field case history data (Cetin et al., 2004; Moss et al., 2006) or through soil mechanics principles and experimental laboratory data. The K_α factor is obtained using experimental laboratory data (e.g., Boulanger 2003a; b; Boulanger and Idriss 2014; Cetin and Bilge 2014). Historically, the case history datasets have not represented a broad enough parameter range to constrain these correction factors for in situ conditions considered in liquefaction triggering evaluations.

3.2 Legacy Models

In this dissertation, I refer to models developed prior to the 2016 NASEM report as “legacy” models. Of these legacy models, common relationships for predicting *CRR* from SPT data include Boulanger & Idriss (2012), Cetin et al. (2004, 2018), Idriss & Boulanger (2008), and Youd et al.

(2001). Frequently used relationships for predicting *CRR* from CPT data include those of Boulanger & Idriss (2016), Idriss & Boulanger (2008), Moss et al. (2006), and Robertson & Wride (1998). Relationships for predicting *CRR* from V_s include Andrus & Stokoe (2000) and Kayen et al. (2013). Some models have been developed based on laboratory testing of soil specimens that were sampled from case history sites (e.g., Matsuo, 2004; PWRI, 2016; Tokimatsu & Yoshimi, 1983). While early relationships were deterministic in nature, recent models have been developed within a probabilistic framework (Boulanger and Idriss 2012, 2016; Cetin et al. 2004, 2018; Kayen et al. 2013; Liao et al. 1988; Moss et al. 2006; Youd and Noble 1997), allowing them to estimate a probability of liquefaction (P_L).

For brevity, not all *CRR* models are discussed here. For the purposes of this dissertation, I provide additional details about the components of the widely used Boulanger & Idriss (2016) CPT-based model only. This does not indicate endorsement by the NGL project of this model over any other model, but it is simply used for the purpose of comparison at several points throughout the dissertation. The parameter range and number of case histories represented in several legacy models are summarized in Table 3-1. Note that the range of $\sigma'_{v,0}$ is limited to less than 200 kPa (and less than 150 kPa in some cases) and the critical depth is generally within about 12 m (and most often less than 8 m) of the ground surface. These relatively shallow critical depths are due in part to manifestation at the surface being less likely for deeper liquefied layers. Thus, there are possibly some cases where liquefaction could have been triggered at depth without producing observable manifestation at the surface.

Table 3-1. Summary of Recent Liquefaction Triggering Case History Databases for Level-ground Conditions Showing Ranges in Values of the Parameters (from NASEM, 2021).

Parameter	SPT		CPT		V_s
	Cetin et al. (2004)	**Boulanger & Idriss (2012)**	**Moss et al. (2006)**	**Boulanger & Idriss (2016)**	**Kayen et al. (2013)**
Number of "yes" cases	109	133	139	180	287
Number of "no" cases	88	118	44	71	124
Number of "yes/no" cases	3	3	0	2	4
Critical depth (m)	1.1-20.5	1.8-14.3	1.4-14.0	1.4-11.8	1.1-18.5
σ'_{v0} (kPa)	8.1-198.7	20.3-170.9	14.1-145.0	19.0-147.0	11.0-176.1
FC (%)	0-92	0-92	--	0-85	--
$N_{1,60cs}$ (blows/30cm), q_{c1Ncs} (atm), or V_{s1} (m/s)	2.2-66.1[a]	4.6-63.7	11.2-252.0	16.1-311.9	81.7-362.9
$CSR_{M7.5}$	0.05-0.66	0.04-0.69	0.08-0.55[b]	0.06-0.65	0.02-0.73
M	5.9-8.0	5.9-8.3	5.9-8.0	5.9-9.0	5.9-9.0

[a] *$N_{1,60}$ values listed for (Cetin et al., 2004) as opposed to $N_{1,60cs}$*

[b] *CSR values listed for Kayen et al. (2013) and Moss et al. (2006), as opposed to $CSR_{M7.5}$*

As is typical of geotechnical engineering research, the projects that produced the legacy models were conducted by individual investigators or small teams of investigators. The investigators collected data, analyzed the data, and developed the models. Datasets used in model development were often never published in full, or if they were, it was after the model development process had been completed. Furthermore, published data products generally consisted of properties of the critical layer selected by the research group, and properties of other layers were not included. Research results were generally not widely shared with the community during model development.

This traditional research approach has drawbacks, such as lack of transparency (case history data not fully presented) and repeatability (case history interpretations made during model development that are not documented) that the NGL project was organized to overcome. These drawbacks can create divergence between how models are applied in forward applications vs how they were developed, which can limit model effectiveness. One of the most important elements of this disconnect is related to critical layer selection, which is examined further in the next section.

3.3 Critical Layer Selection

The concept, meaning, and identification of critical layers as representing the characteristics of an entire liquefiable soil profile are complex. They are, however, central to both the development and use of legacy triggering models. Their importance warrants recognition and discussion as background to the development of new triggering models.

3.3.1 Non-uniqueness

The legacy models described in Section 3.2 utilized a critical layer framework in which the layer most likely to produce manifestation was selected as being representative of the profile or site. For "yes" cases, the critical layer is selected as the layer that is considered to have been most likely to have liquefied. In some cases, this layer can be established with a high degree of confidence. For example, the Wildlife Liquefaction Array in California (NGL site ID 187; Holzer & Youd, 2007) and the Nakashimo levee site in Japan (NGL site ID 423; Zimmaro et al. 2020a) include piezometers in layers that developed significant excess pore pressures, which confirms that liquefaction triggered in those layers. At the Sandholdt Road site from Moss Landing, California, an inclinometer indicated lateral deformation within a layer during the Loma Prieta earthquake (NGL site ID 696; Boulanger et al. 1995, 1997), which indicated that liquefaction-induced strength loss likely occurred in that layer. However, in most cases, the only evidence of liquefaction is surface manifestation such as sand boils, ground cracking, or other deformations. In such cases, the case history interpretation is often inconclusive with respect to which layer produced manifestation.

One approach is to assign the critical layer as the weakest link in the chain, which is accomplished in the case of CPT data by finding the layer with smallest continuous interval of tip resistance with low friction ratio, or the susceptible layer with the smallest *CRR* (Cetin et al. 2018; Kayen et al. 2013; Moss et al. 2006). Although the documentation of these studies does not clearly distinguish manifestation from triggering in the reasoning behind critical layer selection, the weakest link approach is a method that favors triggering. A complication with the weakest link framework is that a pre-existing model is used to compute *CRR*, which is then used to select the critical layer

whose properties are used to develop a new model. The use of pre-existing models in critical layer selection and model development can lead to confirmation bias, as discussed in Section 3.3.2.

Consider, for example, the Landing Road Bridge site (NGL site ID 161), for which surface manifestation was observed in the form of lateral spreading, surface cracks, sand boils, and damage to the foundations of a nearby bridge following the 1987 Edgecumbe, New Zealand earthquake. Figure 3-2 shows a CPT profile for this site, interpreted using procedures described in Sections 5.3-5.4. Layer numbers are indicated to the right of the profile of q_{c1Ncs}. While many layers at the site are likely not susceptible, layers 2 and 6 near depths of 1.5m and 5m, respectively, are loose granular soils (low I_c) with somewhat higher relative density (q_{c1Ncs}) in the deeper layer than the shallower one (115 vs. 90, respectively). It could be reasonably argued that either is the critical layer. Layer 2 is closer to the ground surface and has the lower q_{c1Ncs} and therefore is most likely to manifest. However, since it is immediately beneath the groundwater table, partial saturation is possible, which would increase its liquefaction resistance. Accordingly, it could be argued that the deeper but thicker layer 6 is more critical. As this example illustrates, the selection of the critical layer often involves considerable judgment, and this judgment naturally varies between different analysts, as described further in Section 3.4.

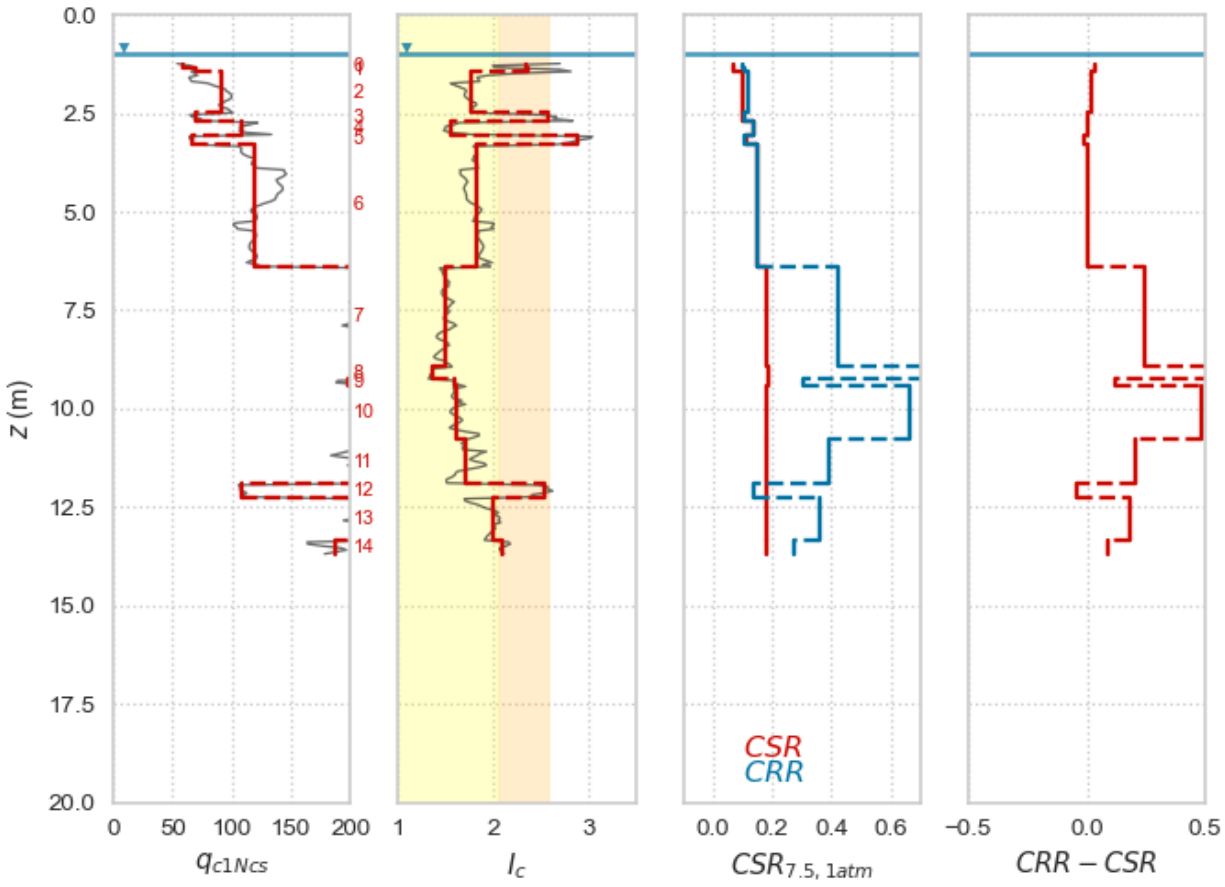

Figure 3-2. Example CPT profile for the Landing Road Bridge site (CPT LRB007) from the 1987 Edgecumbe, New Zealand earthquake derived using procedures presented in Sections 5.3-5.4. This is an example of a site for which multiple critical layers could be selected for use in model development.

One way to resolve ambiguities like that illustrated in Figure 3-2, in cases where sand boils form, is to identify the critical layer by matching gradation and coloration characteristics of ejecta to soils at depth (Cetin et al. 2000; Green et al. 2011; Liao and Whitman 1986). However, upward flowing sand can entrain soil from overlying layers with it and/or deeper soils might have also liquefied but not formed ejecta. As a result, uncertainties in critical layer identification remain.

These uncertainties are also present for “no” manifestation cases. In such cases, the critical layer is intended to represent the layer that most likely would have liquefied and manifested had the intensity of shaking been larger or the duration longer (Seed & Idriss, 1971; Whitman, 1971). Consider for example the Radio Tower site (NGL site ID 318), for which no surface manifestation was observed following the 1979 Imperial Valley earthquake. Figure 3-3 shows a CPT profile for this site, interpreted using procedures described in Sections 5.3-5.4. While many of the layers at the site are likely not susceptible, layers 3-4 near 2.5 m depth and layer 7 near 5 m depth are granular soils (low I_c) with apparently similar relative densities (by correlation to q_{c1Ncs}). It could be reasonably argued that either is critical. In the case of layers 3-4, it is close to the ground surface and therefore is most likely to manifest if liquefaction triggers. However, because it is immediately beneath the groundwater table, partial saturation is possible, which would increase liquefaction resistance. Accordingly, it could be argued that layer 7 is more critical. On the other hand, layer 5 or layer 9 could also be considered critical, despite being less likely to be susceptible (high I_c), given that they have lower q_{c1Ncs} values and are as thick or thicker than layers 3, 4, and 7.

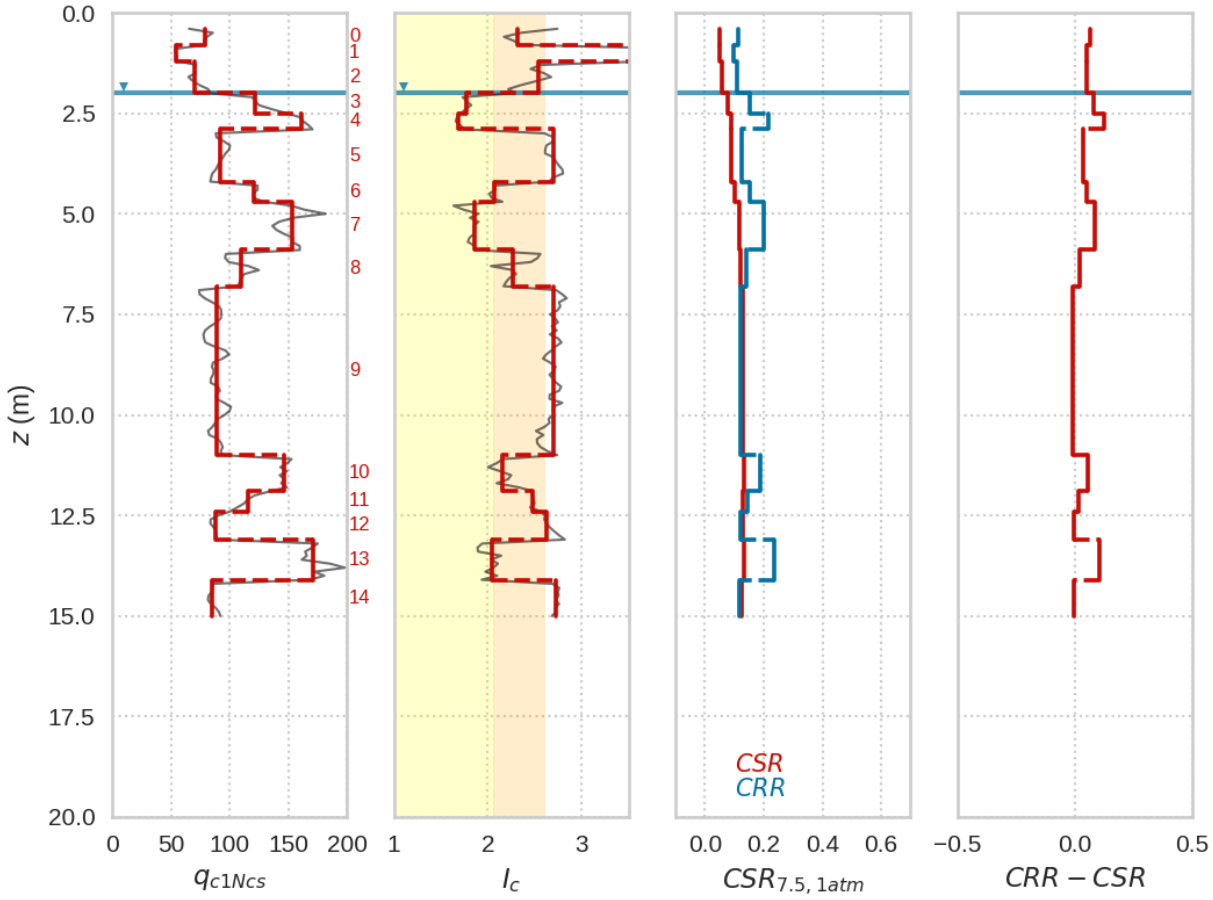

Figure 3-3. Example CPT profile for site Radio Tower (CPT R4) from the 1979 Imperial Valley earthquake derived using procedures presented in Sections 5.3-5.4. This is an example of no manifestation for which multiple critical layers could be selected for use in model development.

As these examples illustrate, in the absence of a model for predicting triggering/manifestation, it can be difficult to identify a single layer within a profile that is most critical for surface manifestation. While some semi-empirical models were developed through use of the "weakest link" approach, the extent to which that process of identifying critical layers considers manifestation is not clear. When manifestation is considered, a great deal of judgment is required. Critical layer selection should consider layer thickness, depth, stratigraphy, surface geology,

spatial variability and lateral continuity of potentially liquefiable layers, and presence of sloping ground or a free face (Boulanger and Idriss 2014; Green and Olson 2015), each of which affect how a complex system of soil layers responds to an earthquake (Cubrinovski et al. 2019). In the development of legacy models, these judgments are operator-dependent, generally not well-documented, and therefore not repeatable. Critical layer selections in some legacy model case histories have been made with consideration of information beyond that represented by a CPT log. This can include multiple CPTs at a given site or boring logs with samples that may include laboratory data. Different modelers looking at these different data sources may consider different data sources in their selections, which can influence variability. The focus in this section has been to develop a model for prediction of liquefaction using CPT data because this represents a common situation for forward applications.

3.3.2 Potential for Confirmation Bias

The need to apply judgment in the selection of critical layers during a process of model development sets up the potential for confirmation bias, which is defined as "the tendency to interpret new evidence as confirmation of one's existing beliefs or theories" (Oxford Dictionary of English 2010). Confirmation bias is often unintentional and can arise from a person's beliefs about a particular outcome. Consider, for example, a case history in which two alternative critical layer selections are essentially equally viable, in which one choice produces a *CSR*-q_{c1ncs} data point that is in agreement with a model (i.e., a "yes" case above the curve or a "no" case below the curve) whereas the other choice places the data point in conflict with the model. The temptation would

be strong to select the choice that agrees with the model, especially if the alternative is a data point that would comprise a strong outlier (i.e., a "no" case well above the curve or a "yes" case well below the curve). This temptation is known as cognitive bias, which is a systematic pattern of deviation from norm or rationality in judgement despite contrary evidence (Haselton et al. 2015). Such cognitive biases are widely recognized in scientific research in other fields (e.g., Nickerson, 1998; Hirschhorn and Schonberg 2024).

The NGL site "Imazu Elementary School" (NGL site id = 539, test ID = 2584), shown in Figure 3-5, is an example of such a case. This site, which experienced surface manifestation of liquefaction from the 1995 Kobe earthquake (NGL field manifestation ID, FLDM ID = 1432). As in the two previously described cases, multiple critical layers could reasonably be identified. Layer 2 might be preferred on account of being near the ground surface (thus liquefaction would be more likely to manifest), although the q_{c1Ncs} is relatively high and its shallow depth below the ground water table could lead to partial saturation. On the other hand, layer 4 could be preferred because it is thicker, has lower q_{c1Ncs}, and its depth below the ground water table makes partial saturation unlikely. As shown in Figure 3-6, the first choice (shallower critical layer) would place the case history below both the triggering curve developed in this study and the BI16 curve, whereas the second choice (deeper critical layer) places the case history above the two curves. The BI16-selected layer was the deeper layer in agreement with models whereas 5 out of 6 of the SMT members selected the shallower layer in the exercise described in Section 3.4.

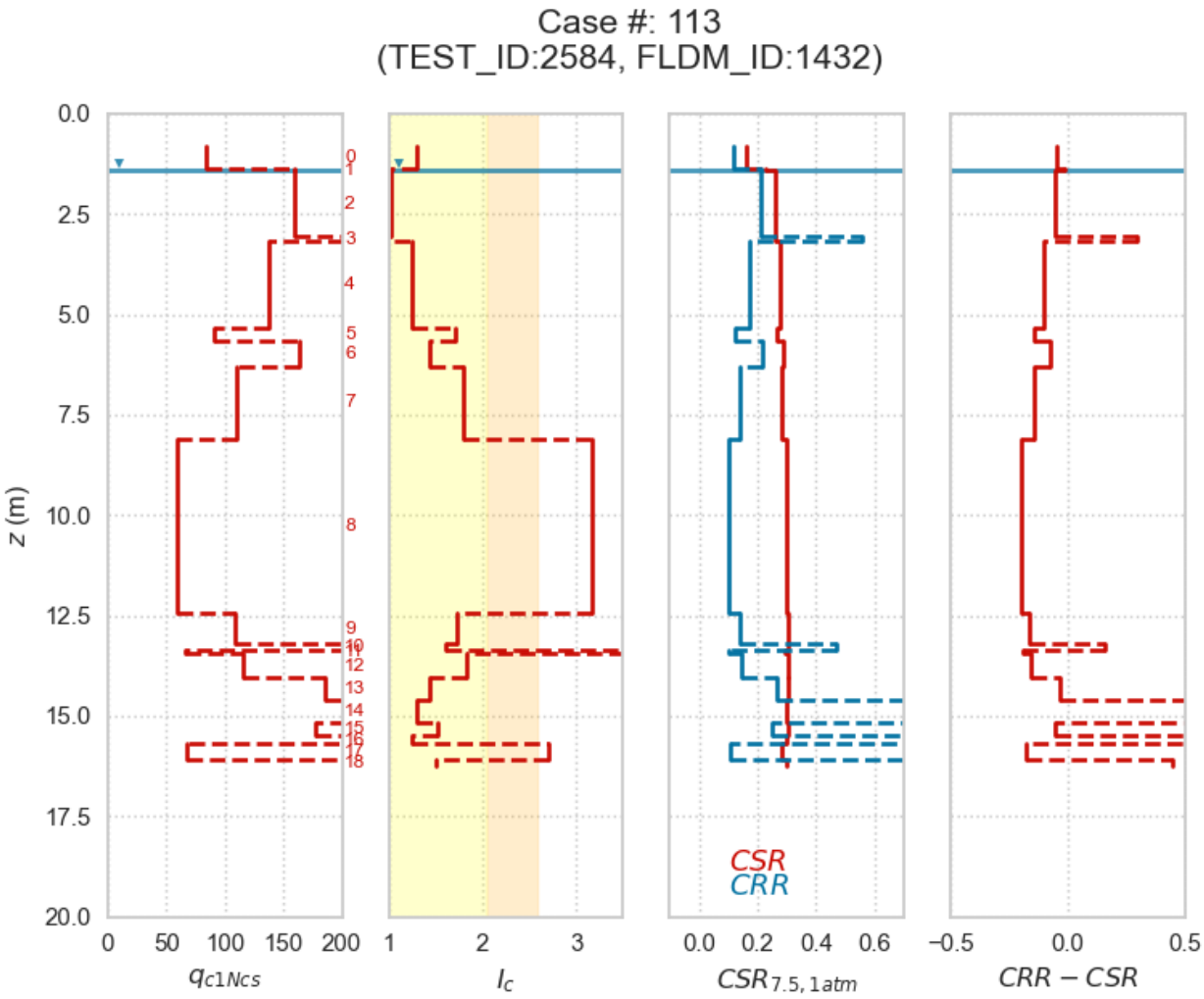

Figure 3-4. Example CPT profiles for Imazu Elementary School site from the 1995 Kobe earthquake derived using procedures presented in Sections 5.3-5.4. Surface manifestation occurred at the site.

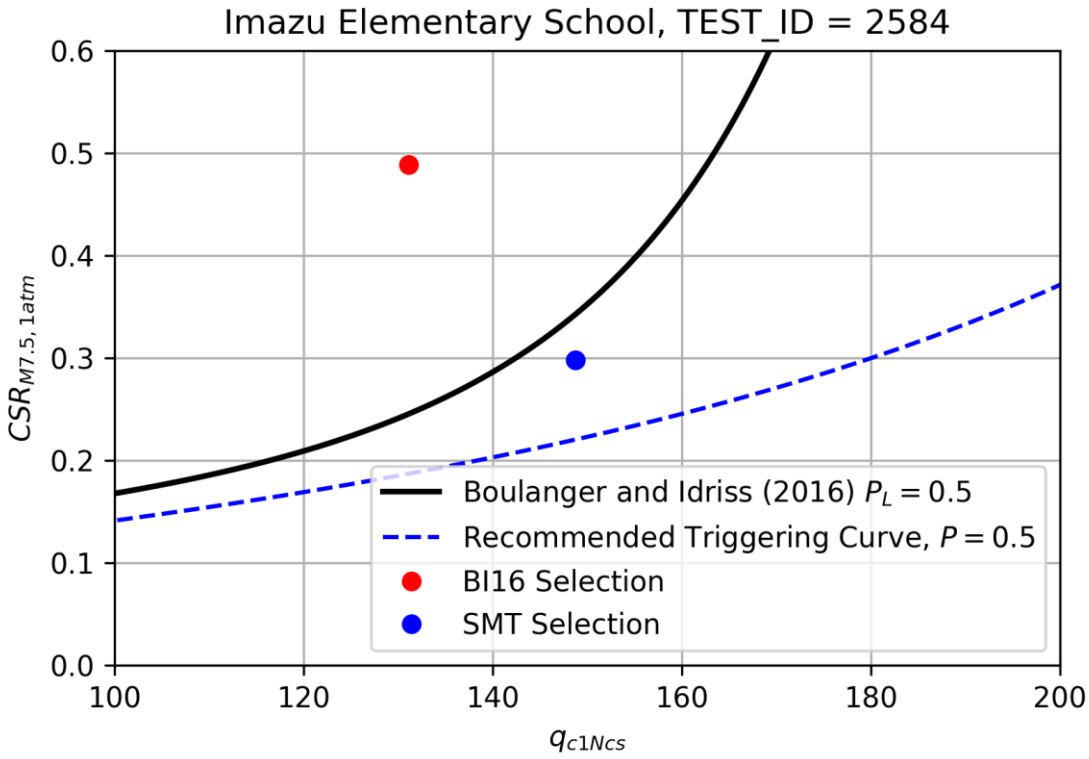

Figure 3-5. Position of Imazu Elementary school case history in $CSR_{M7.5,1atm}$ - q_{c1Ncs} space using alternate critical layer selections.

The NGL site "Port of Oakland, 7th Street Terminal (POO7)" (NGL site ID = 562), CPT "POO7-3" (NGL test ID = 2651) during the 1989 Loma Prieta earthquake (NGL FLDM ID = 1467) provides another example. In this case, the interpreted CPT logs for which are shown in Figure 3-7. As in the profiles illustrated in Figure 3-2 through Figure 3-4, multiple critical layers could reasonably be identified. Layers 4-5 might be preferred on account of being near the ground surface (thus liquefaction would be more likely to manifest), although the q_{c1Ncs} is relatively high and its shallow depth below the ground water table could lead to partial saturation. On the other hand, layer 13 could be preferred because it is relatively thick, has lower q_{c1Ncs}, and is likely saturated,

however the greater depth could suppress manifestation potential. As shown in Figure 3-8, the first choice (shallower critical layer, e.g., layers 4-5) would place the case history well below both the laboratory-based triggering curve developed in this study and the BI16 curve, whereas the second choice (deeper critical layer, e.g., layer 13) places the case history near to these two curves. Adopting the BI16-selected layer using their computed q_{c1Ncs} and *CSR* places the case history well above both curves. An interesting aspect of this case study is the varying interpretations of whether liquefaction occurred or not. POO7-3 was initially identified as an area that had “no surface manifestations of liquefaction” (Kayen et al., 1998), but subsequent interpretations indicated that this site could be considered as having experienced liquefaction (Cetin et al., 2004, 2018) or "marginal" liquefaction (Idriss and Boulanger, 2012; Boulanger et al., 2014). No sand boils were observed within 15-20 meters of POO7-3, but the CPT is located approximately 20-30m away from a zone of ample fissures and sand boils, deformations toward the free-face, and a small lateral spread into the San Francisco Bay. This is not to take a position on the field observations, but rather point out that the intense scrutiny of this case was likely a consequence of its being an outlier, particularly if the original field observation of no manifestation is adopted. A relatively high degree of scrutiny for strong outliers is another characteristic of cognitive bias.

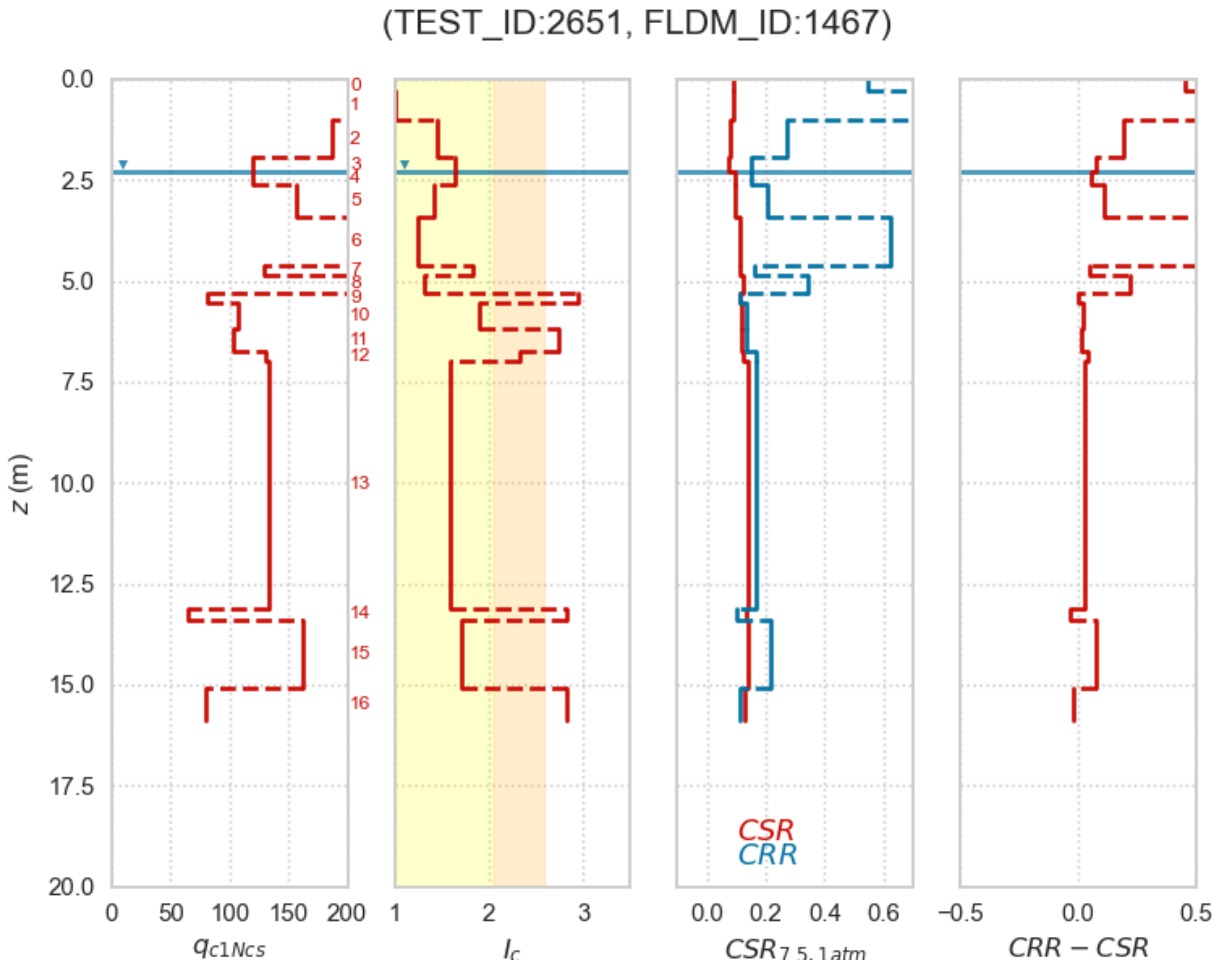

Figure 3-6. Example CPT profiles for Port of Oakland, 7th Street Terminal (POO7) site (CPT POO7-3) from the 1989 Loma Prieta earthquake derived using procedures presented in Sections 5.3-5.4. This is an example where the manifestation or lack of manifestation of liquefaction is unclear.

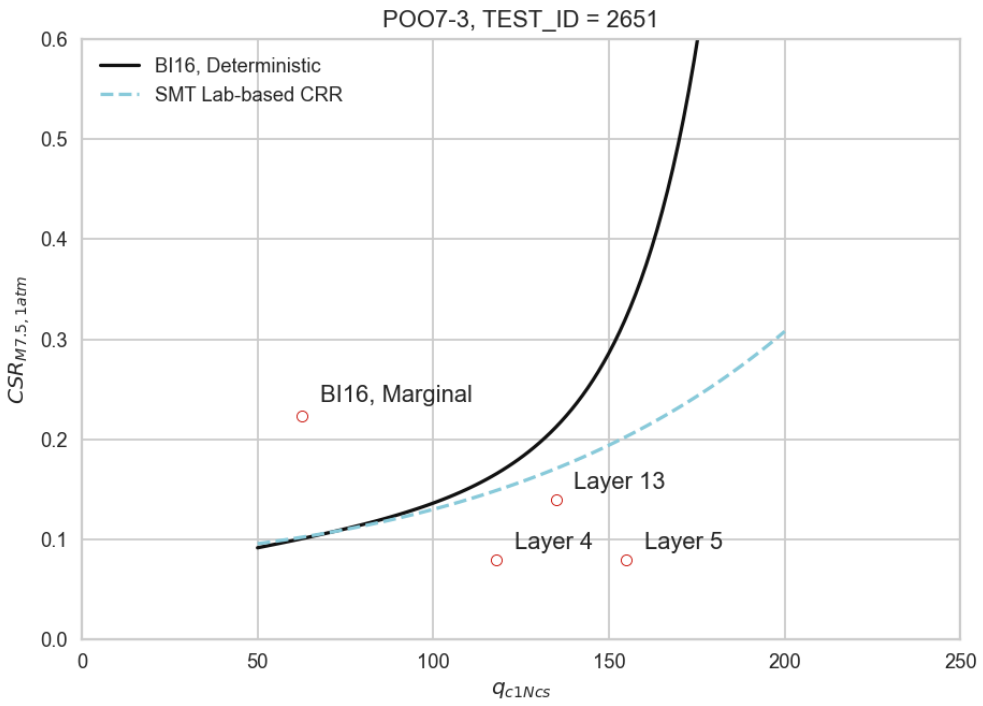

Figure 3-7. Position of Port of Oakland, 7th Street Terminal (POO7-3) case history in $CSR_{M7.5,1atm}$ - q_{c1Ncs} space using alternate critical layer selections and alternate selections of whether manifestation did or did not occur.

It cannot be known the extent to which confirmation bias may or may not have affected the development of any particular semi-empirical legacy triggering model. However, the circumstances for it to have influenced decision making were clearly present, especially given the traditional research approaches that led to the models (i.e., small teams of investigators who assemble their own database and develop a model with relatively limited outside interaction). Independent assessments of model performance have indicated large numbers of mis-predictions (Geyin et al. 2020; Maurer et al. 2015), especially false positives, which could be interpreted to suggest that absent cognitive bias in the critical layer selections, less favorable performance may be achieved. In a similar manner, the following section shows an appreciable rate of different

critical layer selections, again suggesting (though not proving) the potential for cognitive bias to have played a role. Ultimately, the problem when cognitive bias influences a fundamental aspect of the model development process, is that it further separates the data analysis undertaken in model development from what is done in application. This can produce outcomes with too-small levels of model uncertainty and potentially other problems.(Maurer et al. 2015a; Geyin et al. 2020a), especially false positives, which could be interpreted to suggest that absent cognitive bias in the critical layer selections, less favorable performance may be achieved. In a similar manner, the following section shows an appreciable rate of different critical layer selections, again suggesting (though not proving) the potential for cognitive bias to have played a role. Ultimately, the problem when cognitive bias influences a fundamental aspect of the model development process, is that it further separates the data analysis undertaken in model development from what can be done in application. This can produce outcomes with too-small levels of model uncertainty and potentially other problems.

3.4 Critical Layer Selection Study

A study was conducted to explore the analyst-to-analyst variabilities in critical layer selection. I randomly selected 40 CPTs from sites utilized in legacy models, and each member of the SMT made critical layer selections. The information available to each analyst was deliberately restricted to be that which is available to an engineer in a forward assessment of liquefaction potential. Specifically, profiles of q_{c1Ncs}, I_c, $CSR_{7.5,1atm}$, and the difference between *CRR* and *CSR* were included where *CRR* was estimated using the laboratory-derived prior relationship as a function of

q_{c1Ncs} (Section 6.2). Prior to selecting critical layers, the SMT agreed that each member would independently identify the layer most likely to cause surface manifestation. The participants recognized that, in some cases, the layer most likely to trigger may not be the layer most likely to manifest because the triggered layer is thin, deep, or was located below a strong non-liquefiable layer.

A screenshot of the tool utilized by the SMT to make critical layer selections is shown in Figure 3-8. No indication of the site name, earthquake, or surface manifestation condition was displayed to the participants to avoid confirmation bias. As indicated earlier, the information provided was that which would typically be available to engineers applying the model in a forward sense. SMT members then selected the single layer identified by the agglomerative clustering algorithm as the critical layer (Section 5.3; Hudson et al. 2023d) they interpreted as being most critical. SMT members could also indicate whether they interpreted interbedding as being present within the critical layer and/or profile, whether the critical layer was particularly deep, whether a strong crust existed at the site, and/or if partial drainage could have occurred in cases with shallow liquefiable layers in the absence of a low-permeability capping layer. They could also indicate whether the critical layer has a high I_c, and therefore might contain plastic fines. Open-ended comments could also be entered.

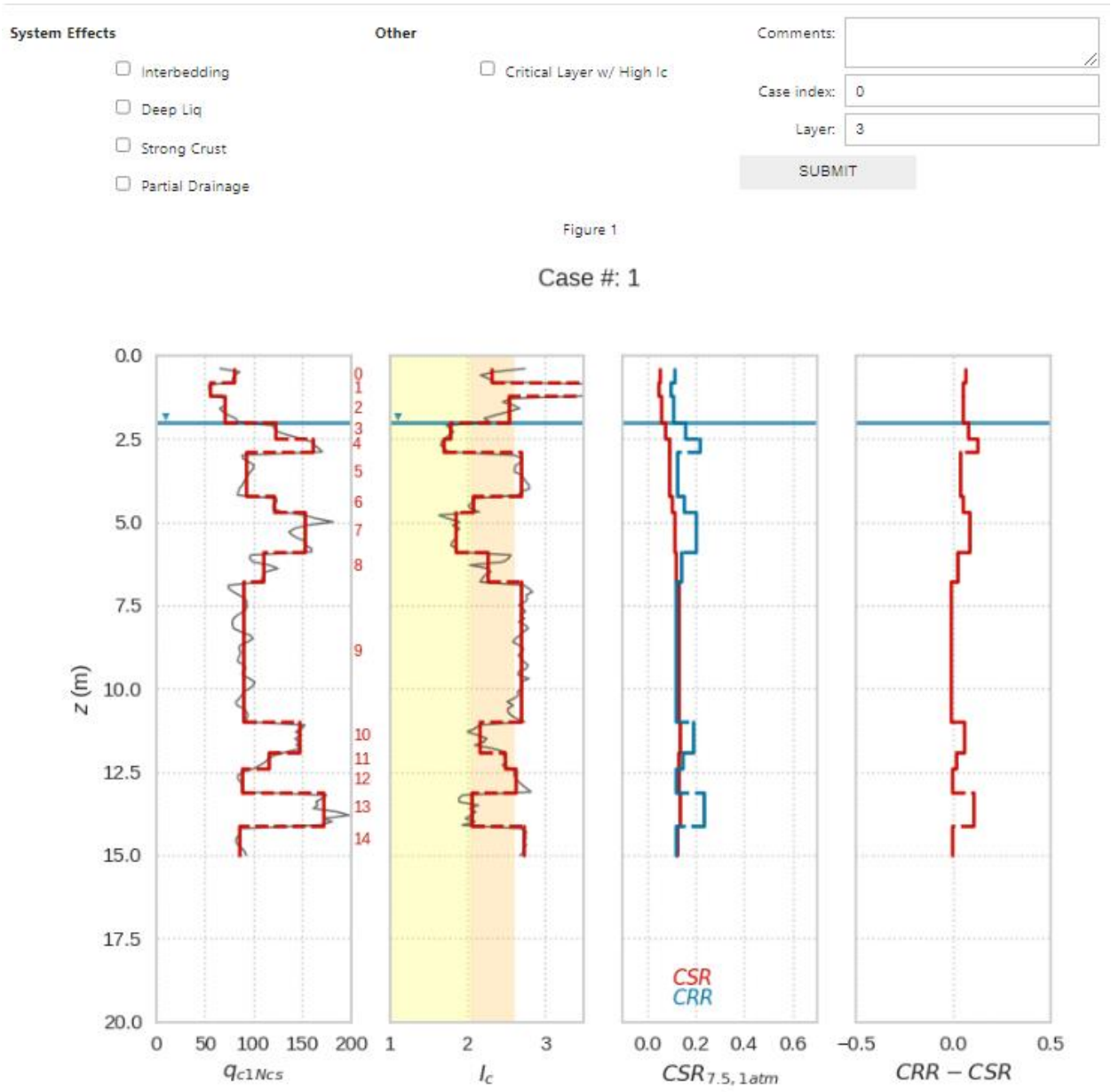

Figure 3-8. Screenshot of the tool used by SMT members to select critical layers.

The depths to the top of the critical layer selected by the SMT members are compared with those selected by Boulanger & Idriss (2016) ("BI16") in Figure 3-9, along with R^2 values indicated in the upper-left corner of each figure. R^2 is the coefficient of determination, the square of the

correlation coefficient which gives a reference for how strong of a linear relationship there is between two variables. An R^2 value of 1 indicates a regression line that perfectly fits all the data and $R^2 = 0$ indicates a line that represents none of the data. Open symbols indicate sites that did not manifest liquefaction, while closed circles did manifest. Significant differences are apparent in the selections made by the SMT members compared with those by Boulanger & Idriss (2016), with R^2 values ranging from 0.22 to 0.37. Notably, differences *between* the SMT members are also significant, as illustrated subsequently. BI16 did not select from the layers identified by the clustering algorithm, and therefore their z_{top} value for a particular profile might not be available as an option for the SMT members. However, differences in the selections are much more significant than can be explained by that detail. In general, members of the SMT tended to select shallower layers than BI16, which may be caused by the SMT team's focus on manifestation over triggering, combined with the expectation that shallower layers are more likely to manifest. Similar figures are provided for I_c, q_{c1Ncs}, and *CSR* in Figure 3-10 through Figure 3-12. The R^2 values tend to be higher, on average, than for z_{top}, but nevertheless exhibit significant differences from BI16.

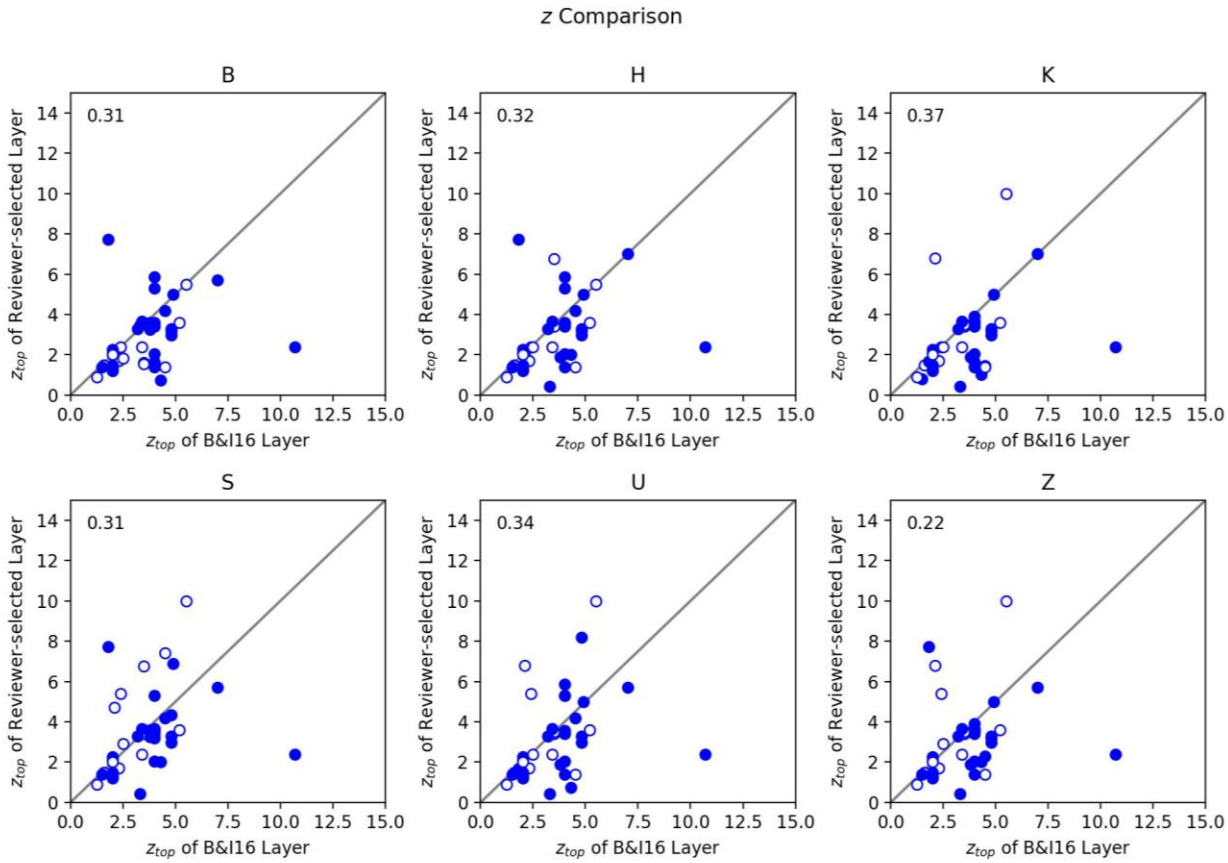

Figure 3-9. z_{top} of critical layers selected by SMT members compared with Boulanger & Idriss (2016). R^2 values shown in upper left corners.

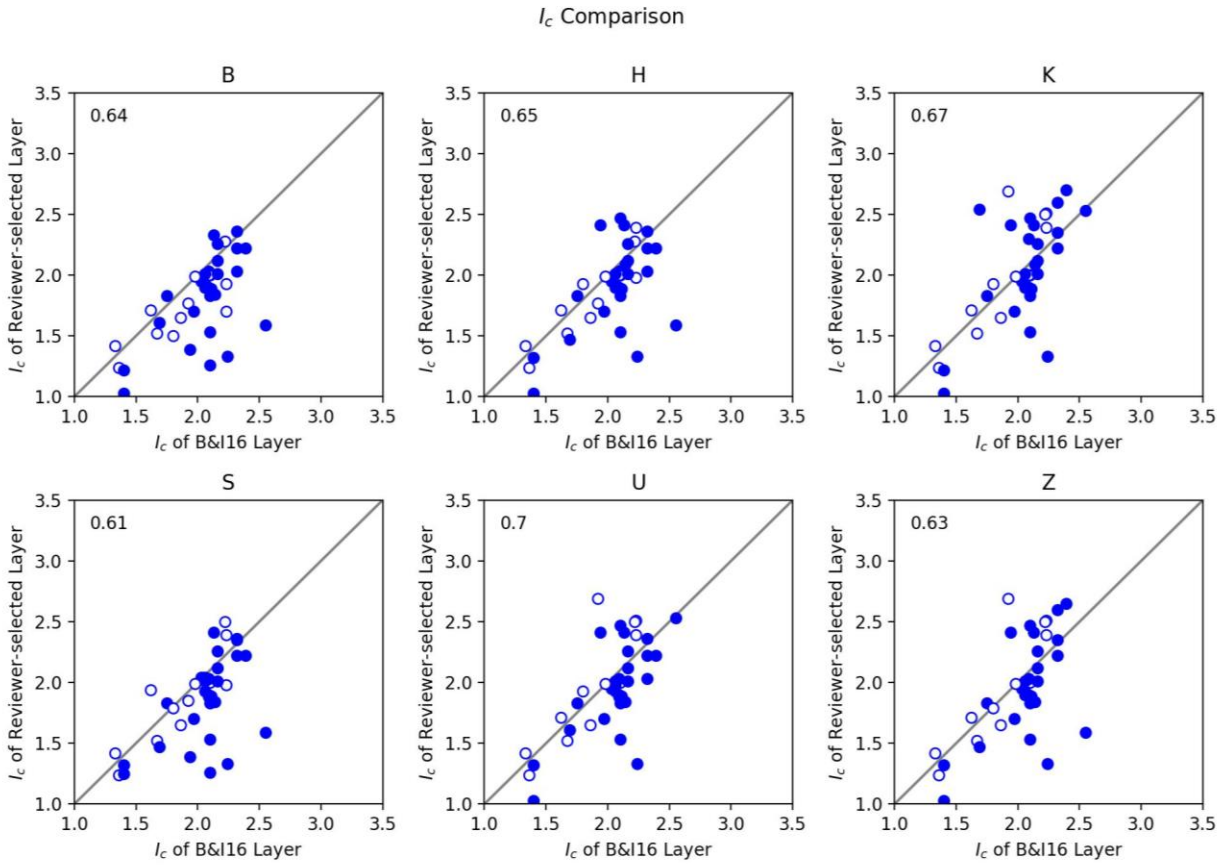

Figure 3-10. I_c, of critical layers selected by SMT members compared with Boulanger & Idriss (2016). R^2 values shown in upper left corners.

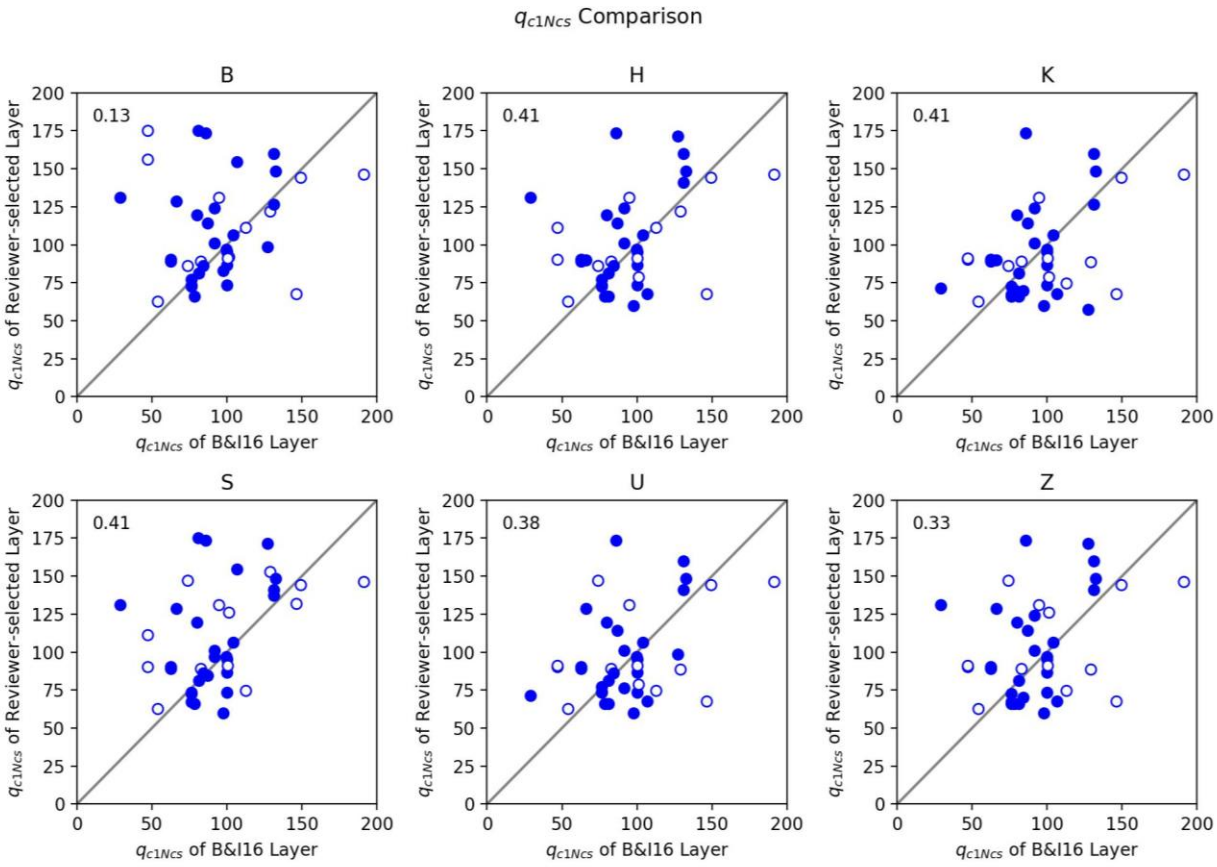

Figure 3-11. q_{c1Ncs}, of critical layers selected by SMT members compared with Boulanger & Idriss (2016). R^2 values shown in upper left corners.

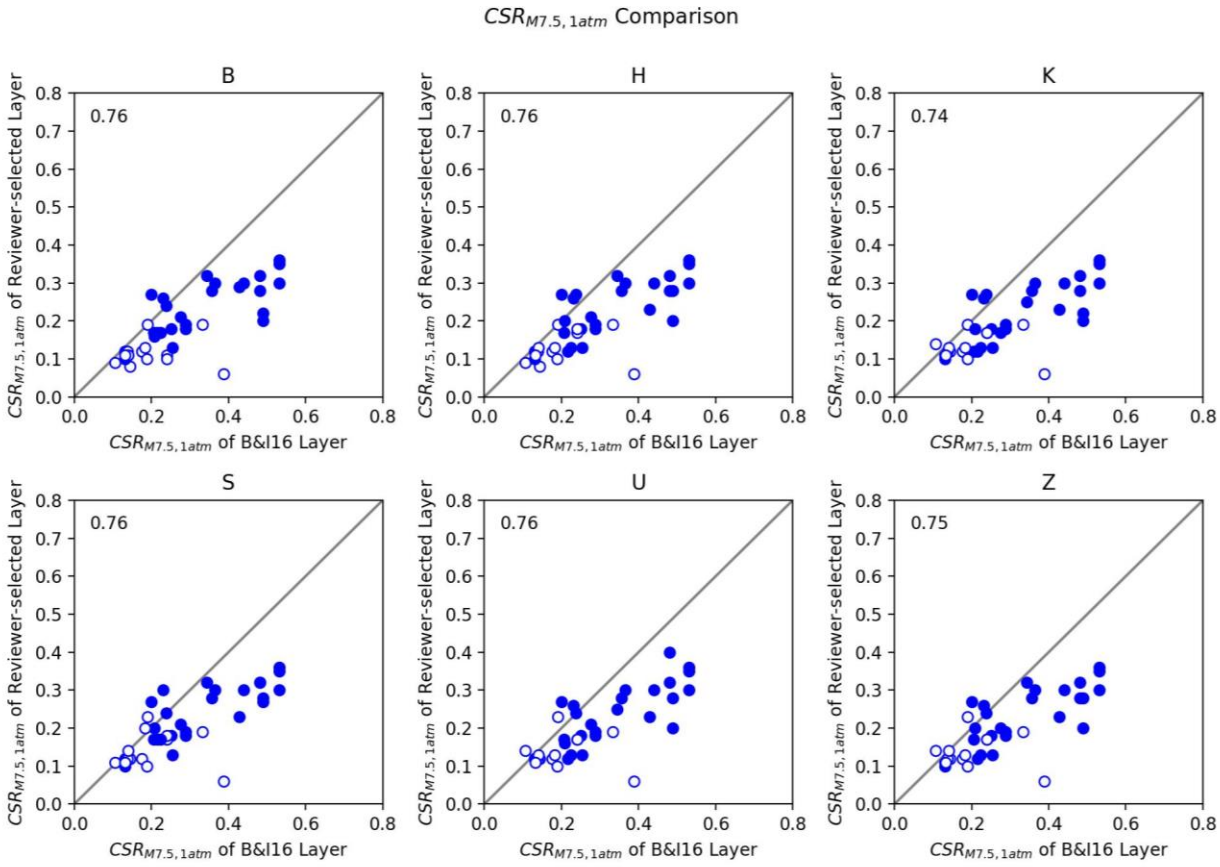

Figure 3-12. $CSR_{M7.5,1atm}$ of critical layers selected by SMT members compared with Boulanger & Idriss (2016). R^2 values shown in upper left corners.

Figure 3-13 compares critical layer selections by the SMT with those of BI16 in q_{c1Ncs}-*CSR* space. Open circles are profiles that did not manifest, while closed circles are profiles that manifested. Significant differences are observed in the positions of the points on these graphs for each SMT member compared with BI16; differences between SMT members also exist. In all cases, the BI16 model represents a broader range of q_{c1Ncs} values. Another important difference is that, among these 40 cases, the BI16 selections do not include any false negatives (FN, false predictions of no manifestation, i.e., closed circles below the curve), whereas the SMT members had 2 to 5 false

negatives. Note that BI16 do have some false negatives among the dataset utilized to form their model; however, those cases were not among the 40 selected for this exercise. The SMT members tended to have fewer false positives (FP, false predictions of manifestation) than BI16, rendering overall accuracy values that are similar. Defining accuracy as the number of true predictions (TP, accurate predictions of manifestation) divided by the total number of cases, the resulting accuracy values are 82.5% for BI16, 82.5% for Brandenberg (SMT member "B"), 77.5% for Hudson, 75% for Kramer, 80% for Stewart, 80% for Ulmer, and 77.5% for Zimmaro. Despite the different selections, the accuracy of the SMT analysts' selections are all reasonably close to each other, and reasonably close to BI16. This indicates that the various individual biases each analyst brings to their selections may have offsetting effects from profile-to-profile with respect to accuracy.

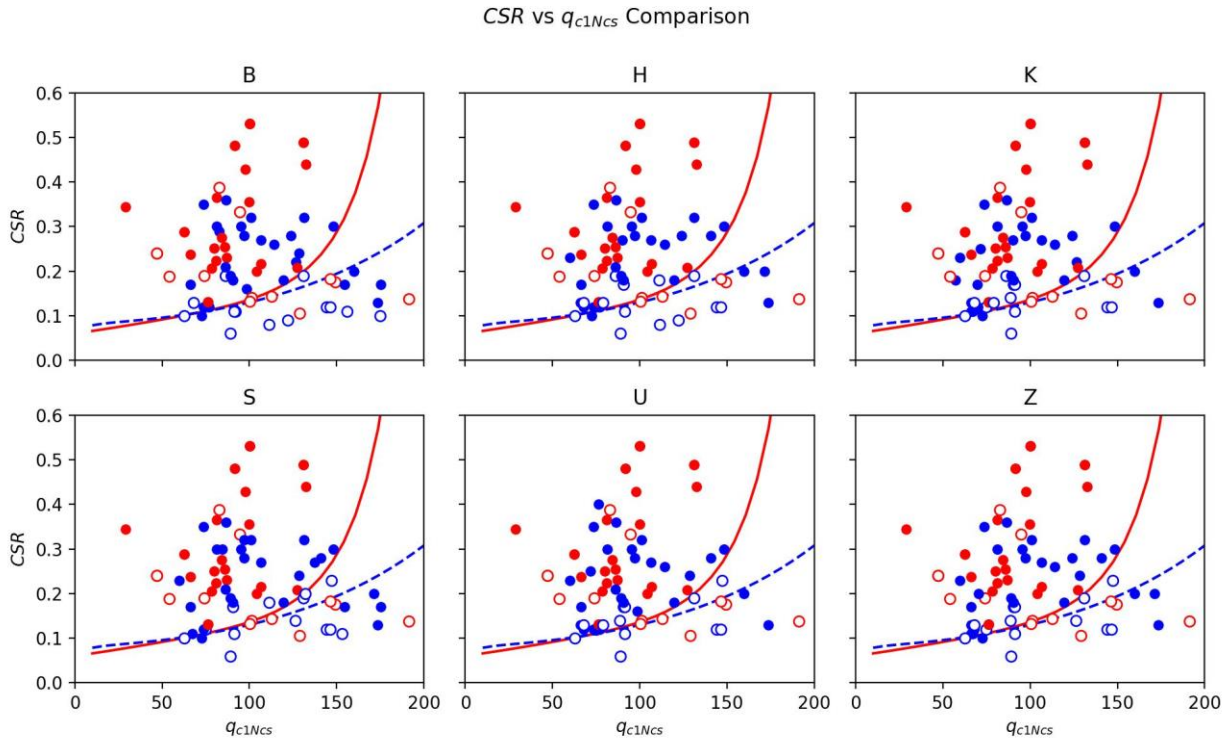

Figure 3-13. Critical layer properties selected by SMT compared with Boulanger & Idriss (2016). Red points represent locations of $CSR_{M7.5,1atm}$ vs q_{c1Ncs} points as defined by BI16-selected critical layers, whereas blue points represent locations as defined by reviewer-selected critical layers. Red line represents the BI16 deterministic *CRR* curve, blue dashed line represents the SMT's *CRR* curve (Section 6.2).

Figure 3-14 through Figure 3-17 compare properties of critical layers selected by the SMT members. In general, R^2 values are higher among the critical layers selected by the SMT members than for each member compared with BI16. This outcome likely reflects differences in information available to analysts at the time the critical layer selections were made. Although the SMT members selections are more similar with each other than with BI16, significant differences nevertheless are observed in the critical layers selected by the SMT members. This is an indication that the judgment of individual analysts is different, even when those analysts have worked closely

together for years. This points to a need for objectivity in critical layer selections so that liquefaction manifestation models are repeatable and independent of any one analysist's view.

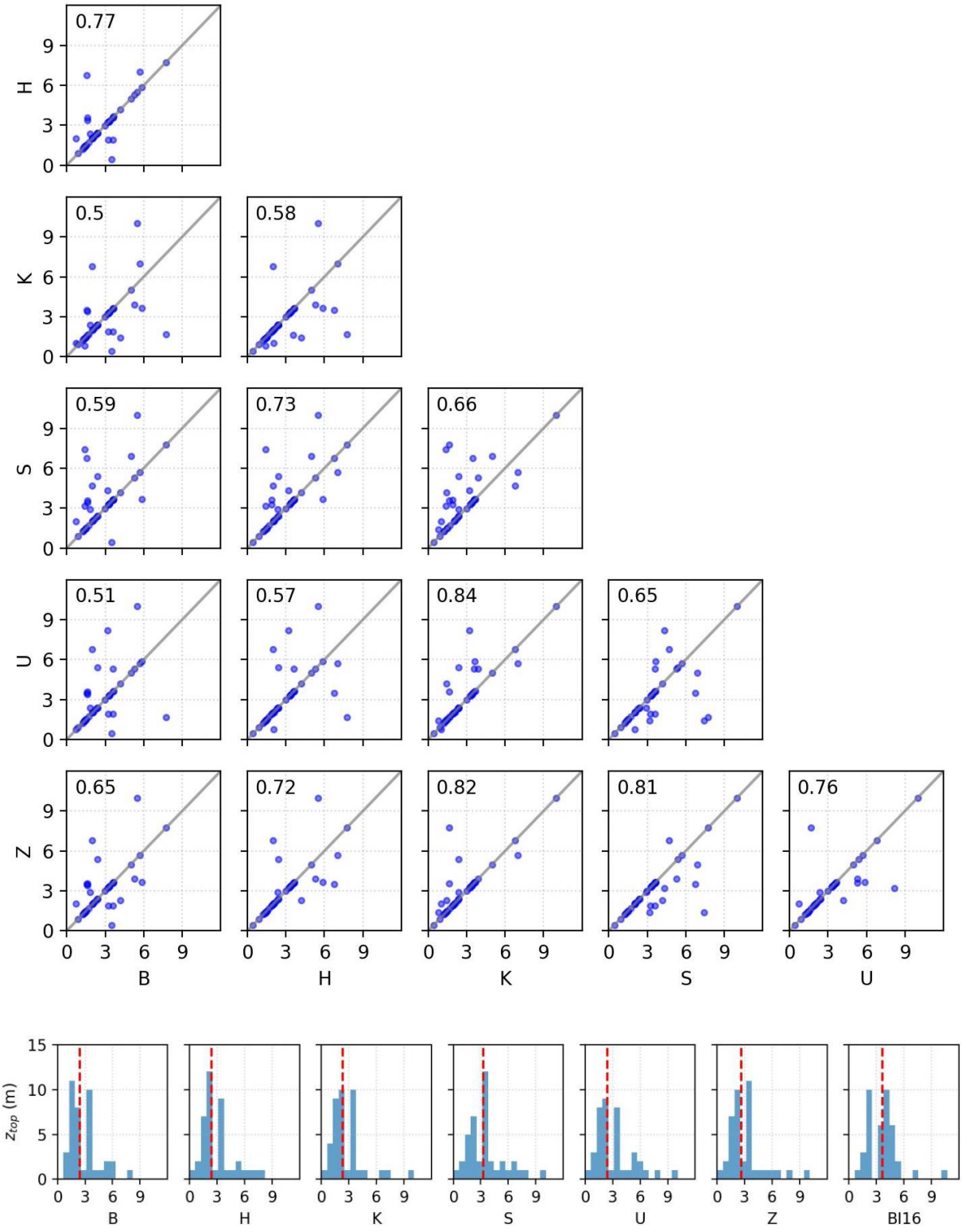

Figure 3-14. Correlation of z_{top} values among critical layers selected by SMT members.

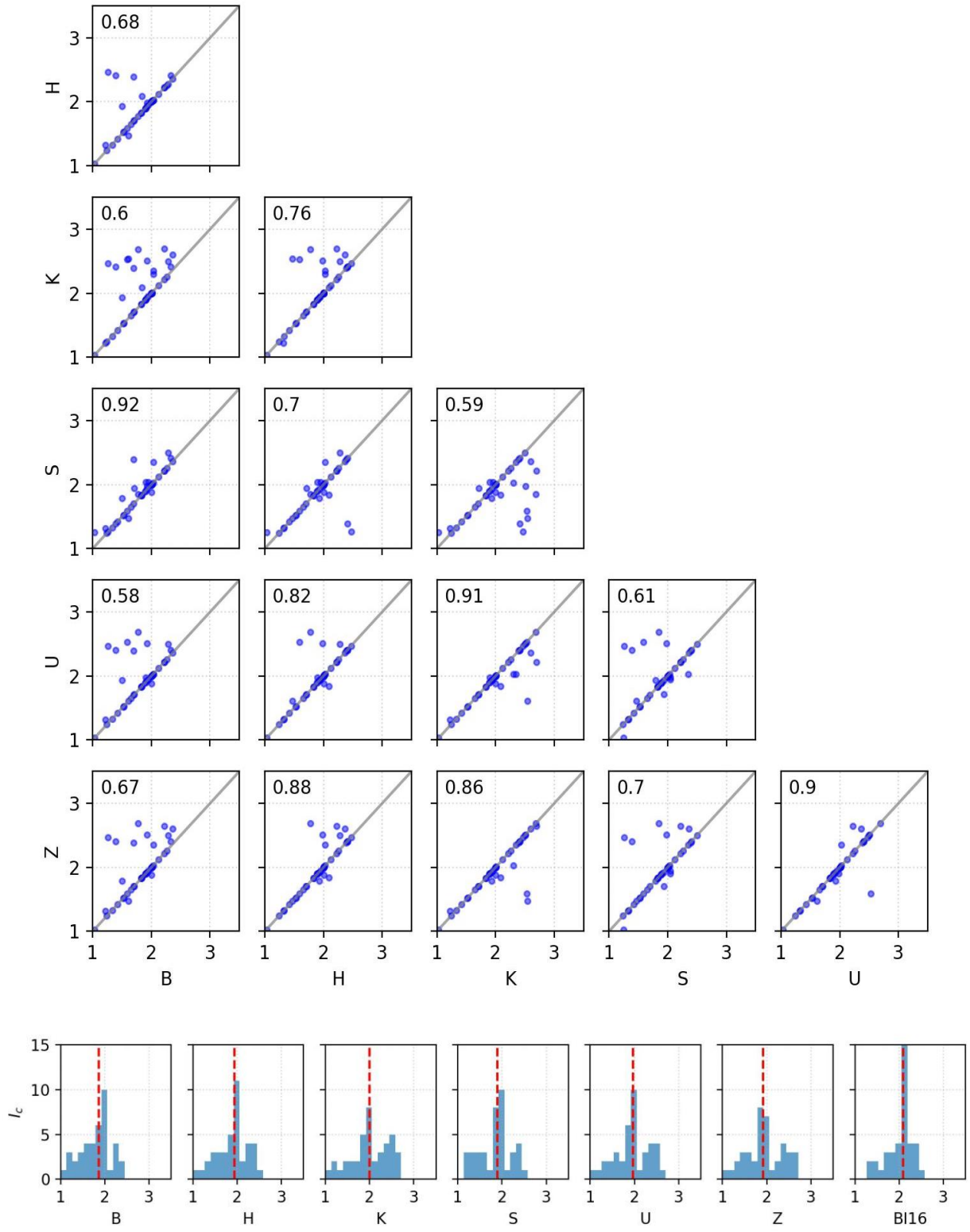

Figure 3-15. Correlation of I_c values among critical layers selected by SMT members.

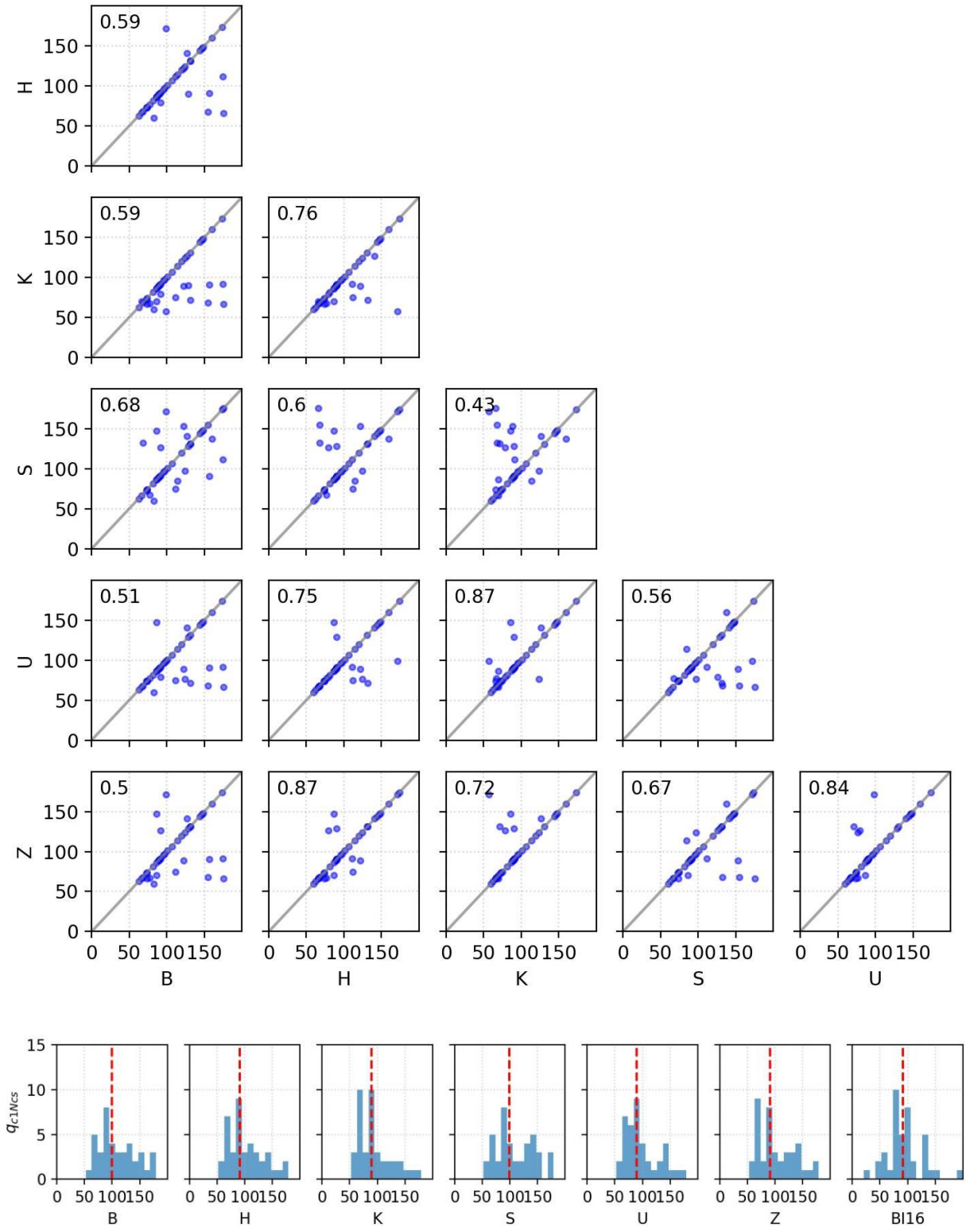

Figure 3-16. Correlation of q_{c1Ncs} values among critical layers selected by SMT members.

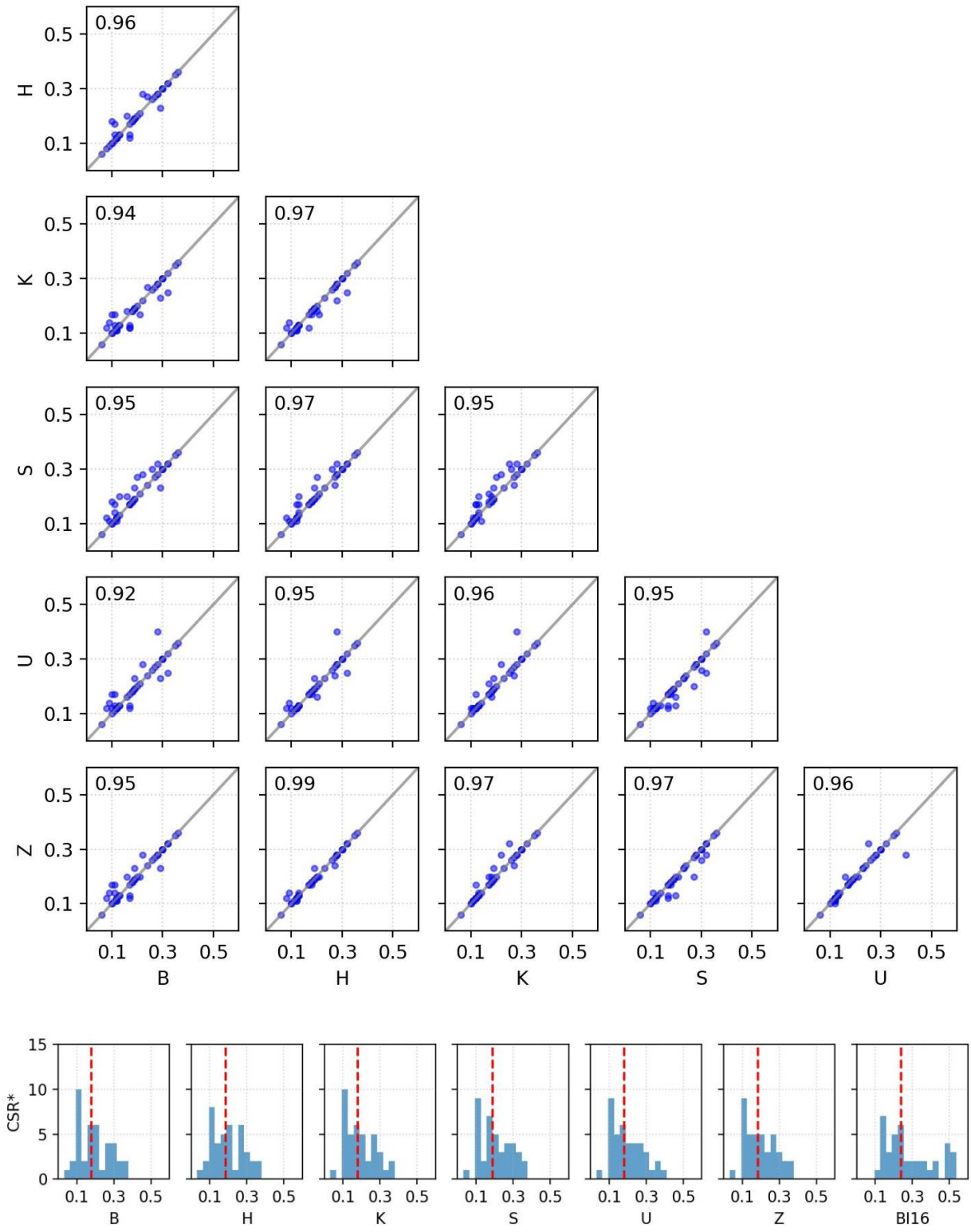

Figure 3-17. Correlation of *CSR** values among critical layers selected by SMT members.

3.5 Examples of Shortcomings of Legacy Models and Critical Layer Framework

Two examples of sites that are not adequately characterized using the critical layer framework are explored in this section. First is a site in Wufeng, Taiwain that experienced strong shaking during the 1999 Chi-Chi earthquake but did not have any surface evidence of liquefaction (Chu et al. 2008). Second is a site in northern Baja California, Mexico that was shaken during the 2010 El Mayor-Cucapah earthquake, where a highway bridge column settled due to an apparent end-bearing capacity failure due to apparent liquefaction of sandy soil near the pile toe (Turner et al. 2015).

3.5.1 Wufeng Site A, Taiwan

After the 1999 Chi-Chi earthquake, site investigations were performed at locations with and without surface evidence of liquefaction (Chu et al. 2004). Wufeng Site A is a site that did not have any observed surface evidence of liquefaction and had a series of CPT soundings performed to characterize the subsurface. The site experienced a PGA ~ 0.47g. Several of the CPT profiles are presented in Figure 3-18 through Figure 3-21 with the tag "SFEV=X" indicating whether surface evidence of liquefaction was (SFEV=1) or was not (SFEV=0) observed. The figures show the original CPT data and resistances within assigned layers (using the algorithm presented in Section 5.3 (Hudson et al. 2023d)) in the two left columns. Layer numbers are provided between the q_{c1Ncs} and I_c plots. To the right of those are profiles of *CSR* and *CRR* (Boulanger and Idriss 2016), which is followed by FS_L on the right side.

Large portions of these profiles consist of high I_c (clay-like) materials and are therefore not susceptible to liquefaction. However, there are several low I_c, sand-like, susceptible layers that have FS_L<1. As shown in Figure 3-22, points representing values of CSR^* and q_{c1Ncs} for several layers from each of the profiles plot above the threshold curve from the (Boulanger and Idriss 2016) model. Mechanistically, these low density, susceptible layers that experienced this severity of shaking should liquefy as the Boulanger and Idriss (2016) model predicts, however no surface manifestations of liquefaction were observed. Accordingly, it is likely that the thick overlying clay layers in the profile suppressed manifestation. However, given the model predictions, an analyst doing a forward prediction of a similar site could easily mistakenly conclude that a liquefaction ground failure problem is likely for such a site, when clearly this is not the case.

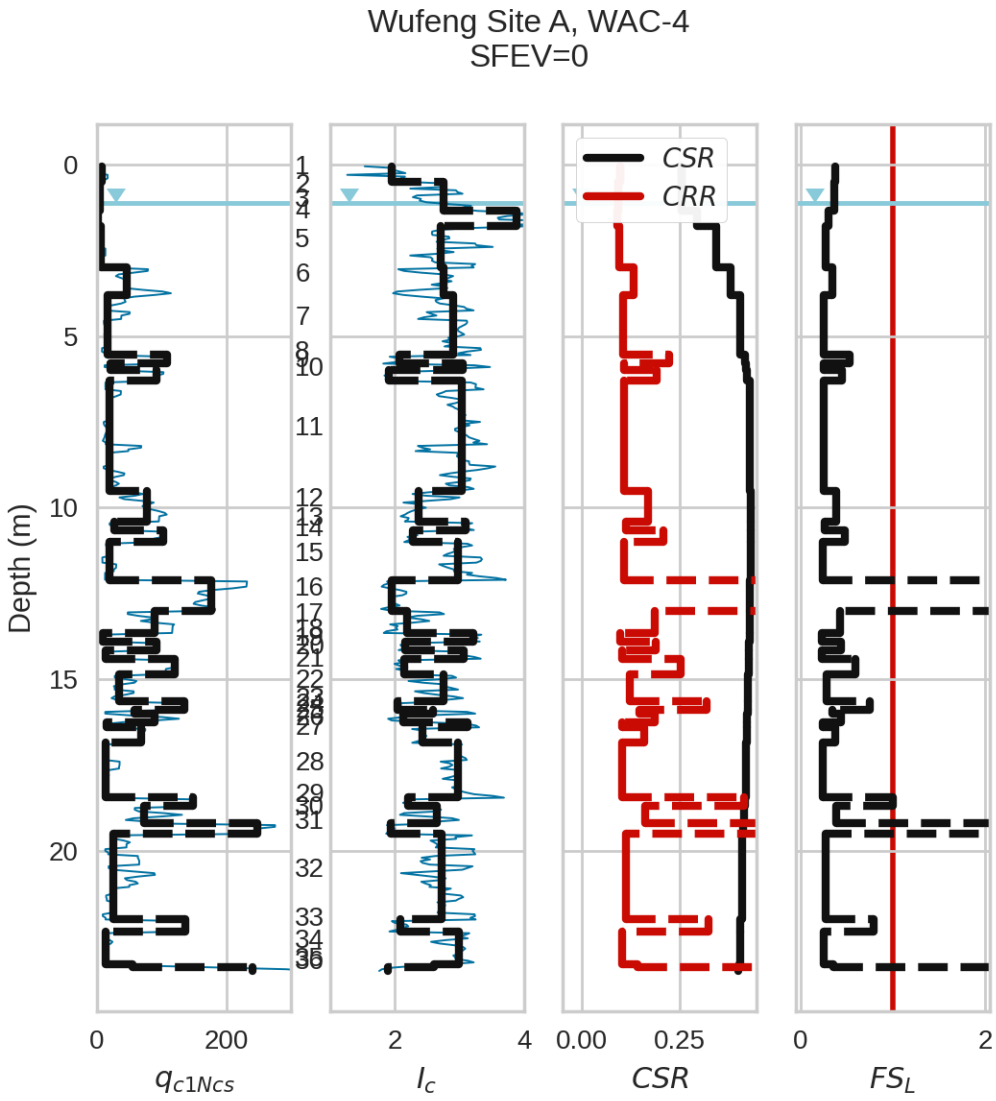

Figure 3-18. CPT "WAC-4" from Wufeng Site A with *CSR* computed using a *PGA* estimate from the 1999 Chi-Chi, Taiwan earthquake and CRR/FS_L estimates from a model currently used in engineering practice (Boulanger and Idriss 2016).

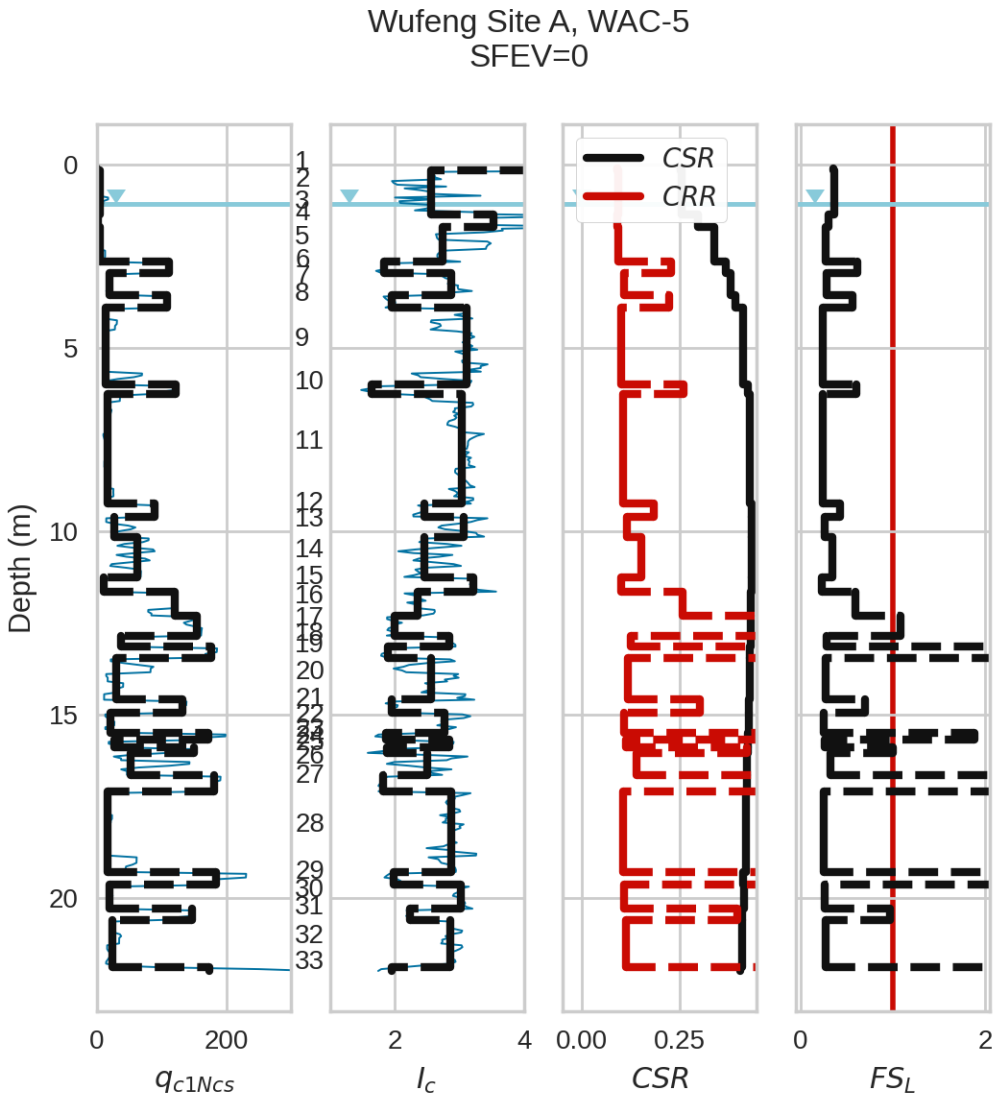

Figure 3-19. CPT "WAC-5" from Wufeng Site A with *CSR* computed using a *PGA* estimate from the 1999 Chi-Chi, Taiwan earthquake and CRR/FS_L estimates from a model currently used in engineering practice (Boulanger and Idriss 2016).

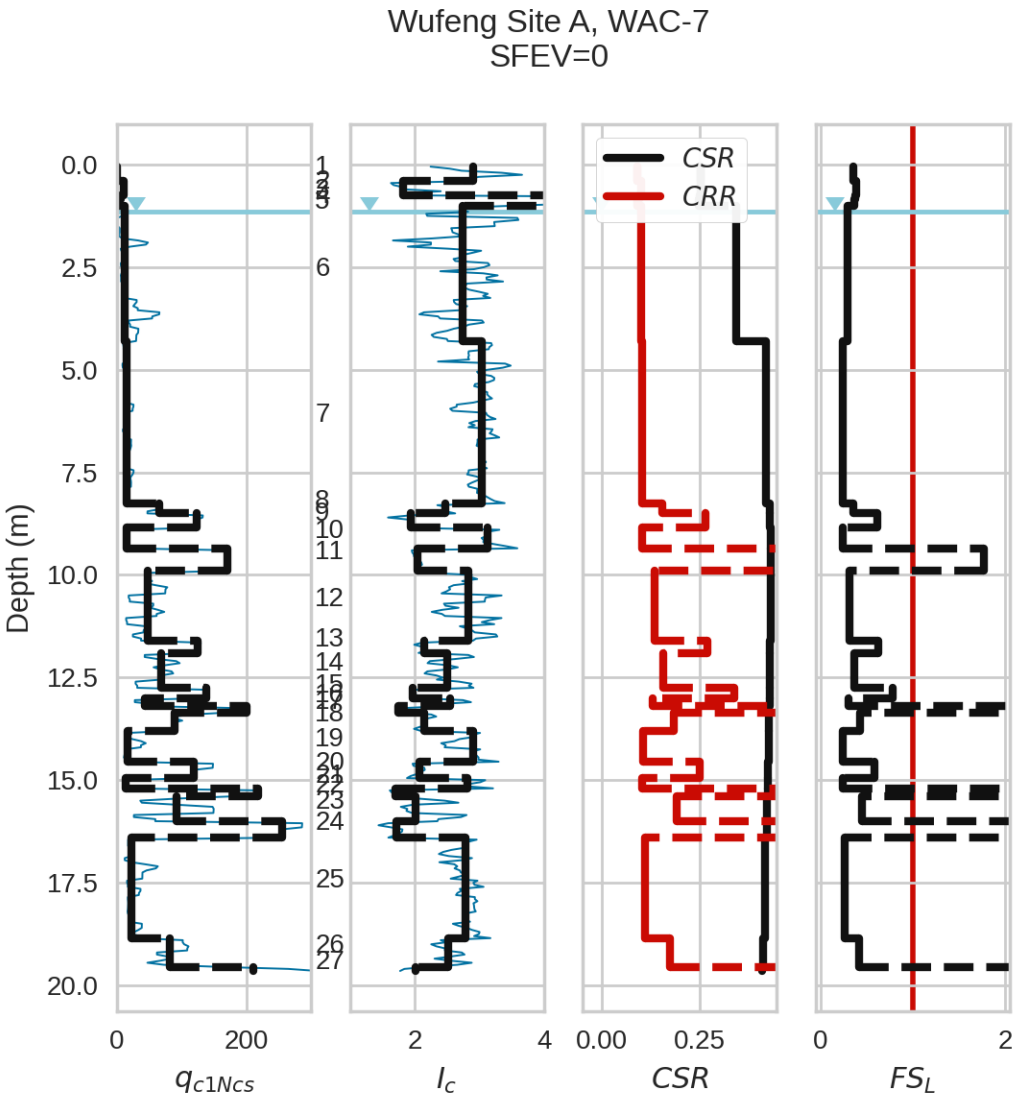

Figure 3-20. CPT "WAC-7" from Wufeng Site A with *CSR* computed using a *PGA* estimate from the 1999 Chi-Chi, Taiwan earthquake and CRR/FS_L estimates from a model currently used in engineering practice (Boulanger and Idriss 2016).

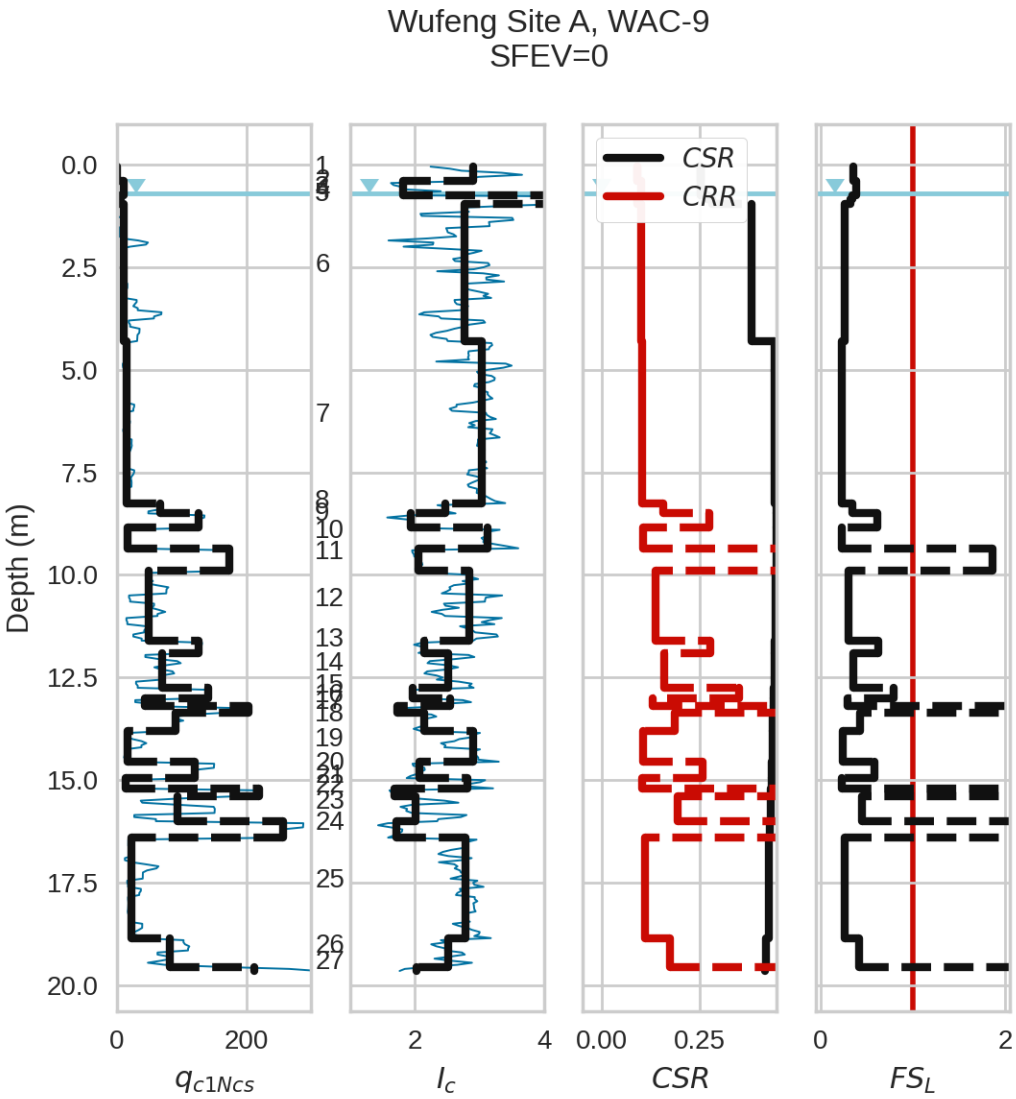

Figure 3-21. CPT "WAC-9" from Wufeng Site A with *CSR* computed using a *PGA* estimate from the 1999 Chi-Chi, Taiwan earthquake and CRR/FS_L estimates from a model currently used in engineering practice (Boulanger and Idriss 2016).

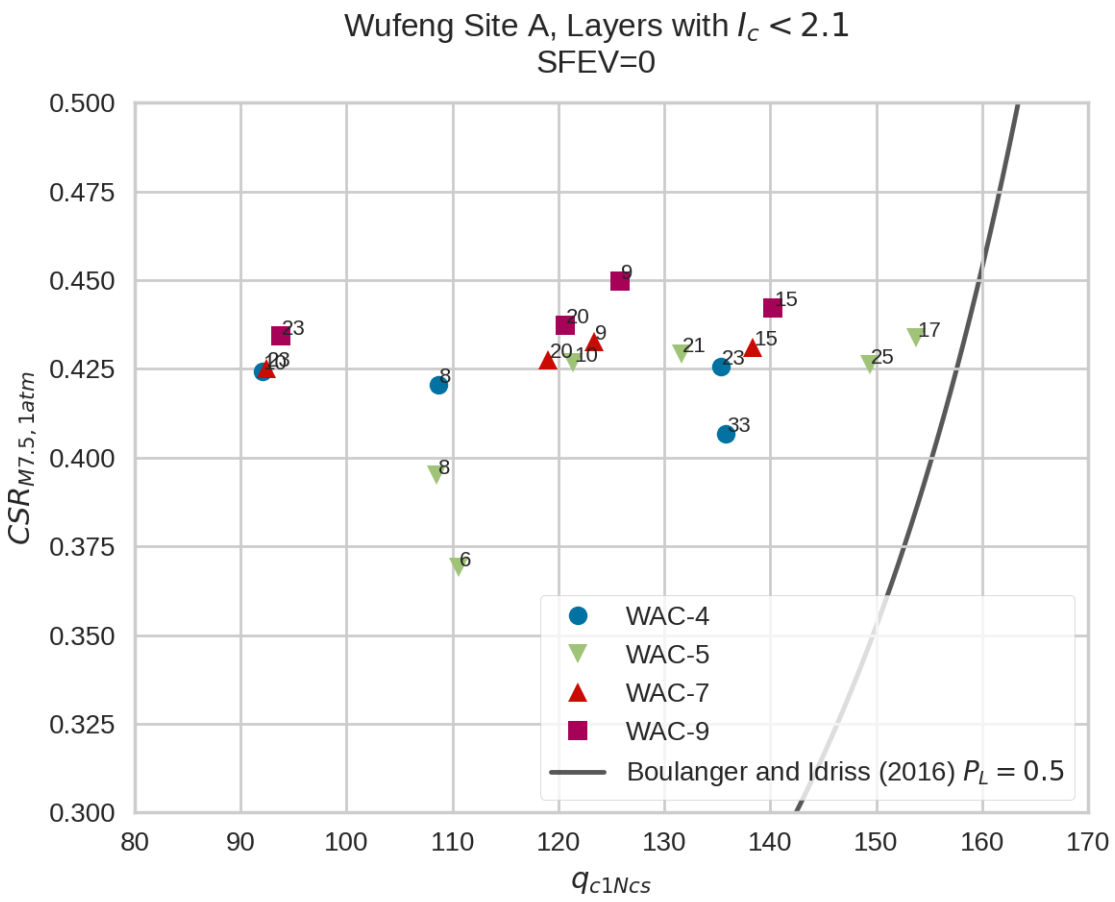

Figure 3-22. Layers from selected CPTs at Wufeng Site A with I_c < 2.1 and FS_L < 1 (Boulanger and Idriss 2016). Each point represents a layer with a color and symbol identifying which CPT it is from and a number identifying which layer within that CPT it is from.

3.5.2 San Felipito Bridges, Baja California, Mexico

The San Felipito Bridge site experienced *PGA*~0.27g during the 2010 **M**7.2 El Mayor-Cucapah earthquake. Portions of the riverbank experienced lateral spreading and the columns for the highway bridge on the east bank experienced settlement of approximately 0.5m and flexural cracking (Turner et al. 2015, 2016). The profile for CPT 2, adjacent to the column that settled 0.5m, is provided in Figure 3-23. The profile shows that liquefaction triggering is predicted for this event

in layer 6 at depths from 2.2 to 4.8m. Layer 6 is likely to be the layer that caused lateral spreading at the site. The volumetric strain is estimated from the CPT data (Cetin et al. 2009) and can be used to compute settlements (Figure 3-23) of approximately 0.06m. However, this settlement is unrelated to the observed column settlement of 0.5m because the bearing layer for the piles supporting the columns is much deeper than Layer 6 (17.5 m). The CPT investigation did not extend beyond 12m, but an adjacent boring, PEB-1, has a susceptible layer with a low blow count at approximately 16 to 18m below ground surface. Additionally, nearby CPT-1 indicates loose, liquefiable layers at these depths. This layer is predicted to trigger based on legacy models. As described by Turner et al. (2015, 2016), if this layer had indeed liquefied the reduced end bearing, combined with side resistance at shallower depths (from non-liquefied materials), would in aggregate not provide adequate total bearing capacity for the column to carry gravity loads. Hence, it appears likely that toe bearing failure occurred.

This example illustrates the importance of considering liquefaction in deep layers when they are influential for stability, while also illustrating the non-applicability of surface manifestation models for such problems (such models would not predict manifestation for such a deep layer).

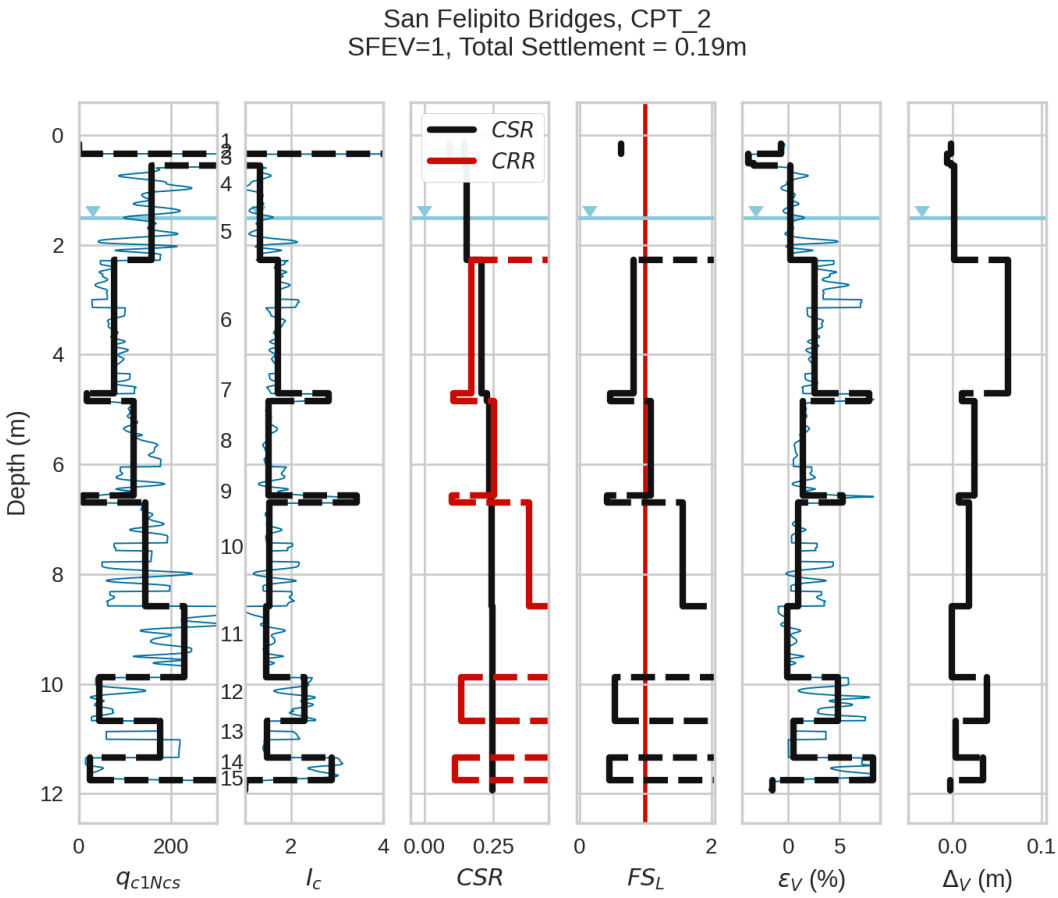

Figure 3-23. CPT 2 profile from San Felipito Bridges, Baja California, Mexico. *CSR* computed using a *PGA* estimate from the 2010 El Mayor-Cucapah earthquake and CRR/FS_L estimates from a model currently used in engineering practice (Boulanger and Idriss 2016). Volumetric strain and displacement estimates are provided in the final two columns (Cetin et al. 2009).

4 Proposed Triggering and Manifestation Framework

As discussed in Chapter 1, the occurrence of liquefaction is often identified by the observation of surficial manifestation of its effects. Historically, it has been common to consider manifestation at case history sites as positive evidence of triggering (i.e., that manifestation = triggering) and the absence of manifestation as positive evidence that triggering did not occur (no manifestation = no triggering). However, it is possible for liquefaction to be triggered in thin, deep susceptible layers without producing surface manifestation. It is also possible for manifestation evidence such as ground failure due to cyclic softening or sand boils to develop at sites where pore pressures in thick, shallow, susceptible layers increase significantly but not to the level of liquefaction triggering (Kramer et al. 2016; Tokimatsu et al. 2012).

Manifestation, or its absence, must therefore be recognized as a consequence of pore pressure generation mediated by the characteristics of the soil profile. Detailed investigations and modeling of sites in Christchurch, New Zealand have illustrated the extent to which interlayering of liquefiable and non-liquefiable soil layers can influence surface manifestation (Cubrinovski et al. 2019; Hutabarat and Bray 2021, 2022).

4.1 Bayesian Framework

The historical reliance on manifestation as an indicator of liquefaction triggering has led to conventional liquefaction procedures being manifestation models rather than triggering models. The most recent versions of these procedures produce a probability of manifestation, P[*M*] (and consequently a probability of no manifestation, P[*NM*] = 1 – P[*M*]). Implicit in the interpretation

of the results of these procedures is the assumption that the probability of triggering is equal to the probability of manifestation, P[T] = P[M] (and the probability of no triggering, P[NT] = 1-P[T]).

Surface manifestation can be important in many situations and can cause damage to light surface structures (e.g., pavements), contribute to settlement of lightweight structures (e.g., private houses), and require significant clean-up efforts (e.g., Christchurch in 2011). However, the actual triggering of liquefaction at both shallow and large depths (Section 3.5.2) is more fundamentally important for many critical structures. For the purposes of damage and loss estimation, a more fundamental and useful analysis would be to estimate the probability of triggering of a layer, P[T_L], and with it, P[NT_L] = 1 – P[T_L], and separately evaluate the probability of manifestation of the profile conditional on triggering of a layer, P[$M_P|T$] or not triggering, P[$M_P|NT_L$]. The subscript "P" indicates that manifestation is observed for an entire profile and the subscript "L" indicates that an individual layer is being evaluated for triggering.

In terms of case history interpretation of triggering, the probability that the soil in a layer triggered needs to be evaluated for case histories where manifestation was observed, i.e., P[$T_L|M_P$] or was not observed, i.e., P[$T_L|NM_P$]. At the same time, the probability that liquefaction did *not* occur in a layer needs to be evaluated for case histories where manifestation was *not* observed, i.e., P[$NT_L|NM_P$] and where it was observed but was attributed to a different layer, i.e., P[$NT_L|M_P$]. To develop this more complete analysis, the difference between triggering and manifestation needs to be distinguished and it needs to be recognized that triggering can occur without manifestation and vice versa. These distinctions can be made using a Bayesian approach.

4.1.1 Bayes' Theorem

Bayes' theorem derives directly from the total probability theorem. The intersection of Events *A* and *B* can be expressed as

$$P[A \cap B] = P[A|B] * P[B] = P[B|A] * P[A] \tag{4.1}$$

Solving for the probability of *A* given *B* yields Bayes' theorem,

$$P[A|B] = \frac{P[B|A] * P[B]}{P[B]} \tag{4.2}$$

In many cases, Event *A* is described as a hypothesis being true and Event *B* as the evidence that the hypothesis is true. In that case, it can be expressed as

$$P[hypothesis|evidence] = \frac{P[evidence|hypothesis] * P[hypothesis]}{P[evidence]} \tag{4.3}$$

The denominator can be expanded by considering the evidence for both cases of the hypotheses, i.e., that the evidence is consistent with the hypothesis and that the evidence contradicts the hypothesis.

$$P[hypothesis|evidence]$$
$$= \frac{P[evidence|hypothesis] * P[hypothesis]}{P[evidence\ when\ hypothesis\ is\ true] + P[evidence\ when\ hypothesis\ is\ false]} \tag{4.4}$$

In the liquefaction triggering problem, the common interpretation hypothesizes that liquefaction has been triggered based on the evidence, or absence of evidence, of surface manifestation. However, because manifestation also depends on hydraulic and system-related factors, in addition

to the actual triggering of liquefaction in one or more soil layers, a direct correlation between surface manifestation and triggering is not possible. Using the previously defined symbols for triggering and manifestation, Bayes' theorem can be expressed in the following manner for a soil layer that is susceptible to liquefaction and fully saturated (i.e., with P[S_L] = 1.0 and S = 1.0)

$$P[T_L|M_P] = \frac{P[M_P|T_L] * P[T_L]}{P[M_P]} = \frac{P[M_P|T_L] * P[T_L]}{P[M_P|T_L] * P[T_L] + P[M_P|NT_L] * P[NT_L]} \quad 4.5$$

The Bayesian framework can also be applied to case histories where no evidence of surficial manifestation was observed. Such cases have historically been interpreted as indicating the absence of triggering (i.e., P[$NT_L|NM_P$] = 1.0) which is not necessarily true. For this case, Bayes' Theorem can be applied as

$$P[NT_L|NM_P] = \frac{P[NM_P|NT_L] * P[NT_L]}{P[NM_P]} = \frac{P[NM_P|NT_L] * P[NT_L]}{P[NM_P|NT_L] * P[NT_L] + P[NM_P|T_L] * P[T_L]} \quad 4.6$$

The Bayesian framework may also be extended to include manifestations from non-susceptible layers. Cyclic softening of clay-like soils may produce manifestations such as surface cracks, lateral ground deformations, and settlement. When manifestations occur in the absence of sand boils, it is often difficult to ascertain whether the cause was liquefaction or cyclic softening. This can be included by expanding the NT_L condition to two conditions: a susceptible soil with NT_L (representing a sand-like soil that does not liquefy i.e., r_u<1.0) and a non-susceptible soil with NT_L (representing a clay-like soil which cannot liquefy but can experience cyclic softening and produce surface manifestations). This yields the following equation, modified from equation 4.5:

$$P[T_L|M_P]$$

$$= \frac{P[M_P|T_L]P[T_L|S_L]P[S_L]}{P[M_P|T_L]P[T_L|S_L]P[S_L] + (P[M_P|NT_L]P[NT_L|S_L]P[S_L] + P[M_P|NS_L]P[NS_L])} \quad 4.7$$

4.1.2 Probabilities of Interest

The probabilities in the Bayesian approach relate to both triggering (or not triggering) and manifestation (or lack thereof). Brief descriptions of each, using the notation in Figure 1-10 in which H_1 is the thickness of the non-liquefied crust and H_2 is the thickness of an underlying liquefaction-susceptible soil (after Ishihara, 1985, see also Section 1.2.3.1), are presented in Table 4-1. Of the six probabilities listed, three are directly computed from their complements, so models for only three independent probabilities, P[T_L], P[$M_P|T_L$], and P[$M_P|NT_L$], are needed to explore their impacts on the relationship between triggering and manifestation.

4.1.3 Illustration of Bayes Calculations

Figure 4-1 illustrates the main components of Bayesian calculations. The left side (to the left of the thin vertical line) represents Event T_L, the triggering of liquefaction in layer L; the right side represents the event of non-triggering, NT_L. Within each of these columns, conditional probabilities are represented. The red zone is the probability of manifestation due to triggering of the liquefiable layer (its probability conditional upon triggering multiplied by the probability of triggering). The blue zone is the probability of manifestation in the absence of triggering, e.g., ground cracking caused by cyclic softening of non-liquefiable soils or sand boils caused by high

(but not high enough to trigger liquefaction) pore pressures in a thick liquefiable layer below a thin crust. As shown in this example, there is a relatively high probability of triggering (loose soil), a high probability of manifestation given triggering, and a low probability of manifestation given no triggering – therefore, the probability that liquefaction actually triggered should be high if manifestation was observed. The probability of triggering given the observation of manifestation is equal to the red area divided by the sum of the areas of the red and blue zones. For P[T_L] = 0.7, P[$M_P|T_L$] = 0.9, and P[$M_P|NT_L$] = 0.2 (approximately the values in the figure), P[$T_L|M_P$] = 0.913, which means that the historical inference that manifestation = triggering is relatively good in this case.

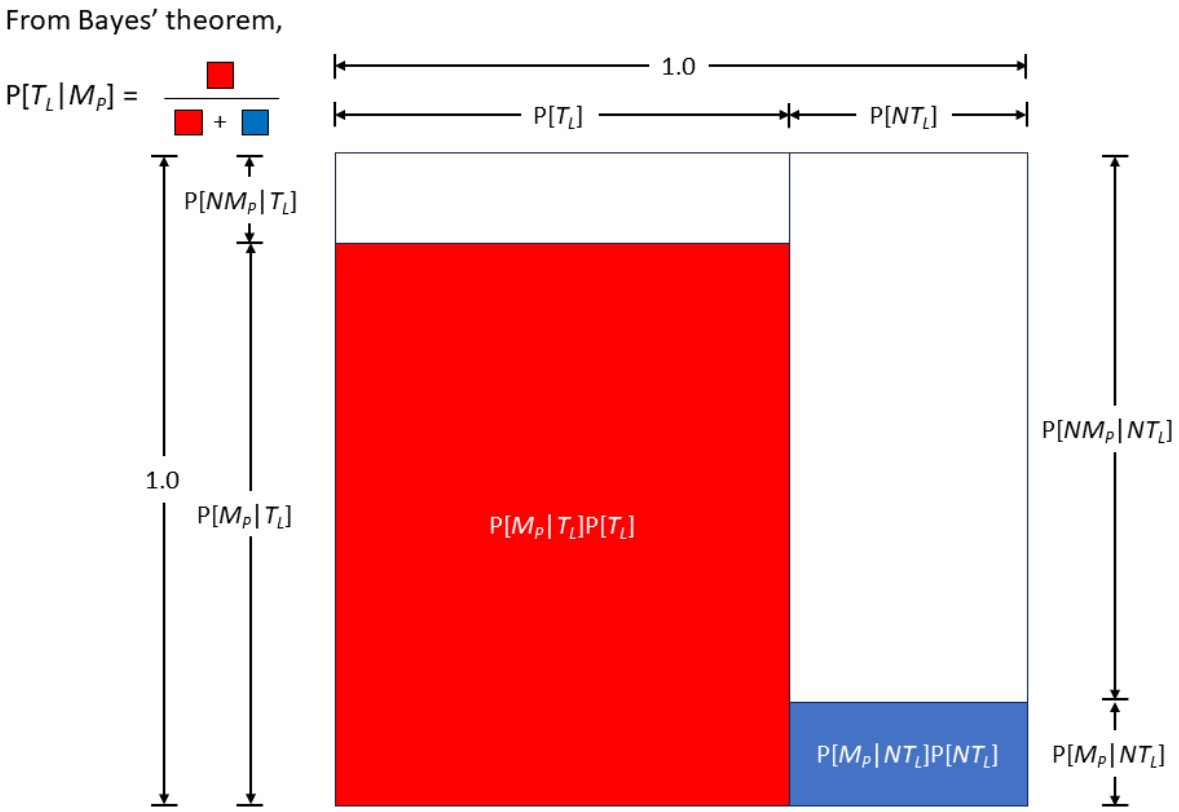

Figure 4-1. Graphical illustration of Bayes' theorem calculation to compute probability of triggering given observation of manifestation.

The historical interpretation of case histories also makes use of observations of no manifestation and has implicitly assumed that no manifestation means that liquefaction was not triggered. This case can also be visualized graphically as shown in Figure 4-2. In this case, the purple zone represents the probability of no manifestation when the liquefiable layer does not trigger. The green zone indicates the probability of no manifestation if liquefaction is triggered. As indicated in this example, there is a relatively high probability of liquefaction (loose soil), a low probability

of manifestation given triggering (the loose layer is deep and/or thin), and a very low probability of manifestation given no triggering – therefore, the probability that liquefaction actually triggered should be high if manifestation was observed. For P[T_L] = 0.7, P[$M_P|T_L$] = 0.1, and P[$M_P|NT_L$] = 0.02 (approximately the values shown in Figure 4-3), P[$T_L|M_P$] = 0.921 which, as expected, is quite high. However, the probability that liquefaction did not trigger if manifestation was not observed, i.e., P[$NT_L|NM_P$], would only have been 0.318. In this case, the historical inference that manifestation = triggering is reasonable (the thin, deep layer would almost certainly have had to trigger in order for surface manifestation to have been observed). However, the assumption that no manifestation means no triggering is not very good, because the probability of triggering given no manifestation P[$T_L|NM_P$] is 0.682, so P[$NT_L|NM_P$] = 1 - 0.682 = 0.318. Because of the hydraulic component of manifestation, an observation of no manifestation only supports a relatively low probability that liquefaction was not triggered.

These concepts have implications for how case histories should be interpreted, particularly with respect to the "critical layer" concept in cases that appear as apparent false positives (that have thin and/or deep critical layers) and false negatives (that may generate surface evidence without actually liquefying the soil). If no surficial evidence of liquefaction was observed for the case illustrated in Figure 4-2, the values of P[$T_L|NM_P$] and P[$NT_L|NM_P$] mean that there is a 0.682 probability that liquefaction *was* triggered even though no manifestation was observed. In the common graphical display of closed and open circles in q_{c1Ncs}-*CSR* space, this case could then be treated with two data points – an open circle with a weighting factor of 0.318 and a co-located closed circle with a weighting factor of 0.682.

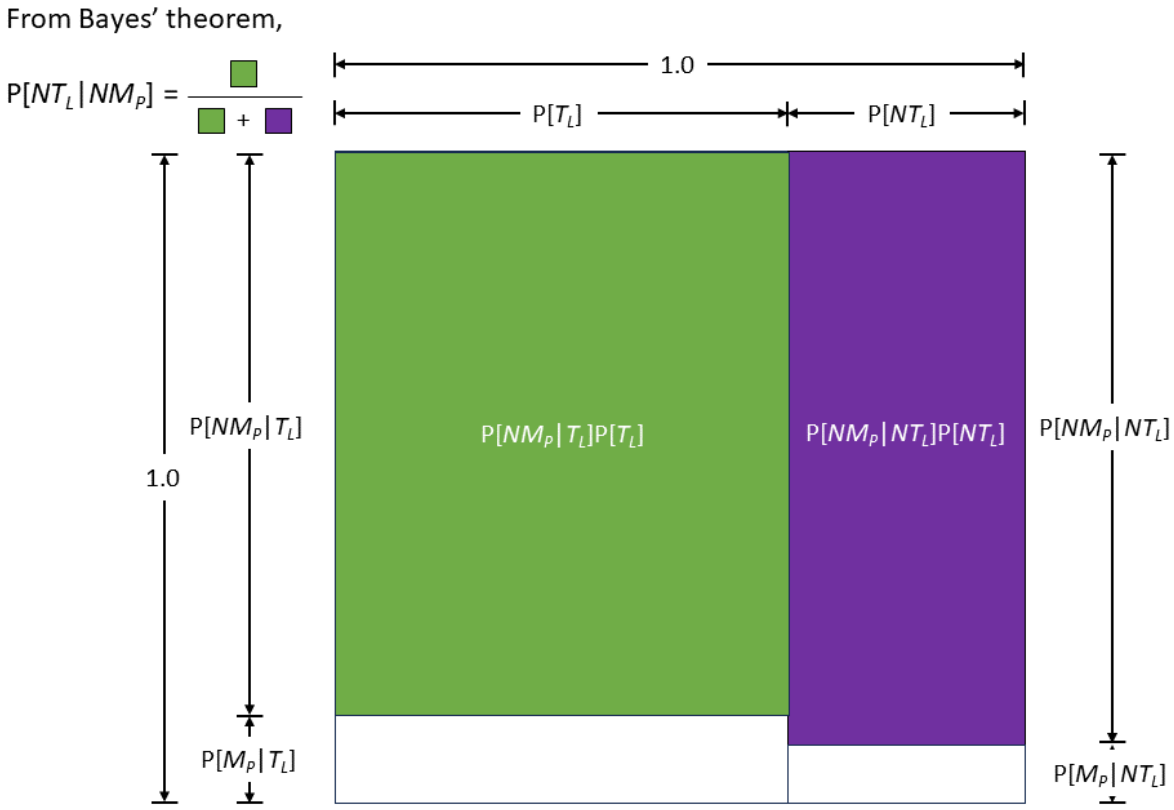

Figure 4-2. Graphical illustration of Bayes' theorem calculation to compute probability of no triggering given the lack of observed manifestation.

4.1.4 Example

As a specific example, consider the Wufeng A, WAC-2 CPT site (NGL site ID = 364, test ID = 1585) where no evidence of surface manifestation was observed following the 1999 Chi-Chi earthquake despite the presence of a loose, susceptible layer being exposed to a very high *CSR*. Figure 4-3 shows a CPT profile for the site with the layering detected by an agglomerative clustering algorithm (details in Section 5.3 and Hudson et al. 2023). Of particular interest is Layer 8 (highlighted green in Figure 4-3), which is 35 cm thick, could reasonably be interpreted as a

critical layer for this profile, and is overlain by a 5.3 m thick crust. With q_{c1Ncs} ~ 80 and I_c ~ 1.9, Layer 7 is loose and susceptible and therefore should have a high probability of triggering when subjected to strong shaking. For illustrative purposes, assume P[T_L] = 0.9. Because Layer 7 is thin and under a thick crust, manifestation seems unlikely so a value of P[$M_P|T_L$] = 0.15 will be assumed. Finally, the chance that manifestation could be produced by this layer with pore pressures insufficient to trigger liquefaction seems miniscule, a value of P[$M_P|NT_L$] = 0.005 will be assumed. These values produce P[$NT_L|NM_P$] = 0.115, which indicates that little confidence should be placed in a "no liquefaction" interpretation of this case history. Instead, the case history could be interpreted as two co-located data points on a classic *CSR* vs. q_{c1Ncs} curve – a solid circle indicating triggering with a weighting factor of 0.885 and an open circle indicating no triggering with a weighting factor of 0.115. Using these weights, instead of a single open circle with an implied weighting factor of 1.0, the response of this soil profile is more realistically characterized in the triggering model development process.

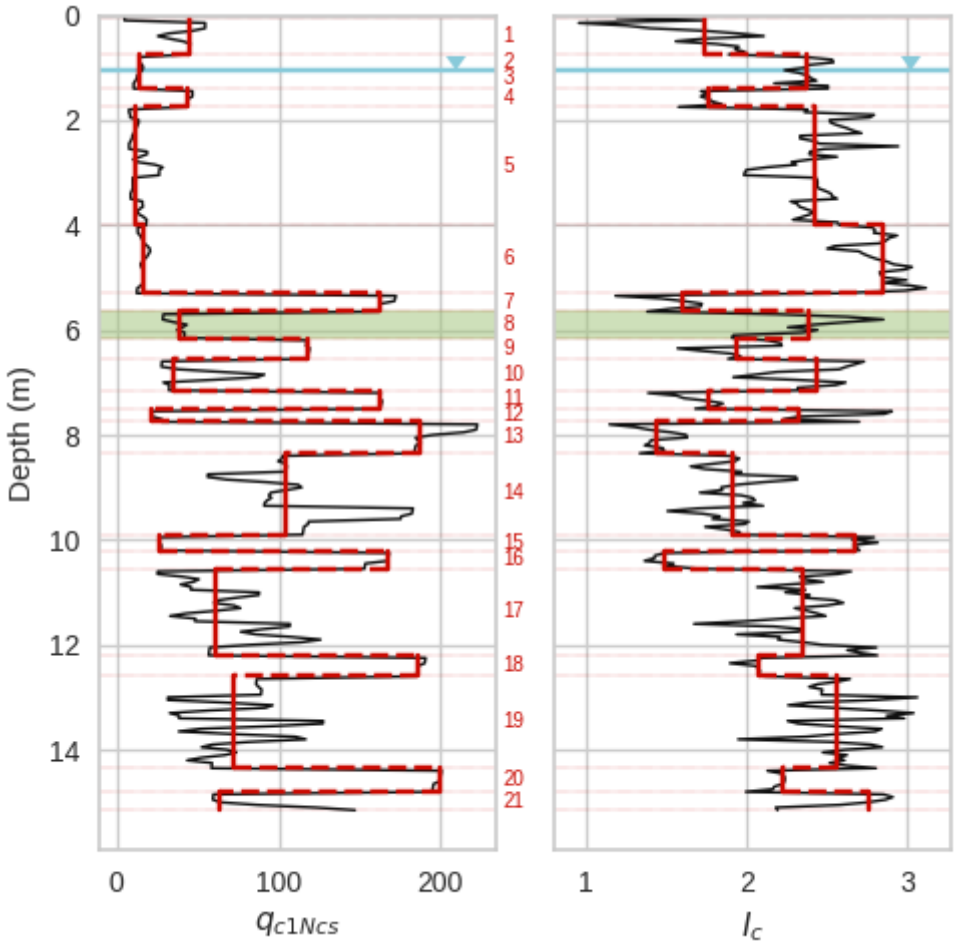

Figure 4-3. CPT profile for Wufeng A WAC-2 site (NGL site ID = 364, test ID = 1585).

4.2 Required Components

Separating triggering from manifestation using the Bayesian framework has potential to reduce bias in the SMT triggering model. It also appears that some, and perhaps a significant amount, of the uncertainty in the model could be associated with “false positive” cases like Wufeng A WAC-

2 that show up as a “no liquefaction” with critical layers that have low penetration resistance and a high *CSR*.

In contrast, prior compilations of liquefaction case histories show data that appear to be outliers in the form of “false positives” (cases where manifestation was not observed for conditions under which triggering was expected) and “false negatives” (cases in which manifestation was observed for conditions under which triggering was not expected). By more appropriately interpreting the case histories in terms of probabilities of triggering (or non-triggering) given the observation (or non-observation) of surface manifestation, what appear to be outliers may not actually be outliers. The Bayesian framework described here allows prior knowledge of liquefaction behavior, as informed by principles of soil mechanics and laboratory test data, to be utilized to advantage in the process of case history interpretation. The types of calculations described in this chapter can address these situations, but they need inputs that are not currently available. These include the quantities listed in Table 4-1.

Table 4-1. Descriptions of Probabilities in the Bayesian Approach

Factor	Probability
$P[S_L]$	Probability of susceptibility of a layer. This is based on mineral composition as inferred from soil behavior type index, I_c.
$P[T_L\|S_L]$	Probability of triggering if soil is susceptible. For this model, it is the probability of triggering itself in a particular layer of soil (not accounting for overlying crusts or other profile-related hydraulic factors). A laboratory-based "prior" is utilized herein to assess triggering.
$P[T_L]$	Probability that the susceptible soil layer (H_2 layer) triggers. Equal to the product of $P[T_L\|S_L]$ and $P[S_L]$
$P[NT_L]$	Probability that H_2 layer does not trigger = 1 – $P[T_L]$
$P[M_P\|T_L]$	Probability of manifestation given that H_2 layer triggers. Depends on H_1-H_2 relationship and other hydraulic factors. This probability has been inferred from observations of manifestation using procedures described in Section 4.4. Triggering is first assessed using the laboratory model, and probability of manifestation of the profile is subsequently assessed conditional on probability of triggering, and other factors such as the penetration resistance, depth, thickness, and soil behavior type index for each layer.
$P[NM_P\|T_L]$	Probability that no manifestation occurs even when H_2 layer triggers. This is the complement of the probability of manifestation if triggering occurs {i.e., $P[NM_P\|T_L] = 1 - P[M_P\|T_L]$}, which inherently assumes that there is no "marginal" manifestation category.
$P[M_P\|NT_L]$	Probability that high pore pressures (but not high enough to trigger liquefaction) cause sand boils or other observations that are usually interpreted as manifestation of liquefaction. Can potentially occur with thick liquefiable layer (high H_2) under thin crust (low H_1).
$P[NM_P\|NT_L]$	Probability that no manifestation is observed when liquefaction is not triggered – equal to $1 - P[M_P\|NT_L]$.

The SMT has opted to rely on laboratory test data as an estimation of the prior probability for this purpose. Data was collected for a wide range of sands and established the within- and between-sand variability in *CRR* given some loading and D_r, which has been used to estimate $P[T_L|S_L]$. The

lab-based expression for P[$T_L|S_L$] is then updated based on observations of manifestation after developing an initial model using the laboratory-based relationship. This approach is described in Section 6.2. Alternatively, one could create a case history database that excludes cases where impedance of drainage was a significant factor affecting manifestation potential, and then develop a triggering model based on that database. This approach was ultimately not pursued because (1) it is difficult to ascertain with a high level of confidence whether triggering would for sure result in a manifestation at a particular site, and (2) the resulting database would be very small and potentially not statistically reliable.

The existence of P[$M_P|NT_L$] and P[$NM_P|T_L$], i.e., manifestation without triggering and triggering without manifestation, can be shown by examination of the data of Hutabarat and Bray (2021, 2022), which shows that the model itself has quite a bit of uncertainty in it. There are, for example, cases of minor, moderate, and severe manifestation that plot within the "None" zone (7 out of 96) for the thick sand sites (left side) and minor and moderate points (3 of 80) within it for the stratified sites (right side). There are also cases of no manifestation that plot above the "None" zone (6 of 96 for the thick sand sites and 3 of 80 for the stratified sites).

Figure 4-4 shows data extracted from the Supplemental Data file of the (Hutabarat and Bray 2022) paper, hereafter abbreviated "HB22". In Figure 4-5, the data from HB22 is combined and plotted using solid circles for cases with manifestation (Minor, Moderate, Severe, or Extreme) and open circles for cases without manifestation. The data is shown with linear and logarithmic L_D scales (L_D = 0.01 was assigned to all cases that HB22 identified as having L_D = 0, which implies no triggering anywhere within the profile). In both plots, the boundary between the None and Minor

states of manifestation severity are shown in red. Of the 176 case histories in the HB22 database, 55 showed some evidence of manifestation and 121 showed no evidence.

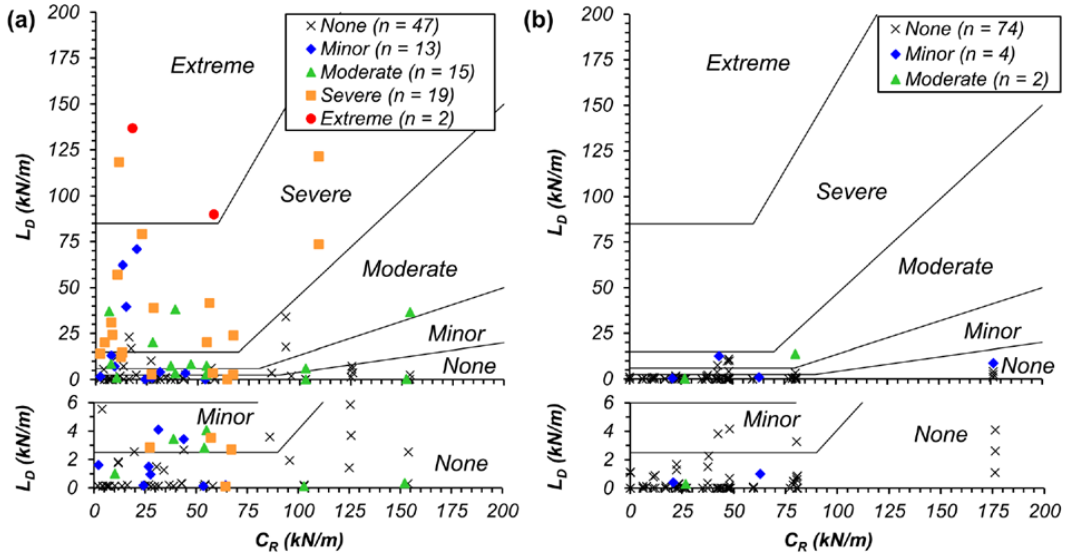

Figure 4-4. Plots of L_D vs C_R (Hutabarat and Bray 2022).

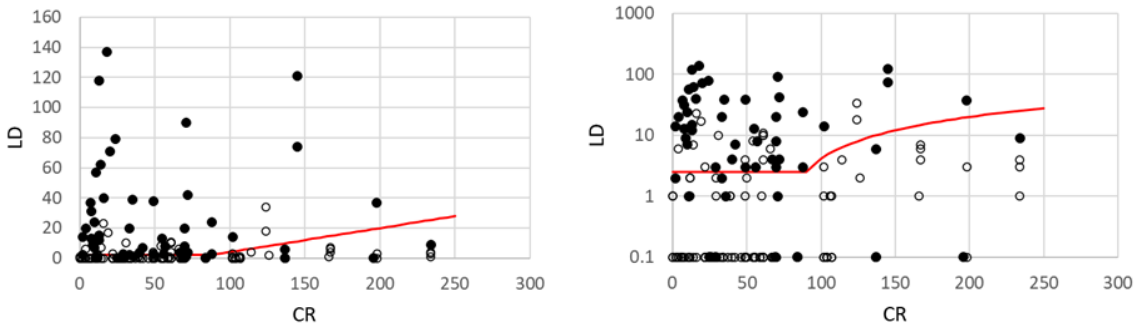

Figure 4-5. Plots of L_D vs C_R in linear-linear and log-linear scales

HB22's bilinear boundary between None and Minor can be viewed as the minimum value of L_D required to produce (any degree of) manifestation for a given C_R, which can be referred to as $L_{D,min}$. To accommodate the sloping part of the boundary, values of L_D for actual case histories can be normalized as $\alpha = L_D / L_{D,min}$. In this form, α can be thought of as the reciprocal of a factor of safety against manifestation. While HB22 did not attempt to characterize uncertainty in their manifestation model, it can be at least crudely approximated by considering the distribution of "missed" predictions of the occurrence of manifestation. Missed predictions can be considered as cases in which an observation of None (marked by an 'x' in Figure 4-4 and an open circle in Figure 4-5) plots above the $L_{D,min}$ boundary and cases in which observations of Minor, Moderate, Severe, or Extreme plot below that boundary. By digitizing the HB22 data and assigning "observation values" of 0 to cases in which manifestation was not observed and 1 to cases in which it was (i.e., Minor, Moderate, Severe, or Extreme), the observation values can be plotted versus the parameter α, as shown in Figure 4-6. Ideally, all points with $\alpha > 1.0$ would show some degree of manifestation and all points with $\alpha < 1.0$ would not. However, Figure 4-7 shows that there are points with $\alpha > 1.0$ for which no manifestation was observed (zero values on y-axis) and points with $\alpha < 1.0$ for which manifestation was observed (1 values on y-axis). The latter of these are cases in which manifestation occurred where HB22 would predict none.

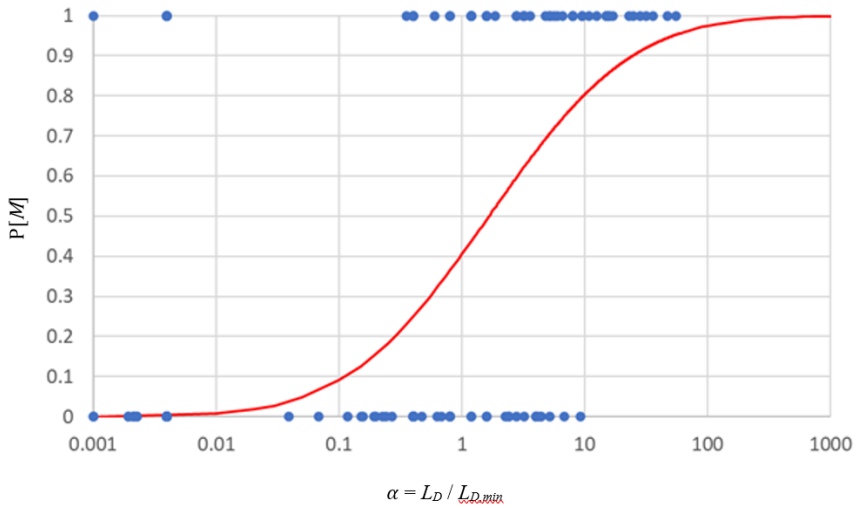

Figure 4-6. P[M] vs α using data from Hutabarat & Bray (2022). For observations, P[M] = 1 for "yes" and P[M] = 0 for "no."

In Figure 4-6, 12 of the 176 case histories (6.8%) have α < 1.0 but showed some degree of manifestation (note that some points plot on top of each other). Of these 12, three have α = 0, which means that FS_L > 1.0, i.e., a no triggering prediction, over the entire depth of the profile – one with moderate manifestation and two with minor. The fact that three of the 55 sites with manifestation were not predicted to trigger, suggests that P[$M_P|NT_L$] = 5.5% for this small sample set – while this percentage is not large, it does indicate that surface manifestation can develop at sites where triggering was not predicted to occur. The HB22 database includes 121 cases where no manifestation was observed. 16 of these cases had α > 1.0 but no observations of surface manifestation. Assuming an average α value of at least 4.0 indicates a very high probability of some manifestation developing, six of the 121 manifestation cases had α > 4.0 but no manifestation was observed. These "outliers" represent cases where liquefaction was triggered but manifestation was not observed, suggesting that P[$T_L|NM_P$] = 5.0% for this small sample set, again showing that

surface manifestation can be absent for cases where liquefaction was almost certainly triggered. Thus, the data and analyses developed by HB22 suggest that both P[$T_L|NM_P$] and P[$M_P|NT_L$] are greater than zero.

4.3 Modeling of Critical Layer Triggering

The Bayesian framework can also be used with the case history database to develop a model for triggering in critical layers, which is analogous to the approach used in legacy models (Section 3.2). This form of model development requires a prior model for P[$T_L|S_L$], assumed manifestation models (P[$M_P|T_L$], and P[$M_P|NT_L$]), and assumed non-manifestation models {P[$NM_P|NT_L$] and P[$M_P|NT_L$]}. Those models would then be applied to all case histories.

Consider, for example, a case history where surface manifestation was observed. Equation 4.5 would be used to establish P[$T_L|M_P$] and the complement would be computed as P[$NT_L|M_P$] =1-P[$T_L|M_P$]. This would lead to two weighted and co-located points. For a case history without surface manifestation, Equation 4.6 would be used to compute P[$NT_L|NM_P$] and its complement would be P[$T_L|NM_P$] =1-P[$NT_L|NM_P$]. In an extended multiple-critical-layer approach, each weighted critical layer data point would consist of two co-located points with its weighting factor multiplied by the same conditional probabilities.

The suite of M_P and NM_P weighted data points would then be used in a regression analysis to establish the boundary curve, which would update the prior P[$T_L|S_L$] model. This outcome would depend on the assumed manifestation models and the assumed non-manifestation models.

4.4 Modeling of Profile Manifestation

This section describes the framework adopted to compute the probability of manifestation of a profile. The probability that a particular layer will manifest depends on factors beyond penetration resistance and cyclic stress ratio. Additional factors include the depth and thickness of the layer, the thickness and/or strength of a crust layer, whether the layer is interbedded or uniform, soil composition, and impeded drainage conditions. Previous models may have included these factors as part of the judgment utilized to select the critical layer. However, those judgments are subjective and were not explicitly documented; this framework seeks an objective method for assessing $P[M_L|T_L]$. Rather than selecting a single critical layer to be representative of the profile, the framework evaluates the probability that each layer within a profile will cause surface manifestation, $P[M_L|T_L]$, where the subscript "*L*" on *M* denotes manifestation resulting from a specific layer. It then aggregates the contributions from all of the layers to define the probability of profile manifestation $P[M_P]$.

4.4.1 Manifestation Probability for a Single Layer

As stated above, there are many variables that could be influential in prediction of $P[M_L|T_L]$ (in this section the subscript "*L*" is excluded because in all cases the probability is referring to a single layer). The variables considered in this model are provided in Table 4-2.

Table 4-2. List of layer variables considered in manifestation model.

Variable	Description
q_{c1N}	Overburden-corrected cone tip resistance
I_c	Soil behavior type index
z_{top}	Depth to top of layer
$\sigma'_{v,0}$	Initial vertical effective stress
t	Layer thickness
CSR	Cyclic stress ratio
τ_{cyc}/s_u	Cyclic shear stress divided by undrained shear strength
$L_{D,l}$	Liquefaction eject demand of a layer (Hutabarat and Bray 2022)
$C_{R,l}$	Crust resistance above a layer (Hutabarat and Bray 2022)

Note that L_D and C_R (introduced in Section 1.2.3) have been converted from profile parameters to layer properties in Table 4-2. This is achieved by integrating from the top to bottom of each layer for the case of $L_{D,l}$ and from the ground surface to the top of the layer for $C_{R,l}$ rather than the full profile.

These variables must be combined in a mathematical framework in a manner that separates "yes" from "no" manifestation cases based on the properties of the variables. A common functional form utilized in binary classification problems is the logistic function, as shown in Equation 4.8.

$$p = \frac{1}{1 + \exp(-\boldsymbol{\beta}^T \boldsymbol{x})} \quad 4.8$$

where p is the probability of an outcome, $\boldsymbol{\beta}$ is an array of coefficients, and $\boldsymbol{x}$ is an array of variables (bold variable names indicate the variable is a vector or array rather than a scalar).

The logistic function has several desirable features that make it useful for binary classification problems. First, p is constrained in the range between 0 and 1, which is the valid range of probabilities of an outcome. Second, $\boldsymbol{\beta}^T\boldsymbol{x}$ is a linear combination of the input variables. Although the resulting logistic function is nonlinear, logistic regression is often considered to be a linear separator because $\boldsymbol{\beta}^T\boldsymbol{x}$ is a linear function. The variables in Table 4-2 can potentially be combined in many different ways using many different functional forms. The simplest approach would be to combine all of the variables in Table 4-2 together in a single logistic function. However, doing so would group together variables that are unrelated to each other. For example, q_{c1N} and I_c are soil properties, and it makes sense to group them together, whereas z_{top} and t are geometric properties that should be grouped together. Therefore, an attempt was made to group variables into distinct classes and multiply the logistic functions for each grouping together. However, this caused large instabilities in regression of model coefficients so the simpler framework with grouping all the chosen variables into one logistic function was chosen. An example is provided by Equation 4.9.

$$P[M|T] = \frac{1}{1 + exp\left[-\left(\beta_0 + \beta_1 q_{c1N} + \beta_2 I_c + \beta_2 z_{top}\right)\right]} \quad 4.9$$

Equation 4.9 forms a four-dimensional surface in P[M|T], q_{c1N}, I_c, z_{top} space that is impossible to visualize in three-dimensional space. However, the components are illustrated schematically in

Figure 4-7. The probability factor depends jointly on all three features, so multiple plots are required to demonstrate key aspects of the function. As evidenced in the top left subplot of Figure 4-7, a layer at the ground surface (z_{top} = 0m) with I_c = 1 (represented as the darkest blue curve) has P[M|T] ~ 1 at q_{c1N} < 75. As q_{c1N} increases, P[M|T] decreases until it is approximately 0 at q_{c1N} = 300. As I_c increases (the color of the curve gets warmer), for the same z_{top} and q_{c1N}, the P[M|T] decreases. Moving to different subplots from left to right and top to bottom, as z_{top} increases P[M|T] decreases for the same q_{c1N} and I_c values.

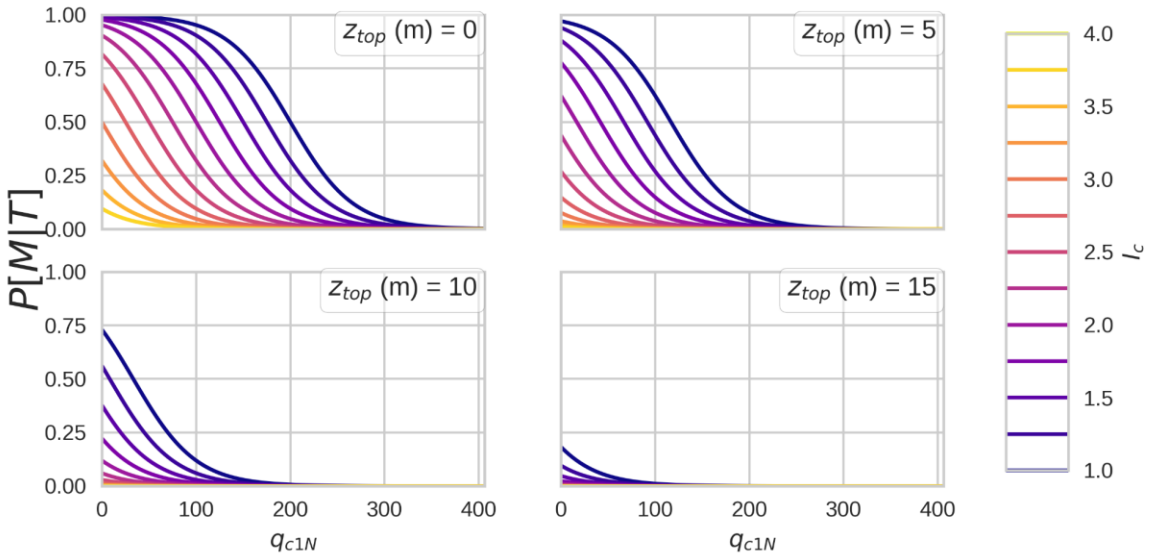

Figure 4-7. Example probability factors for layer manifestation conditioned on q_{c1N}, I_c, and z_{top}.

As presented in Section 4.1.1, probabilities of manifestation that occur due to no triggering (P[M|NT]) can be separated into probability of manifestation given no triggering of a susceptible layer (r_u < 1.0 but producing large strains) and manifestation in a non-susceptible layer (cyclic

softening). Each are given their own set of logistic functions and combined to produce the total probability of manifestation of a layer P[M_L] in Equation 4.10.

$$P[M_L] = 1 - (1 - P[M|T]P[T|S]P[S]K_{Sat}) * (1 - P[M|NT]P[NT|S]P[S]K_{Sat}) * (1 - P[M|NS]P[NS]K_{Sat}) \quad 4.10$$

where P[T|S], P[S], P[NT|S], and P[NS] are all obtained from probabilistic model priors. P[M|T], P[M|NT], and P[M|NS] are each logistic functions similar to Equation 4.9 but with variables important for the respective scenarios (e.g., q_{c1N} for P[M|T] and τ_{cyc}/s_u for P[M|NS]). K_{Sat} is a term introduced to take into account the saturation of the soil. In future work a K_{Sat} model could be developed using information such as P-wave velocity and partial saturation zones around the groundwater table. For this manuscript and model, however, it is taken as a binary value: K_{Sat} = 0 above the groundwater table and K_{Sat} = 1 below the groundwater table. Saturation has been shown to affect triggering; specifically as saturation decreases from S = 1, the *CRR* for a given D_R increases (Arab et al. 2011; Okamura and Soga 2006; O'Donnell et al. 2017; Tsukamoto et al. 2002; Yang et al. 2004). Rather than including a K_{Sat} term as done in Equation 4.10, a saturation effect could be applied to the P[T_L|S_L] function using an estimated saturation that could be derived from proximity to the groundwater table and/or measured p-wave velocity (V_p). The framework presented here uses a simplified, binary saturation effect, therefore it is applied to the P[M_L] equation rather than the P[T_L|S_L] function because it would cause the same effect. Future work needs to be done on Saturation effects within the presented framework.

4.4.2 Manifestation Probability for a Profile

The probability of manifestation of a profile P[M_P] is computed using Equation 4.11, where N_L is the number of layers in the profile, t_i is the thickness of the i^{th} layer, and t_c is a constant characteristic thickness. Equation 4.11 is a simplified case that only considers contribution to manifestation from liquefaction triggering and ignores cyclic softening and non-triggering manifestations. Equation 4.11 consists of multiple pieces that warrant separate discussions. First, $PF_{ML|TL}$ is the *probability factor* of manifestation of a layer given triggering of the layer, defined exactly as P[$M_L|T_L$] in Equation 4.9. PF_{TL} is the probability factor of triggering which is the product of the probabilistic triggering and susceptibility prior models (P[$T|S$]*P[S]). The reason these are denoted as probability factors rather than probabilities now is because in the profile manifestation framework with the t/t_c exponent (explained later in this Section), these quantities are not the true probabilities of manifestation or triggering of a layer.

Second, the expression $\left(1 - PF_{M_L|T_L} PF_{T_L}\right)^{t/t_c}$ is equal to the probability that the layer will not manifest liquefaction, P[NM_L] = 1 - P[M_L]. If none of the layers manifest liquefaction, then the profile does not manifest liquefaction. Therefore, P[NM_P] is computed as a product sum of P[NM_L]. However, a direct product sum (i.e., without the t/t_c term in the exponent) inherently assumes that P[NM_L] for each layer is statistically independent from all other layers. This is generally not true. The t/t_c exponent has removed the influence of discretization by tying layer thickness to the characteristic length. The characteristic thickness is the layer thickness for which $PF_{ML|TL}$ is statistically independent of the other layers. If all layers have a thickness equal to the characteristic

thickness, then Equation 4.11 reduces to a simple product sum. If a layer is thicker than the characteristic thickness, it becomes more likely to manifest, and vice versa, as illustrated in Figure 4-8. Thickness as a variable within the logistic regression instead of as an exponent was considered, but ultimately included as an exponent instead for this reason.

$$P[M_P] = 1 - \prod_{i=1}^{N_L} \left(1 - PF_{M_L|T_L} PF_{T_L} K_{Sat}\right)^{t_i/t_c} \qquad 4.11$$

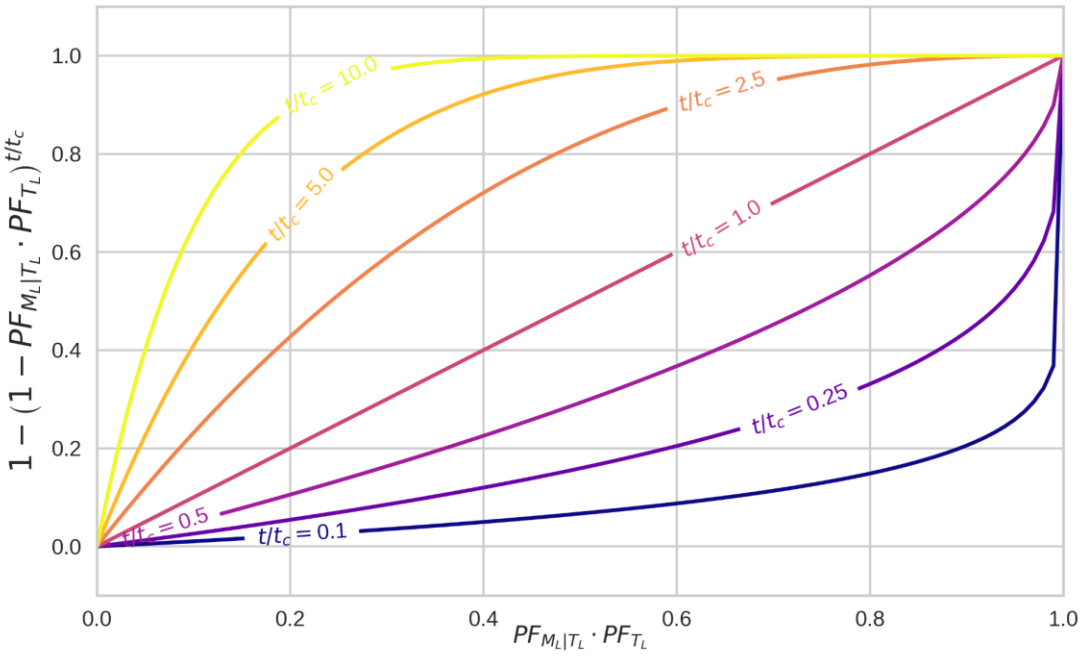

Figure 4-8. Influence of t/t_c exponent on probability of layer manifestation.

Consider the example profile in Figure 4-9, which has three layers with thicknesses of 3 m (also using t_c = 3m for simplicity), and groundwater table at the ground surface. Layer 1 has a high q_{c1N} and I_c (300 and 3.2, respectively), layer 2 has a low q_{c1N} and high I_c (50 and 3.2, respectively), and layer 3 has low q_{c1N} and low I_c (50 and 1.5, respectively). A strong ground motion with CSR=0.6 is assumed. The first step is to compute P[T|S] for each layer; layer 1 has P[T|S]~0 due to its high q_{c1N}, whereas layers 2 and 3 have relatively low q_{c1N} and high CSR, therefore P[T|S]~1. The P[S] is low for layers 1 and 2 due to high I_c. The product of P[T|S] and P[S] is PF_{TL}, which is 0, 0, and 1 for layers 1, 2, and 3 respectively. The logistic functions in Figure 4-7 and Equation 4.9 are used with the profile data to compute $PF_{ML|TL}$. Layer 1 has $PF_{ML|TL}$ = 0, layer 2 has $PF_{ML|TL}$ = 0, and layer 3 has $PF_{ML|TL}$ = 0.5. These results are combined in Equation 4.11 to provide profile manifestation probability P[M_P] = 0.5, which is entirely caused by layer 3.

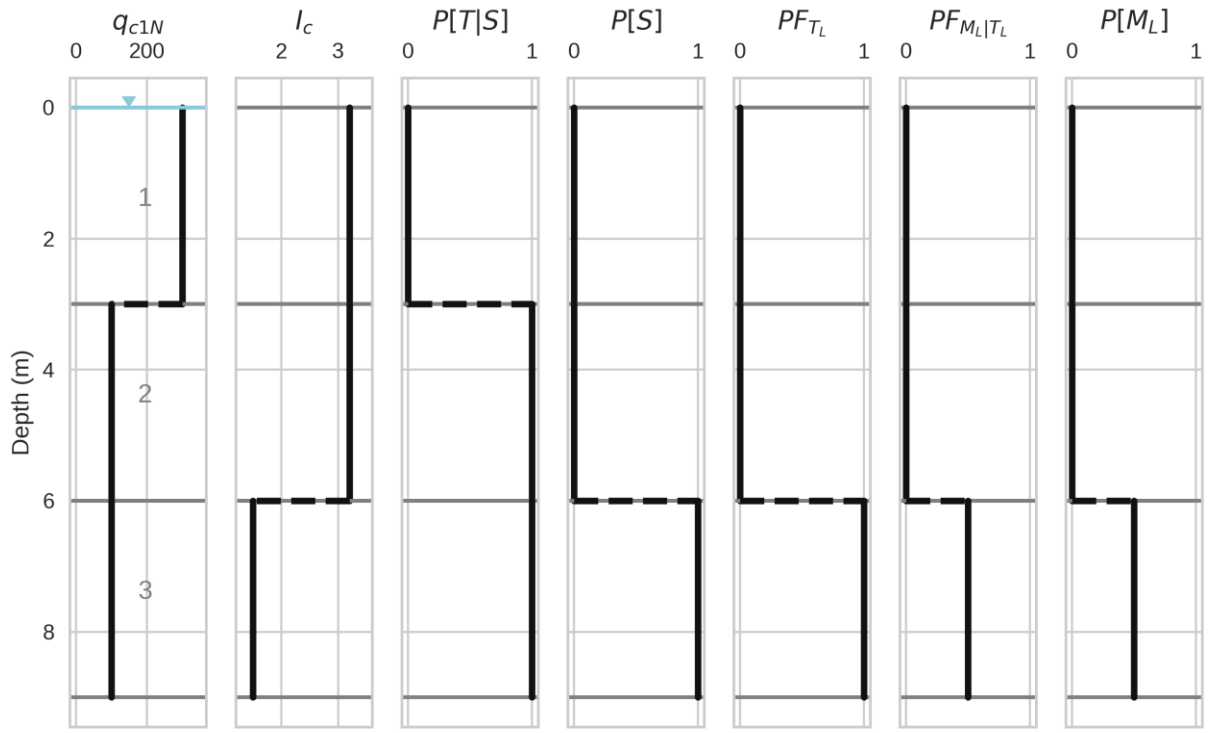

Figure 4-9. Simplified CPT profile demonstrating the computation of P[M_P].

In addition to layer properties, there may be profile properties that could improve a manifestation model's predictive accuracy such as ground motion intensity measures other than *PGA* or variables such as H_1 and *LPI* which are computed for an entire profile rather than an individual layer. These could help capture system effects or ground motion properties that are not reflected in layer properties or *CSR*. Therefore, P[M_P] can be expanded from the form presented in Equation 4.11 to the following:

$$P[M_P] = 1 - \left(\prod_{i=1}^{N_L} \left(1 - PF_{M_L|T_L} PF_{T_L} K_{Sat}\right)^{\frac{t_i}{t_c}} \right) * (1 - PF_P) \quad 4.12$$

Where PF_P is the probability factor for the profile-scale manifestation effects defined using the same logistic functional form as Equation 4.8. Any combination of profile variables can be included in PF_P and Table 4-3 lists the different profile variables that were considered during formulation of the manifestation model.

Table 4-3. List of profile variables considered in manifestation model.

Variable	**Description**
H_1	Nonliquefiable crust thickness
C_R	Crust strength
L_D	Liquefaction Demand
PGV	Peak Ground Velocity
CAV	Cumulative Absolute Velocity
I_a	Arias Intensity
LPI	Liquefaction Potential Index
LSN	Liquefaction Severity Number

4.4.3 Profile-Based Regression Framework

Computing P[M_P] requires specification of the prior distributions for the coefficients in the PF_S, $PF_{T|S}$, and $PF_{M|T}$ functions, and the characteristic thickness, t_c. Independently regressing all of these based on case history data is infeasible and undesirable because (i) the amount of field case history data is inadequate to isolate so many different variables with nonlinear relationships, and (ii) there is a body of knowledge from laboratory testing that help constrain PF_S and $PF_{T|S}$. This approach is therefore to develop prior distribution functions for PF_S and $PF_{T|S}$ from laboratory data and then use Bayesian regression to update uninformed $PF_{M|T}$ and PF_P coefficients and the more strongly informed PF_S and $PF_{T|S}$ coefficients. This section presents the framework utilized to infer the coefficients based on observations of manifestations at NGL sites. The functional forms of the probability factors and results of the inferences are presented in Chapter 6.

In Bayesian regression, coefficients are characterized with prior distributions and then guesses of posterior distributions are sampled using a Hamiltonian Monte Carlo algorithm (Hoffman and Gelman 2011, 2014) along with the distribution of data and Bayes theorem to produce a posterior belief about the coefficients (Gelman et al. 2014). This regression seeks coefficients within the components of Equation 4.12 that maximize the Bernoulli log-likelihood likelihood function given by

Equation 4.13, where y_k is a binary indicator of whether manifestation was observed at the k^{th} site (y_k = 1 if manifestation was observed, y_k=0 if it was not), and N_P is the number of profiles in the database. This likelihood function is similar to those used in other probabilistic liquefaction models (e.g., Cetin et al. 2018; Moss et al. 2006).

$$L = \frac{1}{N_P}\sum_{k=1}^{N_P}[y_k \ln(P[M_P]_k) + (1 - y_k)\ln(1 - P[M_P]_k)] \quad 4.13$$

The likelihood function exhibits several notable properties. First, if y_k=1, only the first part of the expression within the square brackets on the right side of Equation 4.13 contributes to the cost function for profile k, whereas only the second expression contributes if y_k=0. Second, if the prediction is a true positive (i.e., if y_k=P[M_P]$_k$ = 1), or a true negative (i.e., if y_k=P[M_P]$_k$ = 0), the contribution to the cost function from that profile is zero. Only values of P[M_P] that do not match the observed manifestation contribute to the cost function. The ideal scenario would therefore be to select an optimal set of coefficients that render P[M_P] values that are either 0 or 1, and perfectly match the observations. In that case, the selected variables perfectly separate the data into distinct domains, and the cost function would be L = 0. For real datasets, this is generally not feasible, and the value of L will therefore be less than zero.

When a single logistic function is utilized to define the probability of occurrence of an event (i.e., in traditional logistic regression), the cost function given by Equation 4.13 is convex, meaning that its second derivative is always positive. Logistic regression is therefore a convex optimization problem that is guaranteed to find the absolute minimum (within a specified threshold) using techniques like the gradient descent method (Cauchy 1847). However, the P[M_P] function is more complicated in this case, involving products of logistic functions raised to an exponent. As a result, the cost function is not convex, and can contain local minima. Furthermore, it is desirable to constrain values of certain variables. As a result, the solution involves a non-convex constrained optimization problem, which is more complicated than logistic regression. Therefore, the approach

is to adopt a No-U-Turn Hamiltonian Monte Carlo sampling (NUTS) algorithm (Hoffman and Gelman 2011, 2014). NUTS uses a recursive algorithm to build a set of likely candidate points that spans a wide swath of the target distribution, stopping automatically when it starts to double back and retrace its steps. The python package PyMC is used to perform NUTS and Bayesian regression (Wiecki et al. 2023).

5 Case History Processing

Case history processing is required to convert data (e.g., CPT profiles, groundwater table measurements, ground motion measurements, observations of liquefaction manifestation) into metrics that facilitate model development (e.g., *CSR*, q_{c1Ncs}). This approach to case history processing combines automated procedures with human inspection and judgment to assign liquefaction observations to nearby in situ tests, identify layers, and process the characteristics of these layers. Whenever feasible, judgments are codified so they are objective and reproducible by other analysts. The development of calibrated automated processes is crucial for analyzing a database as large as the NGL database, and provides a repeatable, consistent, and objective initial view of the data.

This chapter describes the steps required to process liquefaction case histories as contained in the NGL database and to assign layer properties for use in model development. These steps include several advances of the state-of-the-art in liquefaction evaluation, such as a revisited relationship between I_c and *FC*, improved estimation of ground motion intensity, and an automated layer detection algorithm.

5.1 Assigning Observations to In-Situ Tests

Observations of surface manifestation (or lack thereof) and site investigations are not necessarily collocated in the NGL database so it is necessary to decide which observation is to accompany which test (i.e., what in situ test data should be used in evaluating the soil layers that contributed

to the surficial manifestation of liquefaction or lack thereof). Observations and in situ tests are associated through a link to a common site in the SQL data structure, but within a site there are often multiple observations and multiple in situ tests. Furthermore, there are often "yes" and "no" observations of manifestations within the same site. To make initial assignments of observations to in situ tests, Python code in Jupyter Notebooks was used to develop the following algorithm.

1. Select a site and identify all the in-situ tests and observations that are associated with that site.

2. Compile the latitude and longitude values for the tests and observations and compute an array containing the distance in meters between every observation and test at the site. Sometimes the latitude and longitude value for an observation is not exactly known when submitted to the database and therefore is collocated with a field test. It is likely there are some "yes" observations that appear to have no separation distance when in reality there was some distance between the manifestation and the field test.

3. Separate the observations by events (some sites have observations from more than one earthquake event).

4. Assign the closest in situ test to each observation for each event so that every observation has an in-situ test assigned to it.

This is an initial automated process to make these assignments, followed by a human review by SMT members examining each test-observation pair. To conduct the review, the SMT developed

a Jupyter notebook to visualize and summarize the available data for each site and event combination. A screenshot of the notebook is shown in Figure 5-1. Red markers indicate “yes” manifestation cases, black markers are “no” manifestation, and green markers are CPT locations. When a manifestation observation and CPT sounding are collocated, the green CPT pins are obscured, and a circle is drawn around the pins to indicate collocation. The purpose of this review was to:

1. Confirm the appropriate assignments of “yes manifestation” and “no manifestation” to an individual CPT or groups of CPTs when more than one CPT could be reasonably assigned to the same field observation

2. Identify and exclude case histories where the distance between a CPT and an observation of “yes manifestation” or “no manifestation” is too great to reasonably adopt (despite being the closest CPT identified by the initial algorithm)

3. Identify CPT data that should be disqualified for reasons not readily detected by the algorithms (e.g., unreliable CPT equipment)

4. Identify case histories where the presence of nearby structures could potentially affect the manifestation of liquefaction

5. Assign weights to CPTs when multiple soundings are assigned to the same observation. In this manner, multiple CPT’s may be paired with a single observation to form a single case history. The assigned weights sum to unity.

At least one member of the SMT and often two or more used this tool to review each case history that the algorithms initially identified. This process yielded 546 total case histories, each with a CPT associated with an observation of "yes" or "no" manifestation. The median distance between site investigation locations and observations is 0m (i.e., over half of the manifestation observations are collocated with a CPT sounding), and the mean distance is 13.7m. A histogram of the pairing distance is presented in Figure 5-2.

Figure 5-1. A screenshot of the Jupyter notebook that the SMT developed for review of individual case histories. Black markers represent observations of "no manifestation", red markers represent "yes manifestation", green markers represent CPTs, red/black lines connect CPTs and observations that the SMT grouped together, and red/black circles indicate a co-located CPT and observation pair (note that the green CPT marker is obscured by the red/black observation marker for collocated CPT/observation pairs).

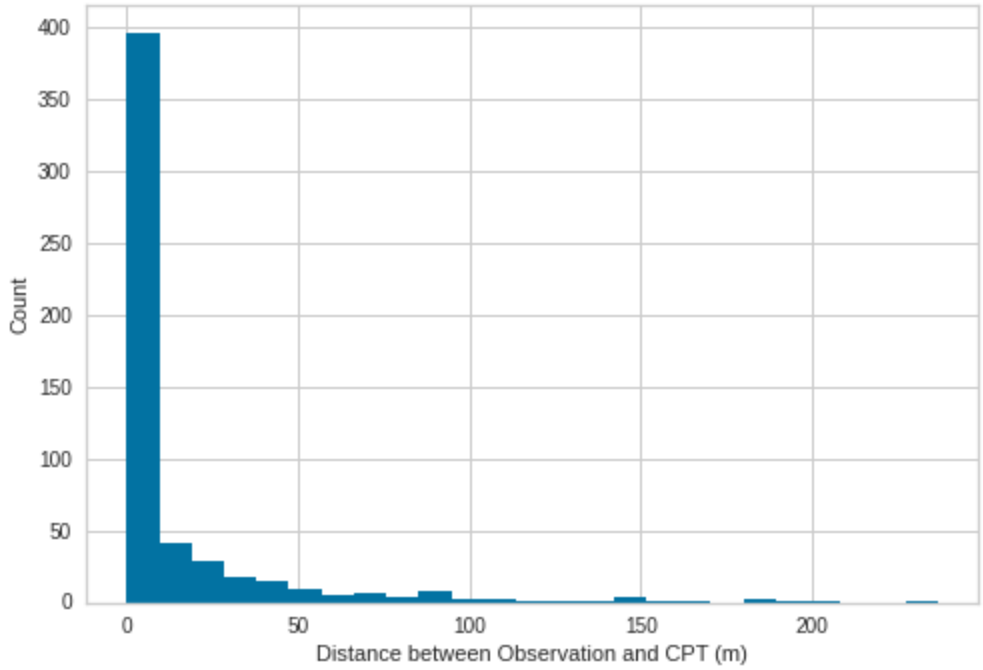

Figure 5-2. Histogram of separation distance between CPT and liquefaction surface manifestation observation for dataset used in model formulation.

5.2 Ground Motion Intensity Measures

Accurate estimates of ground motion intensity measures (IMs) at liquefaction case history sites is crucial as it is the demand side of the equation for regressing liquefaction triggering and consequence models. Therefore, it is desirable to have a more accurate estimate than that provided from ground motion models (GMMs) or direct interpolation of IMs between recording stations. Instead, a spatial interpolation of IM residuals can provide an earthquake-specific modification to GMM predicted IMs. It is ideal to do the Kriging interpolation on the within-event residuals (δW)

rather than directly on IM values because doing so removes systematic path effects and first-order site effects. The following section was also published (Hudson et al. 2023b).

5.2.1 Method

The following subsections describe the mathematical formulation of the proposed procedure for estimating ground motion IMs at liquefaction sites.

5.2.1.1 Recording Station Residuals

An earthquake is identified for which liquefaction case histories have been compiled and IM estimation is needed. Event information is first collected, particularly moment magnitude (**M**), fault rupture mechanism, and fault rupture geometry. Protocols for assembling this information have been developed in Next Generation Attenuation (NGA) projects, and the most recent procedures are given in Contreras et al. (2022). Ground motion stations that recorded the event are next identified and the ground motion IMs are retrieved from a public database (generally either NGA-West2 or NGA-Sub databases; Ancheta et al. 2014; Bozorgnia and Stewart 2020). The NGA-West2 database has been linked to the NGL database for most events to streamline this application. Also recovered from the databases are recording site locations, Joyner-Boore distances (R_{JB}), and site characterization information (mainly the time-averaged shear wave velocity within the upper 30 meters, V_{S30}). The combination of event, path, and station metadata enables IM

estimation from published ground motion models (GMMs), such as Boore et al. (2014). The natural log mean ground motion from the GMM is denoted μln(**M**, R_{JB}, V_{S30}).

The natural log of the recorded IM (denoted ln(Y)) and μ_{ln}(**M**, R_{JB}, V_{S30}) are differenced to compute residuals for all sites that recorded the event:

$$R_{ij} = \eta_{E,i} + \delta W_{ij} = \ln(Y_{ij}) - \mu \ln(\mathbf{M}, R_{JB,ij}, V_{S30,j}) \quad 5.1$$

where *Rij* is the total residual for event *i* and station *j*, $\eta_{E,i}$ is the event term for event *i*, and δW_{ij} is the within-event residual. The event term is estimated from mixed effects analysis, and is available as part of NGA documentation for events used in GMM development. For newer events, it can be estimated roughly as the average of the total residuals for all recordings. Once the event term is known, the δW for all recordings are computed using Equation 5.1. Then the δW is normalized by φ, the within-event residual standard deviation. This can be either computed by taking the standard deviation of all the δW values being computed for an event or estimated using certain GMMs. The normalized δW is written as $\delta \grave{W}$.

5.2.1.2 Semivariogram Model Regression

Using data for a specific event, or more generally using data from multiple events in a particular region, an empirical semivariogram, $\hat{\gamma}(h)$, can be estimated using the $\delta \grave{W}$ computed for every recording in the collection. A semivariogram model can then be fit to the empirical semivariogram using least-squares regression. There are many forms for semivariogram models, but after

comparison between the different model forms, and following Jayaram and Baker (2009), an exponential function was selected. An example of the function is shown in Figure 5-3.

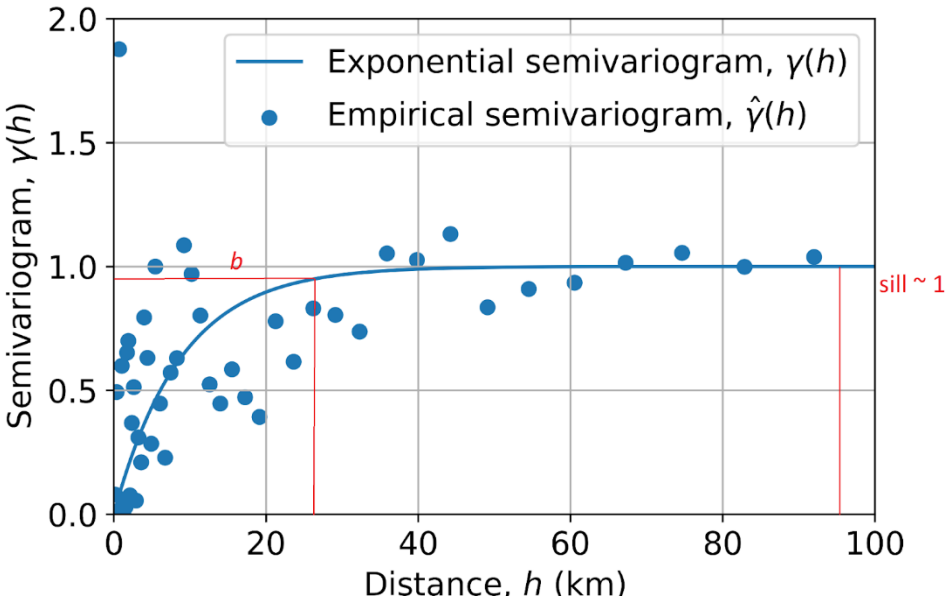

Figure 5-3. Empirical semivariogram and exponential semivariogram model for the 1989 Loma Prieta Earthquake.

where b is the range, φ^2 is the variance, h is the separation distance, and $\gamma(h)$ is the semivariogram. The variance of $\delta\dot{W}$ will always be equal to one if the normalization was done using the standard deviation of δW from the dataset or approximately one if a GMM-estimated φ is used for

normalization. Because it is assumed to be approximately equal to one, the only parameter needing regression in the exponential function is *b*.

Jayaram and Baker (2009) regressed *b* for a number of events and established a global model of *b* for spectral periods (*T*) from PGA to 10 seconds for two cases: (1) where the geologic condition of the soil varies widely over the region where the event occurred (i.e., there is no clustering of V_{S30} values at the recording stations being used) and (2) where there are clusters of recording stations in similar geologic conditions (i.e., clustering of V_{S30} values at recording stations). The analyst must determine whether using the global *b* model or the regressed b is more appropriate for a particular event's dataset; if there is statistical significance of the number of records for the event, then the regressed b should be used instead of the global *b*. If the global *b* is determined to be more appropriate, then a distribution of the V_{S30} values should be checked for clustering and determine whether case 1 or 2 for the global *b* model should be used. With an appropriate *b*, the semivariance at any location can be estimated using the semivariogram model implemented in a Kriging interpolation process. Figure 5-3 shows a semivariogram model regressed using the Loma Prieta PGA data, which resulted in an event-specific *b*=26.4 km. This is reasonable when compared with the spread of b from the global Jayaram and Baker (2009) values at PGA (8.5 to 40.7 km).

5.2.1.3 Kriging Interpolation

A field of interpolated $\delta\grave{W}$ values using ordinary Kriging is obtained in this case using a Python package developed by Müller et al. (2022). Kriging is a minimum-mean-squared-error method of spatial prediction that depends on the second-order properties of the process, in this case $\delta\grave{W}$

(Cressie 2015). To estimate the IM using the interpolated $\delta\dot{W}$ at a liquefaction site of interest, the following is computed,

$$\ln(Y_{ij}) = \delta\dot{W}_{ij} + \eta_{E,i} + \mu \ln(\mathbf{M}, R_{JB,ij}, V_{S30,j}) \quad 5.2$$

Note that this requires rupture distance and V_{S30} to be estimated for the site of interest. The Kriging result is sampled at the site location to estimate $\delta\dot{W}$ and its uncertainty.

Equation 5.2 provides a natural log mean estimate. The uncertainty in the estimate includes contributions from $\eta_{E,i}$ estimation error (i.e., its standard error) and uncertainty in $\delta\dot{W}$, which is a standard output of a Krige analysis. The latter will dominate for well-recorded events.

A few examples illustrate the method application. Site 1 is co-located with a ground motion instrument, Site 2 is located at a large distance (> b) from any ground motion instrument, and Site 3 is at an intermediate distance. For Site 1, $\delta\dot{W}$ is exactly the recording's within-event residual with no uncertainty, so the IM uncertainty is practically nil. For Site 2, $\delta\dot{W}$=0, the prediction reverts to the sum of the GMM natural log mean and the event term, and the uncertainty is φ. Site 3 is an intermediate case in which the ground motion is informed by nearby recordings, which reduces uncertainty relative to φ.

I began this project building the framework for using kriging on residuals (Hudson et al. 2023b) but it was handed to Renmin Pretell as I focused on the modeling aspect of this project, therefore the details of this project are not included in this manuscript and details can be found in (Ulmer et al. 2023c). All of the updated IMs predicted using this new method have been uploaded into the NGL database.

5.3 Layer Detection

Liquefaction triggering analyses are typically performed considering the representative properties of each soil layer rather than a point-by-point basis within a CPT profile. This is because liquefaction occurs as a process of pore pressure generation that typically is only meaningful if it occurs across a large enough depth range to produce manifestations. Furthermore, the CPT measurement represents an average of soil properties within a zone of influence around the cone tip, and measurements at points near layer boundaries may therefore not be representative of the soil properties at that point.

An individual CPT sounding may contain thousands of data points that provide an essentially continuous profile of tip resistance (q_c) and sleeve friction (f_s) with depth over the length of the CPT sounding. An engineer or geologist will generally use judgment to assign layer boundaries based on the CPT sounding, and subsequently select representative properties. Different analysts may make different judgments, and therefore assign layer boundaries differently. The process is therefore non-unique and unlikely to be repeatable. Furthermore, manual layer selection becomes inefficient when sufficiently large numbers of soundings require interpretation. Therefore, it is desirable to establish an algorithm that can efficiently assign layers to CPT data with repeatable, objective results that are compatible with sound human judgment to the greatest extent possible. A repeatable algorithm can also reduce bias that can be introduced by a sole analyst or small group of analysts.

A number of different techniques have been developed to create simplified profiles from CPT data. For example, (Wang et al. 2013) developed a Bayesian approach to assign layer boundaries and assign a probability that soil within a particular layer falls within a soil behavior type category. (Ching et al. 2015) developed a procedure that utilizes the wavelet transform method to distinguish sudden changes in CPT tip resistance from smaller amplitude changes due to within-layer soil variability. Ntritsos & Cubrinovski (2020) developed an algorithm that minimizes the within-layer coefficient of variation of q_{c1Ncs} and I_c for the purpose of developing finite element meshes for one-dimensional ground response analysis. The first two of these three methods are rather complicated and require a significant number of calculations. The third is conceptually and computationally simpler and was shown to produce similar results to analyzing the full profile with respect to liquefaction potential.

An algorithm that utilizes a machine learning technique called agglomerative clustering to identify layer boundaries and representative layer properties is described below. This method shares some conceptual features with Ntritsos and Cubrinovski (2020) (the methods were developed nearly simultaneously but independently); preliminary comparisons indicate that the clustering technique is more efficient. The following subsections describe the agglomerative clustering algorithm and illustrate its use on a CPT sounding from Moss Landing, an important liquefaction site in California. The method described here is also published as a paper (Hudson et al. 2023d). Similarly to how Ntritsos and Cubrinovski (2020) caution that the algorithm may result in fictitious layers at layer boundaries, this algorithm is not intended to replace engineering judgment.

Clustering is an unsupervised machine learning technique that separates data into different groups, often based on distance between data points and the clusters in a desired multi-dimensional

parameter space (Pedregosa et al. 2011). The simplest clustering algorithm is called K-means, which groups data based on the aggregate distance between the data point and the centroid of each cluster. Gaussian mixture models assign probabilities that each data point belongs within each cluster based on the cluster statistics and may be thought of as an extension of K-means clustering that also considers covariance. Prior to clustering, variables are generally standardized, meaning that the mean is subtracted, and the resulting quantity is divided by the standard deviation. This is because the variables often have different units and ranges, and standardization eliminates unintentional weighting of variables that happen to have large numbers.

An example can be used to illustrate various approaches for clustering to identify layers. Figure 5-4 displays profiles of q_c, f_s, I_c, and q_{c1Ncs} for CPT UC-4 that was obtained at Moss Landing near Sandholdt Road, a location that had severe liquefaction manifestation observations due to the 1989 **M**6.9 Loma Prieta earthquake (Boulanger et al. 1995, 1997). The inverse-filtering method by Boulanger and Dejong (2018) was utilized to identify thin layers and sharpen their edges. Visual inspection of the data makes it obvious that there are alternating layers of fine-grained and coarse-grained materials that compose this site's stratigraphy. Standardized versions of the variables are denoted $\hat{I}_c$ and $\hat{q}_{c1Ncs}$ and are plotted in Figure 5-5.

K-means and Gaussian mixture model clustering is applied in $\hat{I}_c$ and $\hat{q}_{c1Ncs}$ using the Scikit-learn Python package (Pedregosa et al., 2011), and plotted in Figure 5-6. The number of clusters is specified to be 14 here. Both algorithms do indeed group data points based on their proximity to each other. However, a problem arises when the clustered data are plotted as profiles with depth. As shown in Figure 5-7, non-contiguous data points may be assigned to the same cluster despite

spatial separation. Figure 5-7 shows the results of K-means clustering, and Gaussian mixture model clustering suffers the same problem.

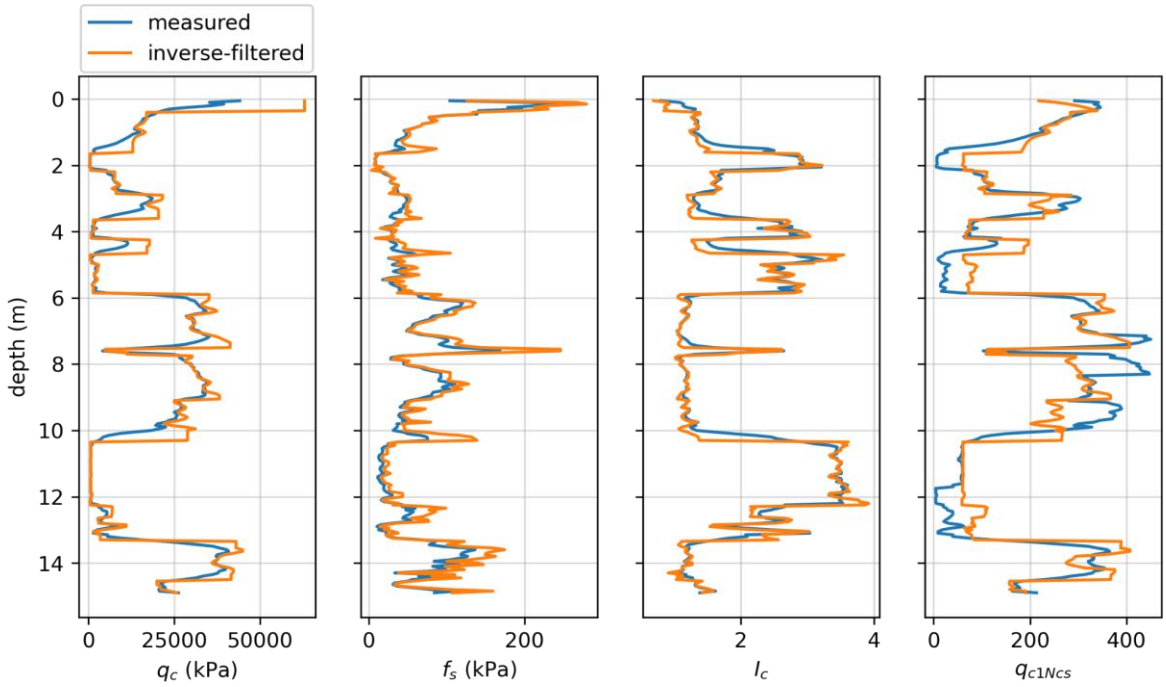

Figure 5-4. CPT data from UC-4 at Moss Landing–Sandholdt Road (original data from Boulanger et al., 1995, 1997).

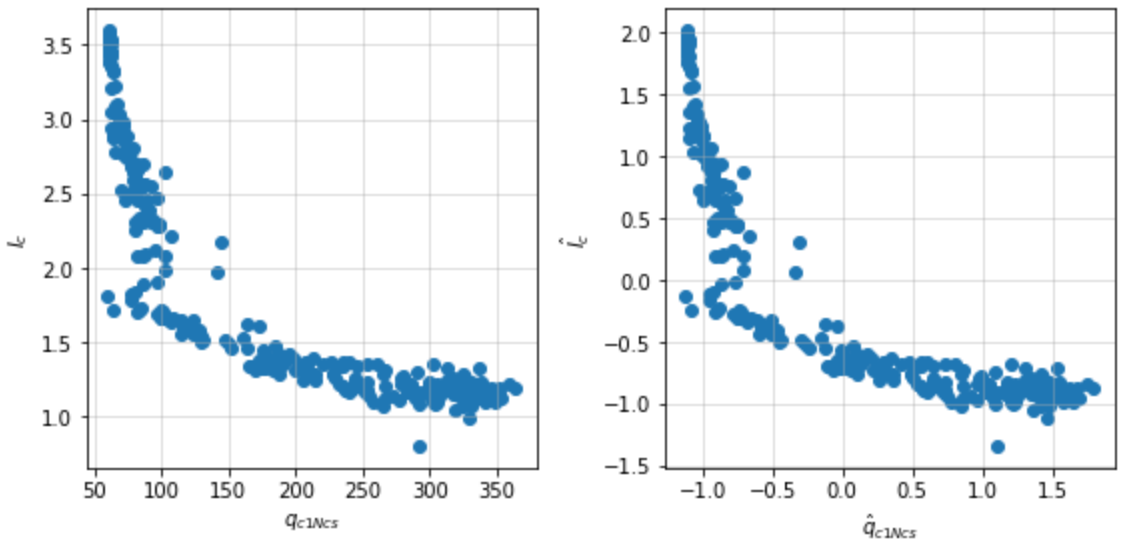

Figure 5-5. Cross plots of I_c vs q_{c1Ncs} and $\hat{I}_c$ vs $\hat{q}_{c1Ncs}$ for UC-4 at Moss Landing–Sandholdt road.

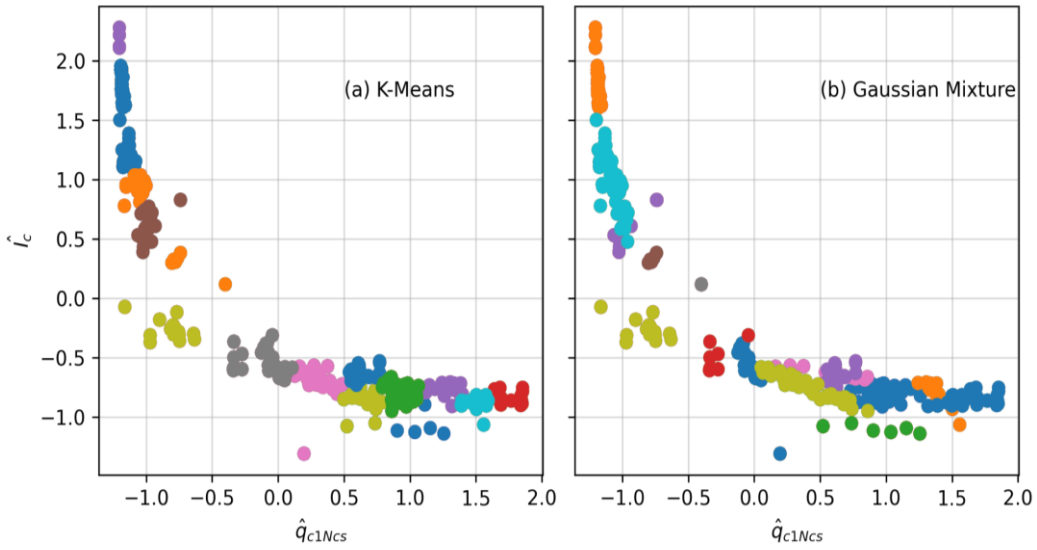

Figure 5-6. (a) K-means and (b) Gaussian mixture clustering algorithm results for UC-4 CPT profile.

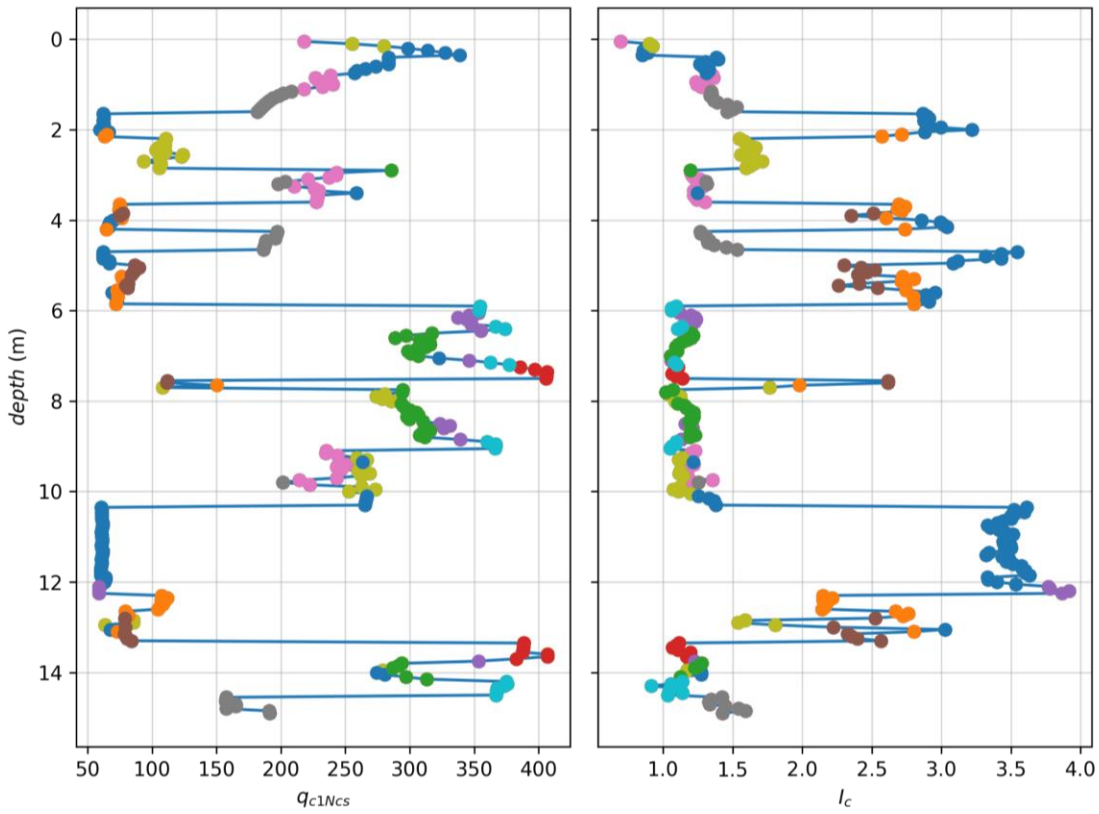

Figure 5-7. Depth profiles for K-means clustering algorithm results for UC-4 CPT profile.

One possible solution would be to include depth as a 3rd variable in the clustering algorithm. While that solution improves continuity with depth, it does not solve the problem. To overcome this problem and obtain vertically contiguous clusters, agglomerative clustering is used, which is a form of hierarchical clustering that groups data based on a cascading "tree" of clusters computed using distances between points (Nielsen 2016). A nearest-neighbor matrix specifies which points are permitted to be considered when assigning clusters. For ordered data, the nearest neighbor matrix is tri-diagonal with ones on the diagonal and the two adjacent diagonals, and zeros elsewhere. This matrix forces the clusters to be contiguous. The algorithm then clusters data by

minimizing the within-cluster variance for the total number of clusters specified. The resulting data is plotted in Figure 5-8, which illustrates that the layers are now vertically contiguous. Some clusters clearly correspond to transition zones (e.g., the cluster beginning at 10m depth) while others clearly belong within a stratum (the cluster immediately below the previously mentioned transition layer).

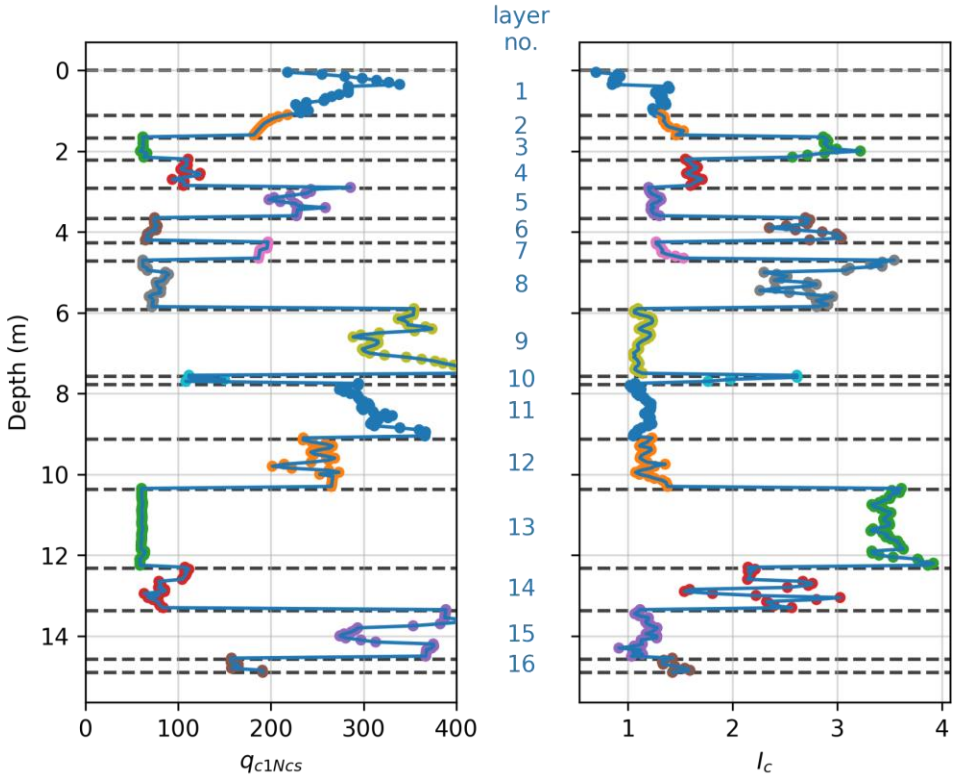

Figure 5-8. Depth profiles for agglomerative clustering algorithm with nearest neighbor Matrix for UC-4 CPT profile.

The success of this method depends on the number of clusters specified, which is not known a priori because different CPT soundings require different numbers of clusters due to differences in

total length and spatial variability of the soil deposit. Selecting the optimal number of clusters must balance two competing factors: (i) increasing the number of clusters reduces within-cluster variance, and (ii) larger numbers of clusters run the risk of over-fitting the data with an excessive number of sparsely populated clusters. The optimal solution will be one that produces a reasonable number of clusters that each have reasonably small variance.

In agglomerative clustering, a distortion score, J_D, is often utilized to identify the optimal number of clusters, and is defined for the two-standardized-variable case considered here in Equation 5.3,

$$J_D = \frac{\sum_{i=1}^{N}\left[\left(\hat{q}_{c1Ncs} - \mu_{\hat{q}_i}\right)^2 + \left(\hat{I}_c - \mu_{\hat{I}_{c_i}}\right)^2\right]}{\sum_{i=1}^{N}\left[\left(\hat{q}_{c1Ncs_i}\right)^2 + \left(\hat{I}_{c_i}\right)^2\right]} \qquad 5.3$$

where $\mu_{\hat{q}_i}$ and $\mu_{\hat{I}_{c_i}}$ are the mean values of $\hat{q}_{c1Ncs}$ and $\hat{I}_c$, respectively, for the i^{th} cluster (i.e., subscript *i* is the index for clusters and identifies values of these parameters for each individual cluster), and *N* is the total number of data points in the profile. Note that J_D decreases as the number of clusters, *K*, increases, and by definition is equal to zero when $K = N$ because every point would constitute its own cluster and the numerator would be zero. The optimal number of clusters therefore cannot be computed by minimizing the distortion score, but rather is a compromise between reducing the distortion score while retaining the smallest possible number of clusters that adequately categorizes the data.

5.3.1 Thickness-Dependent Cost Function and Combined Cost Functions

A cost function, J_T, that penalizes the average layer thickness within a profile was defined using Equation 5.4.

$$J_T = 0.2\left(\frac{\beta_t}{t_{avg}}\right)^3 \tag{5.4}$$

The average thickness is defined as $t_{avg} = z_{max}/K$, where z_{max} is generally the total depth of the CPT profile. Note that predrilling is sometimes necessary for CPT profiles, in which case the first depth at which data is recorded is nonzero. In those cases, z_{max} is the difference between the deepest and shallowest CPT measurement. The purpose of Equation 5.4 is to penalize selection of a high value of K if it results in average layer thicknesses that are too small to be considered geotechnically significant. β_t is a coefficient with units of m that can be adjusted to either produce thinner layers (when β_t is small) or thicker layers (when β_t is large). Based on inspections and analyses of hundreds of CPT profiles in the NGL database, 0.5 m was decided upon as a fairly thin stratum, and $\beta_t = 0.5$ m was set in Equation 5.4 which causes $J_T = 0.2$ for this condition. The cubic form of Equation 5.4 was adjusted until the achieved average layer thickness accorded well with my judgment. The β_t coefficient can be adjusted to favor thicker or thinner layers depending on the user's preference and application. A combined cost function is then defined in Equation 5.5, where w_D and w_T are weights assigned to the components of the cost function. Herein $w_D = w_T = 1.0$ was utilized, but these weights can be adjusted based on user judgment in a site- or region-specific manner.

$$J = w_D J_D + w_T J_T \tag{5.5}$$

5.3.2 Elbow and min(*J*) methods

Two methods were considered for utilizing the distortion score and the combined cost function to select the optimal number of layers. First, the "elbow" method graphically interprets a plot of J_D vs. K, which has a negative curvature over the full range of K but flattens as K increases (Figure 5-9). The optimum value of K (9 in the case of Figure 5-8) is identified on the basis of curvature having decreased to a sufficiently low level, which is subjective. As such, the elbow method is based only on J_D and not on J_T. The Yellowbrick (Bengfort et al. 2022) Python package was utilized to implement the elbow method which identifies the point of maximum curvature of the J_D vs. K curve and assigns that as the optimum number of layers. The silhouette method (Bengfort et al. 2022) is also often utilized to identify the optimal number of clusters. This method is based on a so-called "silhouette" value that measures the similarity of data points within a cluster compared to other clusters. It produced similar results to the elbow method. Thus, results from this method are not reported in Figure 5-9. Molina-Gómez et al. (2022) utilize the silhouette method to define the number of clusters in their algorithm. An alternative method was also applied in which K is selected as the point where J [from Equation 5.5] is minimized. For this reason, this is denoted the min(J) method. The combined cost function is minimized for K = 16 clusters for the example of CPT UC-4 in Figure 5-9.

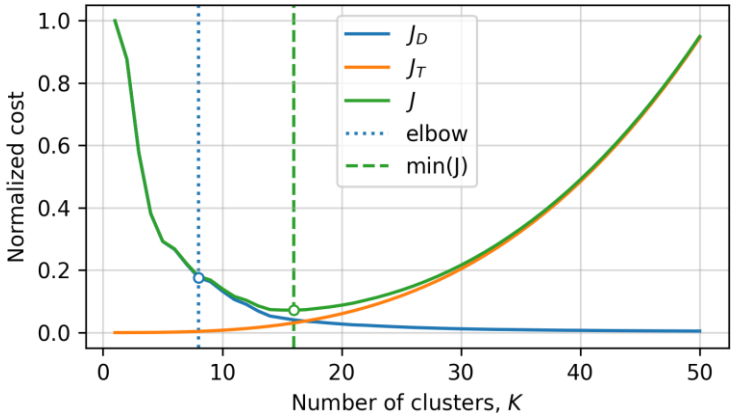

Figure 5-9. Cost functions and layer selection for CPT profile UC-4.

Profiles of 16 and 9 layers are shown in Figure 5-10, where (a) and (b) have 16 layers by using the min(J) method, whereas (c) and (d) have 9 layers by using the elbow method. The primary differences between these two profiles are in layers number 3, 4, and 6 for the 9-layer profile. These layers clearly contain within-layer regions that are vertically contiguous with different q_{c1Ncs} and I_c values (e.g., the layer for the 2.2-3.8 m depth range), yet they are clustered together in the 9-layer profile. By contrast, they are separated into different layers in the 16-layer profile. The 16-layer profile accords better with my judgment, and similar observations observed across diverse profiles with a wide range of depths (as described in the next section) caused the preference for use of the min(J) approach over the elbow method when selecting the number of layers. A different curvature threshold in the application of the elbow method would have produced a different number of layers and, possibly, a solution that accords better with one's judgment. However, the superiority of the min(J) method is related to the fact that it is based on layer thickness, which is a

physically meaningful quantity, whereas the gradient of J_T vs. K used in the elbow and silhouette methods does not have a clear physical meaning.

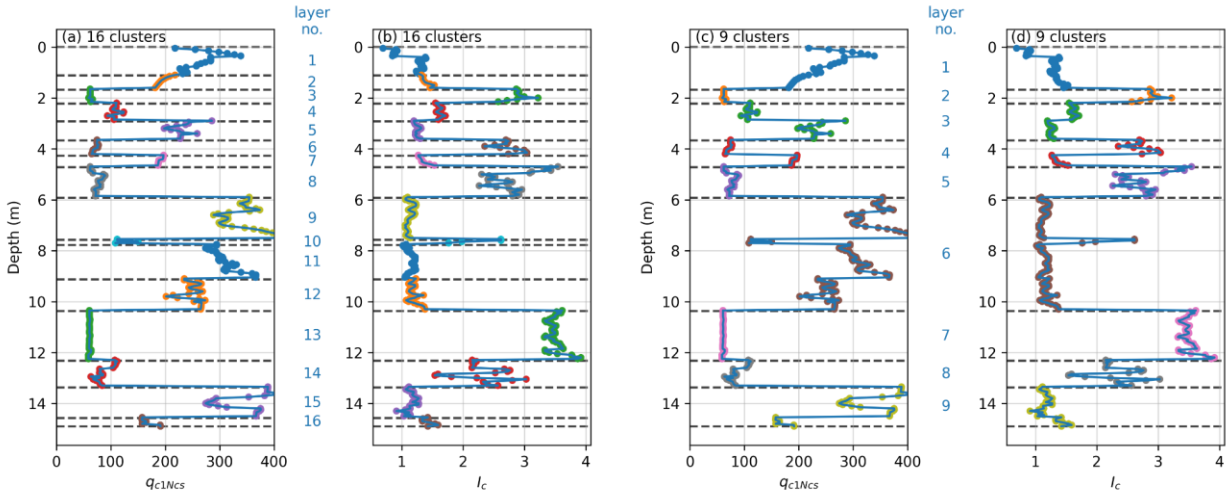

Figure 5-10. Profiles of q_{c1Ncs} and I_c with 16 layers by using the min(J) method (a and b) and 9 layers by using the elbow method (c and d).

5.3.3 Calculations for Many CPT Profiles

Calculations of the optimal numbers of layers were performed for a total of 272 CPT profiles contained in the NGL database. Additional CPT profiles were added to the NGL database after developing this algorithm, and they are not presented in this section, but were ultimately interpreted using the algorithm for the purpose of defining the manifestation model. Both the elbow method and the min(J) method were utilized to identify the optimal number of layers. t_{avg} should be independent of z_{max} because t_{avg} depends upon vertical heterogeneity of the soil profile, which is controlled by the geological processes that formed the soil deposit, whereas z_{max} arises from a

decision controlled by the objectives of the site investigation. For example, z_{max} may be higher for a site investigation for a pile-supported tall building with a corresponding deep zone of influence than for a single-story building supported by spread footings with a corresponding shallow zone of influence.

Values of t_{avg} vs. z_{max} are plotted in Figure 5-11. The elbow method exhibits a strong positive correlation in which t_{avg} increases essentially linearly with z_{max}. This is an undesirable outcome since t_{avg} is anticipated to be independent of z_{max}. By contrast, values of t_{avg} are essentially independent of z_{max} using the min(J) method, particularly for values of z_{max} > 12m. For liquefaction triggering evaluation, profiles shorter than about 15m may miss layers that could potentially liquefy and produce surface manifestation. In this regard, the slight bias in the min(J) method for shallow profiles has little practical impact.

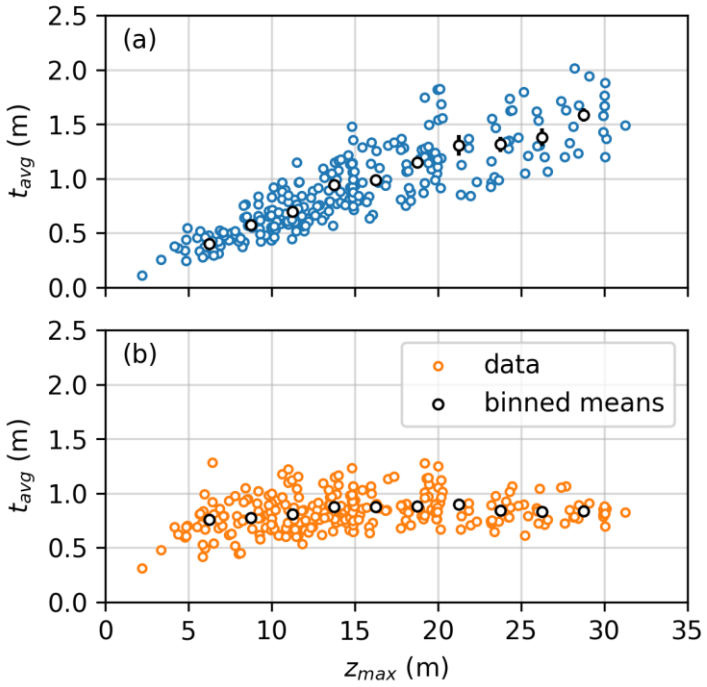

Figure 5-11. Average layer thickness, t_{avg}, versus total CPT profile length, z_{max} for (a) elbow method and (b) min(J) method.

The influence of maximum depth on average layer thickness is further explored in Figure 5-12, which illustrates normalized cost versus number of clusters for (a) a shallow profile with z_{max} = 5.1m from CPT_8933 at Site 76 in Edgecumbe, New Zealand, and (b) a deep profile with z_{max} = 31.3m from CPT001 at the Inage site in Urayasu City, Japan (CPT names are those reported in the NGL database). Note that the J_T functions are significantly different for these two profiles because the same average thickness in Equation 5.4 produces fewer layers for the shallow profile than for the deep profile. For the shallow profile, the elbow method indicates that 8 layers is ideal (t_{avg} = 0.64m), while the min(J) approach provides 7 layers (t_{avg} = 0.73m). These results are very similar. By contrast, for the deep profile, the elbow method indicates that 8 layers is ideal (t_{avg} = 3.9m),

while min(J) provides 36 sublayers (t_{avg} = 0.87m). These results are significantly different, and the average layer thickness using the elbow method is too large to capture potential critical layers of sand-like soil with low q_{c1Ncs}.

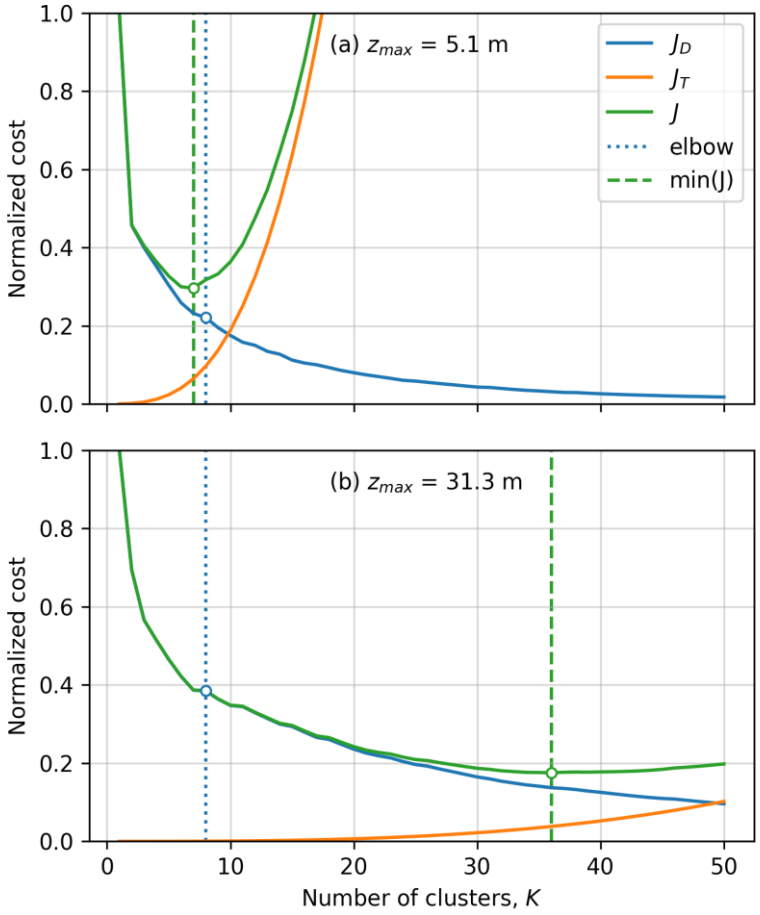

Figure 5-12. Normalized cost versus number of clusters for (a) a shallow profile with z_{max}=5.1m corresponding to CPT_8933 at Site 76 in Edgecumbe, New Zealand and (b) a deep profile with z_{max}=31.3m corresponding to CPT001 at the Inage site in Urayasu City, Japan.

Note that when K=8, J_D is near 0.2 for the shallow profile and near 0.4 for the deep profile. A fundamental limitation of the elbow method is that it considers only the curvature of the cost function, and not the value of the cost function itself.

The two profiles are illustrated in Figure 5-13 with a common depth axis to illustrate the clear differences in the maximum penetration depth. The average layer thicknesses determined using the min(J) method are similar for these two profiles despite the different total depths. Furthermore, it is clear that reducing the number of layers for the deeper site from 36 [using the min(J) method] to only 8 (using the elbow method) would result in significantly higher average layer thickness and would miss much of the stratigraphic detail within that profile.

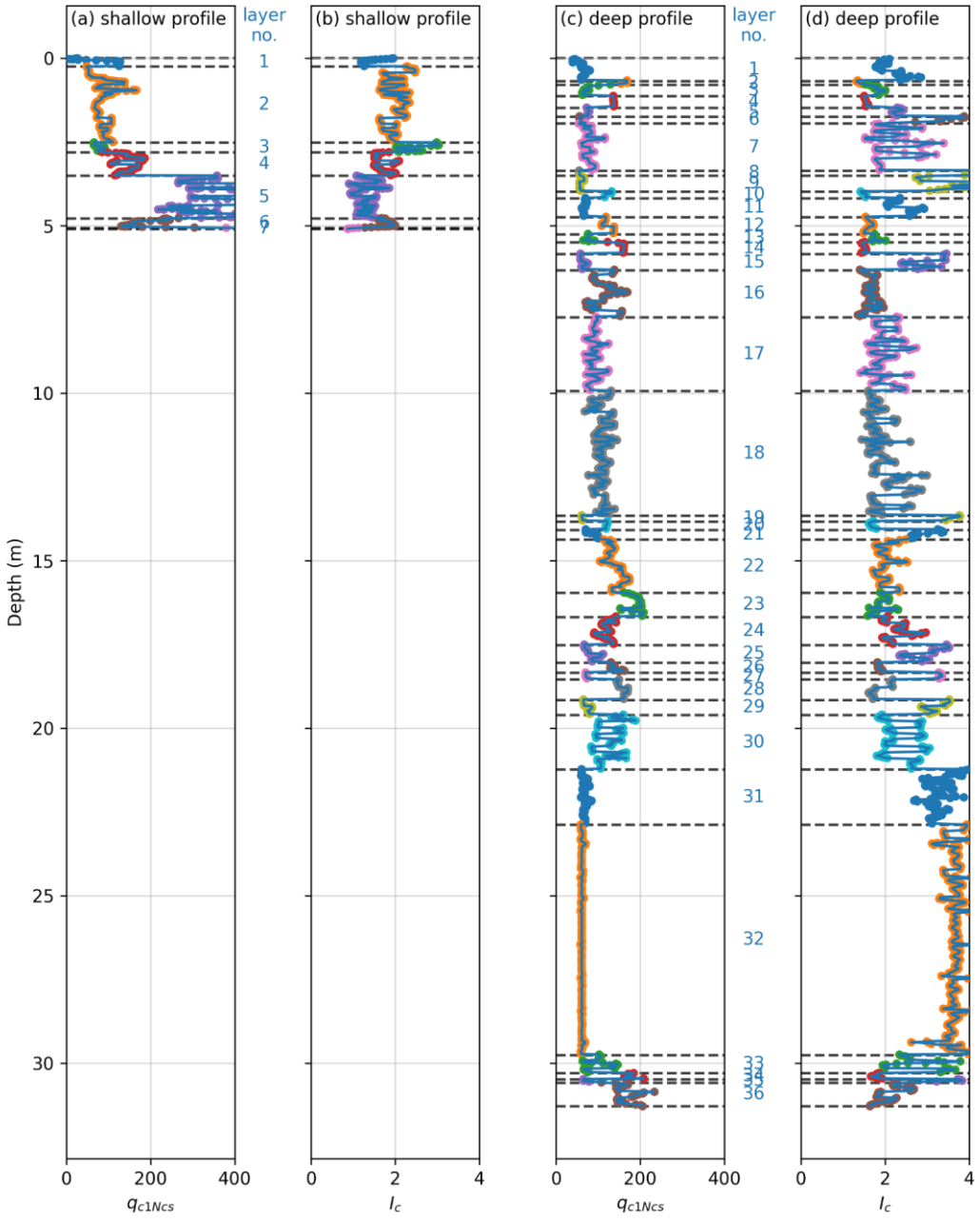

Figure 5-13. Profiles of q_{c1Ncs} and I_c for (a) and (b) a shallow profile corresponding to CPT_8933 at Site 76 in Edgecumbe, New Zealand, and (c) and (d) a deep profile corresponding to CPT001 at the Inage site in Urayasu City, Japan.

5.4 Assigning Layer Properties

After identifying layers using the agglomerative clustering algorithm, a number of different attributes are computed for each layer in the profiles. Some attributes are computed directly from the CPT data, while others are computed using a combination of CPT data and demand for the purpose of identifying the critical layer within the profile. Section 5.4.1 describes attributes obtained directly from CPT data and stress normalization. Section 5.4.2 describes a new relationship for estimating *FC* which is also described in a technical note submitted for publication. Section 5.4.3 describes the calculation of *CSR*.

5.4.1 Basic Layer Properties and Stress Normalization

Attributes computed directly from the CPT data are listed in Appendix A. A total of 16 different layer parameters for the case history dataset were considered in model development, including layer depth, layer thickness, cone tip resistance, overburden- and fines-corrected cone tip resistance, sleeve friction, soil behavior type index, modified soil behavior type index, vertical total stress, vertical effective stress, groundwater table depth, cyclic stress ratio, magnitude scaling factor, K_σ, strength of nonliquefied layers above the layer, and ejecta severity index within the layer. These attributes are computed in Python and stored in a pickle file format (with a .pkl file extension) that is well suited to being read into a Pandas dataframe. These data will be published as part of this project to facilitate use by other model development teams. One pickle file has been created for the measured CPT data, and another has been created for CPT data that has been inverse-filtered using the algorithm by Boulanger & Dejong (2018).

To calculate q_{c1Ncs} for a profile, the total and effective stress profiles are needed. An estimate of the unit weight profile is created using the specific gravity (G_s) and water content (w_c) measurements from the nearest boring to the CPT. If one or neither of these values are present at a particular depth range or in the closest boring, then the unit weight (γ) is assumed to be 18.4 kN/m^3. Assuming the soil is fully saturated, the unit weight is computed as 9.81kN/m^3*(e+G_s)/(1+e) where e is the void ratio equal to G_s*(w_c/100%). If there is an associated groundwater table depth in the WATR table assigned to the CPT, that value is selected for case history processing. If there is no associated entry in the WATR table assigned to the CPT, the closest groundwater table depth at any in situ test at the site is assigned (e.g., a borehole). These quantities are all used to compute the total and effective stress profile for the CPT.

The equations to compute q_{c1N} as recommended by Boulanger & Idriss (2014) are:

$$q_{c1N} = C_N \frac{q_c}{p_a} \tag{5.6}$$

$$C_N = \left(\frac{P_a}{\sigma'_v}\right)^m \leq 1.7 \tag{5.7}$$

$$m = 1.338 - 0.249(q_{c1Ncs})^{0.246} \tag{5.8}$$

where q_c is the cone tip resistance and p_a is atmospheric pressure (i.e., 1 atm = 101.325 kPa). Equations used to compute q_{c1Ncs} as recommended by Boulanger & Idriss (2014) are

$$q_{c1Ncs} = q_{c1N} + \Delta q_{c1N} \tag{5.9}$$

$$\Delta q_{c1N} = \left(11.9 + \frac{q_{c1N}}{14.6}\right) exp\left(1.63 - \frac{9.7}{FC + 2} - \left(\frac{15.7}{FC + 2}\right)^2\right) \quad 5.10$$

where FC is fines content. The crust thickness (H_1) is taken as the sum of the thickness of layers above the water table and layers directly beneath the water table with continuous I_c greater than or equal to 2.6.

5.4.2 Estimation of Fines Content from CPT Data

The liquefaction potential of an element of soil is related to its degree of contractiveness, which is a function of its state. At a given effective stress level, the state of a particular soil is a function of its relative density, which can be measured in the laboratory. The in-situ relative density, however, is difficult to measure directly and typically inferred from penetration resistance. The cone penetration test (CPT) provides an effectively continuous profile of tip resistance (q_t), sleeve friction (f_s), and sometimes pore pressure (u_2), and is commonly utilized to assess soil liquefaction (e.g., Boulanger and Idriss, 2016; Moss et al., 2006; Robertson and Wride, 1998) because q_t correlates well with relative density of clean sands. However, q_t alone is inadequate to assess relative density of sandy soils with appreciable fines because the amount and plasticity characteristics of fines present in the sand influence its compressibility and drainage characteristics, and therefore influences the q_t for a given relative density. For these reasons, CPT soundings should be accompanied by sampling and laboratory testing when feasible to measure fines content and plasticity characteristics, either using a collocated borehole or by using sampling equipment that can be affixed to the CPT rods. However, many projects proceed without soil sampling, in

which case susceptibility and fines content are inferred from CPT measurements. The presence and plasticity characteristics of fines also influence liquefaction susceptibility and cyclic resistance ratio (e.g., Park and Kim, 2013), albeit in a different manner from their effect on CPT measurements (investigated by Carraro et al., 2003; Ecemis and Karaman, 2014). The fines correction applied in liquefaction evaluation does not distinguish these two effects, but rather jointly captures both effects in a combined manner. This section focuses on the influence of fines on CPT measurements, and not on the influence of fines on liquefaction susceptibility or resistance. The method described here has been submitted as a technical note (Hudson et al. 2023a), and the dataset is available on DesignSafe (Hudson et al. 2023c).

Soil behavior type index, I_c, is an indicator of the manner in which a particular soil behaves and is defined by Equation 5.11. Robertson (1990) developed relationships between I_c and soil behavior type in which fine-grained soils tend to have I_c>2.6, sand-like soils with appreciable fines (i.e., silty sand to sandy silt) tend to have I_c = 2.05 to 2.6, and clean sand to silty sand tends to have I_c = 1.31 to 2.05. Soil behavior type is different from soil classification because the Unified Soil Classification System uses fines content (*FC*) of 50% to distinguish fine-grained soils from coarse-grained soils, whereas the mechanical behavior of soils with *FC* as low as 35% is generally considered to be dominated by the fines (Thevanayagam 1998).

$$I_c = \sqrt{(3.47 - logQ_{tn})^2 + (logF_r + 1.22)^2} \tag{5.11}$$

Robertson & Wride (1998) developed a relationship between "apparent fines content" and I_c as specified by Equation 5.12. Furthermore, they indicated that plasticity index (*PI*) influenced the relationship between I_c and *FC* and specified separate relationships for high plasticity fines

(*PI* > 20%) and non-plastic fines (*PI* < 5%). For a given I_c, *FC* tended to be lower for high plasticity fines. They utilized the phrase "apparent fines content" rather than "fines content" as an acknowledgment that the relationship between I_c and *FC* was approximate, and influenced by plasticity, mineralogy, sensitivity, and stress-history. They indicated that the approximate relationship provided by Equation 5.12 may nevertheless be useful for small projects.

$$FC(\%) = \begin{cases} 0 & for\ I_c < 1.26 \\ 1.75I_c^{3.25} - 3.7 & for\ 1.26 \le I_c \le 3.5 \\ 100 & for\ I_c > 3.5 \end{cases} \qquad 5.12$$

Robinson et al. (2013) developed a relationship between I_c and *FC* for soils in Christchurch and found that the apparent fines content was 10% for soils with I_c<1.7, and reasonably followed the Robertson & Wride (1998) relationship for non-plastic fines for soils with I_c>1.7.

Boulanger & Idriss (2016) developed a relationship between I_c and *FC* based on approximately 200 I_c-*FC* pairs from Suzuki et al. (1998) supplemented with approximately 120 I_c-*FC* pairs from liquefaction case histories. They regressed their relationship using *FC* as the independent variable, and I_c as the dependent variable, and subsequently inverted the equation to obtain the relationship given by Equation 5.13, where C_{FC} is a parameter that may be calibrated on a site-specific basis. The mean value of C_{FC} from their dataset is 0.0, and the standard deviation is 0.29. Note that the standard deviation reflects uncertainty in I_c for a given *FC* because they regressed the model with *FC* as the independent variable.

$$FC = 80(I_c + C_{FC}) - 137\,, \qquad 0\% \le FC \le 100\% \qquad 5.13$$

Cetin & Ozan (2009) compiled a dataset containing 484 measurements of *FC*, CPT measurements, and plasticity indices. A total of 474 pairs have *FC* and CPT measurements, while 388 have Atterberg limits. They do not report I_c, but rather utilized Bayesian methods to estimate *FC* directly from measured cone tip resistance and sleeve friction. This research sought to develop a new probabilistic relationship for *FC* conditioned on I_c using CPT and *FC* data from the NGL dataset.

5.4.2.1 Dataset

At the time the NGL database was queried to develop this relationship, a total of 2,714 layers with I_c computed using CPT soundings were associated with a measured *FC* from a sample at the same depth in a nearby boring. These data come from 111 different sites and 227 different collocated CPT/boring log pairs. All data used herein were reviewed by two independent reviewers to check for accuracy of information in the database relative to source documents. This association of a CPT sounding with a boring was applied to pairings separated by 10m or less, with most separated by less than 3m (206 of the 227 CPT-boring pairs). Each CPT sounding was inverse-filtered to account for layer effects using the procedure by Boulanger & Dejong (2018), and strata from the inverse-filtered profiles were identified using an agglomerative clustering method (Hudson et al. 2023d). The representative value of I_c for each stratum was then computed as its median value over the length of the specimen used to measure *FC* computed as the percent passing the No. 200 sieve (75 μm). Where the specimen length is unknown, the sample length is used instead. In cases where the length of the specimen or sample is less than 15cm, the bottom depth was extended so that it was 15cm long to increase the number of CPT data points for the median I_c computation.

An example boring log and I_c profile is shown in Fig. 1 for Adapazari Site B (PEER 2000a; Bray et al. 2004a), which has 13 measured *FC* values. For example, *FC* in the upper 4 m of Adapazari Site B (Figure 5-14) is generally higher than 50% with a median I_c of 2.7, whereas in the sand layer from about 6 to 9 m depth I_c = 1.3 with *FC* = 5%. In some cases, *FC* was measured for multiple specimens within a sample, and the *FC* values varied significantly. This is consistent with interbedding in the upper 4m of this profile. Computing I_c as the average value over the layer thickness instead of specimen/sample length was considered. It was opted to take the median over the specimen length because the layer thickness is often quite large and might miss important stratigraphic details, and because multiple specimens are often tested from a single sample, often with significantly different *FC* and I_c within the specimen depth range.

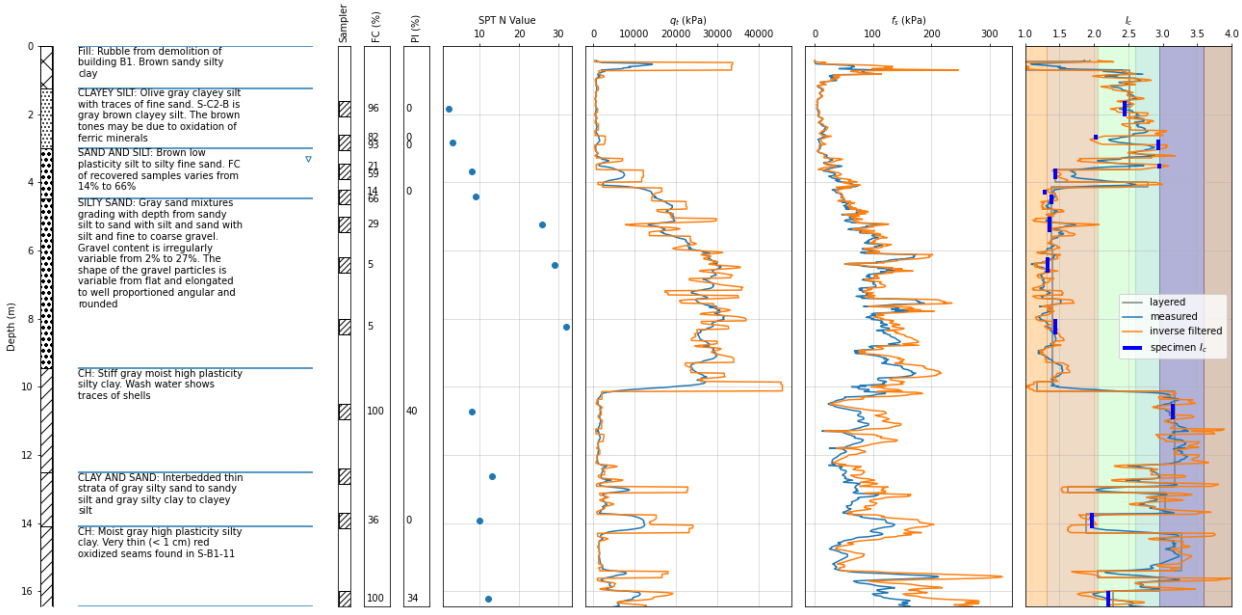

Figure 5-14. Boring log and CPT data from Adapazari Site B illustrating how *FC* values are related to I_c.

The processing illustrated in Figure 5-14 was repeated for all collocated CPT soundings and boring logs, resulting in the values plotted in Figure 5-15, along with binned means that illustrate trends in the data. I_c-*FC* pairs were obtained from sites in California (1928), Turkey (319), Taiwan (191), New Zealand (94), Japan (88), China (60), and Mexico (34), and reflect geological conditions including Holocene and Pleistocene aged alluvial, beach, eolian, estuarine, floodplain, fluvial, lacustrine, and marine deposits as well as artificial fill. A general trend of increasing *FC* with increasing I_c is evident from the binned means. Standard errors of the binned means are smaller than the icons used to plot them. When I_c = 2.6, the mean value of *FC* is about 60%, which is consistent with Robertson's (1990) soil behavior type concept because soil with *FC* this high is dominated by the fine fraction. When I_c=2.0, the mean value of *FC* is about 35%, often considered the transition where the soil becomes fines-dominated. Furthermore, the mean *FC* drops to about 10% for I_c near 1.5, which is also consistent with Robertson (1990). Significant scatter exists in the data, which indicates that I_c is not a unique indicator of *FC*. The model shown in Figure 5-15 is described subsequently. The data from Figure 5-15 is repeated in Figure 5-19 instead colored by region to show trends by region.

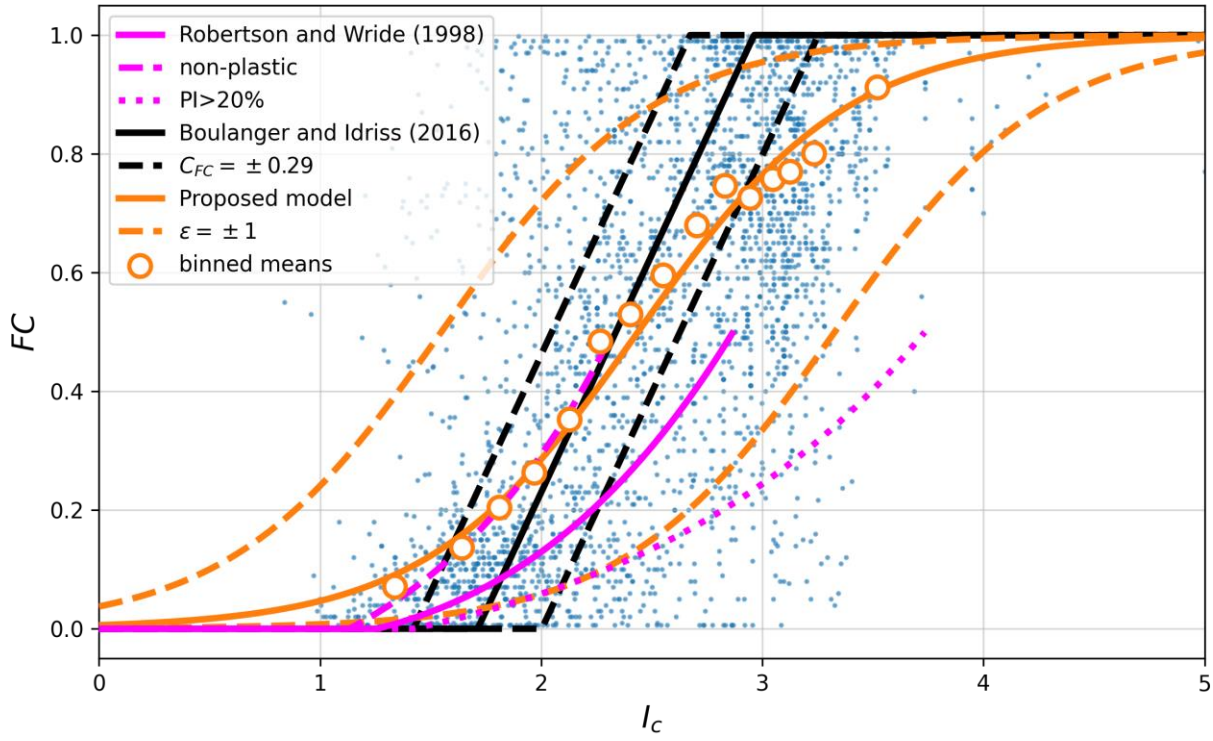

Figure 5-15. Fines content (*FC*) vs. soil behavior type index (I_c) for collocated CPT soundings and boring logs in Next Generation Liquefaction (NGL) database compared with proposed model, Robertson & Wride (1998), and Boulanger & Idriss (2016). Each bin contains an equal number of data points.

5.4.2.2 Proposed FC-I_c Model

FC is bounded between 0 and 1, which poses a complication for least-squares regression because the functional form must enforce these boundary conditions, which precludes linear regression. Rather than formulate a complicated functional form, instead the data had a logistic transform imposed on it (Johnson 1949) as indicated by Equation 5.14. Note that $\widehat{FC}$ is unbounded, and becomes infinity when *FC* = 1.0, and negative infinity when *FC* = 0.0. To avoid infinite values,

the data was set to the nearest measured value that is not 0 or 1 (i.e., 0's are set to 0.6% and 1's are set to 99.8%).

$$\widehat{FC} = ln\left[\frac{FC}{1 - FC}\right] \tag{5.14}$$

Subsequently, linear least squares regression was used to identify the slope and intercept of the $\widehat{FC}$ vs Ic relationship as 2.096 and -5.108, respectively shown in Figure 5-16. The standard deviation of the residuals is σ_ε = 1.864, where residuals are defined by Equation 5.15. Residuals of the fit in transformed variable space approximately follow a normal distribution as shown in Figure 5-17.

$$R_{FC} = \widehat{\mathrm{FC}} - (2.096 I_c - 5.108) \tag{5.15}$$

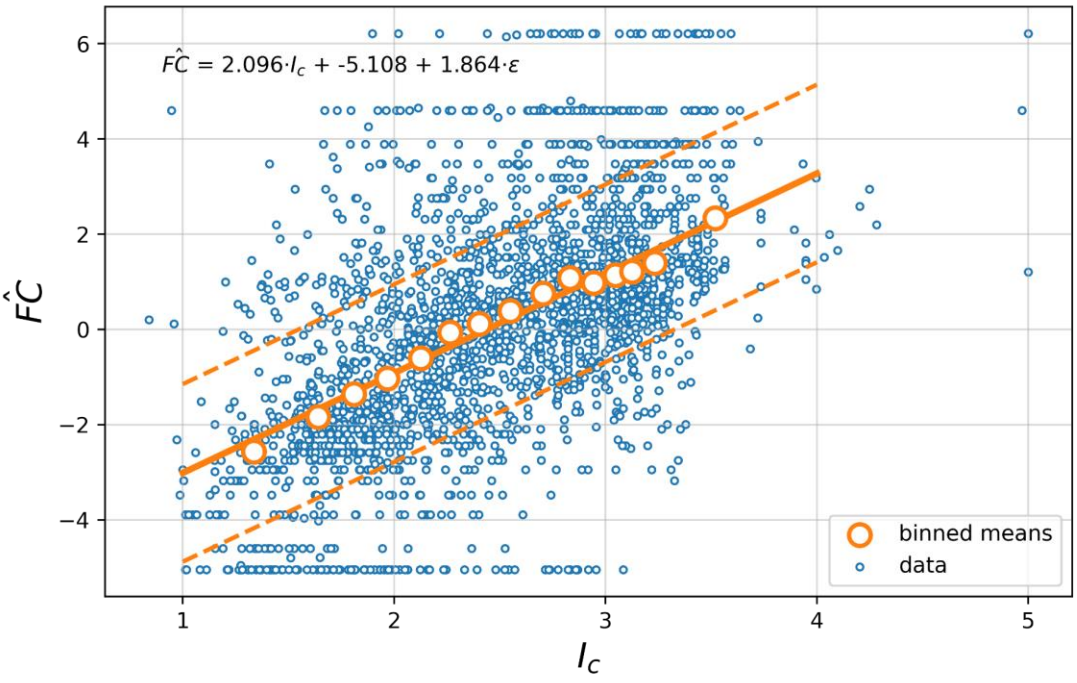

Figure 5-16. Linear least squares regression of standardized quantities.

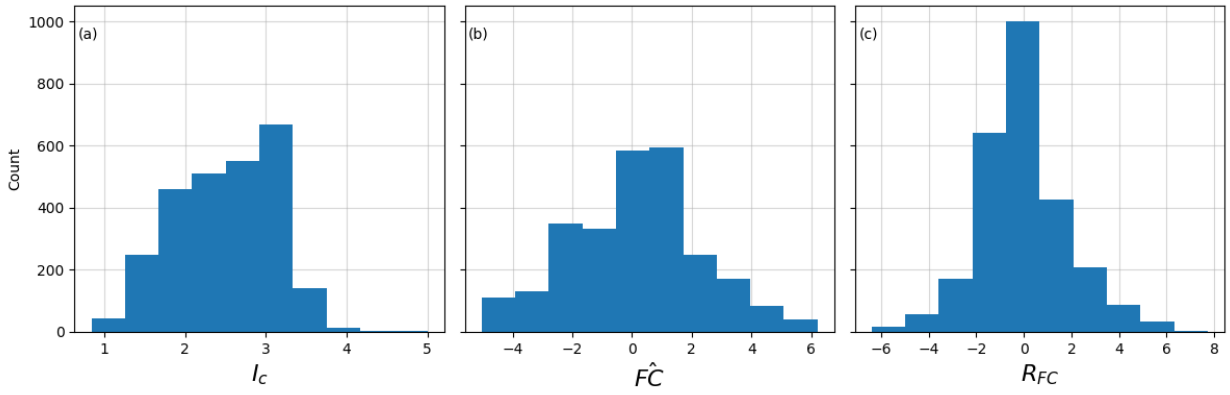

Figure 5-17. Distributions from dataset used in regression of (a) I_c, (b) $\widehat{FC}$, and (c) residuals (R_{FC}) as computed in Equation 5.15.

Values of $\widehat{FC}$ must be de-transformed to obtain a form of the equation in I_c – FC space. The result is provided by Equation 5.16.

$$\mathrm{FC} = \frac{\exp(2.096 \cdot \mathrm{I_c} - 5.108 + 1.864 \cdot \varepsilon)}{1 + \exp(2.096 \cdot \mathrm{I_c} - 5.108 + 1.864 \cdot \varepsilon)} \qquad 5.16$$

where ε is a unit normal random variable. The proposed relationship is plotted in Figure 5-15 in I_c – FC space for the mean relationship and ε = ±1 values. The mean curve agrees well with the binned means of the data, indicating that the fit is reasonable. The ε = ±1 relationships reflect the significant scatter in the data.

The relationships of Robertson & Wride (1998) and Boulanger & Idriss (2016) are also plotted in Figure 5-15. The recommended Robertson & Wride (1998) model is lower than the binned means, indicating under-prediction of FC for this dataset. The Robertson & Wride (1998) model for non-plastic fines, however, is very close to the binned means of this dataset, which is consistent with the findings of Robinson et al. (2013) for the soils in Christchurch. The model of Boulanger & Idriss (2016) tends to under-predict FC for values of I_c < 2.0 and over-predict FC for values of I_c > 2.0 and does not represent the smooth variation of FC with I_c indicated by the binned means for the NGL dataset. Furthermore, the range corresponding to C_{FC} ± 0.29 is rather small, and significantly smaller than the range for the proposed model corresponding to ± 1σ.

5.4.2.3 Influence of Plasticity

Robertson & Wride (1998) found that plasticity index (PI) influenced the relationship between I_c and FC. Specifically, FC was noted to decrease as PI increased for a given I_c. This trend is intuitive

because a small amount of plastic fines would be expected to exert more influence on soil behavior than the same amount of non-plastic fines. Of the 2,714 I_c-FC pairs in the NGL dataset, 1,063 have measured Atterberg limits. An additional 299 samples were inferred as non-plastic based on stratigraphic layer descriptions containing the words “non-plastic”, “sand”, and/or “gravel” and not containing any of the following words: “plastic”, “clay”, “silt”, “fat”. The model was re-regressed for the subset with known or inferred *PI*, and a new set of residuals were computed and are plotted in Figure 5-18.

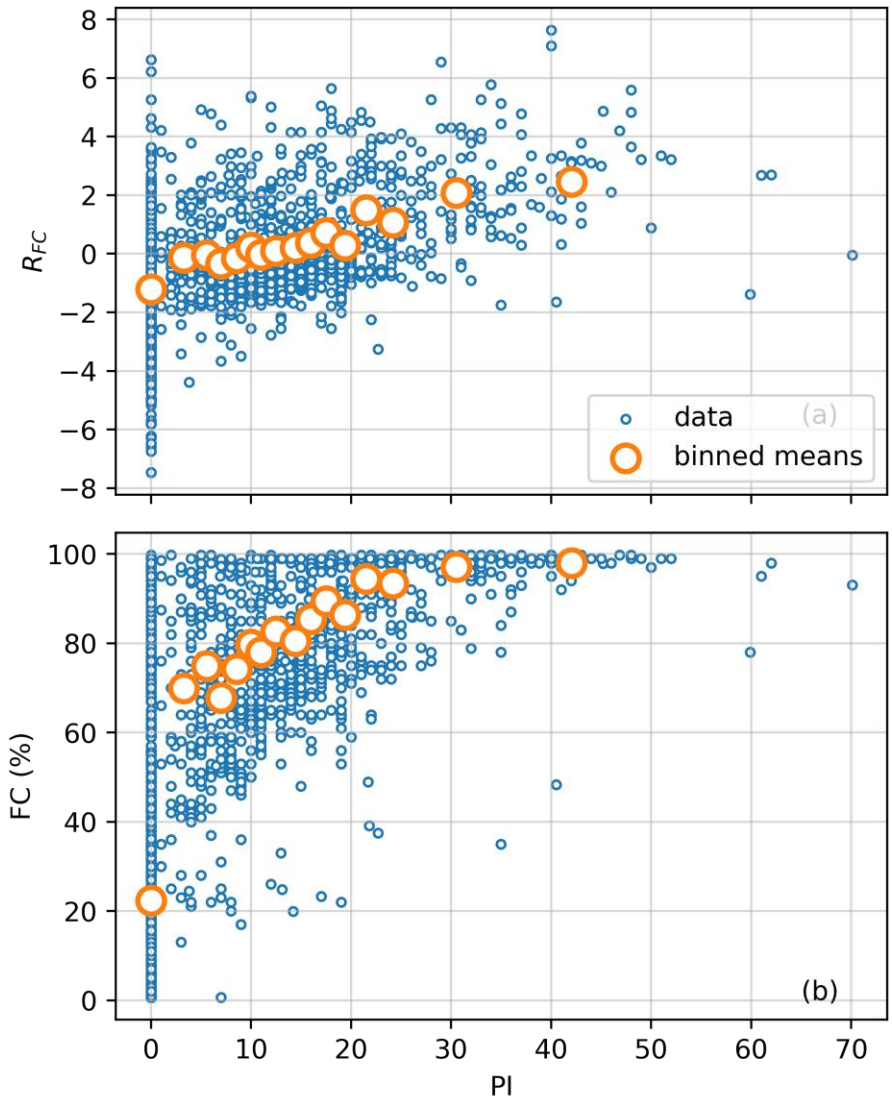

Figure 5-18. (a) Residuals of proposed model (Eq. 6) versus *PI*, (b) positive correlation of *FC* with PI in database.

The binned means of the residuals are negative (model overpredicts) for *PI* < 20%, and positive (model underpredicts) for *PI* > 20%. This implies that, for a given I_c, the fines content is higher for high *PI* soils, which is the opposite of the trend presented by Robertson and Wride (1998). To

investigate the cause of this finding, Fig. 4b shows a positive correlation between *FC* and *PI*; i.e., higher *FC* soils are more likely to have high *PI*. As a result, an I_c-*FC* pair with an unusually high *FC* (thus producing a positive residual) is likely to also have a high *PI*, whereas a pair with an unusually low *FC* (producing a negative residual) is likely to have a non-zero but low *PI*. This parameter correlation is not surprising because Atterberg limits are tested on specimens passing the #40 sieve, which therefore include sand-size particles and fines. Accordingly, low *FC* materials likely have large granular fractions in plasticity test specimens, reducing *PI*, whereas high *FC* materials will have limited granular fractions, increasing *PI*. Incomplete sampling could also affect the results in unknown ways – perhaps Atterberg limits tests on low-*FC* soils are more likely to be performed if the plasticity is low (because such samples are more likely susceptible to liquefaction). If so, this would represent a type of sampling bias. Another potential sampling bias would occur if Atterberg limits on high *PI* soils with low *FC* are under-represented relative to the frequency of their occurrence in nature, which is a possibility that cannot be excluded. Given these uncertainties, it was not attempted to adjust the relationship to recover the trend that would exist in the absence of correlation between *FC* and *PI*. Furthermore, the influence of *PI* on the I_c-*FC* relationship has little practical impact because in cases where *PI* is measured, *FC* should also be measured and therefore should not be inferred from I_c.

5.4.2.4 Regional Variations

The data used to develop the model in Equation 5.16 originate from various regions including California, China, Japan, Mexico, New Zealand, Taiwan, and Turkey. Variations in soil

composition and geologic conditions might be anticipated across, as well as within, these regions. To investigate these potential effects, residuals between each data point and the model prediction given the I_c for the data point were computed using Equation 5.15. After grouping the data by region, the residuals and the regional means are as shown in Figure 5-20. California and Taiwan are similar to the global trend. Japan and China have negative mean residuals, indicating over-prediction of *FC*, whereas Mexico, Turkey, and New Zealand have positive residuals. The mean residuals (μ_{RFC}) shown in Figure 5-20 could be used to adjust the model predictions by subtracting μ_{RFC} for a particular region from the computed $\widehat{FC}$.

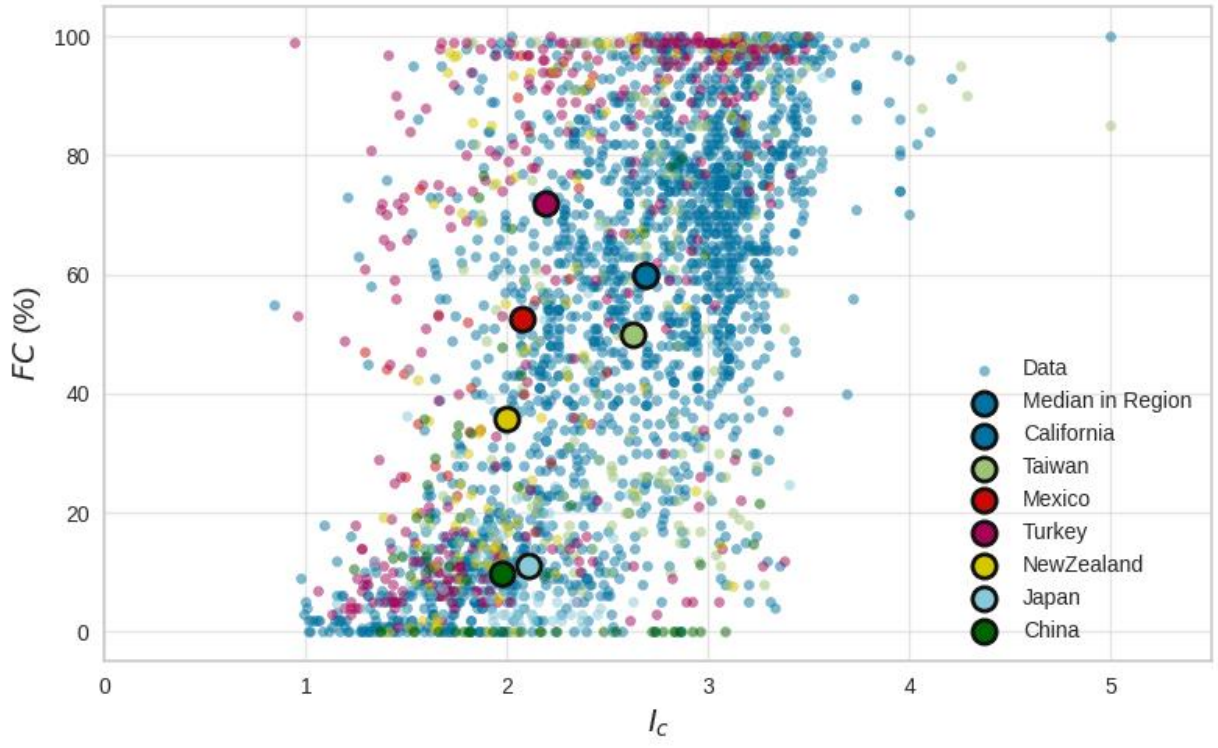

Figure 5-19. Paired *FC*-I_c dataset colored by region with medians of each region shown as the large circle.

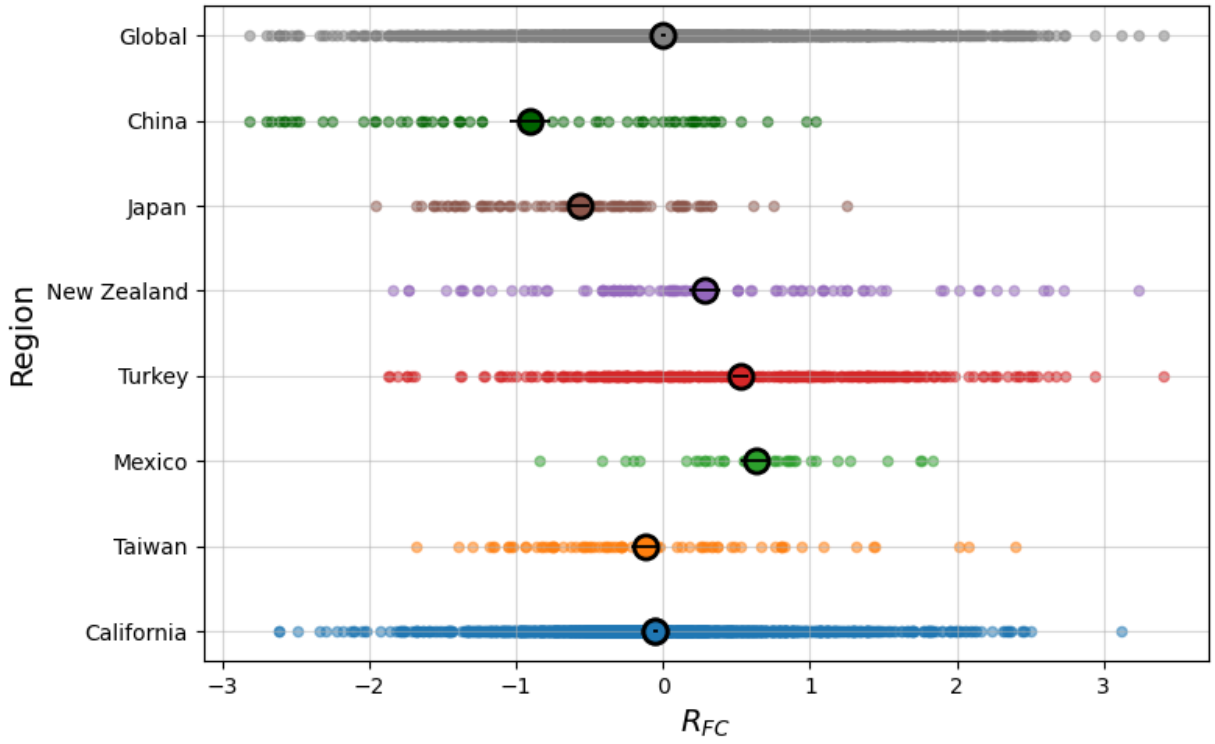

Figure 5-20. Residuals of proposed model (Equation 5.15) by region. Individual residuals are shown along with the regional mean and the 95% confidence intervals in the mean (horizontal black lines).

5.4.3 Cyclic Stress Ratio

Seismic demands on soil layers were computed in the form of a cyclic stress ratio, $CSR_{\mathbf{M}7.5,1atm}$ [Equation 1.6 with adjustments MSF and K_σ]. $CSR_{\mathbf{M}7.5,1atm}$ was computed for a given earthquake event and ground motion that has been associated with an observation of surface manifestation (or lack thereof) at or near the location of the CPT sounding. Some locations have been shaken by multiple earthquakes; in which case the CPT data was repeated in the summary pkl file (see Appendix B for full list of quantities in the pkl file). The quantities that describe the earthquake

event are summarized in Table 5-1. For each field observation, the nearest CPT sounding within the site was selected as being representative of that observation. The distance between the observation location and CPT sounding was recorded and stored in the pkl file.

Table 5-1. Summary of Values Queried or Computed for Each Layer Based on Quantities from the Database or Derived from CPT Data.

Variable Name	Description
EVNT_ID	The primary key from the NGL database for the earthquake associated with this observation/CPT pair
EVNT_NAME	The event name from the NGL database for the earthquake associated with this observation/CPT pair
EVNT_MAG	The event magnitude from the NGL database for the earthquake associated with this observation/CPT pair
PGA	The *PGA* from the NGL database for the observation location (FLDO location)
FLDM_ID	The primary key from the NGL database for the observation of manifestation
FLDM_SFEV	The flag from the NGL database for the observation of manifestation (1 if manifestation observed, 0 if not)
FLDM_DIST	The distance between the CPT/observation pair
CSR	Cyclic stress ratio

$CSR_{\mathbf{M}7.5,1atm}$ values computed at the center of each layer are taken to be representative of the layer. As shown by the equations below, $CSR_{\mathbf{M}7.5,1atm}$ is computed using the *PGA* stored in the GMIM

table associated with the observation (using the estimates from the Kriging approach outlined in Ulmer et al. 2023b, where possible), the moment magnitude of the event associated with the observation, the total and effective stress profiles computed for use in the q_{c1N} calculation, the *MSF* and N_{eq} equations by Lasley et al. (2017), and the r_d relationship presented in Lasley et al. (2016). The K_σ model is from Ulmer, et al. (2023).

$$CSR_{M7.5,1atm} = 0.65 \cdot \frac{PGA}{g}\frac{\sigma_v}{\sigma'_v} r_d \frac{1}{MSF}\frac{1}{K_\sigma} \tag{5.17}$$

$$r_d = (1-\alpha)exp\left(\frac{-z}{\beta}\right) + \alpha \tag{5.18}$$

$$\alpha = exp(-4.373 + 0.4491\boldsymbol{M}) \tag{5.19}$$

$$\beta = -20.11 + 6.247 * \boldsymbol{M} \tag{5.20}$$

$$ln(N_{eq}) = 0.4605 - 0.4082ln(a_{max}) + 0.2332\boldsymbol{M} \tag{5.21}$$

$$MSF = (14/N_{eq})^{0.2} \tag{5.22}$$

$$K_\sigma = \begin{cases} \left(\frac{\sigma'_{v0}}{p_a}\right)^{a_1} & for\ \sigma'_{v0} < p_a \\ \left(\frac{\sigma'_{v0}}{p_a}\right)^{a_2} & for\ \sigma'_{v0} \geq p_a \end{cases} \tag{5.23}$$

$$a_1 = \frac{-0.49}{1 + \exp[0.121(11.67 - FC)]} \tag{5.24}$$

$$a_2 = \begin{cases} -3.8 \times 10^{-6}(FC)^3 + 4.88 \times 10^{-4}(FC)^2 - 1.358 \times 10^{-2}(FC) - 0.13 & for\ FC < 70 \\ -0.148 & for\ FC \geq 70 \end{cases} \quad 5.25$$

where z is the depth in meters, p_a is atmospheric pressure (1 atm) in the same units as σ'_v, and $\boldsymbol{M}$ is the moment magnitude.

6 Updated Models

As described in Chapter 4, the necessary components of the probabilistic liquefaction model developed in this research include estimates of the probability of susceptibility, P[*S*], probability of triggering conditioned on susceptibility, P[*T*|*S*], probability of manifestation conditioned on triggering, P[*M*|*T*], and probability of manifestation conditioned on no triggering P[*M*|*NT*]. The following sections outline the approaches adopted by the SMT to estimate these probabilities. The P[*M*|*NT*] was evaluated at various stages of model development, but ultimately excluded following discussion with the NGL advisory board. The model presented herein assumes P[*M*|*NT*] = 0.

This chapter has four sections. Section 6.1 presents the selected model to estimate P[*S*] based on existing models from literature. Section 6.2 describes development of a triggering model from laboratory cyclic test results that were compiled by Kristin Ulmer (a member of the SMT) (Ulmer et al. 2023a). The laboratory-based triggering model is subsequently utilized as a Bayesian prior when developing the manifestation model. Section 6.3 presents the model for manifestation using the profile-based regression framework described in Section 4.4. Included within Sections 6.3.2 is a description of updates to the prior triggering and manifestation models using Bayesian analysis of the case history dataset. Finally, Section 6.4 illustrates sensitivities of the profile manifestation model that have been investigated as part of the model development process.

6.1 Probability of Susceptibility, P[*S*]

Based on the definition of susceptibility in Section 1.2.1, the susceptibility model is based on soil's material characteristics, specifically its mineral composition as inferred from *PI* or I_c, and excludes

non-compositional factors such as state, saturation, and manifestation potential. Note that in this approach, saturation is multiplied by the $P[T_L|S_L]$ term, as discussed in Section 4.4.1. The susceptibility model is probabilistic to reflect epistemic uncertainties associated with the complexity of liquefaction and cyclic softening, as well as the natural variability of soil behavior for materials with similar values of soil indices. Following a public workshop on the topic (Steudlein et al. 2023), a framework for creating new susceptibility models using the laboratory component of the NGL database was formulated. However, the implementation of this framework is in its beginning stages and has not yet produced a final model. Therefore, I am using currently available models, namely Maurer et al. (2017) in which the authors used borings and co-located CPTs in New Zealand to correlate I_c to Atterberg limits which in turn is converted to an I_c-based probability of susceptibility using four models from literature: Boulanger and Idriss (2006), Bray and Sancio (2006), Polito (2001), and Seed et al. (2003). The Maurer et al. (2017) adaptations of those four models are shown in Figure 6-1, and use the following functional form:

$$P[S] = 1 - \frac{1}{1 + exp\left(-\frac{1.702}{\sigma_m} * \left(\frac{I_c}{x_m} - 1\right)\right)} \quad 6.1$$

The range of results in Figure 6-1 constitute a partial representation of epistemic uncertainty. I account for this uncertainty using a logic tree approach to obtain a combined model, using equal weighting between the models. This approach produces the combined model shown in Figure 6-1, which has x_m = 2.635 and σ_m = 0.115. To incorporate the susceptibility model into the Bayesian inference framework utilized to obtain the manifestation model coefficients, a distribution function must be assigned to each model parameter. The uncertainty in these parameters was quantified by

taking the standard deviation of the x_m and σ_m values from the four criteria, yielding 0.0204 and 0.0865, respectively. The Bayesian prior distributions were assumed to be normal with the means and the standard deviations of the x_m and σ_m values as given above. The sensitivity of the P[M_P] model (Section 6.3) to variations across the different P[S] models is discussed in Section 6.4.2.

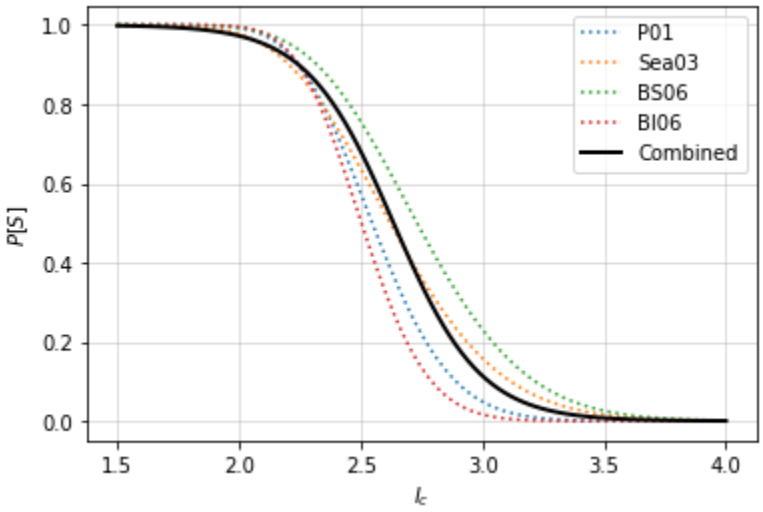

Figure 6-1. Probability of susceptibility models as a function of I_c as defined by Maurer et al. (2017).

6.2 Probability of Triggering Conditioned on Susceptibility, P[T|S]

As described in Chapter 4, the approach adopted in this research for modeling liquefaction triggering and manifestation requires a "prior" model for the probability of triggering. This prior triggering model was developed based on cyclic laboratory test data, as described in this section. The data collection and initial analyses were performed by SMT member Kristin Ulmer, as documented in Chapter 6.2 of Ulmer et al. (2023c).

The use of a laboratory-based prior has advantages and disadvantages. A wealth of knowledge from laboratory testing over the past several decades has not been fully utilized in many legacy models. The main advantage is that the relationship unambiguously represents the correlation of cyclic stress ratios (*CSR*s) required to trigger liquefaction given the soil's relative density. As a result, such relationships are not influenced by the complex effects of surface manifestation in the manner of legacy liquefaction "triggering" models (Section 3.2). The main disadvantage is that sample disturbance is known to modify the liquefaction resistance of soils as tested in the laboratory relative to their resistance under field conditions (e.g., Seed 1979). As described in detail by (Ulmer et al. 2023c), such effects are considered during model development by utilizing data both from intact and reconstituted specimens and through the Bayesian updating process of the lab prior.

6.2.1 Data Sources

The data considered in the development of the liquefaction triggering model consists of cyclic undrained test results that has been presented in a series of papers, reports, and data repositories. The data were derived from both cyclic triaxial (CTX) and cyclic direct simple shear (CDSS) testing and from both intact and reconstituted specimens. Only test results corresponding to a pre-shear vertical effective stress of 1.0 atm were considered. The data span a range of relative densities of 0.19 to 0.99 and represent a diverse array of sand materials, although the sands were predominantly of quartz mineralogy.

As described in detail by Ulmer et al. (2023c), while the database developed for this work is the largest yet produced (a total of 246 test results), the data is nonetheless unevenly sampled, which creates challenges in model development. The data that was compiled is shown in Figure 6-2. The main sampling problem is that while the database contains large numbers of CTX and CDSS tests, and significant numbers of tests for both reconstituted and intact specimens, the CDSS results apply almost exclusively for reconstituted specimens and the CTX results are from a combination of intact and reconstituted specimens. The test type that arguably would be most directly applicable would be CDSS tests on intact specimens because the CDSS stress path is applicable to free-field conditions and intact specimens include effects of soil density but also secondary effects of fabric and age. Due to a relative lack of such tests, the SMT sought to compare reconstituted CDSS results to the available intact CTX results with the aim of investigating differences due to sample type. However, this was complicated by the observation that CTX resistances on reconstituted specimens exceed DSS resistances, which is a consequence of anisotropy. As a result, it was not possible to develop an empirical adjustment for the reconstituted CDSS results to account for sample disturbance. However, it is observed that CTX results for the two specimen types (intact, reconstituted) are difficult to distinguish, suggesting the sample type effect may be smaller than the anisotropy effect.

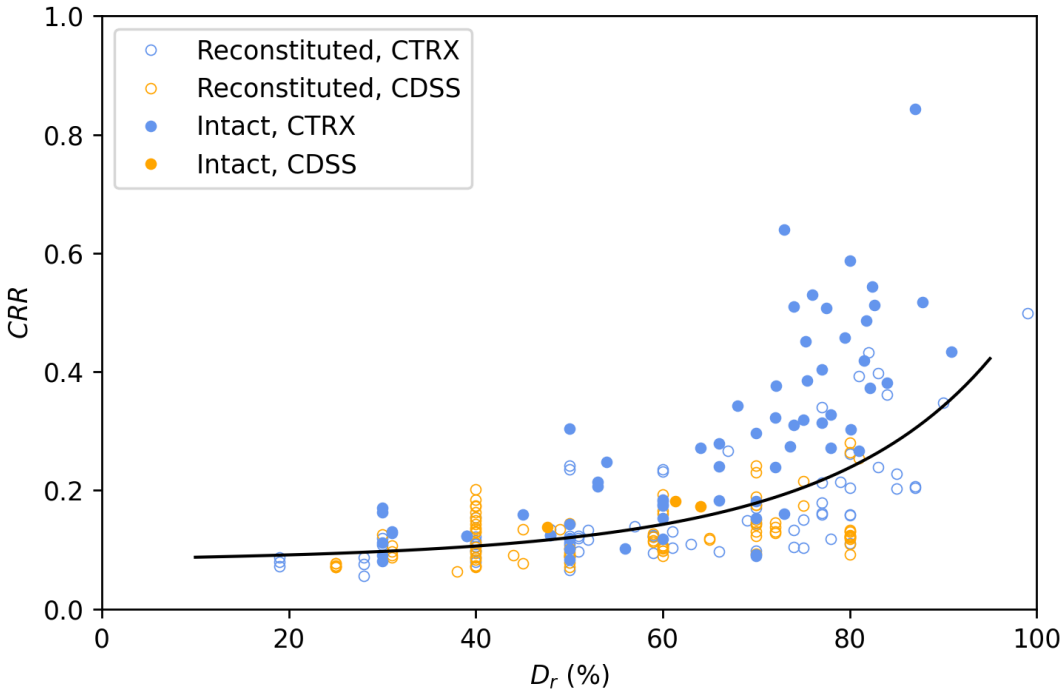

Figure 6-2. Data points used in model development sorted by test and sample type (courtesy of Kristin Ulmer)

6.2.2 Functional Form of P[*T*|*S*] Model

A key modeling decision for development of the triggering prior was whether to produce separate models for CTX and CDSS conditions. Had this been done, as suggested by the results in Figure 6-2, the CDSS model would produce relatively low resistances without appreciable increases at large D_R. This feature was considered unrealistic, and in order to avoid it, all the data was grouped together to develop the triggering prior. In Ulmer et al. (2023c), a 3rd order polynomial was fit to the data, which comprises the initial model that is revisited in this section. This model includes modest increases in resistance for $D_R > \sim 70\%$.

Figure 6-3 replots the dataset, which has significant sampling bias that effects the results of model fitting. The sampling bias is towards more laboratory tests performed between 40-80% D_R compared to D_R<40% and D_R>80%. The numbers of tests in bins of [0-40%], (40-60%], (60-80%], and (80-100%] are shown in Figure 6-4 {note that a square bracket is inclusive such that (40-60%] is equivalent to 40% < D_R <= 60%}. In order to reduce the sampling bias, each data point is weighted by the inverse of the number of points within the bin it resides in (normalized by the mean weight). The weights of the points are shown by the coloration in Figure 6-3.

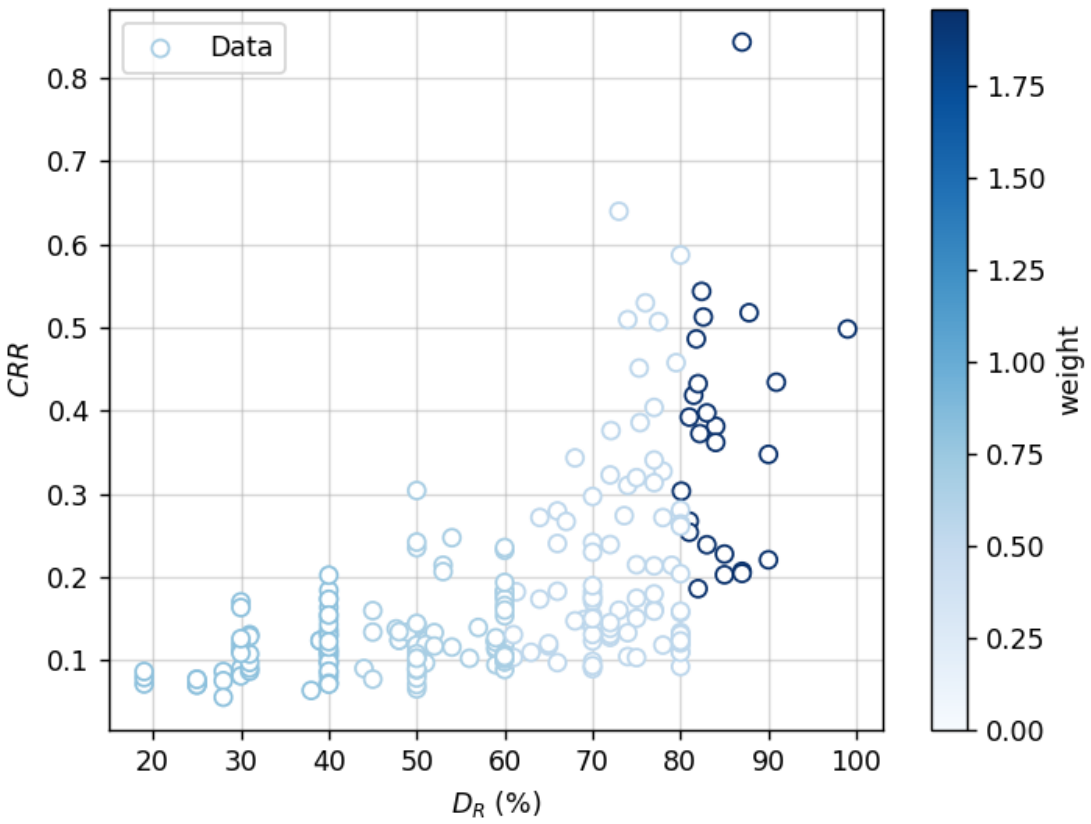

Figure 6-3. Dataset used for determining triggering prior. Datapoints are weighted by the inverse proportion of points within histogram bins presented in Figure 6-4.

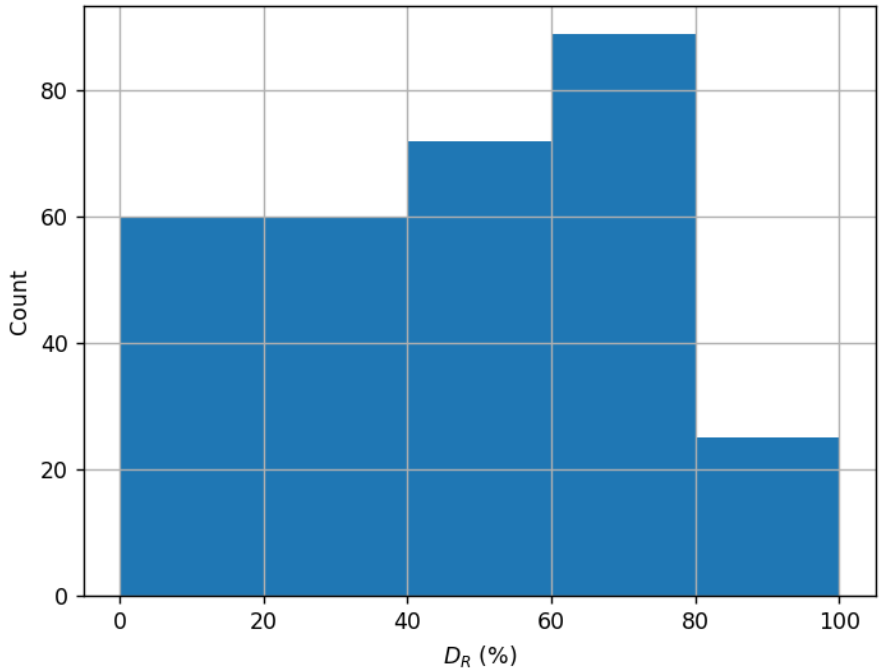

Figure 6-4. Histogram of the triggering dataset D_R values with bin edges defined at [0,40], (40,60], (60,80], and (80,100]. The proportion of counts within each bin was applied as weight for regressing the triggering prior.

The initial model was updated to address two issues: (1) account for the weights shown in Figure 6-3 and (2) to stabilize the regression using a simpler linear model in transformed parameter spaces in which the data distribution is approximately normal and homoscedastic, i.e., with a consistent level of dispersion across the range of the independent variable. This model is referred to as a linear P[T|S] model subsequently. The transformation of the dataset was accomplished by applying a Box-Cox transformation (Box & Cox, 1964; Equation 6.2) to both the D_R and *CRR* values, as follows,

$$\hat{x} = \frac{x^{\lambda} - 1}{\lambda} \qquad 6.2$$

where λ is taken as the value that transforms the dataset as close as possible to a normal distribution. The λ values for D_R and CRR (λ_{D_R} and λ_{CRR}, respectively) were determined to be 1.202 and -0.657, respectively, calculated using the SciPy Python package (Virtanen et al. 2020). The dataset in the transformed $\widehat{CRR}$-$\widehat{D_R}$ space is presented in Figure 6-5.

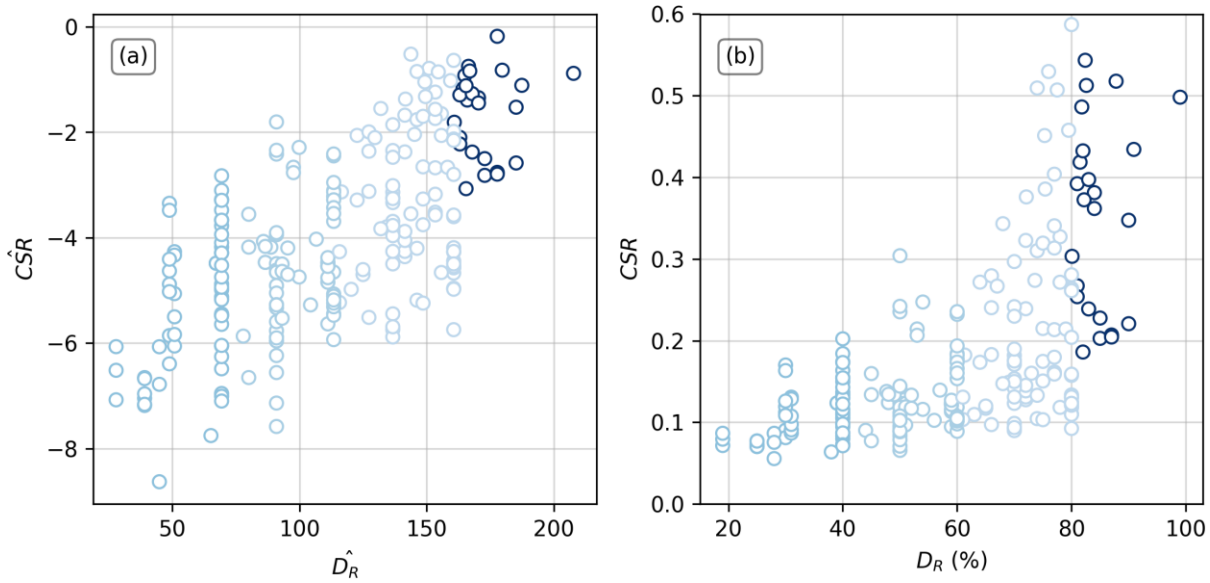

Figure 6-5. Dataset for triggering model development in (a) Box-Cox transformed ($\widehat{CRR}$-$\widehat{D_R}$) space and (b) CSR-D_R space. The data points are colored by the weights in Figure 6-3.

Following this transformation, the dataset was fit using a linear model:

$$\widehat{CRR} = \zeta_0 + \zeta_1 * \widehat{D_R} + \varepsilon * \sigma_\zeta \quad 6.3$$

where ζ_0, ζ_1, and σ_ζ are model coefficients to be regressed as described in the next section and ε is the standard normal variate (zero mean and unit standard deviation). Alternatively, the equation can be rewritten in the untransformed space as:

$$CRR = \sqrt[\lambda_{CSR}]{\left[1 + \lambda_{CSR}\left(\zeta_0 - \zeta_1\lambda_{D_R}\right)\right] + \left(\zeta_1\lambda_{CSR}\lambda_{D_R}\right){D_R}^{\lambda_{D_R}} + \left(\lambda_{CSR}\sigma_\zeta\right)\varepsilon} \quad 6.4$$

6.2.3 P[T|S] Model Prior

Bayesian inference was performed using the PyMC Python package (Wiecki et al. 2023) to determine prior distributions of the coefficients in Equation 6.3. Bayesian inference was used instead of a typical least-squares regression because of the advantages gained in determining distribution of the coefficients so that uncertainty can be quantified for later updates to the model in the form of posterior coefficient distributions (Section 6.3.2). An "uninformed" prior distribution was adopted for each coefficient from Equation 6.3 using a normal distribution with mean of zero and standard deviation of 10. The weighted dataset (Figure 6-3) was used in the inference. Four Markov chains (Gagniuc 2017; Markov 2006) with 1000 samples drawn from each chain and the resulting distribution of parameters and drawn samples are presented in Figure 6-6. Note that each distribution seems homogeneous and stationary (there are no large drifts or other odd patterns) indicating a stable regression.

The posterior distributions of the triggering model coefficients reflect uncertainty in how well the model represents the laboratory data. Additional uncertainty that is not reflected in the coefficient uncertainty is caused by (1) sample disturbance that creates uncertainty regarding applicability of laboratory data to field conditions and (2) uncertainty in the correlation between q_{c1Ncs} and D_R. For these reasons, it was decided to increase the standard deviation of each model coefficient in the posterior laboratory-based triggering model by a factor of 4, and to use the results of this adjusted model as the prior triggering model in developing the manifestation model, as described later. To account for correlations between the three coefficients, the covariances were computed (Table 6-2). The covariance matrix was used to create multivariate normal distribution priors for updating the triggering model as described in Section 6.3. The correlation matrix (a transformation of the covariance matrix) is presented in Table 6-3 to present the correlation coefficients between the three $PF_{T|S}$ coefficients; note there is a strong negative correlation between ζ_0 and ζ_1 and weak correlations between both the slope and intercept to σ_ζ.

The regressed model is linear and the error term, defined by σ_ζ, is normally distributed within Box-Cox space ($\widehat{CSR}$). The probability density for the regressed model, shown in Figure 6-8, is a normal distribution in Box-Cox space, but skewed in *CSR* space. The skewed distribution is similar in shape to a log-normal distribution, however it is not identical because the Box-Cox transformation is not logarithmic. Instead, it can be called a "Box-Cox normal" distribution.

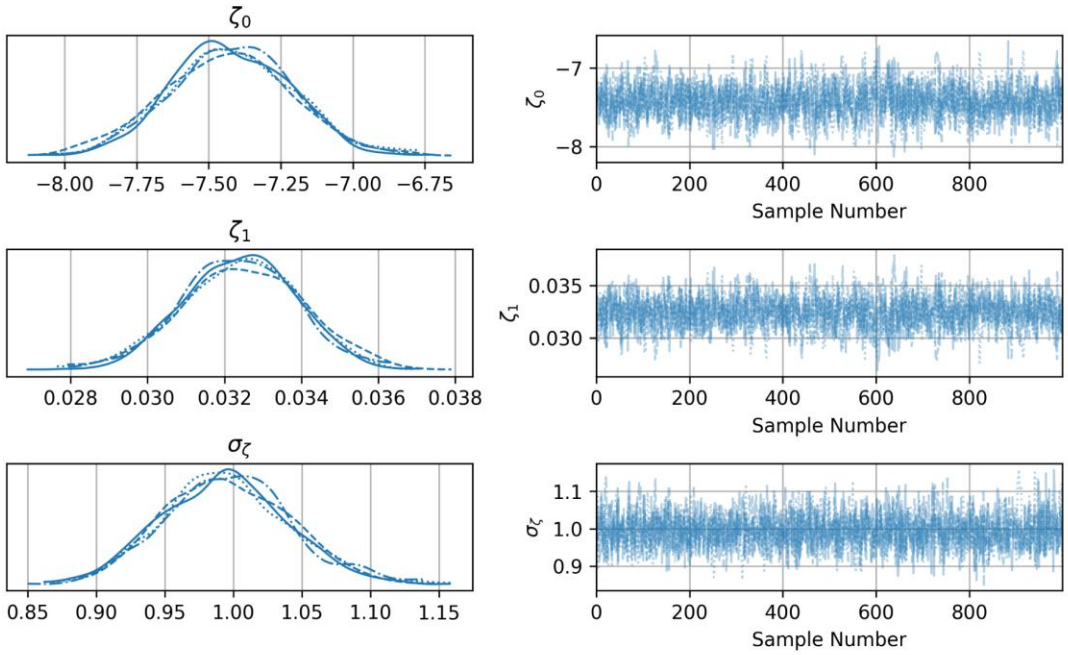

Figure 6-6. Distribution of triggering model coefficients (left column) and sampling draws for each coefficient (right column).

Table 6-1. Means and standard deviations for the coefficients in Equation 6.3 taken from Bayesian inference.

Variable	***Value***
μ_{ζ_0}	*-7.43*
σ_{ζ_0}	*0.196*
μ_{ζ_1}	*0.0325*
σ_{ζ_1}	*0.00141*
μ_{σ_ζ}	*0.994*
σ_{σ_ζ}	*0.0459*

Table 6-2. Covariance matrix of the three $PF_{T|S}$ coefficients in the after Bayesian inference sampling. Note the diagonals are squared standard deviations from Table 6-1.

	ζ_0	ζ_1	σ_ζ
ζ_0	3.844e-02	-2.597e-04	-6.792e-04
ζ_1	-2.597e-04	2.007e-06	5.106e-06
σ	-6.792e-04	5.106e-06	2.102e-03

Table 6-3. Correlation matrix of the three $PF_{T|S}$ coefficients after Bayesian inference sampling.

	ζ_0	ζ_1	σ_ζ
ζ_0	1	-0.935	-0.0755
ζ_1	-0.935	1	0.0786
σ	-0.0755	0.0786	1

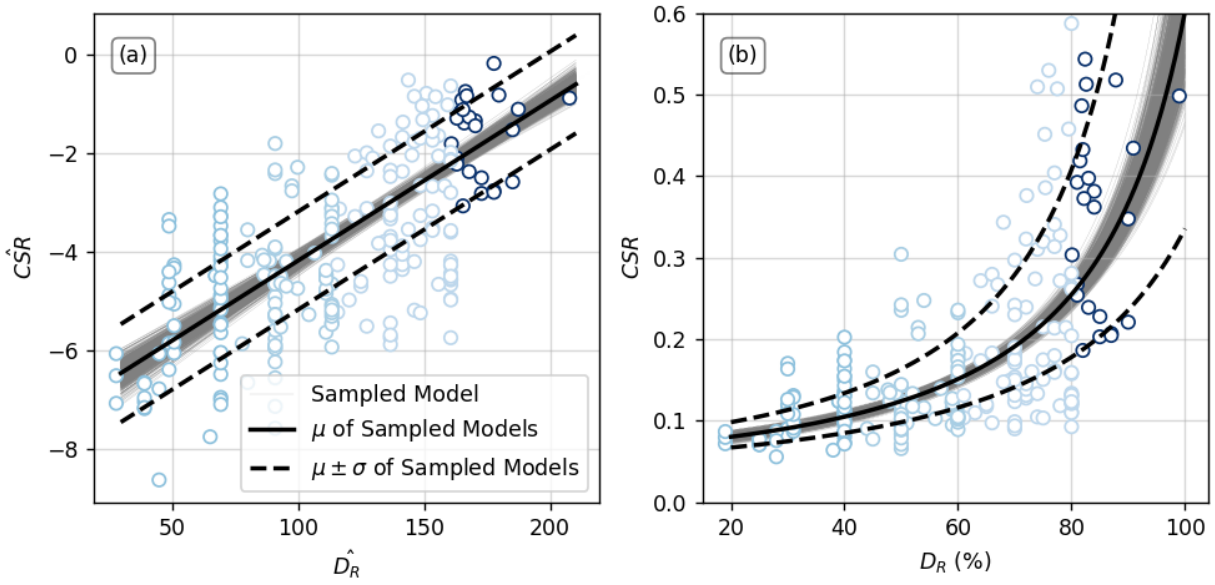

Figure 6-7. Triggering model fit shown in (a) box-cox transformed space and (b) untransformed parameter space. Samples of the mean model are shown as light gray lines and the recommended mean and mean plus or minus one standard deviation are plotted as solid and dashed black lines, respectively.

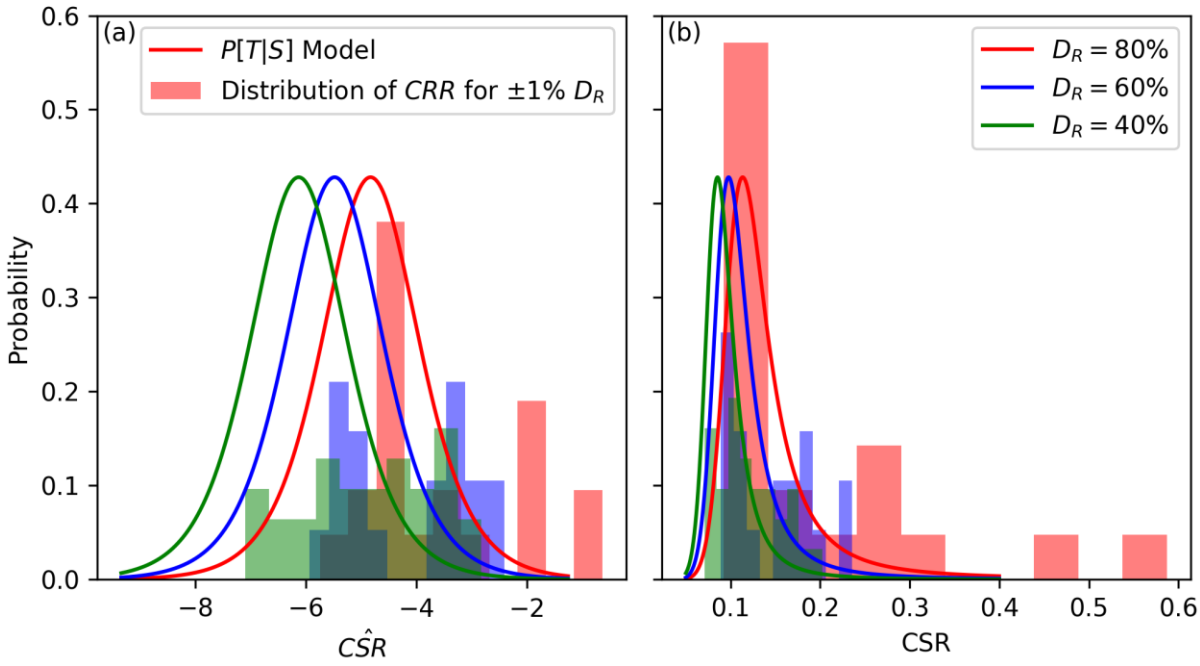

Figure 6-8. Probability density of the regressed triggering model for D_R = 80, 60, and 40% and histograms of laboratory *CRR* data within $\pm$ 1 of the target D_R. Plotted in (a) Box-Cox transformed space and (b) CSR space. The distributions in CSR space can be described as "Box-Cox normal".

6.3 Probability of Manifestation, P[$M|T$]

The model formulation applied in this research includes manifestation given triggering but does not include manifestation given no triggering nor manifestation given no susceptibility (Section 4.4.2). Potential contributors to surface manifestations of ground failure aside from liquefaction triggering were not included in the final model because:

1. Versions of models that include effects, such as substantial strains related to cyclic softening of clays, did not improve predictive power significantly compared to models that neglected such effects.

2. The NGL advisory board voiced skepticism about manifestation in the absence of triggering,
3. By not including these other mechanisms, the resulting model is simpler to adopt for end users.

The model that only considers manifestation caused by triggering therefore involves three models that each have coefficients that can be updated: susceptibility, triggering given susceptibility, and manifestation given triggering. The formulation in Equation 4.11 can be expanded to show the susceptibility, triggering, and manifestation models that go into the profile manifestation prediction as follows:

$$P[M_P] = 1 - \prod_{l=1}^{N_L} \left(1 - PF_{M|T_l} PF_{T|S_l} PF_{S_l} K_{Sat_l}\right)^{t_l/t_c} \quad 6.5$$

Variable t_c is the characteristic thickness as introduced in Section 4.4.2. This variable could potentially be treated as a model coefficient in the Bayesian inference, but it causes instability in the results. Several t_c values ranging from 0.5m to 5m were tested in the regression, and the likelihood, L, was maximized at $t_c \sim$ 2m. The value was thereafter fixed at 2m.

The development of the manifestation model is presented in a step-by-step approach in the following subsections to clarify the model development process. First, a simple manifestation model conditioned on one parameter is presented. That relationship was developed only allowing the manifestation model ($PF_{M|T}$) priors to update to posteriors while fixing the triggering ($PF_{T|S}$) and susceptibility (PF_S) priors. Next, both the manifestation and triggering priors were updated simultaneously within the single parameter model. Finally, other manifestation model parameters

were explored, and a two-parameter version of the manifestation model was selected as the recommended model.

6.3.1 $PF_{M|T}$ Inference with Single Parameter Model

The modelling began with a one-dimensional logistic function in which the single independent variable was the depth to the top of the potentially liquefiable layer z_{top}. The conditional probability factor is then described by

$$PF_{M|T} = \frac{1}{1 + \exp\left(-\left(\beta_0 + \beta_1 \cdot z_{top}\right)\right)} \tag{6.6}$$

As discussed in Section 6.2.3, the coefficients updated through Bayesian inference needed to be assigned prior distributions. It was not desired to impose any prior belief about the relationships for manifestation given triggering, therefore β_0 and β_1 were initialized as having normal distributions with mean (μ) = 0 and standard deviation (σ) = 1000 (Gelman (2006) recommend a normal distribution centered at 0 with a standard deviation set to a very high value for a noninformative prior distribution). The other models, $PF_{T|S}$ and PF_S, are given the mean prior model coefficients presented in Sections 6.1 and 6.2 but are not given the opportunity to update so that they remain fixed while the $PF_{M|T}$ coefficients update.

The model was developed using a dataset reduced from the full dataset described in Section 5 to a subset that only contained CPT profiles with total lengths of at least 15m. This filter was applied because shorter profiles were observed to cause significantly reduced model performance since the short profiles did not represent all of the soil layers that could contribute to surface

manifestation. The threshold of 15m was selected based on a series of tests in which different depth thresholds were used and manifestation models developed. Review of the model coefficients and performance produced the conclusion that 15m gave a practical balance between the size of the dataset and the performance of the model. Application of the >15m threshold reduces the case history dataset to 204 profiles that include 5091 soil layers. Each case history is also weighted to account for cases in which multiple CPTs are associated with a single observation, as described in Section 5.1.

The results of the $PF_{M|T}$ model coefficient inference are presented in Figure 6-9. For this and the following inferences, a local maximum a posteriori probability (MAP) estimate (i.e., mode of the a posteriori distribution) (Bassett and Deride 2016) is evaluated to approximate the mean for each coefficient rather than sampling which would produce posterior distributions of each coefficient. The MAP provides a point estimate using the dataset and the priors and was used during exploratory analyses (and for this simplified illustrative model) for computational efficiency. The final recommended model will present the results of sampling the full distributions of the model coefficients.

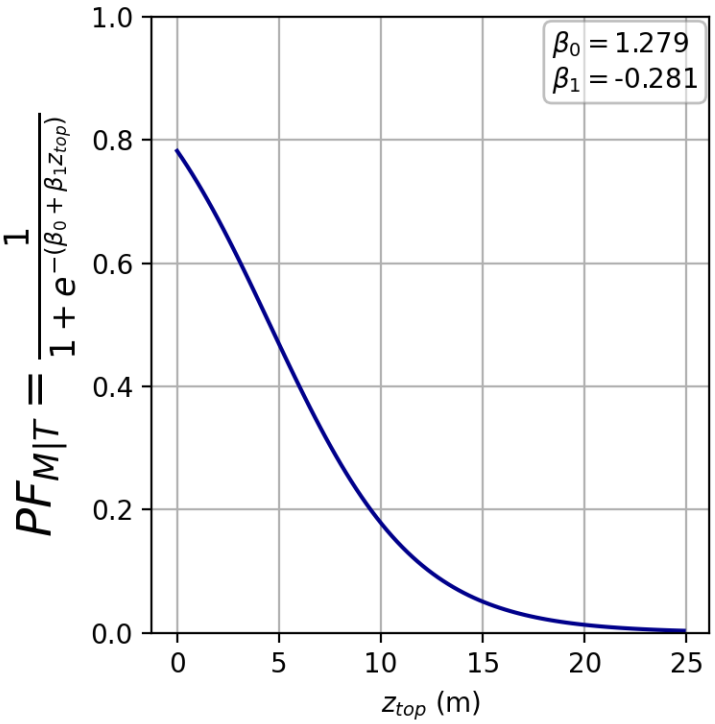

Figure 6-9. $PF_{M|T}$ function conditioned on z_{top} based on MAP estimates of model coefficients. The Bayesian inference that produced this model used fixed $PF_{T|S}$ and PF_S priors.

The MAP estimates for β_0 and β_1 are 1.279 and -0.281, respectively. The negative coefficient on β_1 ensures that $PF_{M|T}$ decreases as the depth of a layer increases. It is also noted that $PF_{M|T}$ never reaches a value of 1, even at z_{top}=0 it only reaches ~0.8.

The probability factor model (Equation 6.6) only produces an equivalent probability P[M_L|T_L] for a layer of thickness t_c. Recall that P[M_L] is influenced by the layer thickness (Section 4.4.2), so while a layer with t=t_c produces P[M|T]=0.8, a layer with t somewhat larger than t_c could produce P[M|T]~1. Therefore, the model is predicting that a layer at the ground surface that has liquefaction triggered will have an ~80% chance of manifesting if it is 2m thick. If t < 2m, P[M] will decrease

and if t > 2m, P[M] will increase. This is also intuitive: a thin layer, even if it is shallow, will be less likely to manifest surface evidence if liquefaction is triggered compared to a thick layer.

To track performance of the regressed models, a cost function (J) is introduced that is very similar to the likelihood function presented in Equation 4.13 except that it incorporates a negative sign so that values are positive. As model performance improves, the value of the cost function decreases, with 0 representing a perfect model.

$$J = -\frac{1}{N_P}\sum_{k=1}^{N_P}[y_k \ln(P[M_P]_k) + (1-y_k)]\ln(1-P[M_P]_k) \quad 6.7$$

When the model is run on the training dataset using the above MAP estimates of the $PF_{M|T}$ coefficients, the cost is J=0.566.

6.3.2 Single Parameter $PF_{M|T}$ Model with $PF_{T|S}$ Inference

Whereas in the previous section the triggering and susceptibility prior models were fixed (not adjusted by Bayesian regression), in this section the Bayesian inference is allowed to simultaneously update both the $PF_{M|T}$ and $PF_{T|S}$ coefficients while the PF_S priors remain fixed. The $PF_{M|T}$ priors were again set at μ=0 and σ=1000. The $PF_{T|S}$ priors were set using the μ inferred from the laboratory test dataset in Section 6.2 (Table 6-1) while the covariance coefficients were increased (multiplied by four) from those directly inferred from the laboratory-based data to incorporate a larger level of uncertainty. As discussed in Section 6.2.3, the σ values determined from the laboratory test dataset represent uncertainty with laboratory tests, but do not incorporate

additional uncertainty that comes from a lack of knowledge of how representative of field conditions these specimens are. This is a somewhat arbitrary modification, but the sensitivity to inference results is explored in Section 6.4.3 where a multitude of different σ multipliers are tested. The 4x multiplier was deemed appropriate to maintain confidence in the laboratory-based triggering prior while accounting for uncertainty for the laboratory tests representing field conditions.

Bayesian inference is performed using the case history dataset and MAP estimates of the $PF_{M|T}$ and $PF_{T|S}$ coefficients were evaluated, with the results shown in Figure 6-10 and Figure 6-11. The $PF_{M|T}$ posterior (Figure 6-10) remains very similar to the posterior inferred in Section 6.3.1 but the $PF_{T|S}$ posterior (Figure 6-11) changes significantly, reducing the *CSR* required to trigger liquefaction at high D_R/q_{c1Ncs}. These posterior models produce J=0.558 which is only a small reduction in cost (small increase in model predictive performance) compared to the model that fixed the $PF_{T|S}$ prior and inferred the $PF_{M|T}$ posterior.

The shift in the $PF_{T|S}$ posterior is potentially important and warrants discussion. While the Bayesian inference shifts down the triggering relationship, this produces only marginal improvement, suggesting that it is only weakly supported by the data. To more carefully evaluate this effect, the shift is re-examined using different assumptions regarding the $PF_{M|T}$ conditioning variables and updating of the PF_S in subsequent sections.

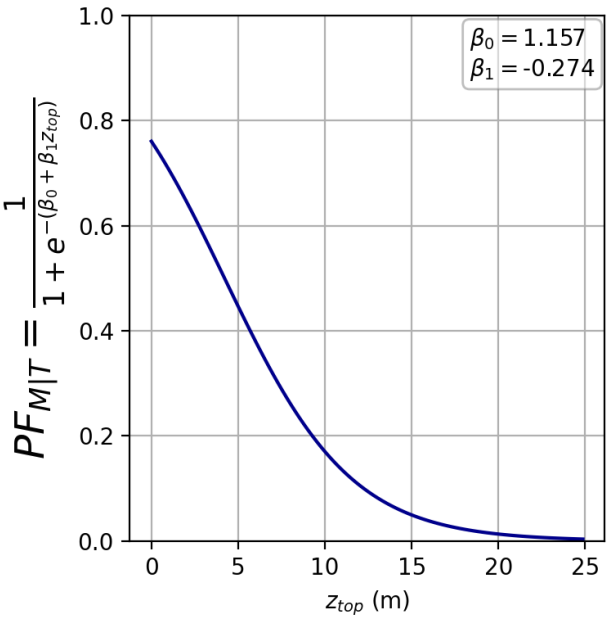

Figure 6-10. $PF_{M|T}$ function conditioned on z_{top} based on MAP estimates of model coefficients in which $PF_{T|S}$ was also updated. The PF_S priors were fixed.

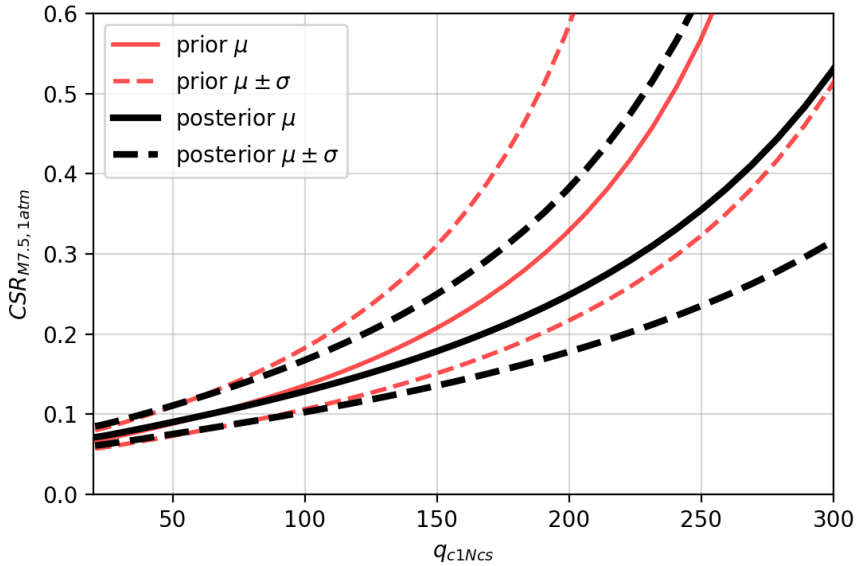

Figure 6-11. $PF_{T|S}$ function conditioned on q_{c1Ncs} based on MAP estimates of model coefficients. The PF_S priors were fixed.

6.3.3 Single Parameter $PF_{M|T}$ Model with $PF_{T|S}$ and PF_S Inference

In this section the Bayesian inference was extended to include the susceptibility prior, which updated the posterior PF_S model. The two PF_S model coefficients, x_m and σ_m, had prior μ and σ values that were described in Section 6.1; those coefficients' priors were assumed to be normally distributed. The Bayesian inference updated these along with the $PF_{M|T}$ and $PF_{T|S}$ coefficient priors. The inference was performed using the same dataset as described previously (Section 6.3.1). MAP estimates of coefficients were produced and the results are shown in Figure 6-12, Figure 6-13, and Figure 6-14.

The $PF_{M|T}$ updated posterior was generally similar to the previous two posteriors; however, it reached higher probabilities at shallow depths. The $PF_{T|S}$ posterior shifted to lower *CSR* at high D_R again, but to a lesser extent, indicating that some of the change may have actually been due to susceptibility effects rather than triggering. The PF_S posterior decreased across the entire range of I_c values, meaning that the susceptibility prior was not adequately decreasing P[*M*] for fine-grained soils with moderate to high I_c. This inference produced J=0.515, which is a significant improvement compared to the prior two iterations, indicating that the susceptibility function update is important for improving manifestation prediction.

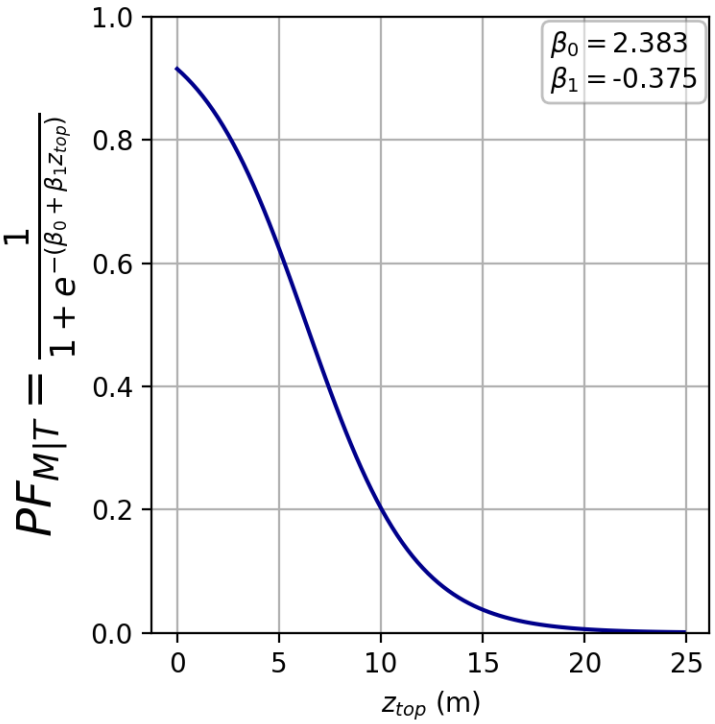

Figure 6-12. $PF_{M|T}$ function conditioned on z_{top} based on MAP estimates of model coefficients in which $PF_{T|S}$ and PF_S were also updated.

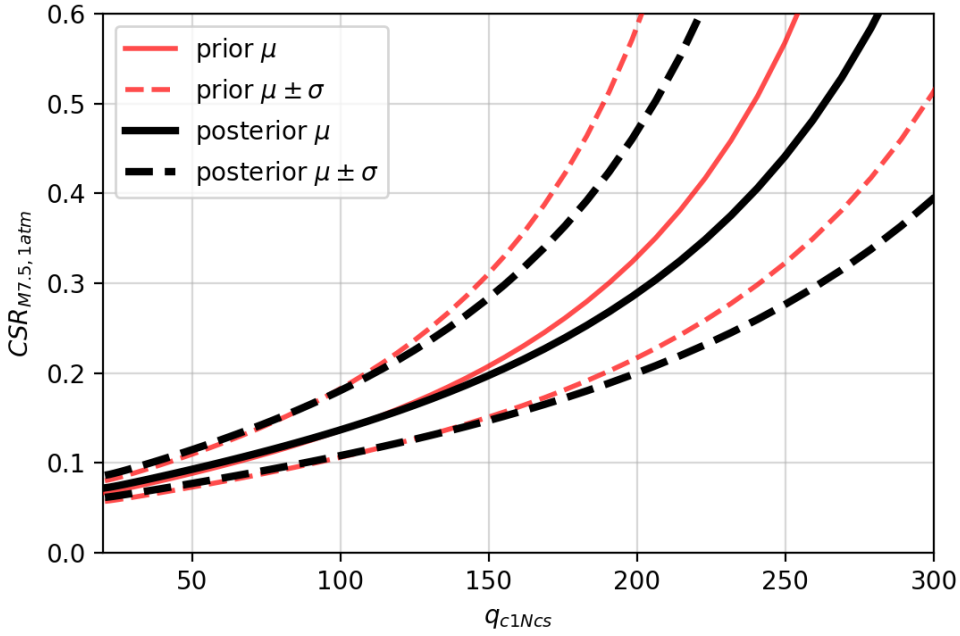

Figure 6-13. $PF_{T|S}$ function conditioned on q_{c1Ncs} based on MAP estimates of model coefficients. The PF_S priors were also adjusted.

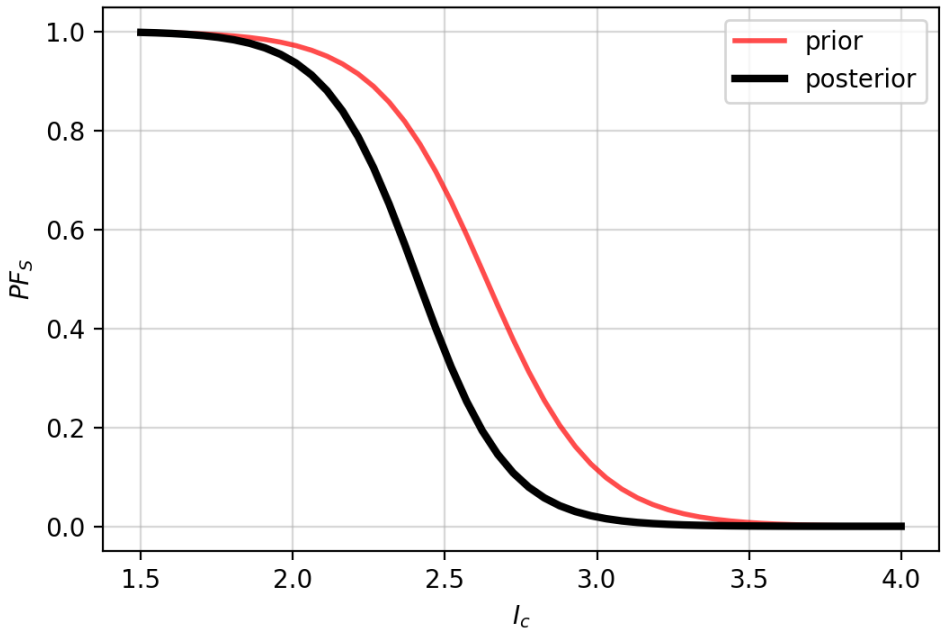

Figure 6-14. PF_S function conditioned on I_c based on MAP estimates of model coefficients.

6.3.4 P[M] Inference using Multi-Parameter $PF_{M|T}$ Models

Up to this point the manifestation given triggering function has only included z_{top} as a predictive feature but other features and combinations of multiple features could help further improve manifestation prediction. Additional layer attributes that could potentially improve the $PF_{M|T}$ function are listed in Table 4-2. Soil layer thickness, t, is not listed in Table 4-2 because it is already included in the t/t_c exponent. MAP estimates that describe the posterior $PF_{M|T}$, $PF_{T|S}$, and PF_S coefficients were obtained for all parameter combinations; a total of 127 combinations of potential predictive features were investigated.

Several feature combinations in the $PF_{M|T}$ function produced physically unrealistic trends (i.e., $PF_{M|T}$ increases as z_{top} increases or $PF_{M|T}$ decreases as *CSR* increases). For each feature, a sign for its multiplying coefficient can be anticipated, representing the physically expected trend (i.e., β_i for z_{top} should be a negative number and β_i for *CSR* should be a positive number). While the Bayesian inferences were not constrained to conform with the expected coefficient signs, any model with at least one coefficient opposite to the anticipated sign was discarded and not listed in Table 6-4. Of the 127 possible $PF_{M|T}$ combinations, 87 were rejected using this process. The 40 remaining models are listed in Table 6-4. The table is sorted first by ascending number of features, and then by ascending *J*. Note that *J* generally decreases as the number of features increases; this trend is shown in Figure 6-15.

Table 6-4. Accepted P[M_P] models with MAP estimated coefficients.

$PF_{M\|T}$ Features	$PF_{M\|T}$, coefficients ($\beta_0, \beta_1, \ldots, \beta_i$)	$PF_{T\|S}$ coefficients (ζ_0, ζ_1, σ)	PF_S coefficients (σ_m, x_m)	*J*
z_{top}	-1.3429, -2.8025	-7.004, 0.0285, 0.9377	0.1054, 2.4093	0.5148
$C_{R,l}$	-1.6795, -3.4581	-6.9896, 0.0287, 0.9597	0.1068, 2.5014	0.5243
σ_v'	-0.8982, -1.1557	-7.0584, 0.0274, 0.9549	0.1041, 2.4394	0.5512
$L_{D,l}$	-1.7139, 1.1218	-7.5775, 0.0258, 1.0229	0.114, 2.566	0.5557
I_c	-2.4065, -3.5026	-7.3687, 0.0331, 0.99,	0.115, 2.6414	0.5658
$CSR_{M7.5,1atm}$	-1.2846, 0.0276	-7.2739, 0.0249, 0.9465	0.1063, 2.4554	0.6004
z_{top}, $L_{D,l}$	-1.9695, -2.4715, 1.2552	-7.4491, 0.0301, 1.0108	0.1097, 2.5266	0.4907
$L_{D,l}$, σ_v'	-1.5557, 1.3474, -1.5057	-7.5004, 0.0296, 1.0285	0.1113, 2.5599	0.499
$C_{R,l}$, $L_{D,l}$	-1.9662, -2.9421, 0.9195	-7.2948, 0.0299, 1.0246	0.1099, 2.5807	0.5051

I_c, z_{top}	-2.1977, -2.6584, -2.0155	-7.3037, 0.0328, 0.9408	0.1148, 2.6223	0.5072
z_{top}, $C_{R,l}$	-1.556, -1.4489, -1.9446	-6.9953, 0.0286, 0.9485	0.1057, 2.4469	0.5154
I_c, $C_{R,l}$	-2.0743, -1.8466, -2.6926	-7.1716, 0.0325, 0.9524	0.1137, 2.6292	0.517
$CSR_{M7.5,1atm}$, $C_{R,l}$	-1.6998, 0.1085, -3.4694	-7.1344, 0.0294, 0.9643	0.1064, 2.5005	0.5241
I_c, σ_v'	-1.8673, -2.7136, -0.9504	-7.3221, 0.0333, 0.9529	0.1147, 2.6313	0.533
I_c, $L_{D,l}$	-2.2372, -2.1159, 0.8318	-7.5346, 0.0317, 1.0475	0.1151, 2.6446	0.5422
$CSR_{M7.5,1atm}$, $L_{D,l}$	-1.7140e+00, 1.3000e-03, 1.1217e+00	-7.5789, 0.0258, 1.0229	0.114, 2.5659	0.5557
$CSR_{M7.5,1atm}$, I_c	-2.4201, 0.0548, -3.5239	-7.4249, 0.0335, 0.9932	0.1149, 2.6416	0.5656
q_{c1N}, I_c	-2.435, -0.3291, -3.4513	-7.3235, 0.0324, 0.9863	0.1151, 2.6412	0.5659
I_c, z_{top}, $L_{D,l}$	-2.3693, -1.6522, -2.2252, 1.0134	-7.4738, 0.0323, 0.9968	0.1147, 2.6284	0.4822
I_c, $L_{D,l}$, σ_v'	-1.9027, -1.3049, 1.1658, -1.4059	-7.4995, 0.0318, 1.0223	0.1145, 2.6313	0.4921
$C_{R,l}$, $L_{D,l}$, σ_v'	-1.6673, -0.8586, 1.2296, -1.1256	-7.4425, 0.0298, 1.0274	0.1108 2.5661	0.4982
$CSR_{M7.5,1atm}$, $L_{D,l}$, σ_v'	-1.5559e+00, 5.0000e-04, 1.3481e+00, -1.5064e+00	-7.5014, 0.0296, 1.0285	0.1113, 2.5599	0.499
I_c, $C_{R,l}$, $L_{D,l}$	-2.143, -1.0562, -2.6921, 0.7581	-7.3044, 0.0319, 1.0139	0.113, 2.6335	0.5016
$CSR_{M7.5,1atm}$, $C_{R,l}$, $L_{D,l}$	-1.9755, 0.0935, -2.9593, 0.9174	-7.3971, 0.0304, 1.0276	0.1096, 2.5778	0.5045
q_{c1N}, I_c, z_{top}	-2.3555, -0.6257, -2.7786, -1.93,	-7.2198, 0.0315, 0.9318	0.115, 2.6218	0.5063
I_c, z_{top}, $C_{R,l}$	-2.1904, -2.5977, -1.9204, -0.1612	-7.2935, 0.0327, 0.9414	0.1147, 2.6217	0.5071
$CSR_{M7.5,1atm}$, z_{top}, $C_{R,l}$	-1.5865, 0.0727, -1.3552, -2.0807	-7.0821, 0.029, 0.9527	0.1054, 2.4501	0.5159
$CSR_{M7.5,1atm}$, I_c, $C_{R,l}$	-2.0901, 0.1001, -1.8697, -2.6906	-7.2762, 0.0331, 0.9568	0.1136, 2.629	0.5164
I_c, $C_{R,l}$, σ_v'	-1.6799, -1.493, -1.9084, -0.0509	-6.8722, 0.03, 0.9195	0.1136, 2.6303	0.5206
q_{c1N}, I_c, σ_v'	-2.0166, -0.6511, -2.7446, -0.9263	-7.2146, 0.0315, 0.9467	0.1149, 2.6293	0.5323

$CSR_{M7.5,1atm}$, I_c, σ_v'	-1.8707, 0.015, -2.7199, -0.9498	-7.3363, 0.0334, 0.9537	0.1147, 2.6312	0.533
q_{c1N}, I_c, $L_{D,l}$	-2.2913, -0.3738, -2.1058, 0.8085	-7.4667, 0.0302, 1.0355	0.1155, 2.6453	0.5416
$CSR_{M7.5,1atm}$, I_c, $L_{D,l}$	-2.2551, 0.0465, -2.1721, 0.8291	-7.5802, 0.0321, 1.0484	0.1151, 2.6446	0.542
q_{c1N}, $CSR_{M7.5,1atm}$, I_c	-2.6119, -1.4734, 0.1968, -3.4726	-7.126, 0.0289, 0.9553	0.119, 2.6262	0.5621
$CSR_{M7.5,1atm}$, I_c, z_{top}, $L_{D,l}$	-2.3816, 0.0369, -1.6528, -2.2449, 1.0197	-7.5292, 0.0326, 0.9972	0.1147, 2.6271	0.4821
$CSR_{M7.5,1atm}$, I_c, $L_{D,l}$, σ_v'	-1.9096, 0.0308, -1.3145, 1.1663, -1.4064	-7.5305, 0.0319, 1.0231	0.1144, 2.6312	0.4921
$CSR_{M7.5,1atm}$, $C_{R,l}$, $L_{D,l}$, σ_v'	-1.6714, 0.043, -0.8765, 1.2254, -1.1205	-7.4869, 0.03, 1.029	0.1106, 2.5646	0.4981
$CSR_{M7.5,1atm}$, I_c, $C_{R,l}$, $L_{D,l}$	-2.1604, 0.1102, -1.0864, -2.6979, 0.7595	-7.4149, 0.0325, 1.0184	0.1129, 2.6323	0.5007
q_{c1N}, $CSR_{M7.5,1atm}$, I_c, z_{top}	-2.4281, -0.8623, 0.0664, -2.8546, -1.8899	-7.253, 0.0315, 0.9311	0.1151, 2.6217	0.5062
q_{c1N}, $CSR_{M7.5,1atm}$, I_c, z_{top}, $C_{R,l}$	-2.4258, -0.8583, 0.0674, -2.834, -1.8717, -0.0398	-7.2538, 0.0315, 0.9328	0.115, 2.6214	0.5062

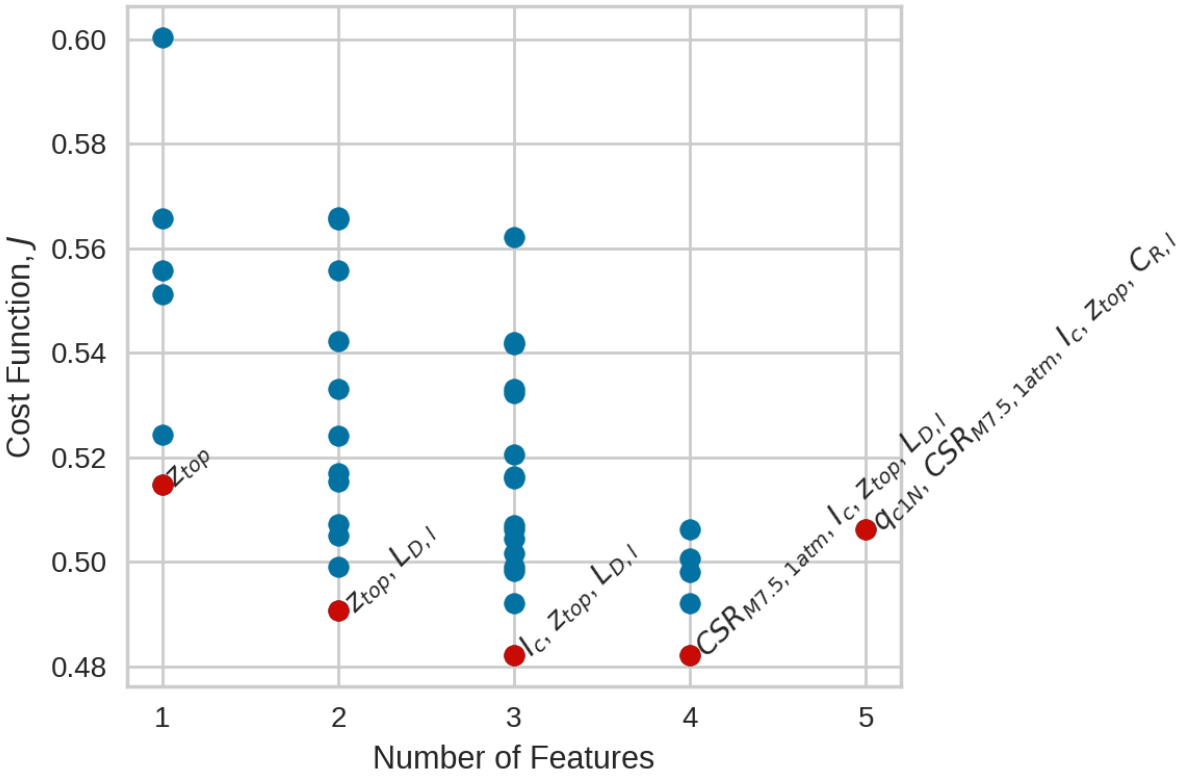

Figure 6-15. Cost (J) of accepted P[M_P] models with MAP estimated coefficients compared with number of features in the $PF_{M|T}$ function. The lowest J model for each number of feature group is highlighted red and the feature(s) in that model's $PF_{M|T}$ function is printed next to it.

The best performing $PF_{M|T}$ model with a single independent variable used z_{top} (the model presented in Sections 6.3.1-6.3.3). The z_{top} parameter also appears in each of the top performing multi-variable models. Based on these results, z_{top} is considered to be the single most important layer parameter for analysis of profile manifestation given triggering. The $L_{D,l}$ parameter also frequently appears in top performing models, indicating it is a useful predictor. However, it incorporates FS_L in its calculation and so requires use of a prior liquefaction model for *CRR*. This complicates the analyses because triggering is incorporated into multiple analysis phases, which may introduce

correlation issues (if the same triggering model is used in $PF_{M|T}$ and $PF_{T|S}$) or incompatibility issues (if different triggering models are used in $PF_{M|T}$ and $PF_{T|S}$). For this reason, $L_{D,I}$-conditioned models were not selected. Ultimately, the two parameter model that includes z_{top} and I_c was selected as the recommended model. Models with three parameters did not significantly reduce the cost function relative to the selected two parameter model.

6.3.5 Recommended P[*M*] Model

The recommended model is Equation 6.5 with t_c=2m and the $PF_{M|T}$, $PF_{T|S}$, and PF_S, functions presented in Equations 6.8 through 6.14 and visualized in Figure 6-16 through Figure 6-20. This model combines z_{top} and I_c in the manifestation given triggering model. The reasoning behind including I_c is that it serves as a proxy of hydraulic conductivity and erodibility of a layer. A soil with low hydraulic conductivity could generate large excess water pressures but not be able to expel water quickly enough to contribute to surface manifestation. This is reflected in Figure 6-17 by reductions of $PF_{M|T}$ as I_c increases, with probability factors approaching zero for $I_c > \sim 2.5$. Similarly, Figure 6-14 shows how fixed values of $PF_{M|T}$ (0.16, 0.5, 0.84) vary with z_{top} and I_c, illustrating the decay of manifestation likelihood as depth increases or I_c increase. This model produces J=0.508, which is notably reduced from the 0.515 value for the single parameter model (Section 6.3.3).

By including I_c in the $PF_{M|T}$ function with a very weak prior, the model recovers a strong dependence on I_c in the manifestation component (Figure 6-16 and Figure 6-17) and the susceptibility posterior is very similar to the prior (Figure 6-20). This is in contrast to the results

in Section 6.3.3 when I_c was not considered in the manifestation model; by allowing I_c to affect manifestation, adjustments of the susceptibility prior are no longer produced. As shown in Figure 6-18, the triggering model posterior shifts up modestly relative to the prior for this model, which is in contrast to no change (Section 6.3.3) or a downward shift (Section 6.3.2). The upward shift with the present model makes the most physical sense, due to the unaccounted for effects of sample disturbance in the prior, which would be expected to increase resistance for a given D_R. However, also it is worthwhile to acknowledge that the improvement in fit produced by these shifts in the triggering model is small. The $PF_{T|S}$ model is visualized with continuous plots against z_{top} for bands of I_c in Figure 6-19.

Because this is the recommended model, I provide not only MAP estimates of coefficients, but I also sample parameter distributions with four Markov chains (Section 4.4.3), each composing of 1000 samples. Recommended coefficients are taken as the mean across the four sampling chains. The distributions of the posterior coefficients are shown in Figure 6-21.

$$PF_{M|T} = \frac{1}{1 + \exp\left(-\left(8.206 - 0.342 \cdot z_{top} - 3.461 \cdot I_c\right)\right)} \tag{6.8}$$

$$PF_{T|S} = \frac{1}{1 + \exp\left(\frac{-1.702 \cdot \left(\widehat{CSR} - \widehat{CRR}\right)}{0.985}\right)} \tag{6.9}$$

$$\widehat{CSR} = \frac{\left({CSR_{M7.5,1atm}}^{-0.6566} - 1\right)}{-0.6566} \tag{6.10}$$

$$\widehat{CRR} = -7.427 + 0.0338 \cdot \widehat{D_R} \tag{6.11}$$

$$\widehat{D_R} = \frac{\left({D_R}^{1.2022} - 1\right)}{1.2022} \tag{6.12}$$

$$D_R(\%) = 47.8 \cdot {q_{c1Ncs}}^{0.264} - 106.3 \tag{6.13}$$

$$PF_S = 1 - \frac{1}{1 + \exp\left(\frac{-1.702 \cdot \left({I_c}/{2.614} - 1\right)}{0.116}\right)} \tag{6.14}$$

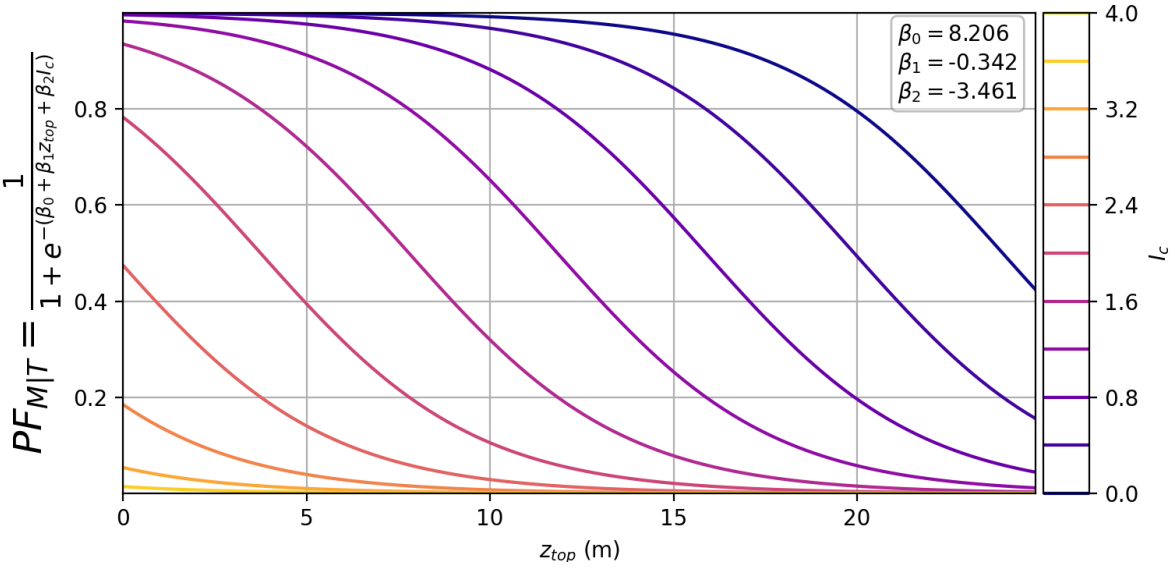

Figure 6-16. $PF_{M|T}$ function conditioned on z_{top} and I_c based on MAP estimates of model coefficients in which $PF_{T|S}$ and PF_S were also updated.

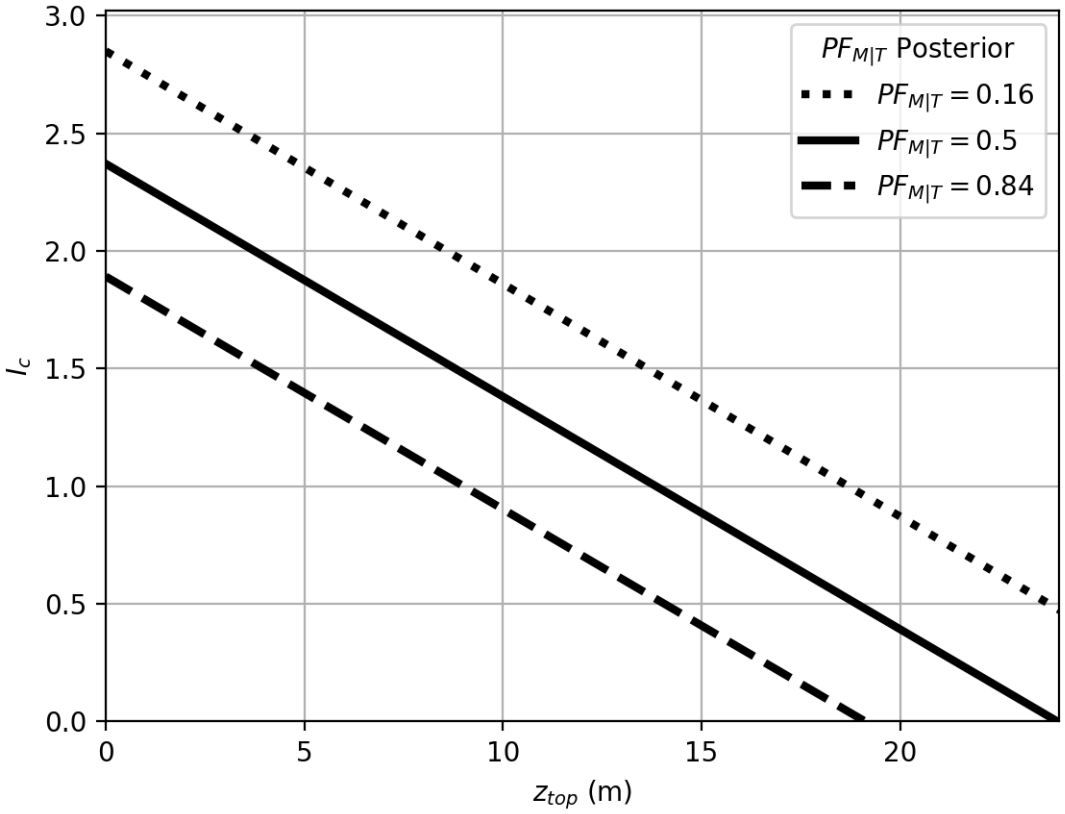

Figure 6-17. Values of z_{top} and I_c that produce probability factors of 0.16, 0.5, and 0.84. As z_{top} increases and I_c increases, the probability of manifestation given triggering decreases.

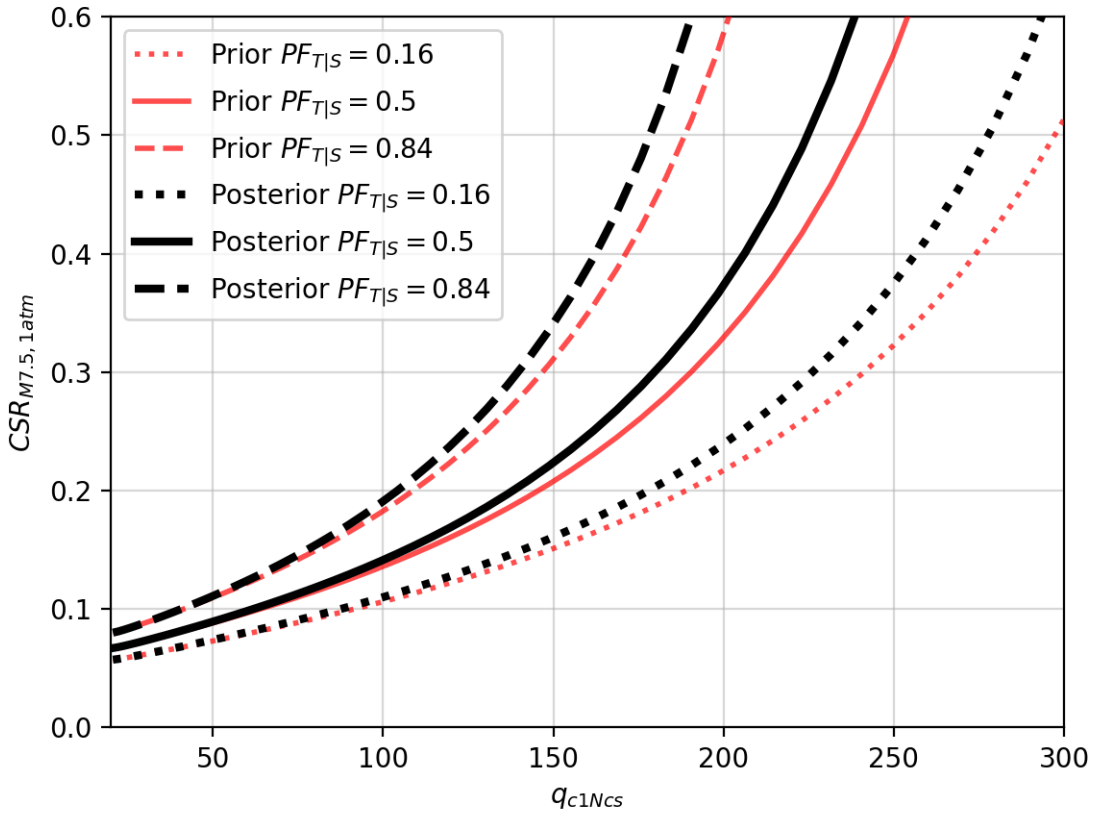

Figure 6-18. Recommended $PF_{T|S}$ function conditioned on q_{c1Ncs} based on MAP estimates of model coefficients. The PF_S priors were also adjusted.

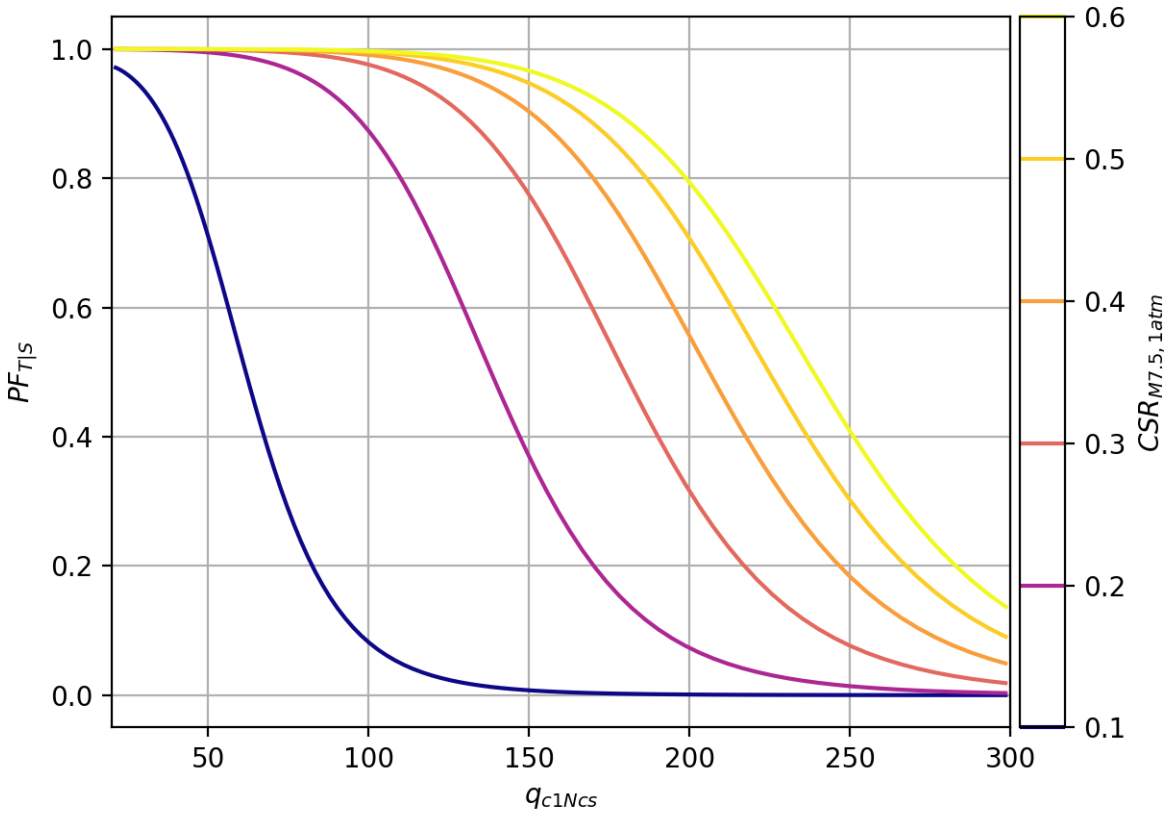

Figure 6-19. $PF_{T|S}$ values for the recommended P[M_P] model for varying q_{c1Ncs} and $CSR_{M7.5,1atm}$ values.

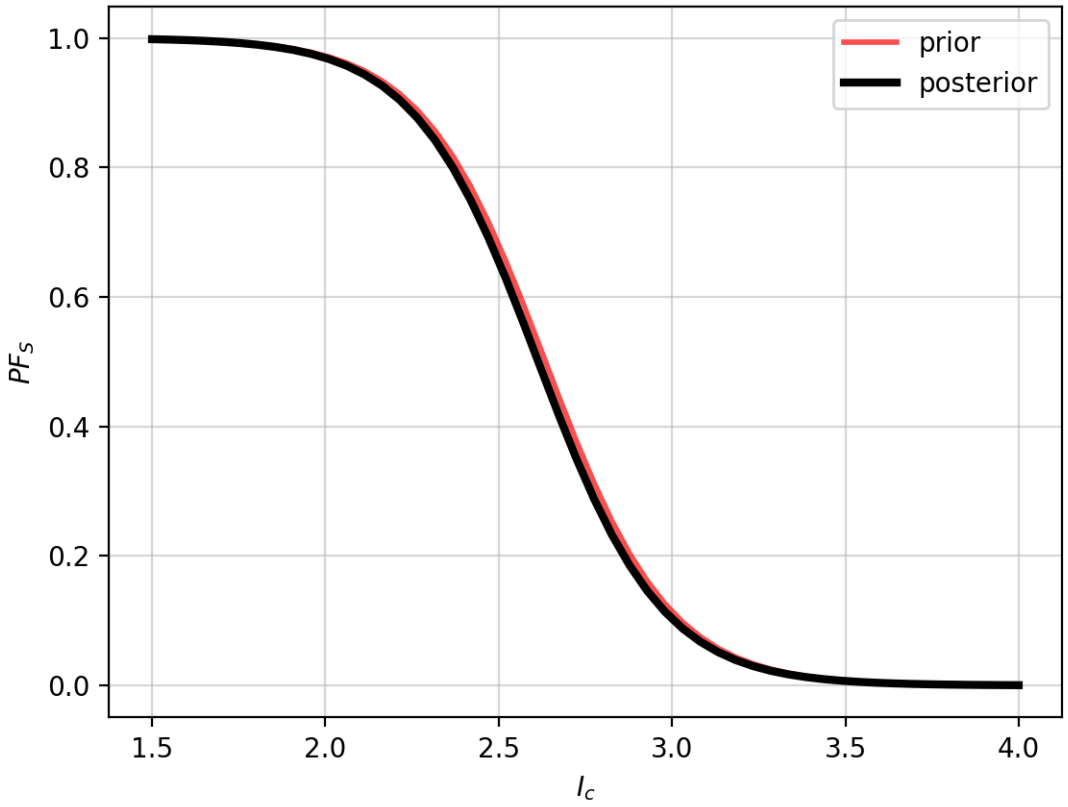

Figure 6-20. PF_S function from recommended model conditioned on I_c based on MAP estimates of model coefficients.

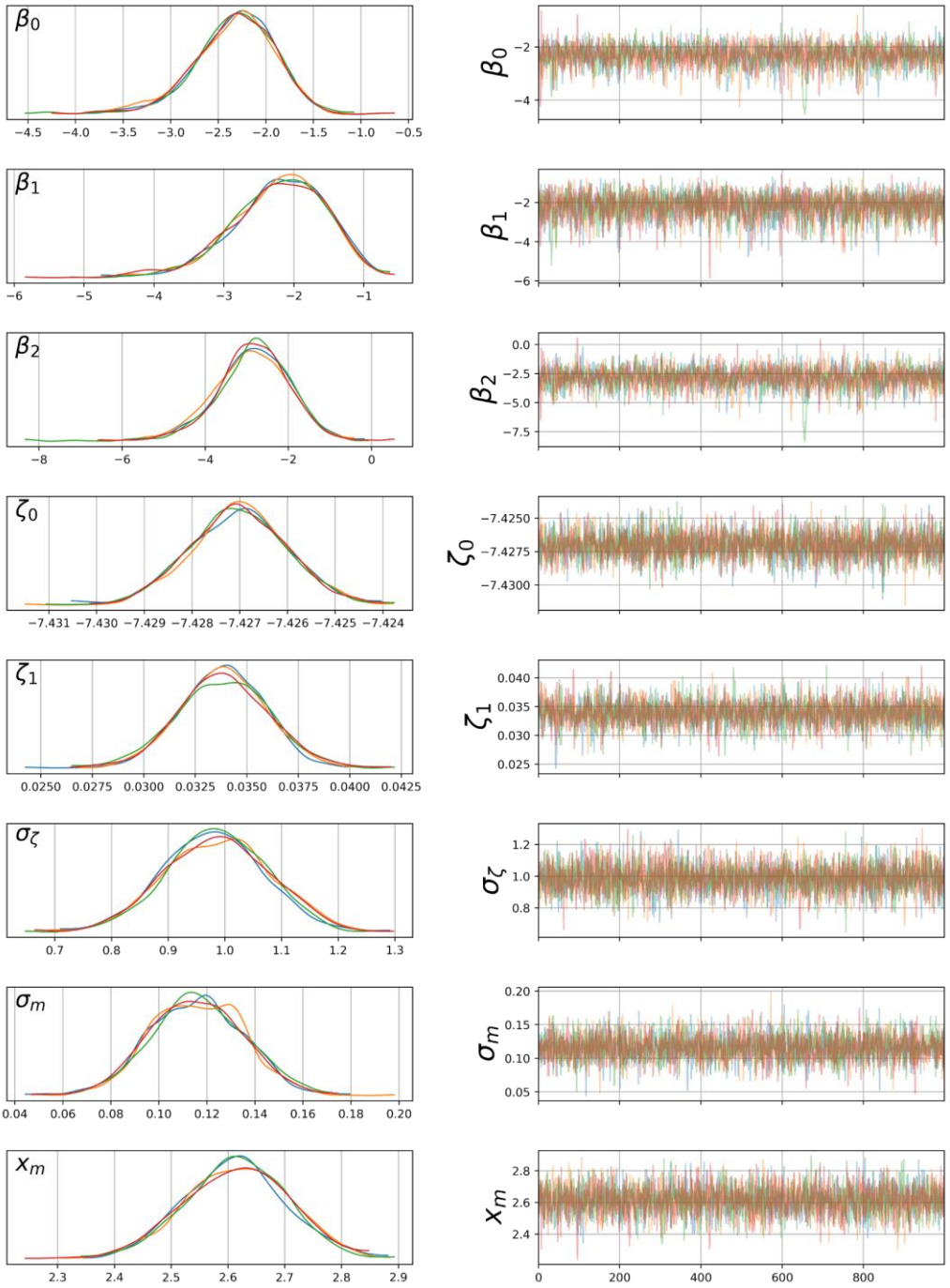

Figure 6-21. Posterior distributions of the coefficients updated with Bayesian for the recommended P[*M*] model. The first three coefficients are for $PF_{M|T}$, the next three are for $PF_{T|S}$, and the final two are for PF_S. Note the $PF_{M|T}$ coefficients are in normalized I_c-z_{top} space and therefore do not match the unnormalized coefficients in Equation 6.8.

6.3.6 Discussion

The manifestation model presented in Section 6.3.5 operates on an entire profile rather than a critical layer, which is a significant break from past practice in liquefaction model development. As noted in Chapter 3, while legacy models are generally considered to predict triggering, because they are based on case histories of surface manifestation (or lack thereof), the manifestation effects considered in this chapter must affect those models to some extent. For this reason, I compare here the predicted probabilities of profile manifestation with predictions from a legacy triggering model.

There are several metrics in statistics for quantifying the predictive accuracy of a model. The recommended model produces a probability of observable surface manifestation of liquefaction, but the physical outcome is always a binary outcome: no manifestation (y_{obs}=0) or manifestation (y_{obs}=1). The P[M_P] value can be categorized as either a yes (y_{pred}=1) or no (y_{pred}=0) prediction if it is above or below a threshold probability. An obvious threshold probability to use would be 0.5, and a confusion matrix using that threshold with the dataset that the model was trained on is presented in Figure 6-22. A confusion matrix shows the proportion of correctly and incorrectly predicted "yes" and "no" cases for binary outcomes; there are four categories: true positives (TP) are correctly predicted "yes" cases, false positives (FP) are incorrectly predicted "no" cases, true negatives (TN) are correctly predicted "no" cases, and false negatives (FN) are incorrectly predicted "yes" cases. The percentages shown are the true positive rate(TPR=TP/(TP+FN)), false positive rate (FPR=FP/(FP+TN)), false negative rate (FNR=FN/(TP+FN)), and true negative rate (TNR=TN/(FP+TN)) Both the TP and TN categories have more cases than their FN and FP

counterparts, indicated by the TPR and TNR percentages higher than 50%. If the model were random, the TPR, TNR, FPR, and FNR values would each be approximately 50% and if the model was able to perfectly predict the outcome for every case, then it would show TPR = TNR = 100% and FPR = FNR = 0%. Figure 6-22 also presents several statistical metrics and their definitions including accuracy, precision, recall, and F1 score.

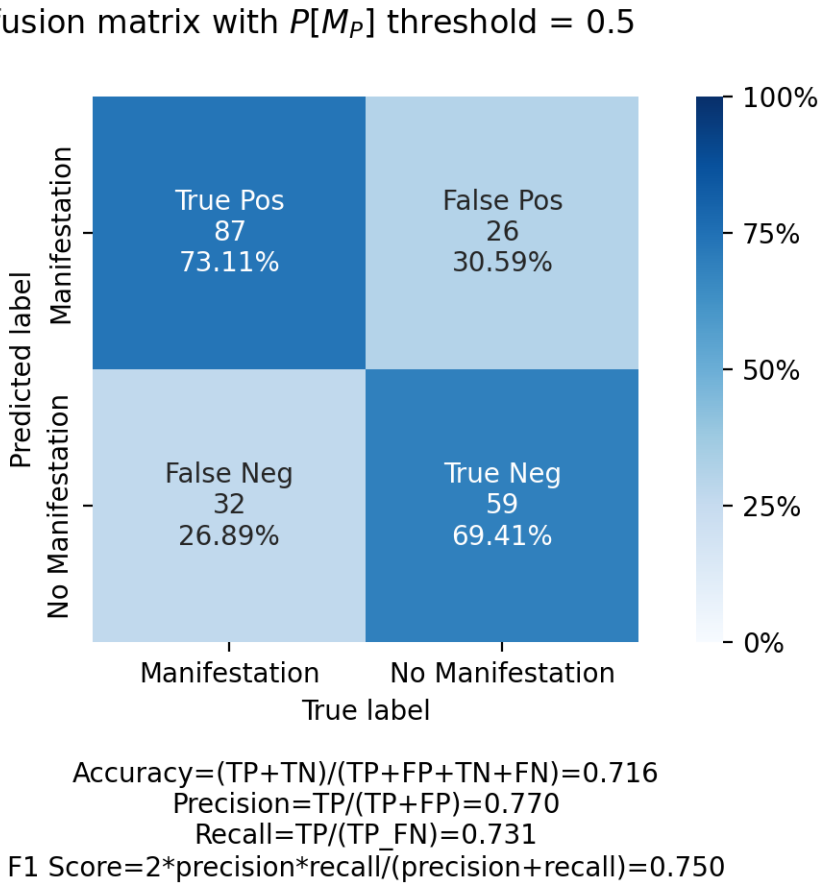

Figure 6-22. Confusion matrix using a P[M_P] threshold = 0.5 for model training dataset.

Instead of looking at predictions based on one P[M_P] threshold, the probability threshold for assigning manifestation to a site can be varied from 0 to 1 and the TPR and FPR calculated for each probability threshold to create a receiver operating characteristic (ROC) curve as shown in Figure 6-23. As the threshold increases from 0 to 1, the TPR and FPR decrease from 100% to 0% and there is a threshold that balances the two values relative to each other called the optimum operating point (OOP), defined as the point that minimizes FPR + (1 – TPR) (Figure 6-24). For this dataset, the OOP=0.51, and the confusion matrix using the OOP as the P[M_P] threshold is displayed in Figure 6-25. The slight change from 0.5 to 0.51 in the threshold changes one TP to a FN and three FPs to TNs, meaning that there were a total of 4 case histories with P[M_P] between 0.5 and 0.51.

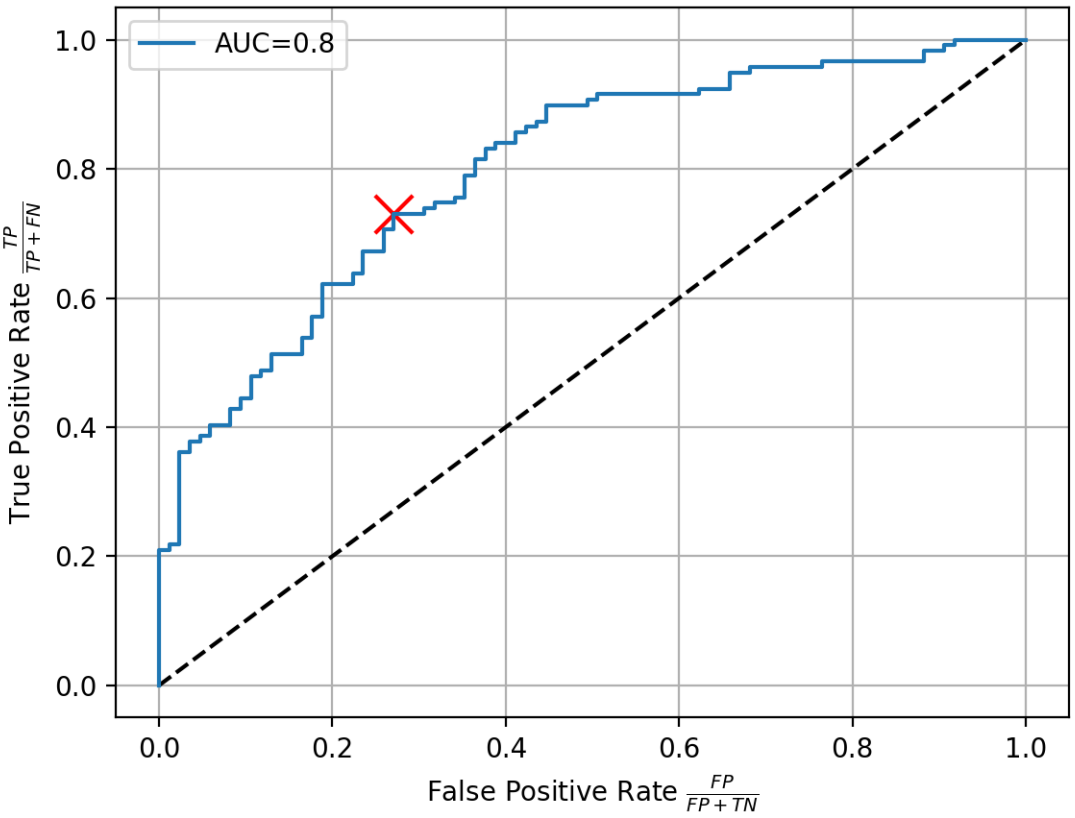

Figure 6-23. Receiver operating characteristic (ROC) curve for the model training dataset. The optimum operating point (OOP) is shown as the red “x”, and the area under the curve (AUC) is printed in the legend.

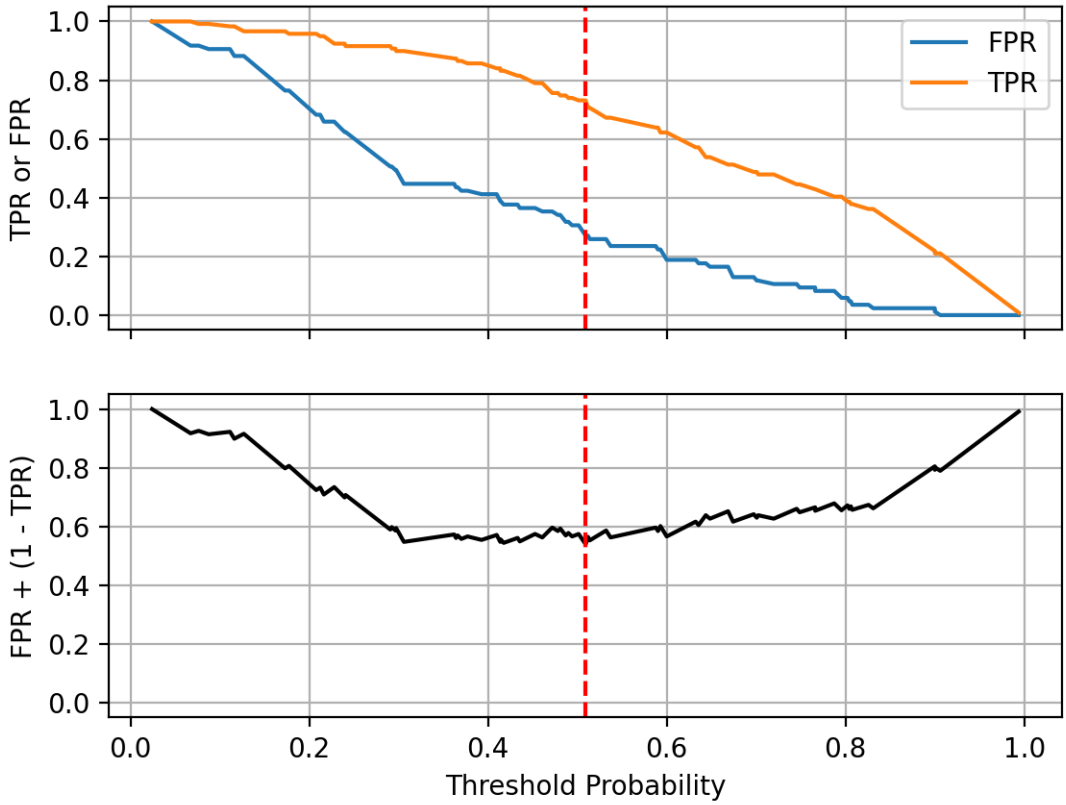

Figure 6-24. Trend of TPR and FPR with threshold probabilities and identification of the optimum operating point (OOP).

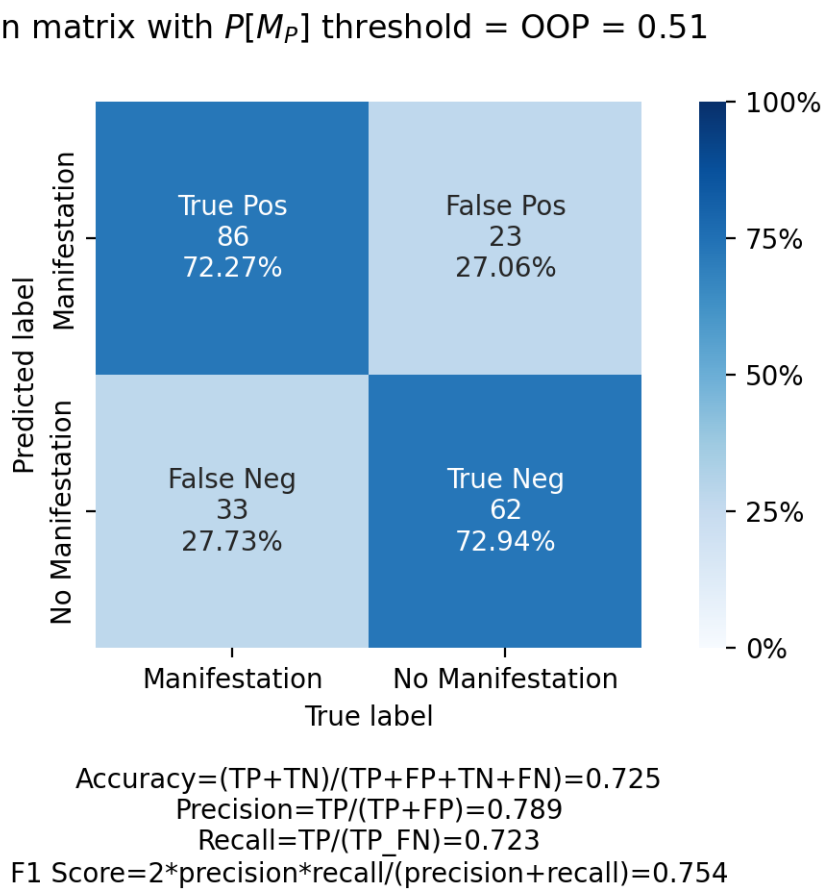

Figure 6-25. Confusion matrix using a P[M_P] threshold = OOP = 0.51 for model training dataset.

A model is expected to perform well on the dataset it is trained on, therefore it is useful to see how the model applies to a test dataset that is independent of the training dataset. A dataset of CPTs and surface manifestation of liquefaction observations from the Canterbury earthquake sequences was published in DesignSafe (Geyin et al. 2020b). All the CPTs with length greater than 15m were obtained from this dataset and used with the recommended model to predict P[M_P]. The resulting ROC curve and confusion matrix are presented in Figure 6-26 and Figure 6-27. All the statistical metrics for the Canterbury liquefaction dataset are very similar to the model training dataset even

though it is a much larger number of case histories exemplifying that the model is not overfit to the training dataset.

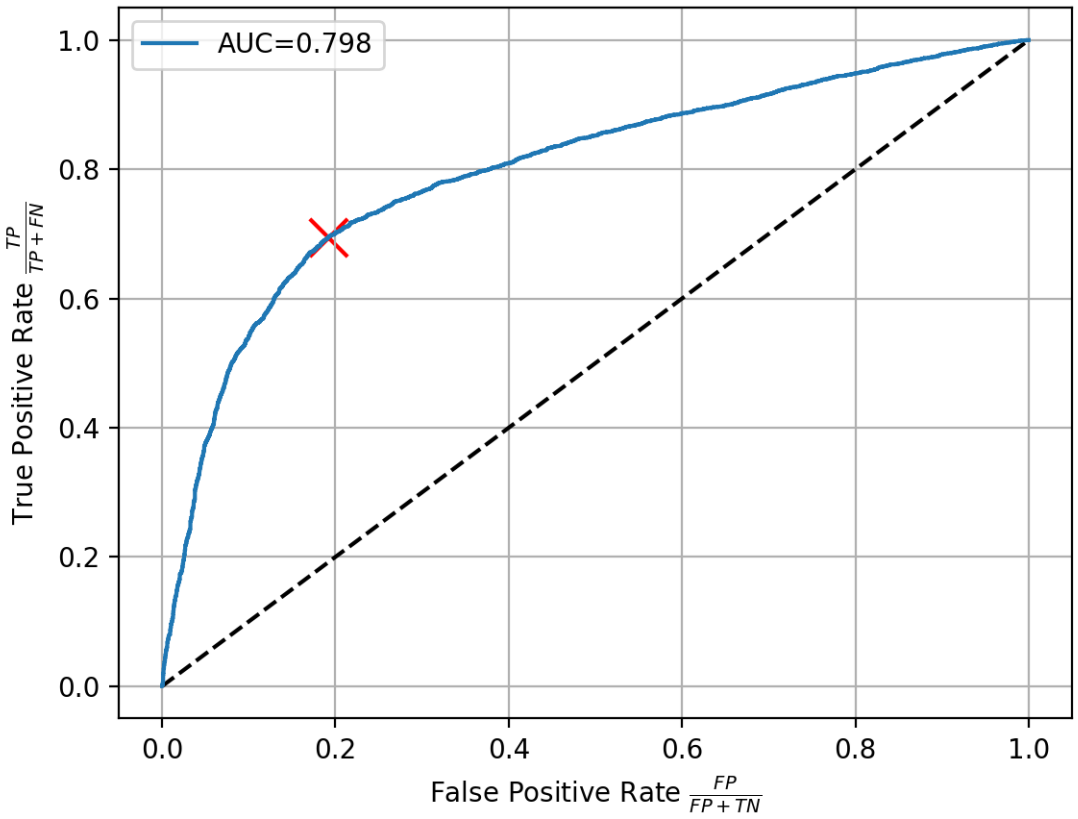

Figure 6-26. Receiver operating characteristic (ROC) curve for the Canterbury liquefaction dataset. The optimum operating point (OOP) is shown as the red "x", and the area under the curve (AUC) is printed in the legend.

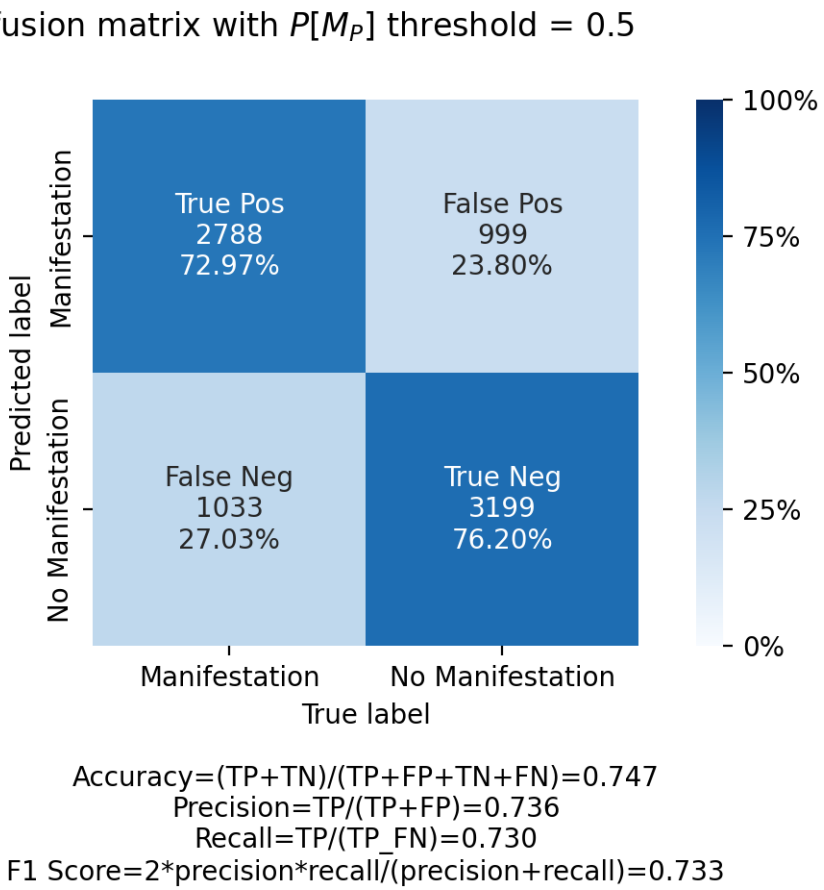

Figure 6-27. Confusion matrix using a P[M_P] threshold = 0.5 for the Canterbury liquefaction dataset.

6.4 Sensitivity Analyses

The proposed P[M_P] model is conditioned on several variables and was derived using prior models for susceptibility and triggering. In this section, sensitivity analyses were performed to demonstrate variations of predicted outcomes from the recommended model from changes of input parameters (Section 6.4.1). Suites of alternative models are also derived using different

susceptibility and triggering priors, to investigate the relative impacts of the Bayesian inference of the data vs. the prior formulation on the characteristics of the posterior (Sections 6.4.2-6.4.3).

6.4.1 Sensitivity to Recommended Model Parameters

To compare the proposed P[M_P] model to legacy models and understand its sensitivity to model parameters, a reference *CSR*, CSR_{ref}, was computed for a target P[M_L], reference depth (z_{top}), reference I_c, and reference t value for a given q_{c1Ncs}. The computed value of P[M_L] was taken as equivalent to the profile manifestation P[M_P], which can be visualized as a profile composed entirely of non-susceptible material (PF_S = 0) except for a single layer with properties defined by the reference conditions (Figure 6-28). The reference properties of the soil can be adjusted to examine the effects on P[M_P] with changing layer conditions.

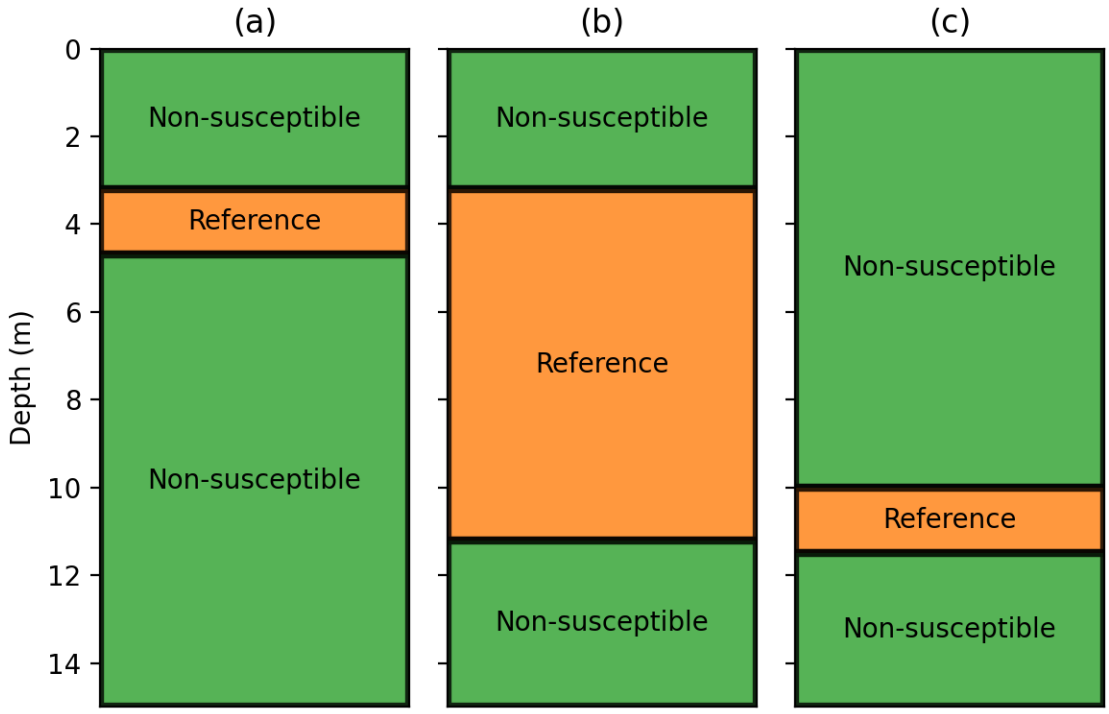

Figure 6-28. Example of profiles with different reference layer geometries that are used to evaluate P[M_P] sensitivity to model parameters: z_{top}, t, I_c. (a) is a relatively shallow and thin layer, (b) is a relatively shallow and thick layer, and (c) is a relatively deep and thin layer.

For a reference condition with a shallow depth, low I_c, and P[M_P]=0.16 or 0.5, CSR_{ref} was computed for a range of q_{c1Ncs} values and shown relative to the $PF_{T|S}$=0.16 and 0.5 curves in Figure 6-29. The CSR_{ref} curve is located above and to the left of the triggering curve, meaning that for a given tip resistance a higher *CSR* is needed for manifestation than for triggering. The difference is modest at low penetration resistances but significant for stiffer soils.

Figure 6-30 to Figure 6-32 show sensitivities of $CSR_{ref} - q_{c1Ncs}$ curves to variations in z_{top}, I_c, and t, respectively. These plots were prepared for a relatively low probability level of P[M_L]=0.16. The rationale for selecting this low probability is because individual layer P[M_L] values are often low

even for sites with high P[M_P] values, due to multiple layers contributing to P[M_P]. As shown in Figure 6-28, as z_{top} increases higher *CSR* values are required for a given q_{c1Ncs} to produce P[M_P] = 0.16, increasing the upward shift relative to the triggering curve. Similarly, as I_c increases, higher *CSR* values are required to produce P[M_P]=0.16 (Figure 6-31). For the case of variable layer thicknesses (Figure 6-32), higher *CSRs* are required for relatively thin layers ($t < t_c$) and lower *CSRs* are required for thick layers ($t > t_c$).

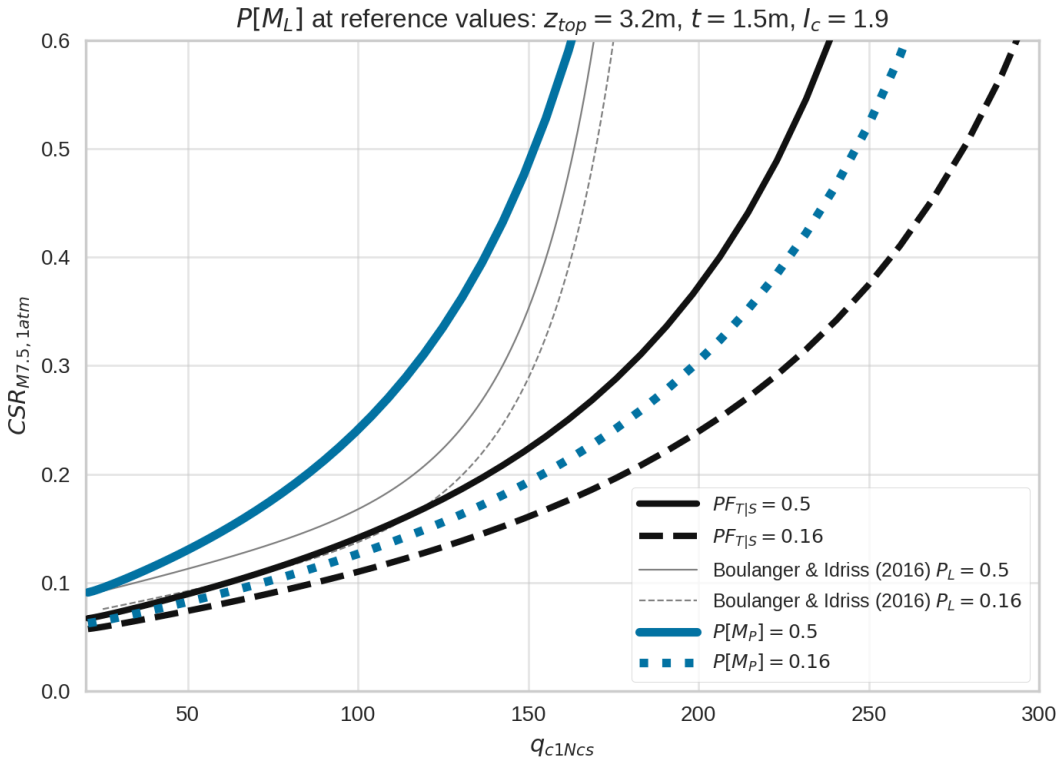

Figure 6-29. Median and 16% $PF_{T|S}$, P_L (Boulanger and Idriss 2016), and P[M_P] from the recommended model presented in this section using reference conditions for z_{top}, t, and I_c obtained as the median z_{top}, t, and I_c from critical layers selected for the Boulanger and Idriss (2016) dataset.

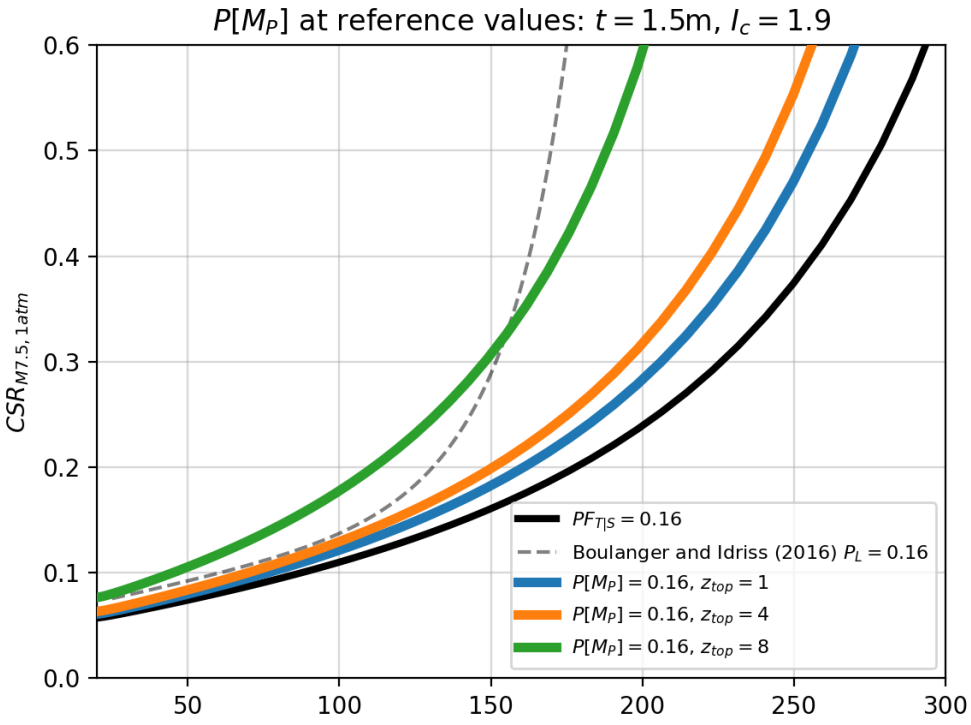

Figure 6-30. Reference condition P[M_P] = 0.16 curve with varying z_{top} values relative to the $PF_{T|S}$ = 0.16 curve.

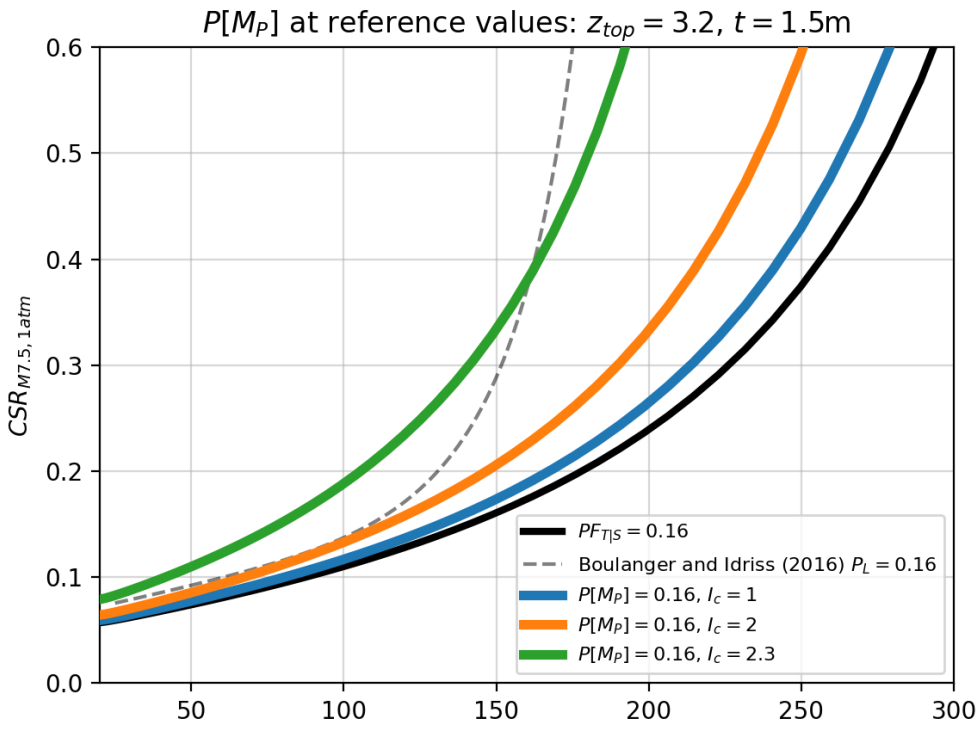

Figure 6-31. Reference condition P[M_P] = 0.16 curve with varying I_c values relative to the $PF_{T|S}$ = 0.16 curve.

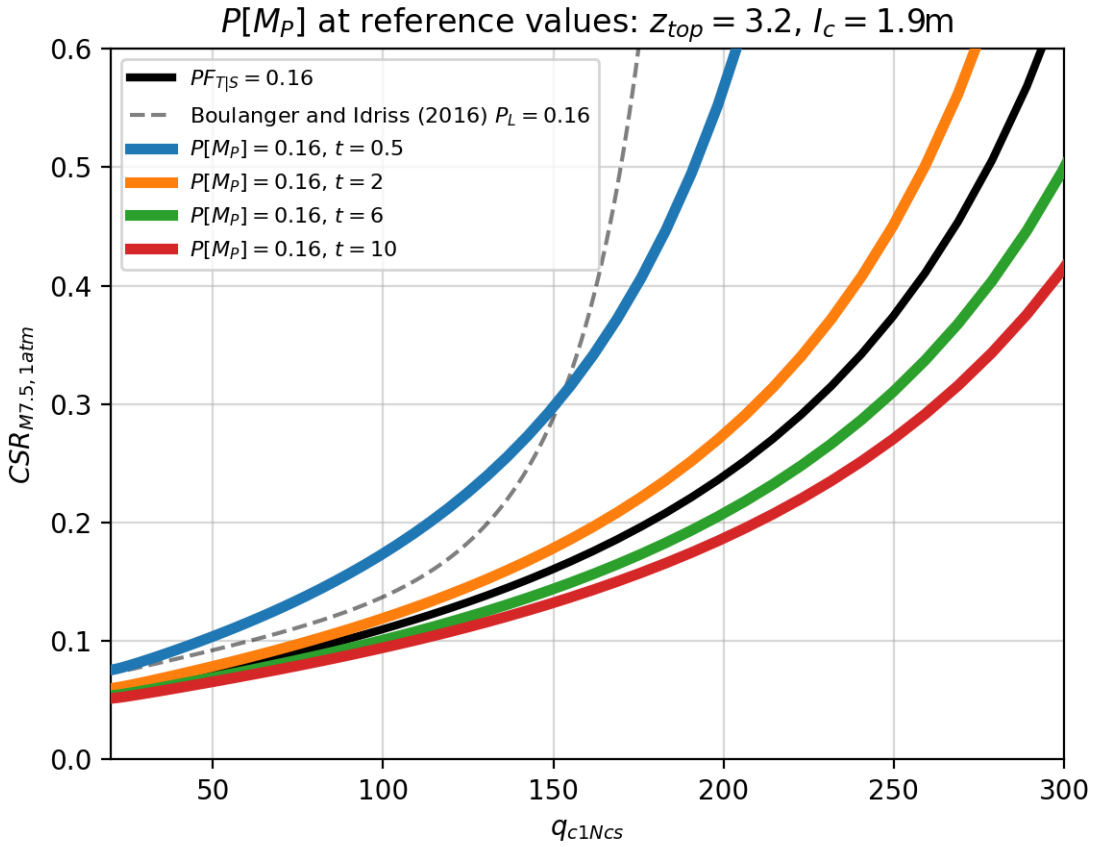

Figure 6-32. Reference condition P[M_P] = 0.16 curve with varying t values relative to the $PF_{T|S}$ = 0.16 curve.

6.4.2 Sensitivity to PF_S priors

In this section, the sensitivity of the P[M_P] model to susceptibility priors is tested. This sensitivity was investigated in two ways: (1) changes to the mean model, (2) changes to the uncertainty level on the mean model coefficients for the original prior (i.e., the prior presented in Section 6.1).

The first evaluation considered each of the four published susceptibility models and the combined model discussed in Section 6.1. The four susceptibility model coefficients were used as the PF_S

prior in the Bayesian inference. The resulting posteriors are presented in Figure 6-33. Figure 6-33 (a) shows that the higher the PF_S relationship, the flatter the trend of the $PF_{M|T}$ lines in I_c-z_{top} space. While the manifestation model is affected, Figure 6-33 (b) shows that the susceptibility posteriors are not significantly modified from the prior. This occurs because the susceptibility prior is given relatively strong confidence (the standard deviations used in the normal distributions for the two PF_S coefficients, x_m and σ_m, are relatively small). The cost function, J, using these four priors were very similar (between 0.506 and 0.508).

The second evaluation modified the confidence levels placed on the PF_S coefficients for the original model (from Section 6.1). The standard deviations on the PF_S coefficients' normal distributions (σ) were increased by factors of 2 and 4. The resulting $PF_{M|T}$ posteriors are presented in Figure 6-34. By increasing the coefficient standard deviations, Bayesian inference has greater freedom to update the posteriors, and the PF_S function shifts to the left such that a soil is less susceptible for a given I_c. However, the $PF_{M|T}$ coefficient on I_c moves in the opposite direction, eventually producing a model that shows increasing manifestation potential for increasing I_c, which is clearly non-physical. While J decreases to 0.491 for the P[M_P] model with a factor of 4 on the PF_S coefficients' normal distributions, because the $PF_{M|T}$ model has a counter-intuitive trend a strong prior for the PF_S function was retained.

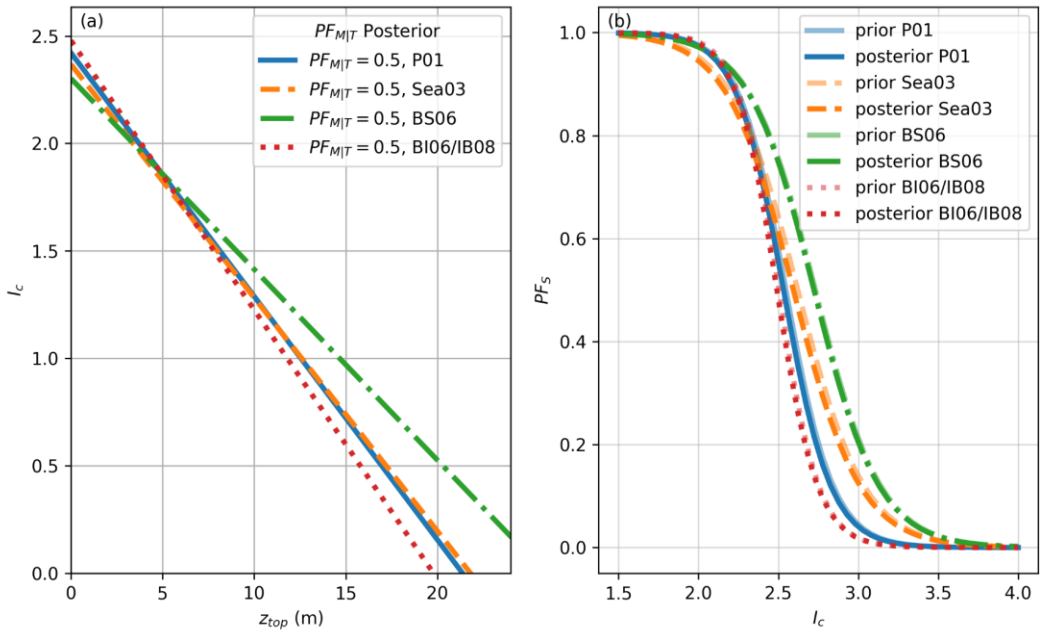

Figure 6-33. Impact of changing initial PF_S model on final P[M] model using the four models recommended in Maurer et al.(2017): P01 (Polito 2001), Sea03 (Seed et al. 2003), BS06 (Bray and Sancio 2006), and BI06/IB08 (Boulanger and Idriss 2006; Idriss and Boulanger 2008). The $PF_{M|T}$ function in (a) shows that the manifestation portion of the model that includes I_c changes to accommodate the change in susceptibility functions. The change in the $PF_{M|T}$ function allow the strongly informed prior PF_S (b) to remain almost unchanged in the posterior.

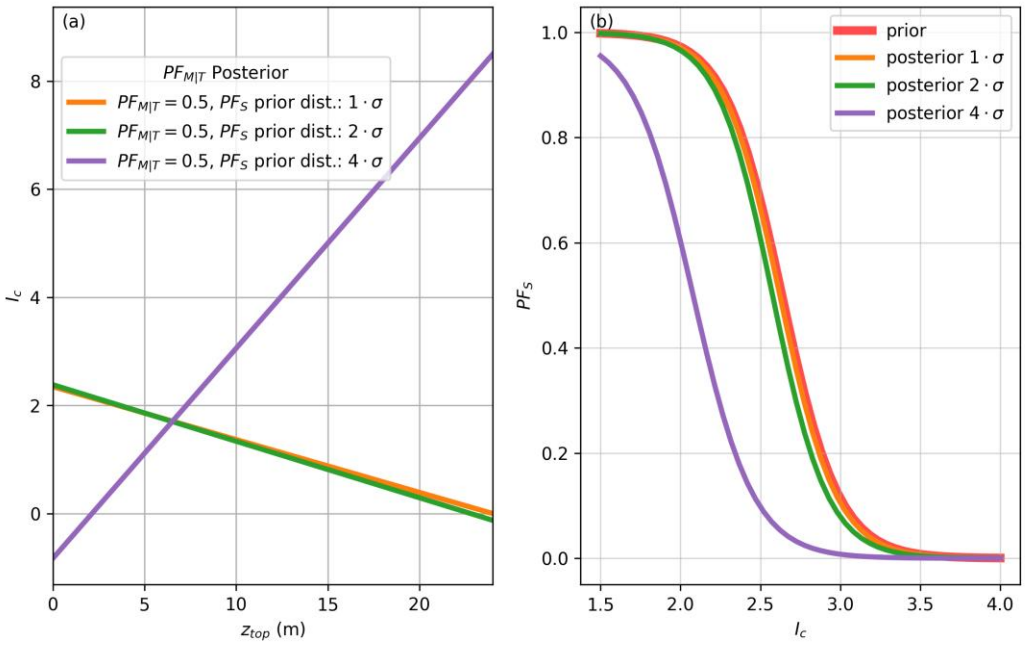

Figure 6-34. Impact of changing the confidence in the original PF_S prior on resulting P[M] model. The $PF_{M|T}$ function in (a) shows that the manifestation portion of the model that includes I_c changes to accommodate the change in PF_S functions posteriors (b).

6.4.3 Sensitivity to $PF_{T|S}$ priors

In this section, the sensitivity of the P[M_P] model to variations in the triggering priors is tested. This was done by considering alternate means and standard deviations for the $PF_{T|S}$ priors' distributions. The effects of these variations on the $PF_{M|T}$ and $PF_{T|S}$ posteriors were evaluated.

First, alternate prior mean values (μ) were considered by increasing or decreasing the mean of each coefficient's prior by five times the standard deviation of that coefficient's distribution and by applying a weak confidence (100 times the standard deviations in the covariance matrix). This produces the prior $PF_{T|S}$ functions plotted in Figure 6-35. Second, different levels of confidence

are explored by changing the multiplier on the standard deviations in the covariance matrix. In the first case where only the mean priors are changed, Figure 6-35 shows that the posterior does not noticeably move relative to the prior. In the second case where the standard deviations are increased, despite the posterior having more freedom to move, the posteriors all converge to curves similar to the priors (Figure 6-36).

The $PF_{M|T}$ and $PF_{T|S}$ posteriors all converge on similar values irrespective of the prior μ so long as they are given enough uncertainty on the standard deviations to find the lowest cost model. The insensitivity of the posterior distributions to changes in the mean and uncertainty of the prior indicates that the approach used in Section 6.3 is appropriate for finding a stable $PF_{T|S}$ posterior.

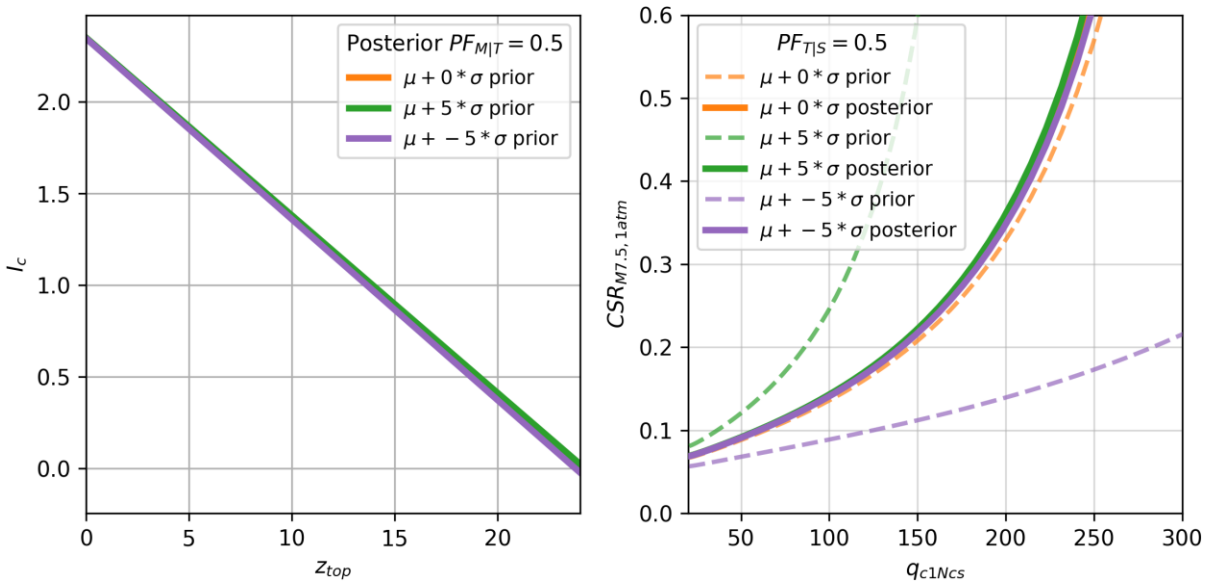

Figure 6-35. Impact of changing the $PF_{T|S}$ prior means on $PF_{M|T}$ and $PF_{T|S}$ posteriors. The posteriors converge on approximately the same values when given a sufficiently large uncertainty on the priors.

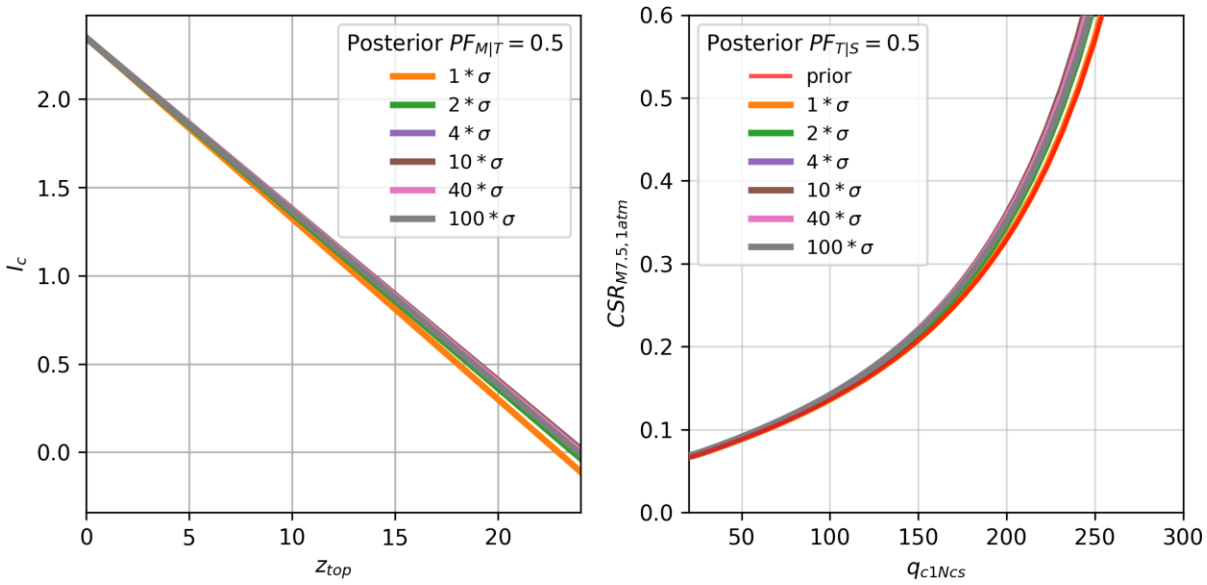

Figure 6-36. Impact of changing the $PF_{T|S}$ prior standard deviations on $PF_{M|T}$ and $PF_{T|S}$ posteriors. The posteriors converge on approximately the same values uncertainty on the priors is increased by a factor of 2 or higher.

7 Example Applications of Proposed Model

This chapter provides two example applications of the P[M_P] model. The first example is Wufeng Site A, which was previously presented in Section 3.5.1 and had no surface manifestation despite very strong shaking during the 1999 Chi Chi Taiwan earthquake. The second example is the Mihama-ward site in Chiba, Japan (Section 2.3.1), which had variable ground performance including major sand boiling and no ground failure during the 2011 **M**9.0 Tohoku earthquake.

7.1 Wufeng Site A Analysis

The four CPT profiles previously shown to have false positive predictions using legacy models (critical layers above the probability of liquefaction = 0.5 curve) in Section 3.5.1 (Figure 3-22) are reexamined. These analyses began at the stage where the raw CPT data had been discretized into layers (using the algorithm in Section 5.3) and converted into q_{c1Ncs} and I_c values for each layer. Another critical step is the assignment of a ground surface PGA value and earthquake magnitude; for the present analysis the conditions for the event that produced the observations were used (Section 5.2), but in general forward applications these would be derived from seismic hazard analyses. In this section, the calculations will be illustrated in detail for CPT WAC-4 and then results are provided for all four CPTs.

Equation 7.1 is used to compute the probability of manifestation for each layer, P[M_L].

$$P[M_L] = 1 - \left(1 - PF_{M|T_l} PF_{T|S_l} PF_{S_l} K_{Sat_l}\right)^{t_l/t_c} \quad 7.1$$

There are four model components within Equation 7.1 ($PF_{M|T_l}, PF_{T|S_l}, PF_{S_l}$, and K_{Sat_l}) and one variable (t_l). Each model component is computed for each layer, given the respective independent variables, with the results tabulated on the right side of Table 7-1 and displayed in Figure 7-1.

Table 7-1. Example Computation of P[M_P] for Wufeng Site A WAC-4 for the first 20 layers in the profile.

Layer #	z_{top} (m)	z_{bot} (m)	t (m)	q_{c1Ncs}	I_c	$CSR_{M\ 7.5,1atm}$	PF_S	$\widehat{CSR}$	D_R (%)	$\widehat{D_R}$	$\widehat{CRR}$	$PF_{T\|S}$	PF_T	$PF_{M\|T}$	K_{Sat}	P[M_L]
1	0.05	0.5	0.45	7.7	1.96	0.26	0.98	-2.21	0.00	-0.8	-7.46	1.00	0.98	0.81	0.00	0.00
2	0.5	1.118	0.618	3.9	2.76	0.26	0.30	-2.21	0.00	-0.8	-7.46	1.00	0.30	0.18	0.00	0.00
3	1.118	1.35	0.232	3.9	2.76	0.26	0.30	-2.21	0.00	-0.8	-7.46	1.00	0.30	0.15	1.00	0.01
4	1.35	1.8	0.45	1.0	3.89	0.30	0.00	-1.86	0.00	-0.8	-7.46	1.00	0.00	0.00	1.00	0.00
5	1.8	3	1.2	5.2	2.72	0.35	0.36	-1.54	0.00	-0.8	-7.46	1.00	0.36	0.14	1.00	0.03
6	3	3.8	0.8	45.3	2.75	0.38	0.31	-1.34	24.50	38.1	-6.14	1.00	0.31	0.09	1.00	0.01
7	3.8	5.55	1.75	16.1	2.91	0.41	0.16	-1.22	0.00	-0.8	-7.46	1.00	0.16	0.04	1.00	0.01
8	5.55	5.8	0.25	108.7	2.08	0.42	0.95	-1.17	58.49	109.9	-3.71	0.99	0.94	0.29	1.00	0.04
9	5.8	6	0.2	20.8	3.06	0.42	0.08	-1.16	0.16	-0.7	-7.45	1.00	0.08	0.01	1.00	0.00
10	6	6.3	0.3	92.0	1.91	0.42	0.98	-1.15	51.43	94.1	-4.25	1.00	0.98	0.38	1.00	0.07
11	6.3	9.5	3.2	19.0	3.03	0.43	0.09	-1.12	0.00	-0.83	-7.46	1.00	0.09	0.01	1.00	0.00
12	9.5	10.4	0.9	76.9	2.37	0.43	0.80	-1.11	44.12	78.10	-4.79	1.00	0.80	0.04	1.00	0.01
13	10.4	10.65	0.25	26.0	3.09	0.44	0.06	-1.11	6.68	7.33	-7.18	1.00	0.06	0.00	1.00	0.00
14	10.65	11	0.35	101.9	2.28	0.43	0.87	-1.11	55.71	103.64	-3.92	0.99	0.86	0.03	1.00	0.01
15	11	12.1	1.1	19.1	2.99	0.43	0.11	-1.11	0.00	-0.83	-7.46	1.00	0.11	0.00	1.00	0.00
16	12.1	13	0.9	176.5	1.95	0.43	0.98	-1.12	81.01	163.04	-1.92	0.80	0.78	0.06	1.00	0.02
17	13	13.65	0.65	89.0	2.20	0.43	0.91	-1.12	50.04	90.99	-4.35	1.00	0.91	0.02	1.00	0.01
18	13.65	13.9	0.25	8.7	3.21	0.43	0.03	-1.12	0.00	-0.83	-7.46	1.00	0.03	0.00	1.00	0.00
19	13.9	14.15	0.25	91.3	2.16	0.43	0.93	-1.13	51.10	93.33	-4.27	1.00	0.92	0.02	1.00	0.00
20	14.15	14.4	0.25	13.2	3.06	0.43	0.07	-1.13	0.00	-0.83	-7.46	1.00	0.07	0.00	1.00	0.00

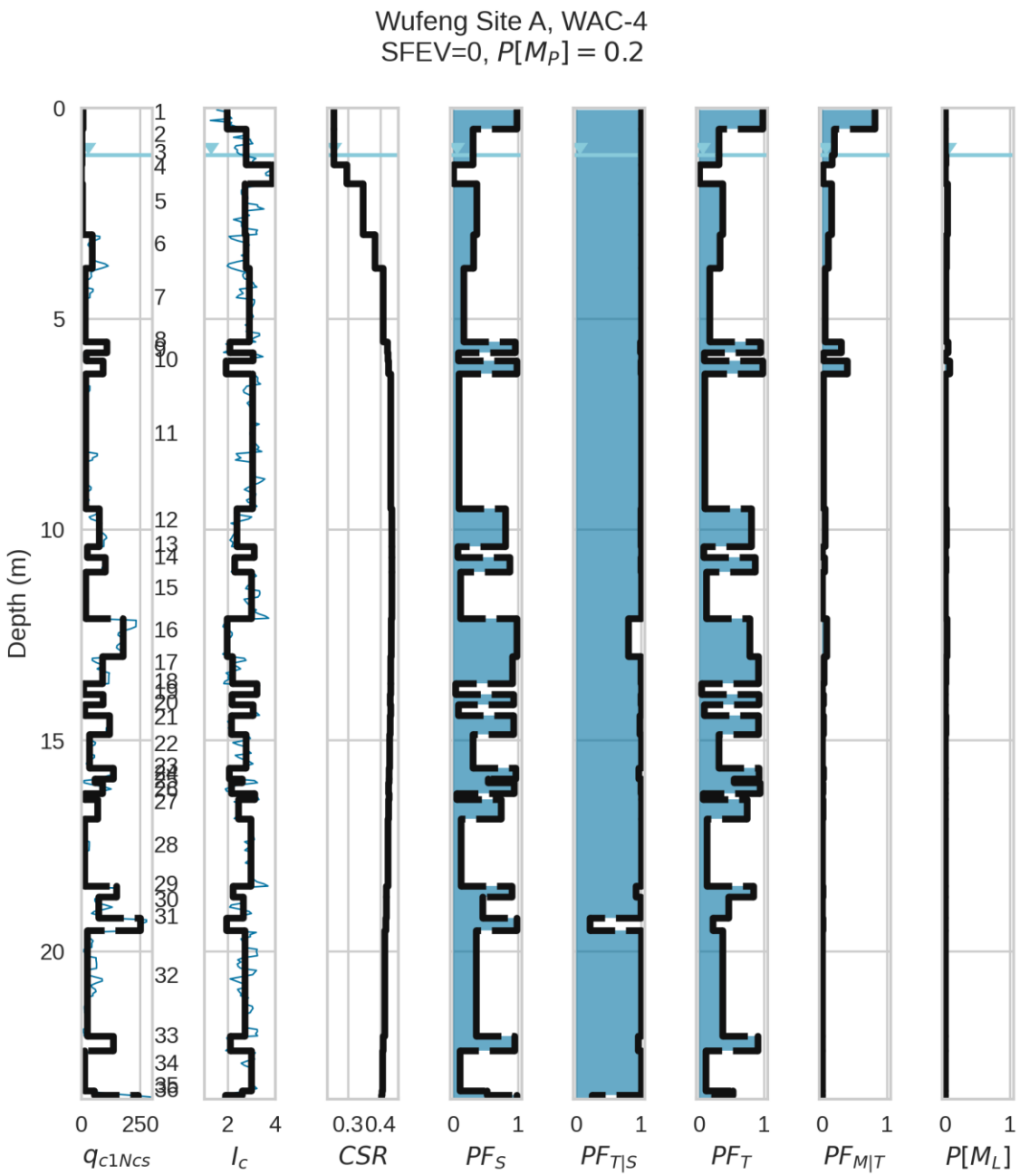

Figure 7-1. CPT "WAC-4" from Wufeng Site A with *CSR* computed using a *PGA* estimate from the 1999 Chi-Chi, Taiwan earthquake and probability factors used to compute P[M_L] for each layer. The total P[M_P] prediction is printed at the top of the figure along with the observation of manifestation (SFEV=1) or lack of manifestation (SFEV=0).

Considering first the PF_S component (probability factor for susceptibility), the independent variable is I_c (Equations 6.1, 6.14). For example, the first layer that is below the ground water table and clearly granular (Layer 8) has I_c=2.08, and produces PF_S = 0.95, indicating a highly susceptible layer,

$$PF_S = 1 - \frac{1}{1 + \exp\left(\frac{-1.702 \cdot \left({I_c}/{2.614} - 1\right)}{0.116}\right)} \qquad 7.2$$

$$= 1 - \frac{1}{1 + \exp\left(\frac{-1.702 \cdot \left({2.08}/{2.614} - 1\right)}{0.116}\right)} = 0.95$$

Next, the probability factor for triggering given susceptibility ($PF_{T|S}$) is computed. This is a function of $\widehat{CSR}$ and $\widehat{CRR}$ (Equation 6.9) and therefore requires some transformations of the CPT data. $\widehat{CSR}$ can be computed directly from $CSR_{M7.5,1atm}$ (Equation 6.10), which is demonstrated for layer 8 in Equation 7.3. Relative density (D_R) is estimated from the q_{c1Ncs} value of the layer (Equation 6.13) yielding D_R=58% in Equation 7.3 which is then converted to $\widehat{D_R}$ = 109.9 (Equation 6.12) in Equation 7.5. $\widehat{CRR}$ can then be computed (Equation 6.11) in Equation 7.6 and combined with $\widehat{CSR}$ to produce $PF_{T|S}$ = 0.99 (Equation 7.7). This indicates that layer 8, being a low tip resistance layer shaken at a high intensity, is likely to trigger.

$$\widehat{CSR} = \frac{(CSR^{-0.6566} - 1)}{-0.6566} = \frac{(0.42^{-0.6566} - 1)}{-0.6566} = -1.17 \qquad 7.3$$

$$0 < D_R < 100\% = 47.8 \cdot {q_{c1Ncs}}^{0.264} - 106.3 = 47.8 \cdot 108.7^{0.264} - 106.3 = 58\% \quad (7.4)$$

$$\widehat{D_R} = \frac{\left({D_R}^{1.2022} - 1\right)}{1.2022} = \frac{(58^{1.2022} - 1)}{1.2022} = 109.9 \quad (7.5)$$

$$\widehat{CRR} = -7.427 + 0.0338 \cdot \left(\widehat{D_R}\right) = -7.427 + 0.0338 \cdot (109.9) = -3.71 \quad (7.6)$$

$$PF_{T|S} = \frac{1}{1 + \exp\left(\frac{-1.702 \cdot \left(\widehat{CSR} - \widehat{CRR}\right)}{0.985}\right)} = \frac{1}{1 + \exp\left(\frac{-1.702 \cdot \left(-1.17 - (-3.71)\right)}{0.985}\right)} = 0.99 \quad (7.7)$$

Taking the product of PF_S and $PF_{T|S}$ gives the probability factor of triggering (PF_T), a metric that accounts for both the susceptibility and triggering potential of the layer. The PF_T for layer 8 is computed in Equation 7.8 to be 0.94.

$$PF_T = PF_{T|S} * PF_S = 0.99 * 0.95 = 0.94 \quad (7.8)$$

The probability factor for manifestation given triggering ($PF_{M|T}$) is a function of I_c and z_{top} (Equation 6.8) and is computed for layer 8 in Equation 7.9. $PF_{M|T}$ is nearly zero for layer 8, which is expected because the layer is thin and deep, being overlain by predominantly clay layers. Therefore, if liquefaction were to occur in this layer, it would be unlikely to produce surface manifestations.

$$PF_{M|T} = \frac{1}{1 + \exp\left(-\left(8.206 - 0.342 \cdot z_{top} - 3.461 \cdot I_c\right)\right)}$$
$$= \frac{1}{1 + \exp\left(-(8.206 - 0.342 \cdot 2.08 - 3.461 \cdot 5.55)\right)} = 0.29 \quad 7.9$$

Finally, the saturation term, K_{Sat}, which is taken as a binary outcome of 0 above the groundwater table and 1 below the groundwater table, is assigned to each layer (taken as 1 for layer 8). With all model components derived, the probability of manifestation for layer 8 can be computed,

$$P[M_L] = 1 - \left(1 - PF_{M|T} PF_{T|S} PF_S K_{Sat}\right)^{\frac{t}{t_c}}$$
$$= 1 - (1 - 1 * 0.29 * 0.99 * 0.94)^{\frac{0.25}{2}} = 0.04 \quad 7.10$$

This shows that layer 8 is unlikely to manifest. Looking at the different layers in Table 7-1, most have no appreciable manifestation potential. Among the different layers, layer 10 has the strongest manifestation potential (0.38), although even this result is modest, which is due mainly to its limited susceptibility potential.

The total manifestation probability for the profile, P[M_P], can now be computed as the product sum of the P[NM_L] = 1-P[M_L] values for all layers using Equation 7.11,

$$P[M_P] = 1 - \prod_{l=1}^{N_L} (1 - P[M_L]_l)^{t_l/t_c} \quad 7.11$$

This yields P[M_P] ~ 0.2 for WAC-4, indicating a low probability of manifestation, making it a "no" surface evidence prediction. This matches the observation of no manifestation for this site in

Wufeng. This prediction occurs despite there being multiple layers beneath the groundwater table that have a high probability factor for triggering, due to the features of the manifestation model. This result can be compared to the prediction of manifestation from legacy models as described in Section 3.5.1 (Figure 3-22). Notably, while the data for this site has been available since the early 2000s (Chu et al. 2004; PEER 2000b) , this site was not included in the databases used to derive legacy models.

Results similar to those for CPT WAC-4 were generated for the other CPTs at the site – WAC-5, 7, and 9. These results are plotted in Figure 7-2 through Figure 7-4. Each of these CPTs correctly predict no manifestation for the profile despite the presence of layers with high PF_T and "yes" manifestation predictions from legacy models. Table 7-2 summarizes the probability of manifestation predicted using Boulanger and Idriss (2016) for the critical layer selected on the basis of being susceptible and having the highest predicted P_L in the profile, as well as the P[M_P] predicted using the recommended model.

Table 7-2. Probability of manifestation predictions for Boulanger and Idriss (2016) and the recommended P[M_P] model compared with surface evidence of manifestations for Wufeng Site A CPTs.

CPT Number	Boulanger and Idriss (2016) P_L	P[M_P]	Surface Evidence?
4	0.99	0.20	No
5	0.99	0.41	No
7	0.99	0.17	No
9	0.99	0.21	No

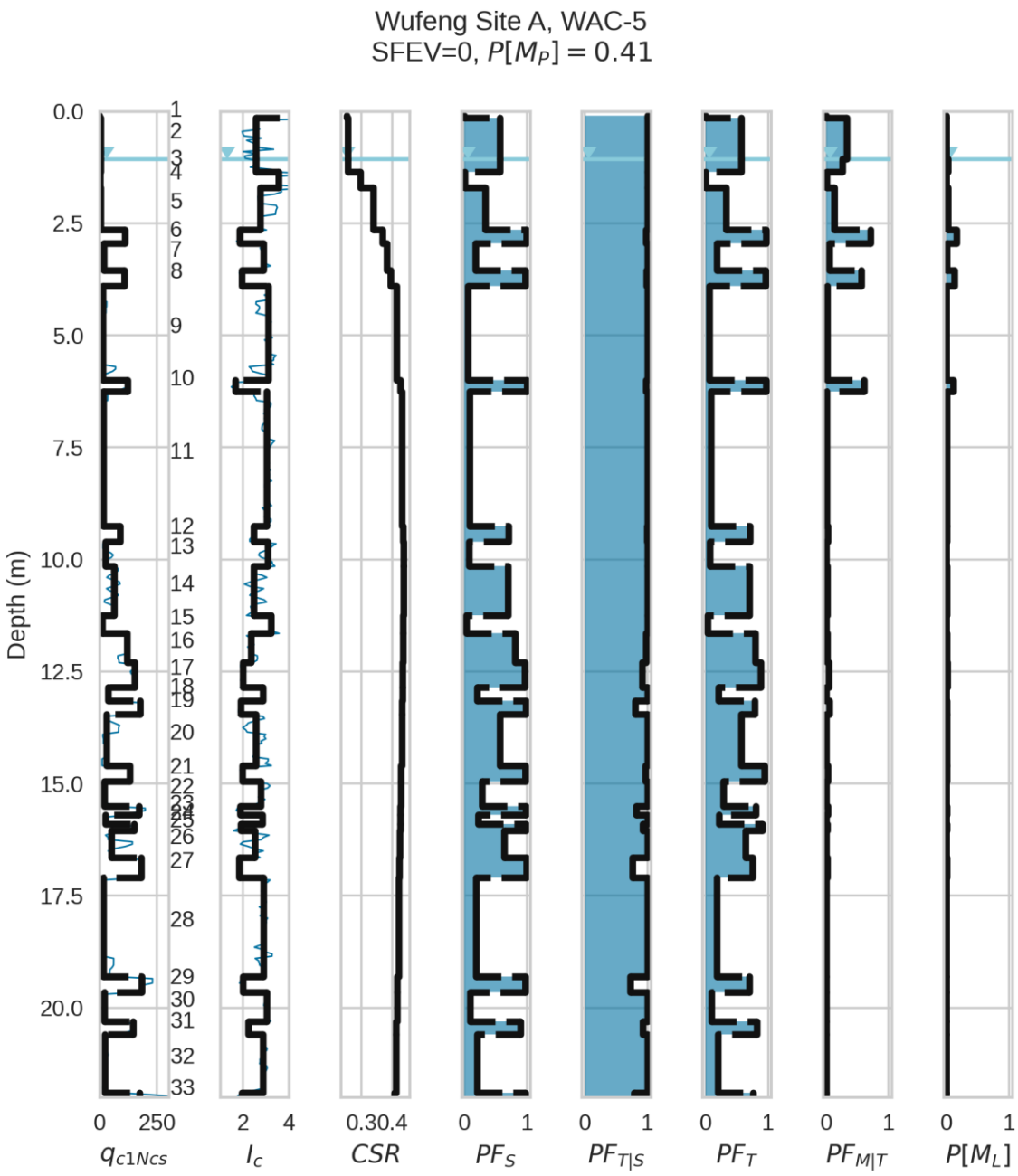

Figure 7-2. CPT "WAC-5" from Wufeng Site A with *CSR* computed using a *PGA* estimate from the 1999 Chi-Chi, Taiwan earthquake and probability factors used to compute P[M_L] for each layer. The total P[M_P] prediction is printed at the top of the figure along with the observation of manifestation (SFEV=1) or lack of manifestation (SFEV=0).

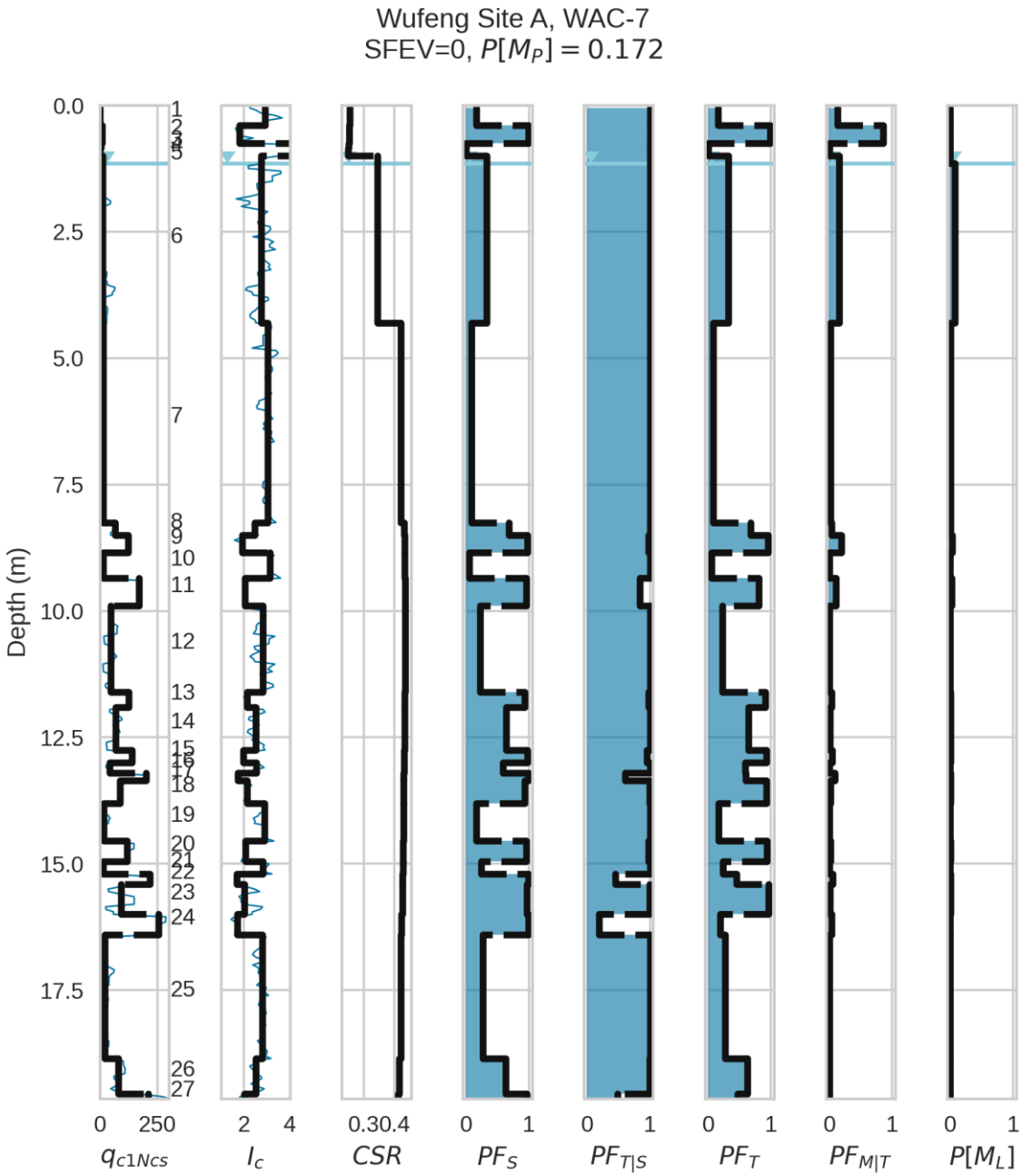

Figure 7-3. CPT "WAC-7" from Wufeng Site A with *CSR* computed using a *PGA* estimate from the 1999 Chi-Chi, Taiwan earthquake and probability factors used to compute P[M_L] for each layer. The total P[M_P] prediction is printed at the top of the figure along with the observation of manifestation (SFEV=1) or lack of manifestation (SFEV=0).

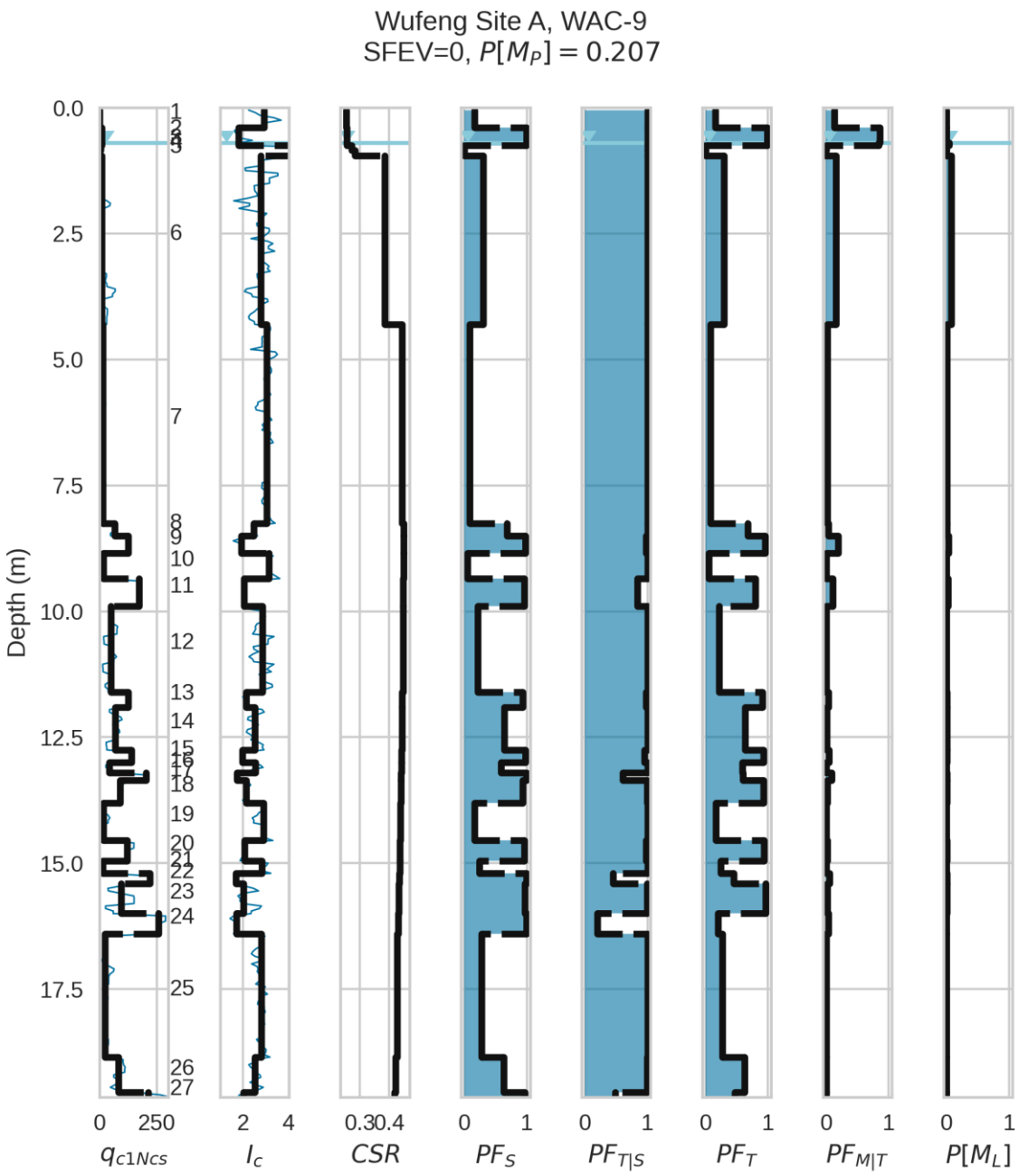

Figure 7-4. CPT "WAC-9" from Wufeng Site A with *CSR* computed using a *PGA* estimate from the 1999 Chi-Chi, Taiwan earthquake and probability factors used to compute P[M_L] for each layer. The total P[M_P] prediction is printed at the top of the figure along with the observation of manifestation (SFEV=1) or lack of manifestation (SFEV=0).

7.2 Mihama-ward Liquefaction Triggering and Consequence Calculations

As described in Section 2.3.1, a site in the Mihama-ward district of Chiba, Japan experienced variable levels of documented ground performance during the 2011 **M**9.0 Tohoku earthquake, including severe surface manifestation of liquefaction including sand boils, no ground failure, and intermediate levels of performance (Nakai and Sekiguchi 2013; Sekiguchi and Nakai 2012). Figure 7-5 shows the location of the site, which is named "8 Chome Meeting Place." This site had an approximate ground shaking level of PGA = 0.47 g, which is similar to that recommended by Nakai and Sekiguchi (2013) of 0.2-0.35 g.

The land in this region was reclaimed between the 1960s and the mid-1980s by discharging dredged soil from the Tokyo Bay seabed that was transported in fluid suspension using pipes (i.e., hydraulic filling). The dredged soil consists of a mixture of sand, silt, and clay. When these materials are discharged from the pipes, the location of which is shown in Figure 7-5, coarser grained particles are deposited close to the pipes where fluid flow velocities are fast enough to suspend finer particles. As the fluid flowed away from the discharge pipes, flow velocities decrease, and finer particles were deposited. This creates a lateral gradation of sand to clay with increasing distance from the discharge pipes. Additionally, the nature of the deposition causes the fill to be very loose as there was no compaction following water pluviation.

The combination of loose clean sand near the discharge pipes and a shallow water table (approximately 2-4 m below ground surface) created a situation where liquefaction would be anticipated. As shown in Figure 7-5, manifestation occurred during the 2011 Tohoku earthquake, as expected, in areas proximal to the discharge pipes. Areas more distant from the discharge pipes

generally did not experience ground failure, presumably because the stratigraphy has finer-grained soils that are less susceptible to liquefaction and its potential manifestation.

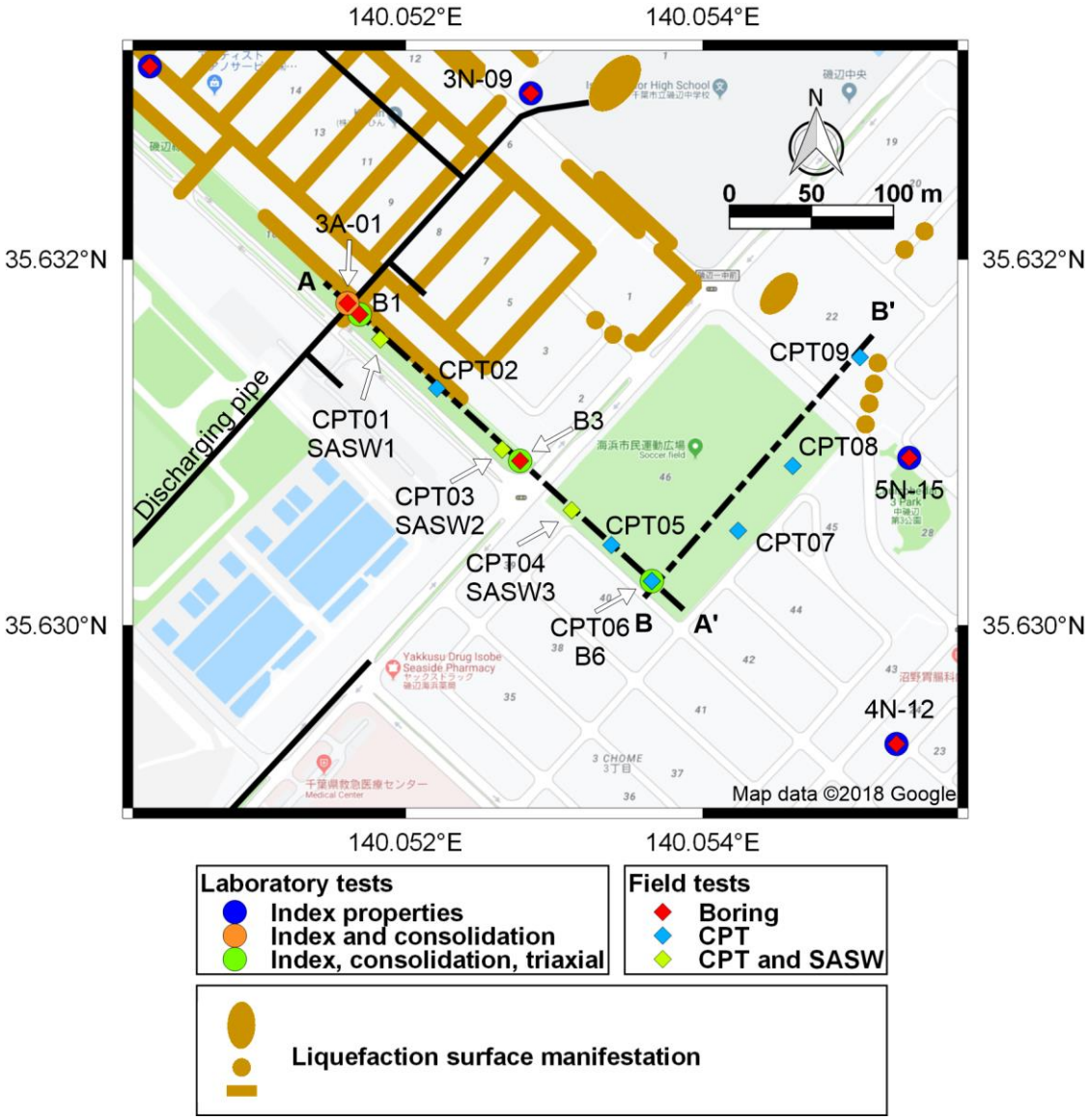

Figure 7-5. Map of the Mihama Ward site showing locations of liquefaction surface manifestations, the discharge pipe used to deposit the hydraulic fill, field tests, and laboratory tests.

The 8 Chome Meeting Place site was characterized in field investigations by a Chiba University team, which conducted 9 CPTs, 3 borings, and 3 SASW tests at the locations shown in Figure 7-5 (Chiba City 2012; Kwak et al. 2018; Stewart et al. 2016). The A-A' transect between CPT1 and CPT6 runs northwest to southeast. CPT1 and CPT2 are in an area where sand boils were observed, whereas CPT3 through CPT6 are in areas where no manifestations were observed. The B-B' transect between CPT6 and CPT9 runs southwest to northeast. CPT6 through CPT8 have no observed manifestations and CPT9 is adjacent to observed sand boils.

For CPT1 through CPT9, critical layers were selected, demands in those layers evaluated using procedures from Section 1.2, and then compared the plotted *CSR**-penetration resistance pairs (Equation 1.7) with the Boulanger and Idriss (2016) legacy model. Assigning critical layers from these CPT profiles for the purpose of plotting a single point on the triggering curve requires judgment. Many different layers might contribute to manifestations, and selecting one single layer to be representative of the profile is subjective and would likely be done differently by different people. For example, some analysts might select the layer with the lowest factor of safety, even if it is deep and/or thin, and other layers with higher FS_L are thicker and/or shallower. In this case, judgment focused on how likely a layer is to manifest liquefaction. Therefore, shallow layers were favored over deeper layers, thicker layers over thinner layers, and looser layers over denser layers, and apply judgment when balancing these criteria. The critical layer selections are summarized in Table 7-3, and plotted in Figure 7-6 along with the Boulanger and Idriss (2016) triggering curves for probabilities of 0.16, 0.5, and 0.86. The "yes" points all plot above the 50% triggering curve and are considered true positives. All but one of the "no" points also plot above the 50% triggering curve and are therefore considered false positives.

Table 7-3. Critical layer properties for Mihama-ward CPT liquefaction triggering evaluation.

CPT	z_{top} (m)	z_{bot} (m)	q_{c1Ncs}	*CSR*
CPT001	3.1	9.6	90	0.18
CPT002	3.0	14.0	85	0.20
CPT003	3.4	5.3	76	0.17
CPT004	3.0	10.0	90	0.20
CPT005	2.5	3.4	88	0.15
CPT006	15.5	19.5	78	0.28
CPT007	10.4	12.0	78	0.27
CPT008	20.0	21.2	146	0.40
CPT009	9.5	11.5	82	0.25

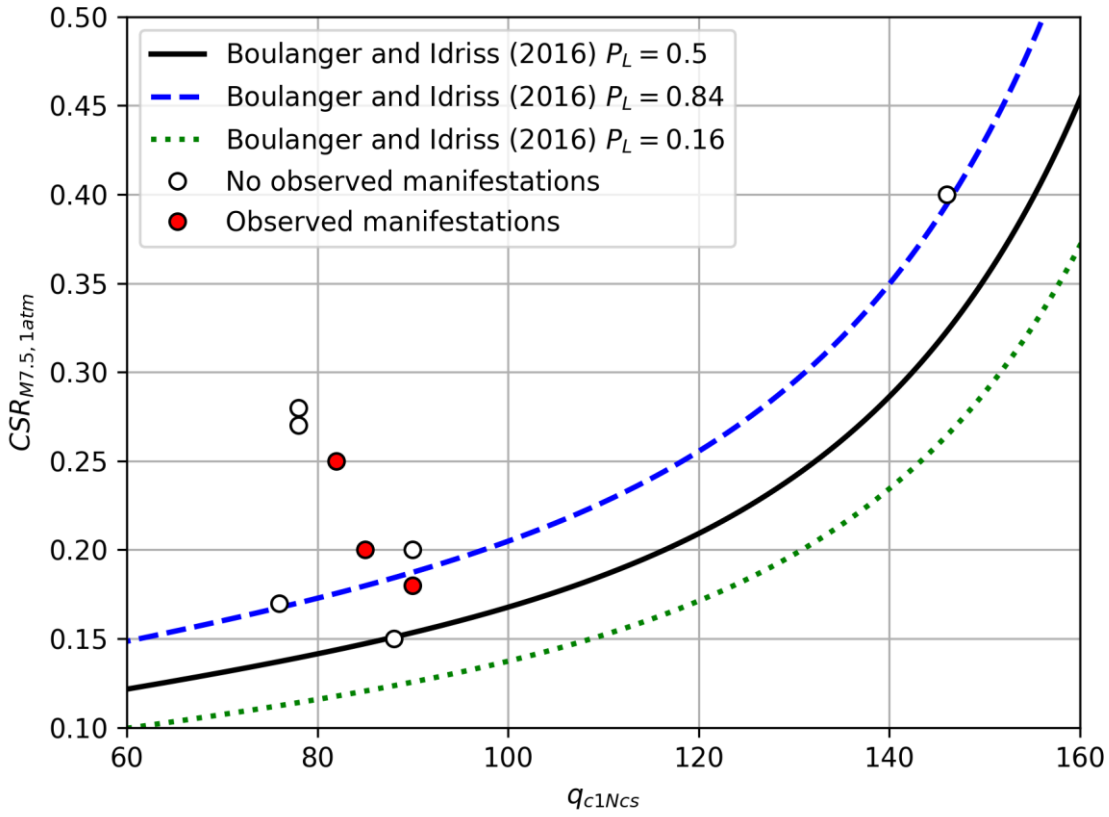

Figure 7-6. Liquefaction triggering evaluation using the Boulanger and Idriss (2016) probabilistic model and critical layers as selected in Table 7-3.

Next, the recommended model developed in this research (Section 6.3) is applied. The layering algorithm (Section 5.3) was applied to CPT1 through CPT7 and CPT9, with the results plotted in Figure 7-7 through Figure 7-14. CPT8 was not included because it did not have a manifestation assigned to it in the dataset. Layer analyses were performed for each CPT with the results shown in Table 7-5 through Table 7-12.

Combining the layer-specific results using Equation 7.11, profile manifestation probabilities were computed as tabulated in Table 7-4. CPT4 and CPT6 have incorrect predictions of manifestation (predicted to manifest although manifestations were not observed) and the other CPTs all have correct predictions. This transect of CPTs shows that the manifestation model worked well for a majority of cases but there were some incorrect predictions. Potential causes of the mispredictions are unmodelled system effects, such as softening deep in the profile that limits shaking demands and multi-dimensional aspects of the manifestation process.

Table 7-4. Probability of manifestation predictions for Boulanger and Idriss (2016) and the recommended P[M_P] model compared with surface evidence of manifestations for Mihama-ward CPTs.

CPT Number	Boulanger and Idriss (2016) P_L	P[M_P]	Surface Evidence?
1	0.80	0.76	Yes
2	0.93	0.78	Yes
3	0.86	0.36	No
4	0.91	0.88	No
5	0.49	0.35	No
6	1.00	0.61	No
7	1.00	0.35	No
9	0.99	0.89	Yes

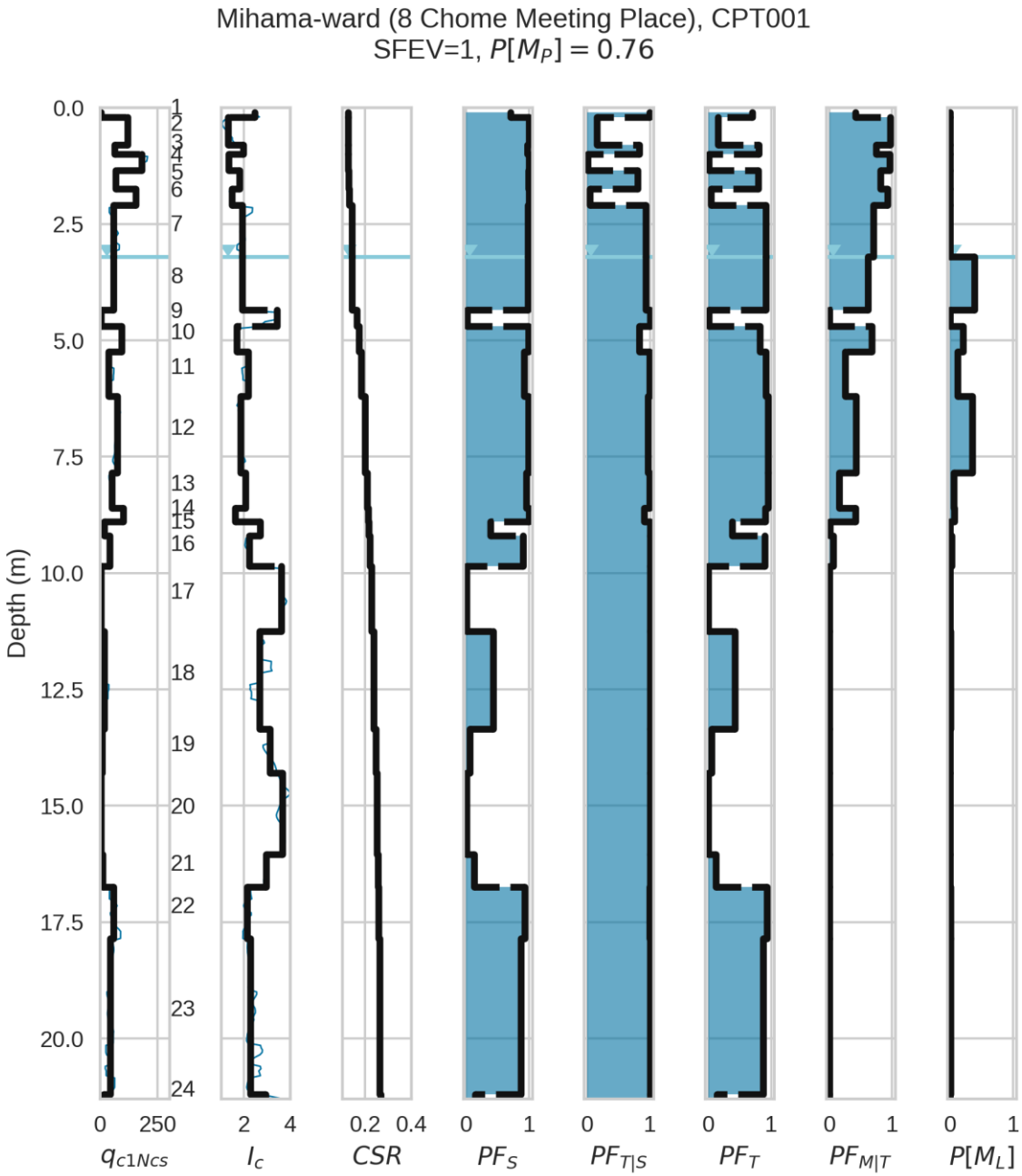

Figure 7-7. CPT1 from Mihama with *CSR* computed using a *PGA* estimate from the 2011 Tohoku earthquake and probability factors used to compute P[M_L] for each layer. The total P[M_P] prediction is printed at the top of the figure along with the observation of manifestation (SFEV=1) or lack of manifestation (SFEV=0).

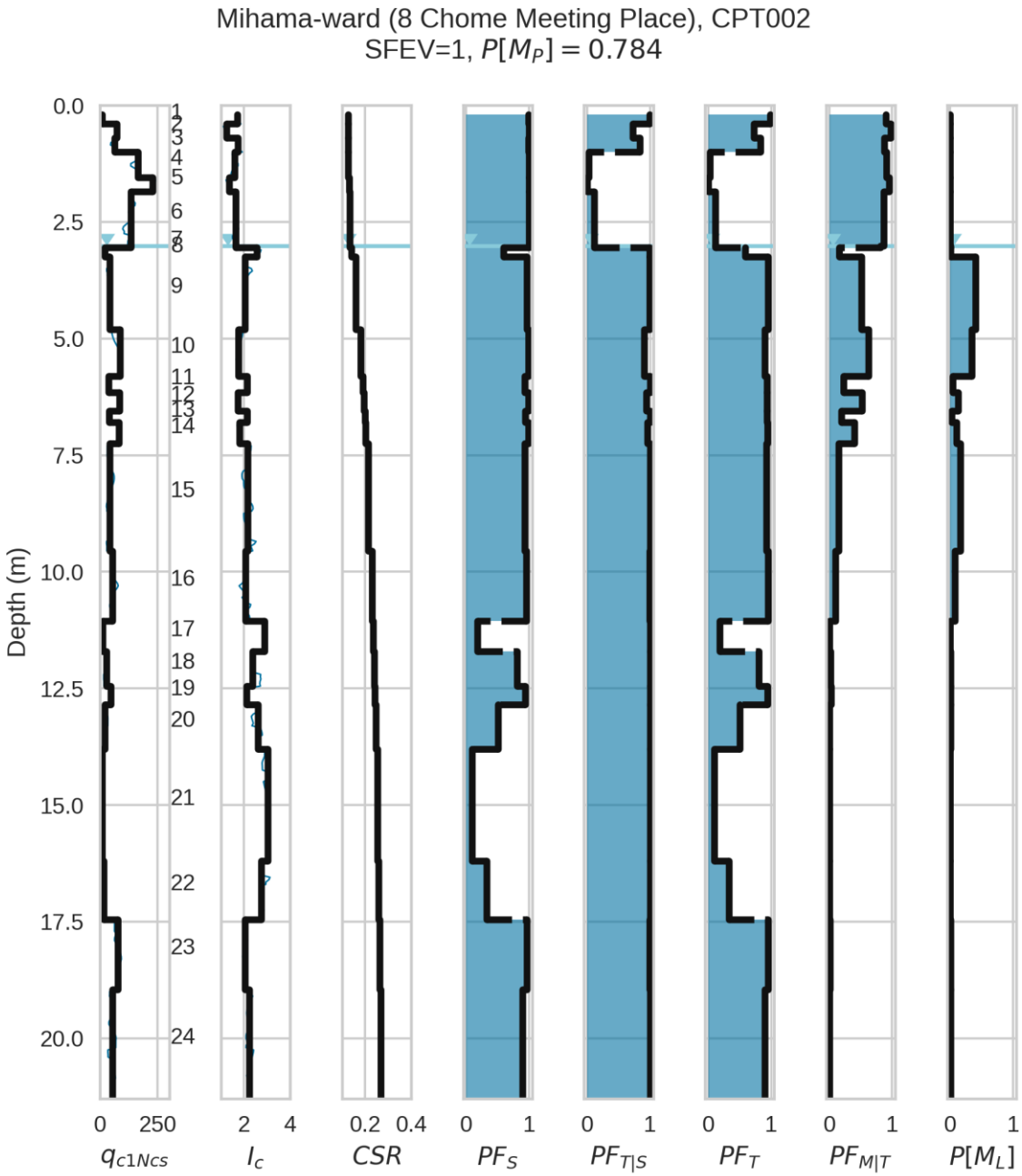

Figure 7-8. CPT2 from Mihama with *CSR* computed using a *PGA* estimate from the 2011 Tohoku earthquake and probability factors used to compute P[M_L] for each layer. The total P[M_P] prediction is printed at the top of the figure along with the observation of manifestation (SFEV=1) or lack of manifestation (SFEV=0).

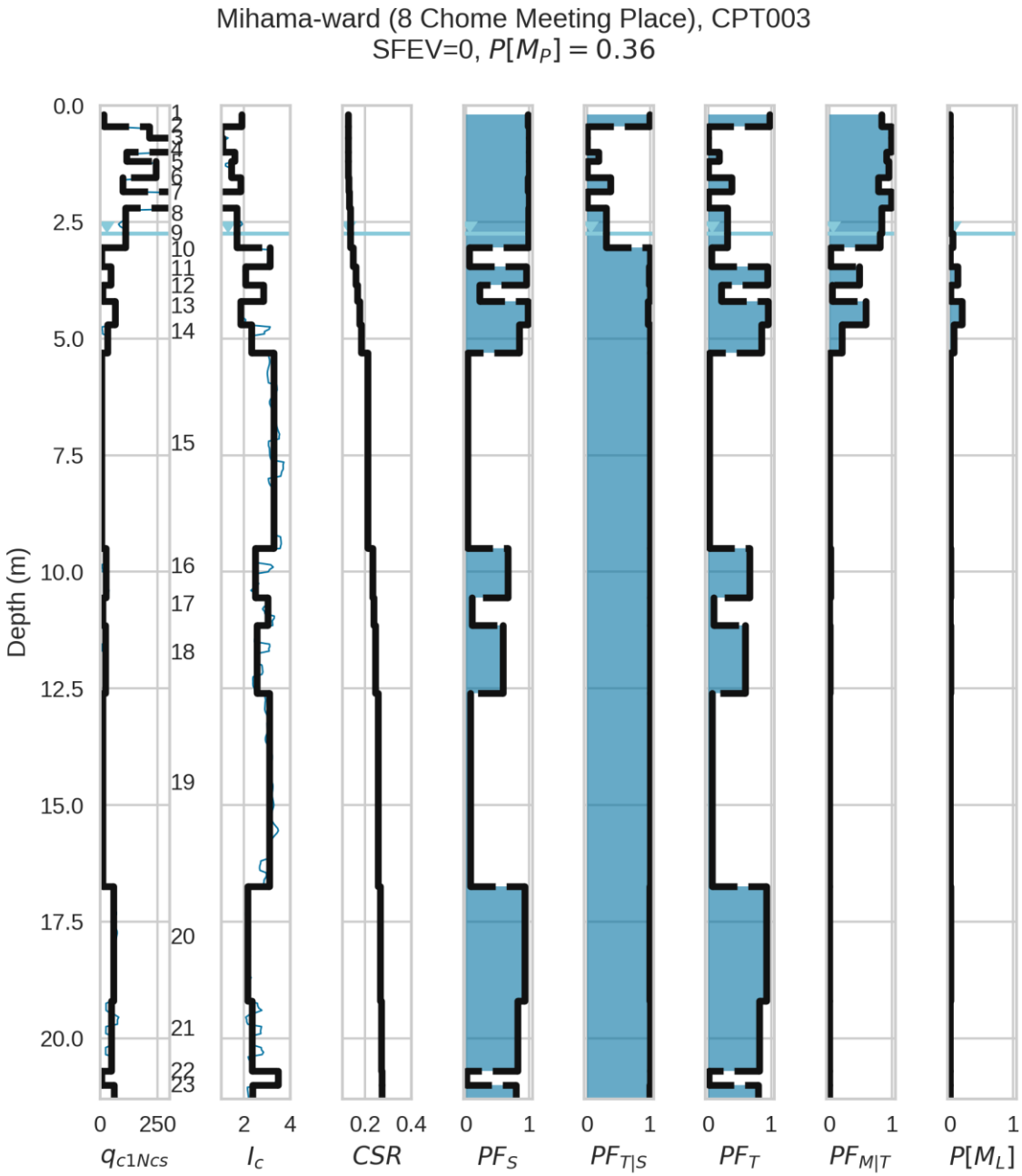

Figure 7-9. CPT3 from Mihama with *CSR* computed using a *PGA* estimate from the 2011 Tohoku earthquake and probability factors used to compute P[M_L] for each layer. The total P[M_P] prediction is printed at the top of the figure along with the observation of manifestation (SFEV=1) or lack of manifestation (SFEV=0).

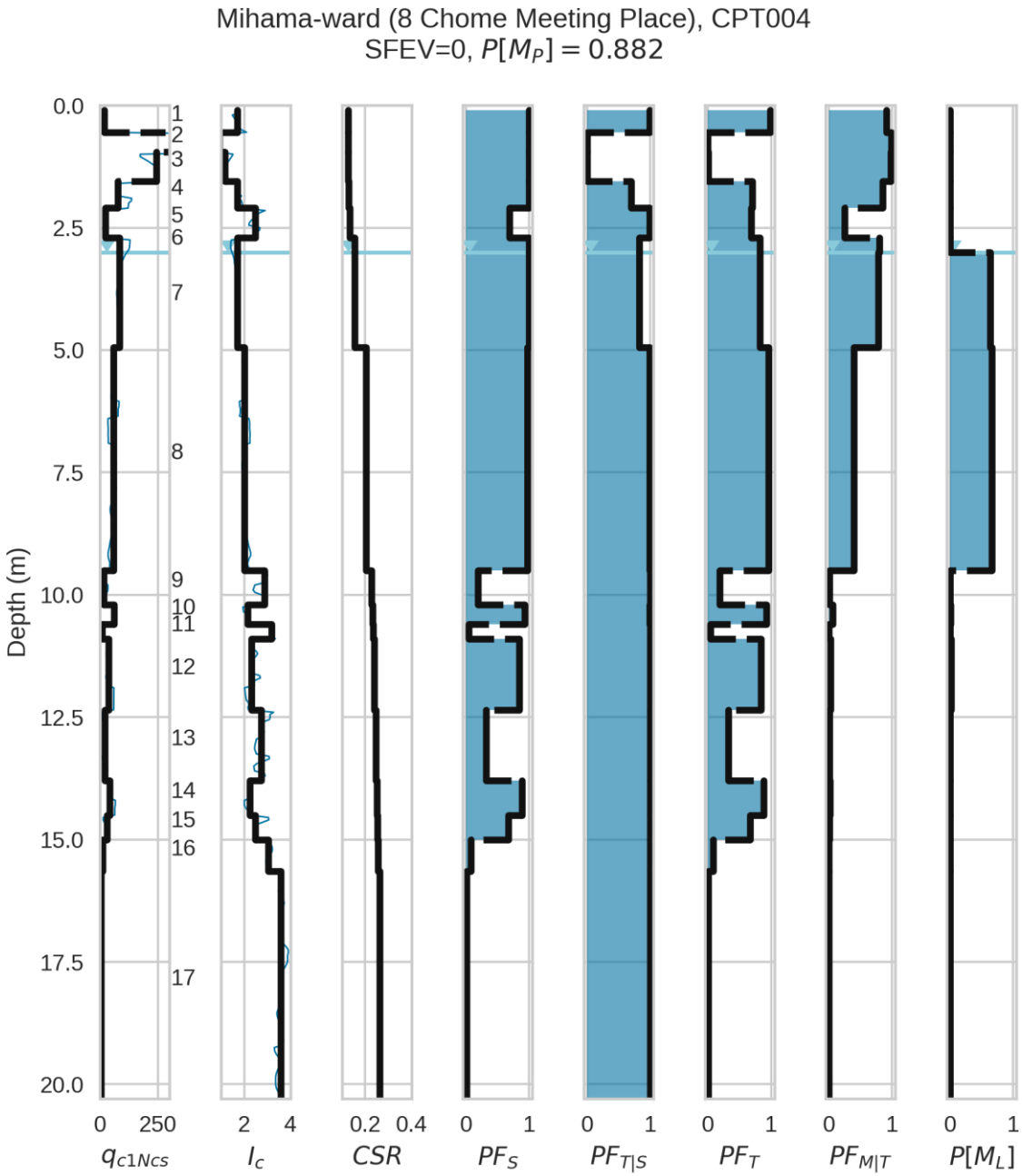

Figure 7-10. CPT4 from Mihama with *CSR* computed using a *PGA* estimate from the 2011 Tohoku earthquake and probability factors used to compute P[M_L] for each layer. The total P[M_P] prediction is printed at the top of the figure along with the observation of manifestation (SFEV=1) or lack of manifestation (SFEV=0).

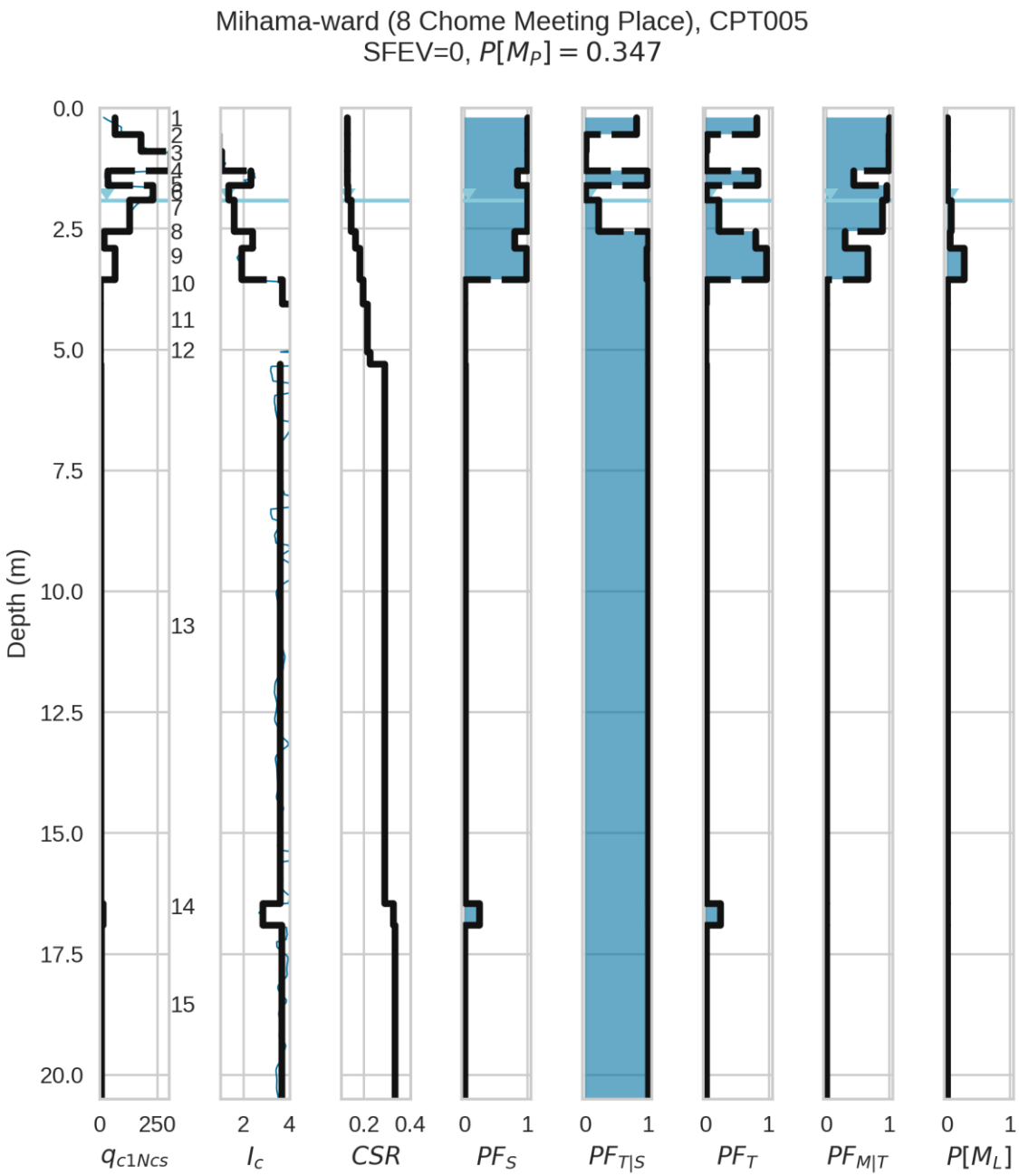

Figure 7-11. CPT5 from Mihama with *CSR* computed using a *PGA* estimate from the 2011 Tohoku earthquake and probability factors used to compute P[M_L] for each layer. The total P[M_P] prediction is printed at the top of the figure along with the observation of manifestation (SFEV=1) or lack of manifestation (SFEV=0).

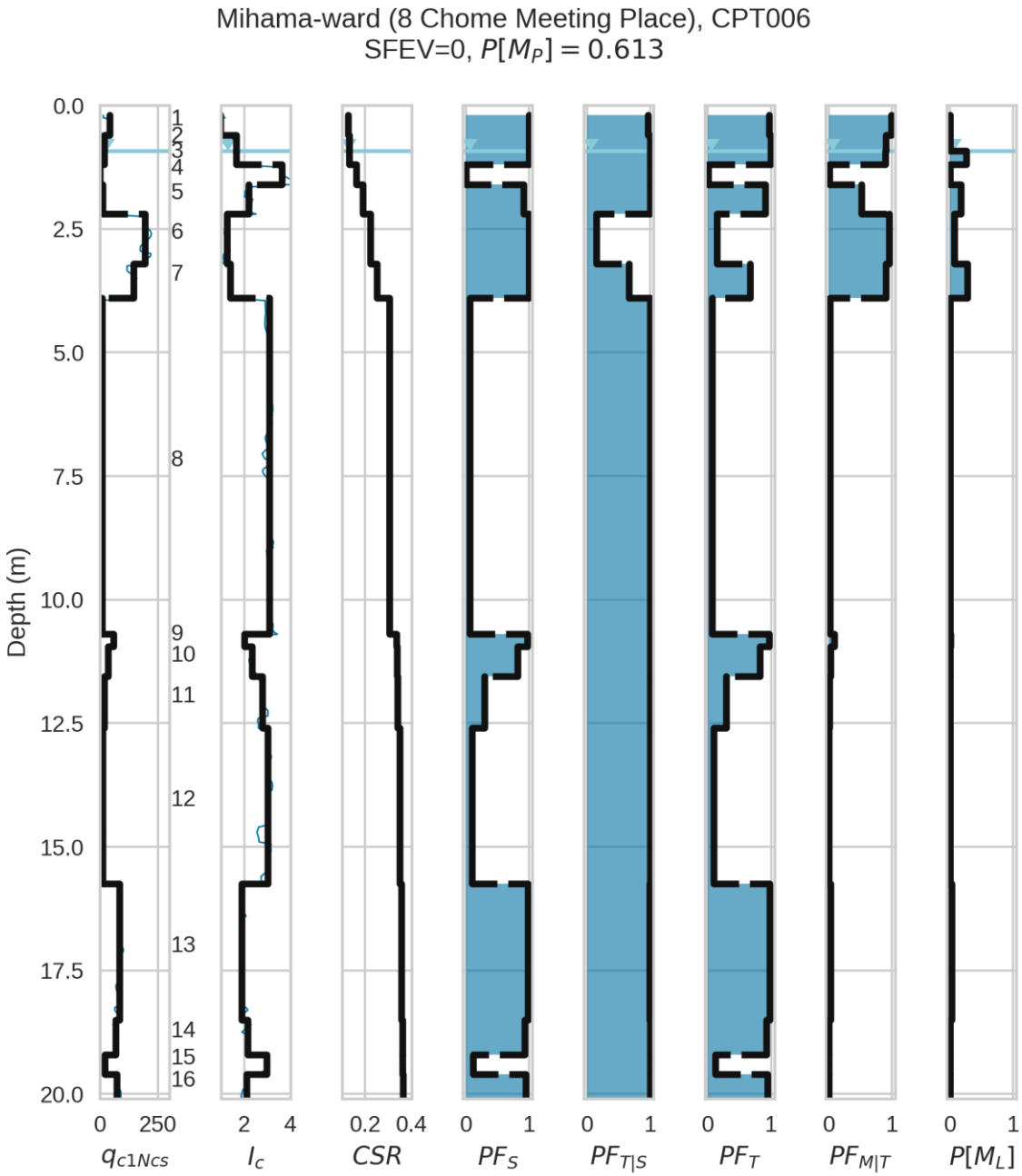

Figure 7-12. CPT6 from Mihama with *CSR* computed using a *PGA* estimate from the 2011 Tohoku earthquake and probability factors used to compute P[M_L] for each layer. The total P[M_P] prediction is printed at the top of the figure along with the observation of manifestation (SFEV=1) or lack of manifestation (SFEV=0).

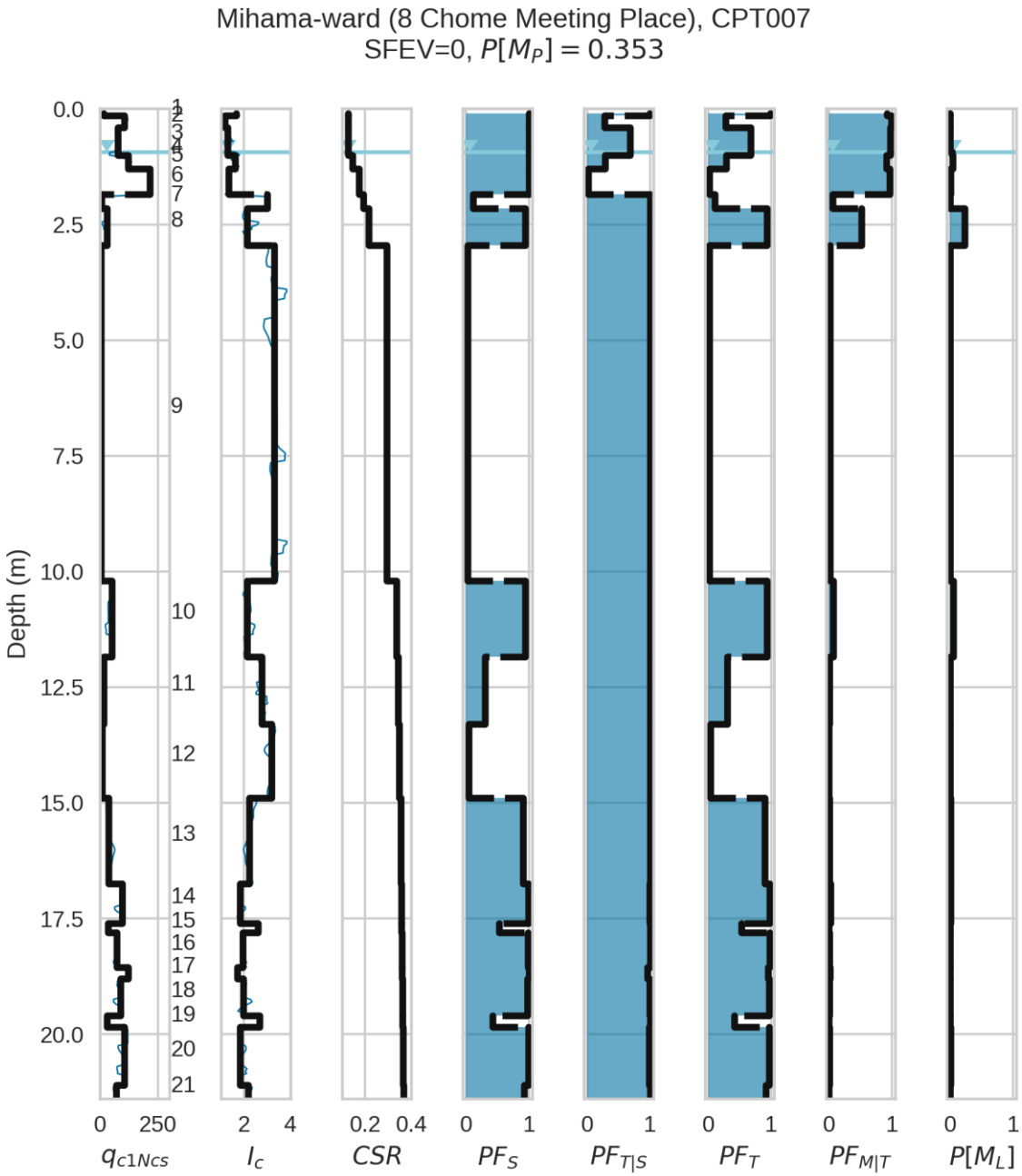

Figure 7-13. CPT7 from Mihama with *CSR* computed using a *PGA* estimate from the 2011 Tohoku earthquake and probability factors used to compute P[M_L] for each layer. The total P[M_P] prediction is printed at the top of the figure along with the observation of manifestation (SFEV=1) or lack of manifestation (SFEV=0).

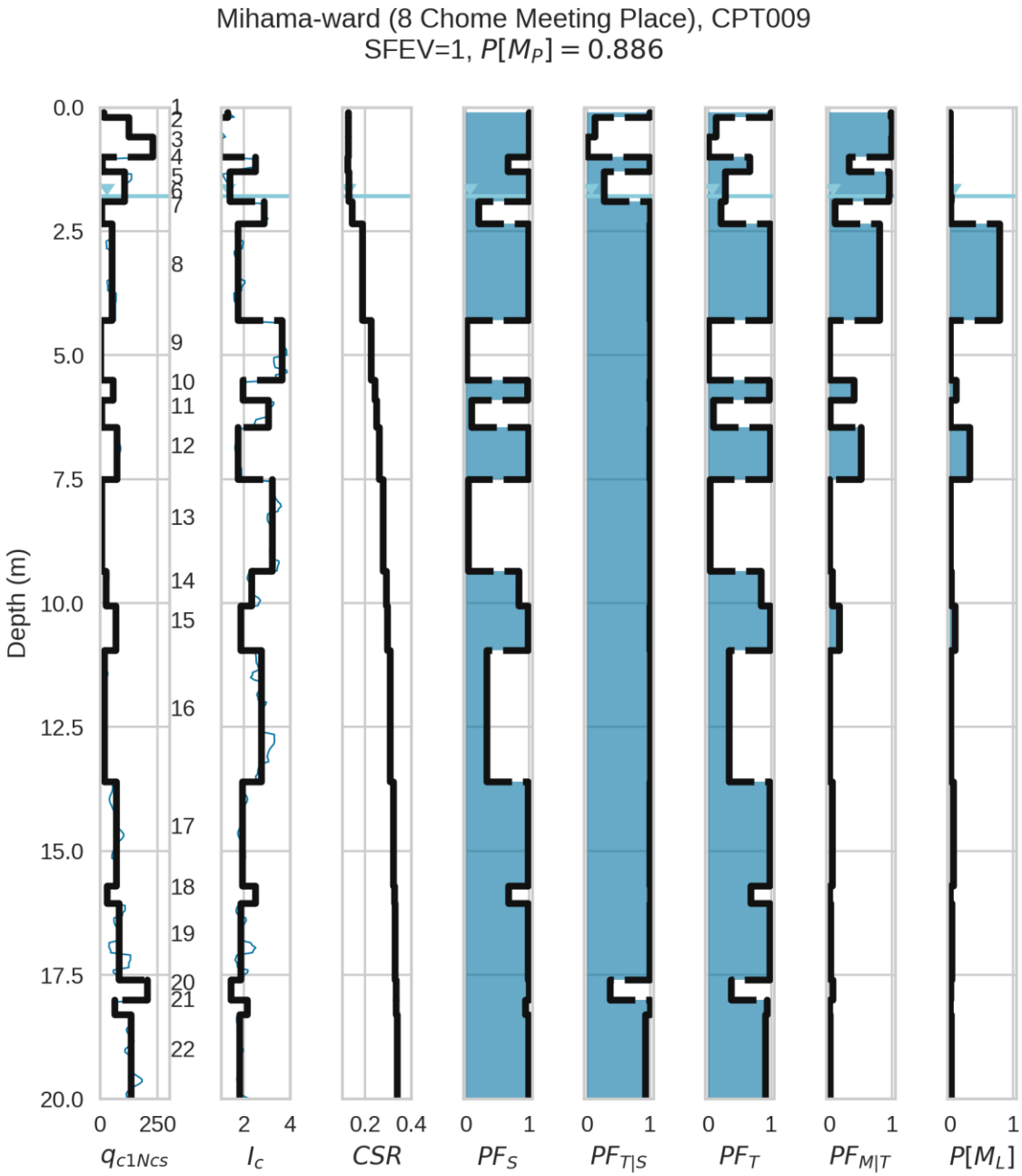

Figure 7-14. CPT9 from Mihama with *CSR* computed using a *PGA* estimate from the 2011 Tohoku earthquake and probability factors used to compute P[M_L] for each layer. The total P[M_P] prediction is printed at the top of the figure along with the observation of manifestation (SFEV=1) or lack of manifestation (SFEV=0).

Table 7-5. Computation of P[M_P] for Mihama-Ward CPT001.

Layer #	z_{top} (m)	z_{bot} (m)	t (m)	q_{c1Ncs}	I_c	$CSR_{M\ 7.5,1atm}$	PF_S	$\widehat{CSR}$	D_R (%)	$\widehat{D_R}$	$\widehat{CRR}$	$PF_{T\|S}$	PF_T	$PF_{M\|T}$	K_{Sat}	P[M_L]
1	0.1	0.2	0.1	3.1	2.46	0.13	0.71	-4.42	0.00	-0.8	-7.46	0.99	0.70	0.42	0.00	0.00
2	0.2	0.8	0.6	118.5	1.31	0.13	1.00	-4.40	62.33	118.7	-3.41	0.15	0.15	0.97	0.00	0.00
3	0.8	1	0.2	62.9	1.98	0.13	0.97	-4.42	36.36	61.7	-5.34	0.83	0.81	0.75	0.00	0.00
4	1	1.35	0.35	180.8	1.33	0.13	1.00	-4.39	82.20	165.9	-1.82	0.01	0.01	0.96	0.00	0.00
5	1.35	1.75	0.4	67.9	1.80	0.13	0.99	-4.31	39.28	67.8	-5.14	0.81	0.80	0.82	0.00	0.00
6	1.75	2.1	0.35	155.5	1.48	0.13	1.00	-4.23	74.85	148.2	-2.42	0.04	0.04	0.92	0.00	0.00
7	2.1	3.2	1.1	59.4	1.92	0.14	0.98	-3.94	34.21	57.3	-5.49	0.94	0.92	0.70	0.00	0.00
8	3.2	4.35	1.15	59.4	1.92	0.14	0.98	-3.94	34.21	57.3	-5.49	0.94	0.92	0.62	1.00	0.38
9	4.35	4.7	0.35	4.4	3.42	0.16	0.01	-3.45	0.00	-0.8	-7.46	1.00	0.01	0.01	1.00	0.00
10	4.7	5.25	0.55	93.3	1.69	0.17	0.99	-3.30	52.01	95.4	-4.20	0.83	0.82	0.68	1.00	0.20
11	5.25	6.2	0.95	36.8	2.17	0.18	0.92	-3.11	17.57	25.3	-6.57	1.00	0.92	0.25	1.00	0.12
12	6.2	7.85	1.65	74.9	1.84	0.20	0.99	-2.88	43.11	75.9	-4.86	0.97	0.96	0.43	1.00	0.35
13	7.85	8.6	0.75	50.2	2.07	0.21	0.96	-2.72	28.11	45.1	-5.90	1.00	0.95	0.16	1.00	0.06
14	8.6	8.9	0.3	99.9	1.61	0.21	1.00	-2.66	54.87	101.7	-3.99	0.91	0.91	0.42	1.00	0.07
15	8.9	9.2	0.3	17.8	2.70	0.22	0.38	-2.63	0.00	-0.8	-7.46	1.00	0.38	0.02	1.00	0.00
16	9.2	9.85	0.65	42.5	2.22	0.22	0.90	-2.58	22.32	34.0	-6.28	1.00	0.90	0.07	1.00	0.02
17	9.85	11.25	1.4	4.5	3.61	0.23	0.00	-2.50	0.00	-0.8	-7.46	1.00	0.00	0.00	1.00	0.00
18	11.25	13.35	2.1	17.6	2.67	0.24	0.43	-2.39	0.00	-0.8	-7.46	1.00	0.43	0.01	1.00	0.00
19	13.35	14.3	0.95	9.3	3.12	0.25	0.05	-2.30	0.00	-0.8	-7.46	1.00	0.05	0.00	1.00	0.00
20	14.3	16.05	1.75	4.6	3.67	0.25	0.00	-2.25	0.00	-0.8	-7.46	1.00	0.00	0.00	1.00	0.00
21	16.05	16.75	0.7	12.4	2.96	0.26	0.13	-2.21	0.00	-0.8	-7.46	1.00	0.13	0.00	1.00	0.00
22	16.75	17.85	1.1	57.6	2.14	0.26	0.93	-2.19	33.08	55.0	-5.57	1.00	0.93	0.01	1.00	0.00
23	17.85	21.2	3.35	44.9	2.27	0.26	0.87	-2.13	24.24	37.6	-6.16	1.00	0.87	0.00	1.00	0.00
24	21.2	21.3	0.1	15.1	2.93	0.27	0.14	-2.08	0.00	-0.8	-7.46	1.00	0.14	0.00	1.00	0.00

Table 7-6. Computation of P[M_P] for Mihama-Ward CPT002.

Layer #	z_{top} (m)	z_{bot} (m)	t (m)	q_{c1Ncs}	I_c	$CSR_{M\ 7.5,1atm}$	PF_S	$\widehat{CSR}$	D_R (%)	$\widehat{D_R}$	$\widehat{CRR}$	$PF_{T\|S}$	PF_T	$PF_{M\|T}$	K_{Sat}	P[M_L]
1	0.1	0.2	0.1	3.1	2.46	0.13	0.71	-4.42	0.0	-0.8	-7.46	0.99	0.70	0.42	0.00	0.00
2	0.2	0.8	0.6	118.5	1.31	0.13	1.00	-4.40	41.7	118.7	-3.41	0.15	0.15	0.97	0.00	0.00
3	0.8	1	0.2	62.9	1.98	0.13	0.97	-4.42	35.9	61.7	-5.34	0.83	0.81	0.75	0.00	0.00
4	1	1.35	0.35	180.8	1.33	0.13	1.00	-4.39	77.4	165.9	-1.82	0.01	0.01	0.96	0.00	0.00
5	1.35	1.75	0.4	67.9	1.80	0.13	0.99	-4.31	94.1	67.8	-5.14	0.81	0.80	0.82	0.00	0.00
6	1.75	2.1	0.35	155.5	1.48	0.13	1.00	-4.23	68.1	148.2	-2.42	0.04	0.04	0.92	0.00	0.00
7	2.1	3.2	1.1	59.4	1.92	0.14	0.98	-3.94	68.1	57.3	-5.49	0.94	0.92	0.70	0.00	0.00
8	3.2	4.35	1.15	59.4	1.92	0.14	0.98	-3.94	0.0	57.3	-5.49	0.94	0.92	0.62	1.00	0.38
9	4.35	4.7	0.35	4.4	3.42	0.16	0.01	-3.45	21.4	-0.8	-7.46	1.00	0.01	0.01	1.00	0.00
10	4.7	5.25	0.55	93.3	1.69	0.17	0.99	-3.30	48.6	95.4	-4.20	0.83	0.82	0.68	1.00	0.20
11	5.25	6.2	0.95	36.8	2.17	0.18	0.92	-3.11	17.8	25.3	-6.57	1.00	0.92	0.25	1.00	0.12
12	6.2	7.85	1.65	74.9	1.84	0.20	0.99	-2.88	47.4	75.9	-4.86	0.97	0.96	0.43	1.00	0.35
13	7.85	8.6	0.75	50.2	2.07	0.21	0.96	-2.72	19.4	45.1	-5.90	1.00	0.95	0.16	1.00	0.06
14	8.6	8.9	0.3	99.9	1.61	0.21	1.00	-2.66	46.5	101.7	-3.99	0.91	0.91	0.42	1.00	0.07
15	8.9	9.2	0.3	17.8	2.70	0.22	0.38	-2.63	22.0	-0.8	-7.46	1.00	0.38	0.02	1.00	0.00
16	9.2	9.85	0.65	42.5	2.22	0.22	0.90	-2.58	30.4	34.0	-6.28	1.00	0.90	0.07	1.00	0.02
17	9.85	11.25	1.4	4.5	3.61	0.23	0.00	-2.50	0.0	-0.8	-7.46	1.00	0.00	0.00	1.00	0.00
18	11.25	13.35	2.1	17.6	2.67	0.24	0.43	-2.39	9.8	-0.8	-7.46	1.00	0.43	0.01	1.00	0.00
19	13.35	14.3	0.95	9.3	3.12	0.25	0.05	-2.30	25.5	-0.8	-7.46	1.00	0.05	0.00	1.00	0.00
20	14.3	16.05	1.75	4.6	3.67	0.25	0.00	-2.25	0.0	-0.8	-7.46	1.00	0.00	0.00	1.00	0.00
21	16.05	16.75	0.7	12.4	2.96	0.26	0.13	-2.21	0.0	-0.8	-7.46	1.00	0.13	0.00	1.00	0.00
22	16.75	17.85	1.1	57.6	2.14	0.26	0.93	-2.19	0.0	55.0	-5.57	1.00	0.93	0.01	1.00	0.00
23	17.85	21.2	3.35	44.9	2.27	0.26	0.87	-2.13	44.3	37.6	-6.16	1.00	0.87	0.00	1.00	0.00
24	21.2	21.3	0.1	15.1	2.93	0.27	0.14	-2.08	30.5	-0.8	-7.46	1.00	0.14	0.00	1.00	0.00

Table 7-7. Computation of P[M_P] for Mihama-Ward CPT003.

Layer #	z_{top} (m)	z_{bot} (m)	t (m)	q_{c1Ncs}	I_c	$CSR_{M\ 7.5,1atm}$	PF_S	$\widehat{CSR}$	D_R (%)	$\widehat{D_R}$	$\widehat{CRR}$	$PF_{T\|S}$	PF_T	$PF_{M\|T}$	K_{Sat}	P[M_L]
1	0.2	0.45	0.25	17.1	1.89	0.13	0.98	-4.40	0.0	-0.8	-7.46	0.99	0.98	0.83	0.00	0.00
2	0.45	0.7	0.25	213.4	0.99	0.13	1.00	-4.40	90.6	186.7	-1.12	0.00	0.00	0.99	0.00	0.00
3	0.7	1	0.3	321.6	1.07	0.13	1.00	-4.41	100.0	210.2	-0.32	0.00	0.00	0.99	0.00	0.00
4	1	1.2	0.2	114.4	1.60	0.13	1.00	-4.42	60.8	115.1	-3.54	0.18	0.18	0.91	0.00	0.00
5	1.2	1.55	0.35	243.2	1.44	0.13	1.00	-4.38	97.5	204.0	-0.53	0.00	0.00	0.94	0.00	0.00
6	1.55	1.85	0.3	99.0	1.85	0.13	0.99	-4.31	54.5	101.0	-4.01	0.38	0.37	0.78	0.00	0.00
7	1.85	2.2	0.35	487.6	0.90	0.13	1.00	-4.25	100.0	210.2	-0.32	0.00	0.00	0.99	0.00	0.00
8	2.2	2.75	0.55	110.7	1.69	0.14	0.99	-4.13	59.3	111.8	-3.65	0.30	0.30	0.83	0.00	0.00
9	2.75	3.05	0.3	110.7	1.69	0.14	0.99	-4.13	59.3	111.8	-3.65	0.30	0.30	0.81	1.00	0.04
10	3.05	3.45	0.4	7.2	3.13	0.15	0.05	-3.80	0.0	-0.8	-7.46	1.00	0.05	0.02	1.00	0.00
11	3.45	3.85	0.4	47.8	2.05	0.16	0.96	-3.57	26.3	41.63	-6.02	0.99	0.95	0.48	1.00	0.11
12	3.85	4.2	0.35	11.3	2.85	0.17	0.21	-3.42	0.0	-0.83	-7.46	1.00	0.21	0.05	1.00	0.00
13	4.2	4.7	0.5	64.7	1.86	0.18	0.99	-3.26	37.4	63.94	-5.27	0.97	0.96	0.58	1.00	0.18
14	4.7	5.3	0.6	31.7	2.31	0.18	0.85	-3.10	12.7	16.88	-6.86	1.00	0.85	0.20	1.00	0.05
15	5.3	9.5	4.2	7.2	3.28	0.21	0.02	-2.70	0.0	-0.83	-7.46	1.00	0.02	0.01	1.00	0.00
16	9.5	10.55	1.05	24.5	2.50	0.23	0.66	-2.44	4.9	4.74	-7.27	1.00	0.66	0.02	1.00	0.01
17	10.55	11.15	0.6	11.4	3.02	0.24	0.09	-2.38	0.0	-0.83	-7.46	1.00	0.09	0.00	1.00	0.00
18	11.15	12.6	1.45	23.8	2.55	0.24	0.59	-2.32	4.0	3.63	-7.30	1.00	0.59	0.01	1.00	0.01
19	12.6	16.75	4.15	10.4	3.09	0.26	0.06	-2.20	0.0	-0.83	-7.46	1.00	0.06	0.00	1.00	0.00
20	16.75	19.2	2.45	57.9	2.16	0.27	0.93	-2.11	33.3	55.36	-5.56	1.00	0.92	0.01	1.00	0.01
21	19.2	20.7	1.5	48.8	2.35	0.27	0.82	-2.07	27.1	43.15	-5.97	1.00	0.82	0.00	1.00	0.00
22	20.7	21	0.3	7.6	3.48	0.27	0.01	-2.05	0.0	-0.83	-7.46	1.00	0.01	0.00	1.00	0.00
23	21	21.3	0.3	59.7	2.37	0.27	0.79	-2.05	34.4	57.62	-5.48	1.00	0.79	0.00	1.00	0.00

Table 7-8. Computation of P[M_P] for Mihama-Ward CPT004.

Layer #	z_{top} (m)	z_{bot} (m)	t (m)	q_{c1Ncs}	I_c	$CSR_{M\ 7.5,1atm}$	PF_S	$\widehat{CSR}$	D_R (%)	$\widehat{D_R}$	$\widehat{CRR}$	$PF_{T\|S}$	PF_T	$PF_{M\|T}$	K_{Sat}	P[M_L]
1	0.1	0.55	0.45	19.0	1.70	0.13	0.99	-4.40	0.0	-0.8	-7.46	0.99	0.99	0.91	0.00	0.00
2	0.55	0.95	0.4	694.3	0.93	0.13	1.00	-4.40	100.0	210.2	-0.32	0.00	0.00	0.99	0.00	0.00
3	0.95	1.55	0.6	242.8	1.16	0.13	1.00	-4.39	97.5	203.8	-0.54	0.00	0.00	0.98	0.00	0.00
4	1.55	2.1	0.55	77.0	1.71	0.13	0.99	-4.29	44.2	78.2	-4.78	0.70	0.70	0.85	0.00	0.00
5	2.1	2.7	0.6	23.9	2.48	0.13	0.68	-4.21	4.2	3.8	-7.30	1.00	0.68	0.25	0.00	0.00
6	2.7	3	0.3	83.2	1.70	0.16	0.99	-3.64	47.3	85.0	-4.56	0.83	0.82	0.80	0.00	0.00
7	3	4.95	1.95	83.2	1.70	0.16	0.99	-3.64	47.3	85.0	-4.56	0.83	0.82	0.78	1.00	0.64
8	4.95	9.5	4.55	57.1	2.00	0.20	0.97	-2.80	32.8	54.4	-5.59	0.99	0.96	0.40	1.00	0.67
9	9.5	10.2	0.7	15.6	2.87	0.23	0.19	-2.50	0.0	-0.8	-7.46	1.00	0.19	0.01	1.00	0.00
10	10.2	10.6	0.4	60.4	2.15	0.23	0.93	-2.46	34.8	58.6	-5.45	0.99	0.92	0.06	1.00	0.01
11	10.6	10.9	0.3	8.9	3.19	0.23	0.04	-2.43	0.0	-0.83	-7.46	1.00	0.04	0.00	1.00	0.00
12	10.9	12.35	1.45	38.0	2.32	0.24	0.84	-2.38	18.5	27.02	-6.51	1.00	0.84	0.03	1.00	0.02
13	12.35	13.8	1.45	19.6	2.75	0.25	0.32	-2.30	0.0	-0.83	-7.46	1.00	0.32	0.00	1.00	0.00
14	13.8	14.5	0.7	40.7	2.25	0.25	0.88	-2.26	20.9	31.27	-6.37	1.00	0.88	0.01	1.00	0.00
15	14.5	15	0.5	29.8	2.49	0.25	0.67	-2.23	10.8	13.69	-6.96	1.00	0.67	0.00	1.00	0.00
16	15	15.65	0.65	12.0	3.05	0.26	0.08	-2.21	0.0	-0.83	-7.46	1.00	0.08	0.00	1.00	0.00
17	15.65	20.3	4.65	4.9	3.57	0.26	0.00	-2.13	0.0	-0.83	-7.46	1.00	0.00	0.00	1.00	0.00

Table 7-9. Computation of P[M_P] for Mihama-Ward CPT005.

Layer #	z_{top} (m)	z_{bot} (m)	t (m)	q_{c1Ncs}	I_c	$CSR_{M\ 7.5,1atm}$	PF_S	$\widehat{CSR}$	D_R (%)	$\widehat{D_R}$	$\widehat{CRR}$	$PF_{T\|S}$	PF_T	$PF_{M\|T}$	K_{Sat}	P[M_L]
1	0.2	0.55	0.35	65.7	0.91	0.13	1.00	-4.39	38.0	65.1	-5.23	0.81	0.81	0.99	0.00	0.00
2	0.55	0.9	0.35	178.1	0.93	0.13	1.00	-4.40	81.4	164.1	-1.88	0.01	0.01	0.99	0.00	0.00
3	0.9	1.3	0.4	307.5	1.05	0.13	1.00	-4.41	100.0	210.2	-0.32	0.00	0.00	0.99	0.00	0.00
4	1.3	1.6	0.3	35.8	2.32	0.13	0.84	-4.42	16.6	23.5	-6.63	0.98	0.82	0.43	0.00	0.00
5	1.6	1.9	0.3	228.9	1.35	0.13	1.00	-4.34	94.3	195.9	-0.81	0.00	0.00	0.95	0.00	0.00
6	1.9	1.91	0.01	128.2	1.58	0.14	1.00	-3.91	65.8	126.9	-3.14	0.21	0.21	0.89	0.00	0.00
7	1.91	2.55	0.64	128.2	1.58	0.14	1.00	-3.91	65.8	126.9	-3.14	0.21	0.21	0.89	1.00	0.06
8	2.55	2.9	0.35	18.7	2.38	0.16	0.79	-3.49	0.0	-0.8	-7.46	1.00	0.79	0.29	1.00	0.04
9	2.9	3.55	0.65	64.1	1.91	0.18	0.98	-3.18	37.0	63.1	-5.29	0.97	0.96	0.65	1.00	0.27
10	3.55	4.05	0.5	2.6	3.68	0.20	0.00	-2.93	0.0	-0.8	-7.46	1.00	0.00	0.00	1.00	0.00
11	4.05	5.05	1	1.7	4.31	0.21	0.00	-2.68	0.0	-0.83	-7.46	1.00	0.00	0.00	1.00	0.00
12	5.05	5.3	0.25	1.2	6.71	0.23	0.00	-2.52	0.0	-0.83	-7.46	1.00	0.00	0.00	1.00	0.00
13	5.3	16.45	11.15	4.7	3.59	0.29	0.00	-1.92	0.0	-0.83	-7.46	1.00	0.00	0.00	1.00	0.00
14	16.45	16.9	0.45	14.0	2.83	0.33	0.23	-1.66	0.0	-0.83	-7.46	1.00	0.23	0.00	1.00	0.00
15	16.9	20.5	3.6	5.4	3.64	0.33	0.00	-1.61	0.0	-0.83	-7.46	1.00	0.00	0.00	1.00	0.00

Table 7-10. Computation of P[M_P] for Mihama-Ward CPT006.

Layer #	z_{top} (m)	z_{bot} (m)	t (m)	q_{c1Ncs}	I_c	$CSR_{M\ 7.5,1atm}$	PF_S	$\widehat{CSR}$	D_R (%)	$\widehat{D_R}$	$\widehat{CRR}$	$PF_{T\|S}$	PF_T	$PF_{M\|T}$	K_{Sat}	P[M_L]
1	0.2	0.6	0.4	41.1	0.97	0.13	1.00	-4.39	21.2	31.9	-6.35	0.97	0.97	0.99	0.00	0.00
2	0.6	0.92	0.32	17.7	1.66	0.13	1.00	-4.22	0.0	-0.8	-7.46	1.00	0.99	0.90	0.00	0.00
3	0.92	1.2	0.28	17.7	1.66	0.13	1.00	-4.22	0.0	-0.8	-7.46	1.00	0.99	0.90	1.00	0.26
4	1.2	1.6	0.4	0.6	3.63	0.16	0.00	-3.51	0.0	-0.8	-7.46	1.00	0.00	0.01	1.00	0.00
5	1.6	2.2	0.6	11.1	2.20	0.19	0.91	-3.01	0.0	-0.8	-7.46	1.00	0.91	0.51	1.00	0.17
6	2.2	3.2	1	193.8	1.26	0.22	1.00	-2.55	85.7	174.5	-1.53	0.15	0.15	0.96	1.00	0.07
7	3.2	3.9	0.7	145.8	1.41	0.25	1.00	-2.26	71.8	140.9	-2.66	0.67	0.67	0.90	1.00	0.28
8	3.9	10.7	6.8	8.3	3.10	0.30	0.06	-1.80	0.0	-0.8	-7.46	1.00	0.06	0.02	1.00	0.00
9	10.7	10.95	0.25	57.2	2.01	0.34	0.97	-1.60	32.8	54.5	-5.59	1.00	0.97	0.08	1.00	0.01
10	10.95	11.55	0.6	35.5	2.35	0.34	0.82	-1.58	16.4	23.2	-6.64	1.00	0.82	0.03	1.00	0.01
11	11.55	12.6	1.05	18.6	2.77	0.34	0.29	-1.56	0.0	-0.8	-7.46	1.00	0.29	0.00	1.00	0.00
12	12.6	15.75	3.15	11.7	3.02	0.35	0.09	-1.52	0.0	-0.8	-7.46	1.00	0.09	0.00	1.00	0.00
13	15.75	18.5	2.75	83.7	1.90	0.36	0.98	-1.47	47.5	85.5	-4.54	1.00	0.98	0.02	1.00	0.03
14	18.5	19.2	0.7	67.0	2.16	0.36	0.93	-1.45	38.8	66.7	-5.17	1.00	0.93	0.00	1.00	0.00
15	19.2	19.6	0.4	19.7	2.98	0.36	0.12	-1.44	0.0	-0.8	-7.46	1.00	0.12	0.00	1.00	0.00
16	19.6	20.1	0.5	73.2	2.09	0.36	0.95	-1.44	42.2	74.0	-4.93	1.00	0.95	0.00	1.00	0.00

Table 7-11. Computation of P[M_P] for Mihama-Ward CPT007.

Layer #	z_{top} (m)	z_{bot} (m)	t (m)	q_{c1Ncs}	I_c	$CSR_{M\ 7.5,1atm}$	PF_S	$\widehat{CSR}$	D_R (%)	$\widehat{D_R}$	$\widehat{CRR}$	$PF_{T\|S}$	PF_T	$PF_{M\|T}$	K_{Sat}	P[M_L]
1	0.1	0.15	0.05	16.3	1.67	0.13	1.00	-4.39	0.0	-0.8	-7.46	0.99	0.99	0.92	0.00	0.00
2	0.15	0.4	0.25	104.2	1.16	0.13	1.00	-4.39	56.7	105.9	-3.85	0.28	0.28	0.98	0.00	0.00
3	0.4	0.93	0.53	76.0	1.27	0.13	1.00	-4.38	43.7	77.1	-4.82	0.68	0.68	0.98	0.00	0.00
4	0.93	1	0.07	76.0	1.27	0.13	1.00	-4.38	43.7	77.1	-4.82	0.68	0.68	0.97	1.00	0.04
5	1	1.3	0.3	120.9	1.61	0.15	1.00	-3.87	63.2	120.8	-3.35	0.29	0.29	0.91	1.00	0.04
6	1.3	1.85	0.55	216.0	1.32	0.17	1.00	-3.29	91.3	188.3	-1.06	0.02	0.02	0.96	1.00	0.01
7	1.85	2.15	0.3	5.6	2.99	0.19	0.11	-2.96	0.0	-0.8	-7.46	1.00	0.11	0.06	1.00	0.00
8	2.15	2.95	0.8	28.9	2.14	0.22	0.93	-2.64	9.9	12.2	-7.01	1.00	0.93	0.52	1.00	0.23
9	2.95	10.2	7.25	5.1	3.30	0.29	0.02	-1.88	0.0	-0.8	-7.46	1.00	0.02	0.01	1.00	0.00
10	10.2	11.85	1.65	50.6	2.14	0.34	0.94	-1.59	28.4	45.6	-5.89	1.00	0.94	0.06	1.00	0.05
11	11.85	13.3	1.45	16.5	2.76	0.34	0.30	-1.55	0.0	-0.8	-7.46	1.00	0.30	0.00	1.00	0.00
12	13.3	14.9	1.6	8.8	3.18	0.35	0.04	-1.52	0.0	-0.8	-7.46	1.00	0.04	0.00	1.00	0.00
13	14.9	16.75	1.85	37.3	2.22	0.35	0.90	-1.49	18.0	26.0	-6.55	1.00	0.90	0.01	1.00	0.01
14	16.75	17.6	0.85	97.0	1.83	0.36	0.99	-1.47	53.7	99.0	-4.08	0.99	0.98	0.02	1.00	0.01
15	17.6	17.8	0.2	34.2	2.59	0.36	0.53	-1.47	15.2	21.1	-6.71	1.00	0.53	0.00	1.00	0.00
16	17.8	18.55	0.75	72.7	1.94	0.36	0.98	-1.46	41.9	73.4	-4.95	1.00	0.98	0.01	1.00	0.00
17	18.55	18.8	0.25	122.6	1.70	0.36	0.99	-1.46	63.8	122.2	-3.30	0.96	0.95	0.02	1.00	0.00
18	18.8	19.6	0.8	87.9	1.96	0.36	0.97	-1.45	49.5	89.8	-4.39	0.99	0.97	0.01	1.00	0.00
19	19.6	19.85	0.25	31.2	2.67	0.36	0.42	-1.44	12.2	16.0	-6.89	1.00	0.42	0.00	1.00	0.00
20	19.85	21.1	1.25	105.5	1.83	0.36	0.99	-1.43	57.2	107.0	-3.81	0.98	0.97	0.01	1.00	0.00
21	21.1	21.4	0.3	70.7	2.19	0.37	0.92	-1.42	40.8	71.1	-5.02	1.00	0.91	0.00	1.00	0.00

Table 7-12. Computation of P[M_P] for Mihama-Ward CPT009.

Layer #	z_{top} (m)	z_{bot} (m)	t (m)	q_{c1Ncs}	I_c	$CSR_{M\ 7.5,1atm}$	PF_S	$\widehat{CSR}$	D_R (%)	$\widehat{D_R}$	$\widehat{CRR}$	$PF_{T\|S}$	PF_T	$PF_{M\|T}$	K_{Sat}	P[M_L]
1	0.1	0.2	0.1	15.9	1.29	0.13	1.00	-4.39	0.0	-0.8	-7.46	1.00	0.99	0.98	0.00	0.00
2	0.2	0.6	0.4	124.4	0.86	0.13	1.00	-4.39	64.5	123.7	-3.25	0.12	0.12	0.99	0.00	0.00
3	0.6	1	0.4	228.5	0.92	0.13	1.00	-4.40	94.2	195.7	-0.81	0.00	0.00	0.99	0.00	0.00
4	1	1.3	0.3	9.6	2.49	0.13	0.66	-4.44	0.0	-0.8	-7.46	0.99	0.66	0.32	0.00	0.00
5	1.3	1.79	0.49	106.7	1.38	0.13	1.00	-4.35	57.7	108.2	-3.77	0.27	0.27	0.95	0.00	0.00
6	1.79	1.9	0.11	106.7	1.38	0.13	1.00	-4.35	57.7	108.2	-3.77	0.27	0.27	0.94	1.00	0.02
7	1.9	2.35	0.45	5.6	2.86	0.14	0.20	-3.91	0.0	-0.8	-7.46	1.00	0.20	0.09	1.00	0.00
8	2.35	4.3	1.95	50.6	1.74	0.19	0.99	-3.05	28.4	45.7	-5.88	0.99	0.99	0.80	1.00	0.78
9	4.3	5.5	1.2	2.4	3.63	0.23	0.00	-2.52	0.0	-0.8	-7.46	1.00	0.00	0.00	1.00	0.00
10	5.5	5.9	0.4	56.0	1.95	0.24	0.98	-2.34	32.1	53.0	-5.64	1.00	0.97	0.40	1.00	0.09
11	5.9	6.45	0.55	6.3	3.05	0.25	0.08	-2.27	0.0	-0.8	-7.46	1.00	0.08	0.01	1.00	0.00
12	6.45	7.5	1.05	73.2	1.72	0.26	0.99	-2.15	42.2	73.9	-4.93	0.99	0.99	0.51	1.00	0.31
13	7.5	9.35	1.85	6.9	3.22	0.28	0.03	-2.01	0.0	-0.8	-7.46	1.00	0.03	0.00	1.00	0.00
14	9.35	10.05	0.7	25.1	2.32	0.29	0.84	-1.90	5.7	5.9	-7.23	1.00	0.84	0.05	1.00	0.01
15	10.05	10.95	0.9	67.8	1.86	0.30	0.99	-1.85	39.2	67.7	-5.14	1.00	0.98	0.16	1.00	0.07
16	10.95	13.6	2.65	18.0	2.74	0.31	0.33	-1.77	0.0	-0.8	-7.46	1.00	0.33	0.01	1.00	0.00
17	13.6	15.7	2.1	69.9	1.92	0.32	0.98	-1.69	40.4	70.1	-5.06	1.00	0.98	0.04	1.00	0.05
18	15.7	16.05	0.35	29.5	2.48	0.33	0.67	-1.66	10.5	13.2	-6.98	1.00	0.67	0.00	1.00	0.00
19	16.05	17.6	1.55	81.2	1.85	0.33	0.99	-1.63	46.3	82.8	-4.63	0.99	0.98	0.02	1.00	0.02
20	17.6	18	0.4	205.3	1.43	0.33	1.00	-1.61	88.6	181.7	-1.28	0.36	0.36	0.06	1.00	0.00
21	18	18.3	0.3	62.0	2.13	0.33	0.94	-1.60	35.8	60.5	-5.38	1.00	0.94	0.00	1.00	0.00
22	18.3	20	1.7	132.8	1.81	0.34	0.99	-1.58	67.4	130.6	-3.01	0.92	0.91	0.01	1.00	0.01

8 Summary

8.1 Scope of Research

In this thesis, I have provided a framework for liquefaction modeling that includes discrete steps for susceptibility, triggering, and manifestation. While the susceptibility model is adapted from prior literature, the triggering and manifestation models have been regressed and updated from a greatly expanded and improved laboratory and case history data. In collaboration with research partners, I have clarified the meaning of key terms in liquefaction analysis and provided a framework by which the different effects can be evaluated in a consistent and rational manner that is probabilistic and performance based. In the preceding chapters, I described several significant aspects of the model development process, such as:

- using the extensive NGL case history database (Chapter 2) to perform analyses that previously would have been logistically impractical,
- exploring the uncertainties in critical layer selection and finding this process to be non-repeatable among several analysts and when compared to critical layers used in legacy models (Section 3.3-3.4)
- using algorithms to process case history data and provide repeatable, consistent, and objective views of the data (Chapter 5),
- identifying layers within continuous CPT profiles (Section 5.3),
- estimating *FC* from CPT data using a new relationship derived using the NGL database (Section 5.4.2),
- interpreting susceptibility in a probabilistic manner using CPT data which captures variability and epistemic uncertainty in current models to define the Bayesian prior probability distribution for susceptibility PF_S (Section 6.1),
- incorporating knowledge from laboratory tests into the model development process by using a rich database of cyclic test results spanning a wide parameter

space to define the Bayesian prior probability for susceptibility-conditioned triggering, $PF_{T|S}$ (Section 6.2),

- modeling surface manifestation conditional on liquefaction having triggered ($PF_{M|T}$) while updating Bayesian posterior models for triggering given susceptibility and susceptibility within one or more layers through probabilistic analysis of the NGL database (Section 6.3); this approach allows for an entire soil profile to be considered within the coupled triggering-manifestation framework (Chapter 4) and does not require identification of a specific critical layer.

The preceding chapters outline the approaches adopted to model critical relationships including probability of susceptibility conditional on I_c (PF_S), probability of triggering for susceptible layers conditional on state and stress demand ($PF_{T|S}$), probability of layer manifestation conditional on a layer triggering ($PF_{M|T}$), and probability of profile manifestation using contribution to manifestation from all layers within the profile (P[M_P]).

8.2 Major Findings and Application of Models

In this research, several impactful scientific advancements were achieved in conjunction with the P[M_P] model. First, liquefaction triggering within a subsurface soil layer is evaluated separately from surface manifestations of liquefaction. There exist case histories that exemplify that liquefaction should have triggered within a layer but caused no evidence of surface manifestations (Section 4.1.4). Cyclic laboratory test data suggest that triggering occurs at lower *CSR* values compared with previous legacy models because the legacy models were developed using evidence of surface manifestations rather than liquefaction triggering within a layer. Therefore, while these legacy models are widely considered to be triggering models, and are applied as such in practice, in effect they reflect variable effects of surface manifestation. Because surface manifestation

effects are not specifically modelled in the models, the degree to which these models apply to a given situation is highly variable, as described through a number of examples in this thesis (Sections 3.5 and 4.1.4).

This research aimed to overcome these issues by modeling both triggering and manifestation. An initial (prior) triggering model was developed using laboratory data, extending work by a collaborating researcher (Kristin Ulmer) who led the development of a database and produced an initial model for triggering probability given relative density of sand. Case history data are then used to develop a separate model that predicts manifestation given triggering of a layer while simultaneously updating the prior triggering model to a posterior. This framework is a significant innovation because it distinguishes between liquefaction triggering and manifestation while utilizing empirical data from both laboratory testing and case histories to train both models.

Another innovative aspect of the framework is that it does not use the historical critical layer approach but instead considers attributes of the entire soil profile. Legacy models require appreciable analyst judgement and do not incorporate profile information beyond attributes of the critical layer, which limits model efficacy. Attributes of individual layers found to be especially impactful regarding surface manifestation include factors affecting susceptibility (soil behavior type index, I_c), factors affecting triggering for susceptible soils (relative density, layer *CSR*), layer thickness (t), layer I_c, and depth to top of layer (z_{top}). These attributes are considered for every layer within the profile in the formulation of models for individual layer and profile manifestation probabilities (P[M_L] and P[M_P], respectively).

An important point about the recommended P[M_P] model is that because it considers the entire soil profile, the model is not intended to be used for prediction of manifestation for a single layer that might be judged as being critical according to whatever criteria an analyst may choose to apply. The manifestation model is trained using profiles that are 15m or longer and therefore is applicable in forward applications to profiles with length ≥ 15m or for shorter profiles for which the engineer is confident that layers below the profile depth are not capable of seismic pore pressure generation. Limitations of the model include the following:

1. The model does not consider all of the system effects that can affect individual sites, such as reductions of demand caused by liquefaction of a deep layer early in the ground motion time series (Cubrinovski et al. 2019).
2. The triggering model represents an average triggering response across a wide range of soil materials and could be biased for individual materials.
3. The susceptibility model is subject to large epistemic uncertainty, and as improved models are developed in the future, the subsequent model components (triggering, manifestation) could be affected.

8.3 Recommendations for Future Work

The innovative framework in this research opens a large number of future research opportunities. One important opportunity is to include contributions from cyclic softening of clay layers to ground failure. There are examples from the NGL case history data set of cases in which manifestation (e.g., ground cracking) was observed but for which the recommended P[M_P] model

incorrectly predicts no manifestations. A number of these cases are likely caused by cyclic softening of clays that were under a static shear stress (e.g., Balboa Boulevard (SITE_ID=429) and Koyo Junior High School (SITE_ID=546)). Additionally, there may be additional attributes of sites (related to profile geometry, hydraulic attributes, or soil properties) that could be investigated for their impact on the $PF_{M|T}$ model. Future work could investigate the benefits of site-specific updates to triggering and susceptibility models, particularly in relation to uncertainty reduction. Future models would also benefit from the introduction of a probabilistic K_{Sat} model that could be based on depth to the ground water table and p-wave velocity measurements and then applied to the triggering relationship to obtain a saturation dependent *CRR* relationship. Work that could be considered in the development of such models was presented by Zhang et al. (2016), among others.

The model developed here is based on a 1D representation of a site, using data from a single CPT sounding. However, the sites from which the observations are made have variable levels of geologic and profile complexity, which likely affect manifestation responses in complex ways. Future work could extend the current framework by considering information from multiple CPTs to capture this variability and potentially improve predictive accuracy. The NGL database has site data that could be used to pursue these lines of investigation.

An important research need is to utilize this framework to create a P[M_P] model that utilizes data from borings with stratigraphic logs and measured blow counts in granular layers. This is the next task for the NGL SMT and is currently being pursued by the team. Further research into the P[S] model is also warranted. While the susceptibility prior remains relatively unchanged in the recommended P[M_P] model, a new project is beginning with several team members from this project that will aim to improve the modeling of liquefaction susceptibility given CPT results, lab-

based index properties, and potentially parameters related to undrained strength normalization. This will update the prior susceptibility model that is used as the PF_S term in the P[M_P] model.

Appendix A

Schema Dictionary of Laboratory Component of NGL Database

Level	Column Name	Data Type	Extra	Description	Units
Table	LAB			Table for laboratory information	
PK	LAB_ID	INT(6)	UNSIGNED AUTO_INCREMENT	Unique ID for entries in the LAB table	
Field	LAB_NAME	VARCHAR(64)		Name of the Laboratory	
Field	LAB_LAT	DOUBLE	NULL	Latitude of the laboratory in decimal degree following WGS84 system	
Field	LAB_LON	DOUBLE	NULL	Longitude of the laboratory in decimal degree following WGS84 system	
Field	LAB_DESC	VARCHAR(1000)		Description of the Laboratory	
Table	LAB_PROGRAM			Table for laboratory testing program information	
PK	LAB_PROGRAM_ID	INT(6)	UNSIGNED AUTO_INCREMENT	Unique ID for entries in the LAB_PROGRAM table	
FK	LAB_ID	INT(6)	UNSIGNED AUTO_INCREMENT	Unique ID for entries in the LAB table	
Field	LAB_PROGRAM_DESC	VARCHAR(1000)		Description of the laboratory testing program	
Table	LAB_PROGRAM_SAMP			Junction table between SAMP and LAB_PROGRAM Tables	
PK	LAB_PROGRAM_SAMP_ID	INT(6)	UNSIGNED AUTO_INCREMENT	Unique ID for entries in the LAB_PROGRAM_SAMP table	
FK	LAB_PROGRAM_ID	INT(6)	UNSIGNED	Unique ID for entries in the LAB_PROGRAM table	

Field	SAMP_ID	INT(6)	UNSIGNED	Unique ID for the table SAMP	
Table	TEST			Table for test information	
Field	TEST_ID	INT(6)	UNSIGNED AUTO_INCREMENT	Unique ID for table TEST	
Field	SITE_ID	INT(6)	UNSIGNED	Unique ID for the table SITE	
Field	TEST_NAME	VARCHAR(64)		Test name	
Field	TEST_TYPE	VARCHAR(4)		Test type (i.e., Boring, Cone penetration testing, Test pit, Geophysical testing using surface wave, Invasive geophysical testing)	
Field	TEST_LAT	DOUBLE	NULL	Latitude of activity in decimal degree following WGS84 system	deg
Field	TEST_LON	DOUBLE	NULL	Longitude of activity in decimal degree following WGS84 system	deg
Field	TEST_REM	VARCHAR(1000)		Remark	
Field	TEST_STAT	tinyint(2)		For upload status (1 = submitted / 0 = temporal)	
Field	TEST_REVW	tinyint(2)		For review status (1 = reviewed / 0 = not reviewed)	
Table	SAMP			Table for sample information	
Field	SAMP_ID	INT(6)	UNSIGNED AUTO_INCREMENT	Unique ID for the table SAMP	
Field	SAMP_NAME	VARCHAR(64)		Name of sample	
Field	SAMP_TYPE	VARCHAR(20)		Sampler type. Example: - Shelby tube - Split-barrel (SPT) - Bulk (test pit) - CPT sampler	
Field	SAMP_TOP	FLOAT	NULL	Depth to the top of sample.	m
Field	SAMP_BASE	FLOAT	NULL	Depth to the base of sample.	m
Field	SAMP_SDIA	FLOAT	NULL	Sample diameter (e.g., 100 mm)	mm

Field	SAMP_DATE	TIMESTAMP		Date of sampling	m
Field	SAMP_REC	FLOAT	NULL	Sample recovery rate (%)	%
Field	SAMP_DESC	VARCHAR(1000)		Sample soil description (e.g., gray silty CLAY)	
Field	SAMP_REM	VARCHAR(1000)		Remark	
Table	SAMP_TEST			Junction table between SAMP and TEST Tables	
PK	SAMP_TEST_ID	INT(6)	UNSIGNED AUTO_INCREMENT	Unique ID for entries in the SAMP_TEST table	
FK	SAMP_ID	INT(6)	UNSIGNED	Unique ID for the table SAMP	
FK	TEST_ID	INT(6)	UNSIGNED	Unique ID for table TEST	
Table	SPEC			General information for laborotary tests, location of specimens	
Field	SPEC_ID	INT(6)	UNSIGNED AUTO_INCREMENT	Unique ID for the table SPEC	
Field	SAMP_ID	INT(6)	UNSIGNED	Unique ID for the table SAMP	
Field	SPEC_REF	VARCHAR(64)		Reference name specified for a specimen within a sample	
Field	SPEC_TOP	FLOAT	NULL	Depth to the top of specimen from the surface of borehole	m
Field	SPEC_BASE	FLOAT	NULL	Depth to the bottom of specimen from the surface of borehole	m
Field	SPEC_CREW	VARCHAR(100)		Name of testing technician and organization (e.g., Dong Youp Kwak / UCLA).	
Field	SPEC_REM	VARCHAR(1000)		Remark	
Table	INDX			Index tests include - density (ASTM D7263-09), - water content (ASTM D2216-10), and - atterberg limit tests (ASTM D4318-10e1). Standards recommended for each test are in parentheses.	
Field	INDX_ID	INT(6)	UNSIGNED AUTO_INCREMENT	Unique ID for the table INDX	
Field	SPEC_ID	INT(6)	UNSIGNED	Unique ID for the table SPEC	

Field	INDX_BDEN	FLOAT	NULL	Total density of soil	g/cm3
Field	INDX_DDEN	FLOAT	NULL	Dry density of soil	g/cm3
Field	INDX_GS	FLOAT	NULL	Specific gravity of solid particles	g/cm3
Field	INDX_WC	FLOAT	NULL	Natural water (moisture) content	%
Field	INDX_FINE	FLOAT	NULL	Fines content (Portion of particle passing the No.200 sieve; 0.075 mm)	%
Field	INDX_METH	VARCHAR(1000)		Method (Standard) used for index tests if different from recommended standards: - density: ASTM D7263-09; - water content: ASTM D2216-10; - atterberg limit: ASTM D4318-10e1.	
Field	INDX_CREW	VARCHAR(100)		#N/A	
Field	INDX_REM	VARCHAR(1000)		Remark	
Table	RDEN			Relative density measurement	
Field	RDEN_ID	INT(6)	UNSIGNED AUTO_INCREMENT	Unique ID for the table RDEN	
Field	SPEC_ID	INT(6)	UNSIGNED	Unique ID for the table SPEC	
Field	RDEN_EMIN	FLOAT	NULL	Minimum of void ratio	
Field	RDEN_EMAX	FLOAT	NULL	Maximum of void ratio	
Field	RDEN_METH	VARCHAR(1000)		Method for measuring relative density	
Field	RDEN_REM	VARCHAR(1000)		Remark	
Table	PLAS			Plasticity test (i.e., Liquid limit and plasticity limit) information	
Field	PLAS_ID	INT(6)	UNSIGNED AUTO_INCREMENT	Unique ID for the table PLAS	
Field	SPEC_ID	INT(6)	UNSIGNED	Unique ID for the table SPEC	
Field	PLAS_LL	FLOAT	NULL	Liquid limit	%

Field	PLAS_PL	FLOAT	NULL	Plastic limit	%
Field	PLAS_METH	VARCHAR(1000)		Method (Standard) used for plasticity test.	
Field	PLAS_REM	VARCHAR(1000)		Remark	
Table	GRAG			General information for particle size distribution analysis	
Field	GRAG_ID	INT(6)	UNSIGNED AUTO_INCREMENT	Unique ID for the table GRAG	
Field	SPEC_ID	INT(6)	UNSIGNED	Unique ID for the table SPEC	
Field	GRAG_METH	VARCHAR(1000)		Method used for particle distribution analysis	
Field	GRAG_REM	VARCHAR(1000)		Remark	
Table	GRAT			Test results (% passing for a specific sieve) from particle size distribution anlaysis	
Field	GRAT_ID	INT(6)	UNSIGNED AUTO_INCREMENT	Unique ID for the table GRAT	
Field	GRAG_ID	INT(6)	UNSIGNED	Unique ID for the table GRAG	
Field	GRAT_SIZE	FLOAT	NULL	Sieve or particle size (mm).	mm
Field	GRAT_PERP	FLOAT	NULL	Percentage passing/finer than sieve size (%).	%
Table	OTHR			Other tests not specified above. Any format of test results can be uploaded.	
Field	OTHR_ID	INT(6)	UNSIGNED AUTO_INCREMENT	Unique ID for the table OTHR	
Field	SPEC_ID	INT(6)	UNSIGNED	Unique ID for the table SPEC	
Field	OTHR_NAME	VARCHAR(100)		Name of the test uploaded.	
Field	OTHR_TYPE	VARCHAR(50)		Other test types - This is a catch all table for tests that do not have a dedicated table in the schema	
Field	OTHR_DESC	VARCHAR(1000)		Description of uploaded file.	

Field	FILE_ID	INT(6)	UNSIGNED	Unique ID for the table FILE	
Table	FILE			Table for files	
Field	FILE_ID	INT(6)	UNSIGNED AUTO_INCREMENT	Unique ID for the table FILE	
Field	FILE_NAME	VARCHAR(256)		File name of uploaded file	
Field	FILE_TYPE	VARCHAR(256)		File type of uploaded file	
Field	FILE_SIZE	VARCHAR(32)		File size of uploaded file	
Field	FILE_FILE	MEDIUMBLOB		File uploaded as a MEDIUMBLOB	
Table	DSSG			Table for direct simple shear test general information	
Field	DSSG_ID	INT(6)	UNSIGNED AUTO_INCREMENT	Unique ID for entries in the DSSG table	
Field	SPEC_ID	INT(6)	UNSIGNED AUTO_INCREMENT	Unique ID for the table SPEC	
Field	DSSG_E0	FLOAT		Initial void ratio	
Field	DSSG_W0	FLOAT		Initial water content (%)	%
Field	DSSG_DIAM	FLOAT		Specimen diameter (cm)	cm
Field	DSSG_H0	FLOAT		Specimen initial height (cm)	cm
Field	DSSG_CREW	VARCHAR(100)		#N/A	
Field	DSSG_DESC	VARCHAR(1000)		Description of test/specimen	
Table	DSSS			Table for information about each direct simple shear test stage	
Field	DSSS_ID	INT(6)	UNSIGNED AUTO_INCREMENT	Unique ID for entries in the DSSS table	
Field	DSSG_ID	INT(6)	UNSIGNED AUTO_INCREMENT	Unique ID for entries in the DSSG table	
Field	DSSS_ST	INT(6)	UNSIGNED AUTO_INCREMENT	Stage Number	

Field	DSSS_TY	TINYINT(2)		Type of Stage (i.e. Consolidation(0), Monotonic Loading(1), Cyclic Load(2), etc.)	
Field	DSSS_DR	TINYINT(2)		Is the stage drained(0), undrained(1), or neither(2)	
Field	DSSS_DESC	VARCHAR(1000)		Description of stage	
Table	DSSD1D			Table for one dimensional direct simple shear test data	
Field	DSSD1D_ID	INT(6)	UNSIGNED AUTO_INCREMENT	Unique ID for entries in the DSSD1D table	
Field	DSSS_ID	INT(6)	UNSIGNED AUTO_INCREMENT	Unique ID for entries in the DSSS table	
Field	DSSD1D_TIME	FLOAT		Time (sec)	sec
Field	DSSD1D_TAU	FLOAT		Shear Stress (kPa)	kPa
Field	DSSD1D_SIGV	FLOAT		Vertical Stress (kPa)	kPa
Field	DSSD1D_YHV	FLOAT		Shear Strain (%)	%
Field	DSSD1D_EPSV	FLOAT		Vertical Strain (%)	%
Table	DSSD2D			Table for two dimensional direct simple shear test data	
Field	DSSD2D_ID	INT(6)	UNSIGNED AUTO_INCREMENT	Unique ID for entries in the DSSD2D table	
Field	DSSS_ID	INT(6)	UNSIGNED AUTO_INCREMENT	Unique ID for entries in the DSSS table	
Field	DSSD2D_TIME	FLOAT		Time (sec)	sec
Field	DSSD2D_TAU1	FLOAT		Shear Stress in axis 1 (kPa)	kPa
Field	DSSD2D_TAU2	FLOAT		Shear Stress in axis 2 (kPa)	kPa
Field	DSSD2D_SIGV	FLOAT		Vertical Stress (kPa)	kPa

Field	DSSD2D_YHV1	FLOAT		Shear Strain in axis 1 (%)	%
Field	DSSD2D_YHV2	FLOAT		Shear Strain in axis 2 (%)	%
Field	DSSD2D_EPSV	FLOAT		Vertical Strain (%)	%
Table	TXG			Table for Triaxial Test general information	
Field	TXG_ID	INT(6)	UNSIGNED AUTO_INCREMENT	Unique ID for entries in the TXG table	
Field	SPEC_ID	INT(6)	UNSIGNED AUTO_INCREMENT	Unique ID for the table SPEC	
Field	TXG_E0	FLOAT		Initial void ratio	
Field	TXG_W0	FLOAT		Initial water content (%)	%
Field	TXG_DIAM	FLOAT		Specimen diameter (cm)	cm
Field	TXG_H0	FLOAT		Specimen initial height (cm)	cm
Field	TXG_B	FLOAT		Measured B value	decimal
Field	TXG_BSTG	INT(6)		Stage number that occurred immediately after the B value test	
Field	TXG_DESC	VARCHAR(1000)		Description of test/specimen	
Table	TXS			General information for triaxial test stages	
Field	TXS_ID	INT(6)	UNSIGNED AUTO_INCREMENT	Unique ID for entries in the TXS table	
Field	TXG_ID	INT(6)	UNSIGNED AUTO_INCREMENT	Unique ID for entries in the TXG table	
Field	TXS_ST	INT(6)	UNSIGNED AUTO_INCREMENT	Stage Number	
Field	TXS_TY	TINYINT(2)		Type of Stage (i.e. Consolidation(0), Monotonic Loading(1), Cyclic Load(2), etc.)	
Field	TXS_DR	TINYINT(2)		Is the stage drained(0), undrained(1), or neither(2)	
Field	TXS_DESC	VARCHAR(1000)		Description of stage	

Table	TXD			Table for the test data from triaxial	
Field	TXD_ID	INT(6)	UNSIGNED AUTO_INCREMENT	Unique ID for entries in the TXD table	
Field	TXS_ID	INT(6)		Unique ID for entries in the TXS table	
Field	TXD_TIME	FLOAT		Time (sec)	sec
Field	TXD_SD	FLOAT		Deviator Stress (kPa)	kPa
Field	TXD_CP	FLOAT		Cell Pressure (kPa)	kPa
Field	TXD_PP	FLOAT		Pore Pressure (kPa)	kPa
Field	TXD_EA	FLOAT		Axial Strain (%)	%
Field	TXD_ER	FLOAT		Radial Strain (%)	%
Field	TXD_EV	FLOAT		Volumetric Strain (%)	%
Table	CONG			Table for the general metadata of a consolidation test	
Field	CONG_ID	INT(6)	UNSIGNED AUTO_INCREMENT	Unique ID for entries in the CONG table	
Field	SPEC_ID	INT(6)	Foreign Key	Unique ID for the table SPEC	
Field	CONG_H0	FLOAT		Initial height of the consolidation specimen (cm)	cm
Field	CONG_D0	FLOAT		Diameter of the consolidation specimen (cm)	cm
Field	CONG_E0	FLOAT		Initial void ratio of the consolidation specimen	
Field	CONG_W0	FLOAT		Initial water content of the consolidation specimen (%)	%
Field	CONG_S0	FLOAT		Initial saturation of the consolidation specimen (%)	%
Field	CONG_DR	BOOLEAN		Drainage state of the consolidation test (0=double, 1=single)	
Table	CON_STGE			Table for consolidation test stage general information	
Field	CON_STGE_ID	INT(6)	UNSIGNED AUTO_INCREMENT	Unique ID for entries in the CON_STGE table	
Field	CONG_ID	INT(6)	Foreign Key	Unique ID for entries in the CONG table	
Field	CON_STGE_NUMB	INT(6)		Consolidation stage number	

Field	CON_STGE_SIGV	FLOAT		Vertical total stress (kPa)	kPa
Table	COND			Table for consolidation test data	
Field	COND_ID	INT(6)	UNSIGNED AUTO_INCREMENT	Unique ID for entries in the COND table	
Field	CON_STGE_ID	INT(6)	Foreign Key	Unique ID for entries in the CON_STGE table	
Field	COND_TIME	FLOAT		Consolidation time (sec)	sec
Field	COND_DISP	FLOAT		Consolidation displacement (cm)	cm

Appendix B

Parameters in the Summary pkl File Containing SMT's Processed Case History Data.

Parameter	Description	Classification
TEST_ID	primary key in test table	metadata
dGWT	depth to groundwater table (m)	layer
ztop	depth to top of layer (m)	layer
zbot	depth to bottom of layer (m)	layer
qc min	minimum qc within layer (kPa)	layer
qc avg	average qc within layer (kPa)	layer
qc 30%	30th percentile qc within layer (kPa)	layer
qc 50%	median qc within layer (kPa)	layer
qc max	maximum qc within layer (kPa)	layer
qc std	standard deviation of qc within layer (kPa)	layer
fs min	minimum fs within layer (kPa)	layer
fs avg	average fs within layer (kPa)	layer
fs 30%	30th percentile fs within layer (kPa)	layer
fs 50%	median qc within layer (kPa)	layer
fs max	maximum fs within layer (kPa)	layer
fs std	standard deviation of fs within layer (kPa)	layer
sigma_v min	minimum vertical total stress (kPa)	layer
sigma_v avg	average vertical total stress (kPa)	layer
sigma_v 50%	median vertical effective stress (kPa)	layer
sigma_v max	maximum vertical total stress (kPa)	layer

sigmap_v min	minimum vertical effective stress (kPa)	layer
sigmap_v avg	average vertical effective stress (kPa)	layer
sigmap_v 50%	median vertical effective stress (kPa)	layer
sigmap_v max	maximum vertical effective stress (kPa)	layer
Ic min	minimum soil behavior type index	layer
Ic avg	average soil behavior type index	layer
Ic 30%	30th percentile soil behavior type index	layer
Ic 50%	median soil behavior type index	layer
Ic 70%	70th percentile soil behavior type index	layer
Ic max	maximum soil behavior type index	layer
Ic std	standard deviation of soil behavior type index	layer
qc1Ncs min	minimum normalized clean sand cone tip resistance	layer
qc1Ncs avg	average normalized clean sand cone tip resistance	layer
qc1Ncs 30%	30th percentile normalized clean sand cone tip resistance	layer
qc1Ncs 50%	median normalized clean sand cone tip resistance	layer
qc1Ncs max	maximum normalized clean sand cone tip resistance	layer
qc1Ncs std	standard deviation of normalized clean sand cone tip resistance	layer
CSR avg	average cyclic stress ratio computed using Idriss (1999) r_d	layer
I_B	modified soil behavior type index	layer
Su	undrained shear strength (kPa)	layer
taucycsu	cyclic shear stress divided by undrained shear strength	layer

IF_layer	layer interbeddedness factor (number of double threshold crossings above the layer, where Ic_thresh1 = 2.34, Ic_thresh2 = 2.93)	layer
H1	thickness of nonliquefiable crust (m)	profile
SITE_ID	primary key of site table	metadata
SITE_NAME	site name	metadata
TEST_NAME	test name	metadata
EVNT_ID	primary key of event table	metadata
EVNT_NAME	event name	metadata
EVNT_MAG	earthquake mangitude	profile
PGA	peak horizontal acceleration (g)	profile
FLDM_ID	primary key of fldm (field observation) table	metadata
FLDM_SFEV	surface evidence of liquefaction (0 = no, 1 = yes)	profile
FLDM_DIST	distance between observation and cone penetration test (m)	profile
TEST weights	weights for observation in regression	profile
alltriggers	Total number of double Ic threshold crossings in the profile, where Ic_thresh1 = 2.34; Ic_thresh2 = 2.93	profile
FLDM_SNBL	sand boils (0 = no, 1 = yes)	profile
FLDM Slope (deg)	slope at observation location from 3-arc second digital elevation model (deg)	profile
TEST Slope (deg)	slope at test location from 3-arc second digital elevation model (deg)	profile
LPI	liquefaction potential index	profile
LSN	liquefaction severity number	profile
CR	crust strength (kN/m)	profile

LD	liquefaction ejecta demand parameter (kN/m)	profile
PGV	peak ground velocity (m/s)	profile
CAV	cumulative absolute velocity (m/s)	profile
I_a	arias intensity (m/s)	profile
CSR Lasley r_d	CSR computed using stress reduction coefficient from Lasley et al. (2017)	layer
MSF B&I	magnitude scaling factor from Boulanger and Idriss (2016)	layer
MSF Green et al	magnitude scaling factor from Green et al. (2019)	layer
MSF Green et al b=0.2	magnitude scaling factor from Green et al. (2019) for b = 0.2	layer
MSF Green et al b=0.28	magnitude scaling factor from Green et al. (2019) for b = 0.28	layer
Ksig I&B	K-sigma from Idriss and Boulanger (2008)	layer
Ksig Carlton	K-sigma for SMT model	layer
LDl	Liquefaction ejecta demand parameter within the layer (kN/m)	layer
CRl	Crust resistance above a layer (kN/m)	layer
qc1N	Overburden corrected cone tip resistance (kPa)	layer

References

American Society for Testing Materials. 2017a. “Test Methods for Determining the Amount of Material Finer than 75-m (No. 200) Sieve in Soils by Washing.” ASTM International.

American Society for Testing Materials. 2017b. “Test Methods for Liquid Limit, Plastic Limit, and Plasticity Index of Soils.” ASTM International.

American Society for Testing Materials. 2018. “Test Methods for Laboratory Determination of Density (Unit Weight) of Soil Specimens.” ASTM International.

American Society for Testing Materials. 2019. “Test Methods for Laboratory Determination of Water (Moisture) Content of Soil and Rock by Mass.” ASTM International.

American Society of Civil Engineers. 1958. “Glossary of Terms and Definition in Soil Mechanics.” *J. Soil Mech. Found. Div.*, 84 (4). https://doi.org/10.1061/JSFEAQ.0000142.

Ancheta, T. D., R. B. Darragh, J. P. Stewart, E. Seyhan, W. J. Silva, B. S.-J. Chiou, K. E. Wooddell, R. W. Graves, A. R. Kottke, D. M. Boore, T. Kishida, and J. L. Donahue. 2014. “NGA-West2 Database.” *Earthq. Spectra*, 30 (3): 989–1005. SAGE Publications Ltd STM. https://doi.org/10.1193/070913EQS197M.

Andrews, D. C. A., and G. R. Martin. 2000. “Criteria For Liquefaction Of Silty Soils.” *12th World Conf. Earthq. Eng.*, 8. Auckland, New Zealand.

Andrus, R. D., H. Hayati, and N. P. Mohanan. 2009. “Correcting Liquefaction Resistance for Aged Sands Using Measured to Estimated Velocity Ratio.” *J. Geotech. Geoenvironmental Eng.*, 135 (6): 735–744. American Society of Civil Engineers. https://doi.org/10.1061/(ASCE)GT.1943-5606.0000025.

Andrus, R. D., and K. H. Stokoe. 2000. “Liquefaction Resistance of Soils from Shear-Wave Velocity.” *J. Geotech. Geoenvironmental Eng.*, 126 (11): 1015–1025. American Society of Civil Engineers. https://doi.org/10.1061/(ASCE)1090-0241(2000)126:11(1015).

Andrus, R. D., K. H. Stokoe, R. M. Chung, and C. Hsein Juang. 2003. *Guidelines for Evaluating Liquefaction Resistance Using Shear Wave Velocity Measurement and Simplified Procedures*. NIST GCR. Gaithersburg, MD: National Institute of Standards and Technology.

Arab, A., I. Shahrour, and L. Lancelot. 2011. “Estudio en laboratorio sobre licuefacción de arena parcialmente saturada.” *J. Iber. Geol.*, 37 (1): 29–36. https://doi.org/10.5209/rev_JIGE.2011.v37.n1.2.

Bassett, R., and J. Deride. 2016. “Maximum a Posteriori Estimators as a Limit of Bayes Estimators.” *Math. Program.*, 174. https://doi.org/10.1007/s10107-018-1241-0.

Bengfort, B., L. Gray, R. Bilbro, P. Roman, P. Deziel, K. McIntyre, M. Morrison, A. Ojeda, E. Schmierer, A. Morris, S. Molin, Sangam Swadik, @Admo1, @Charlesincharge, and U. Nussbaum. 2022. “Yellowbrick v1.5.” Zenodo.

Bennett, M. J., T. L. Youd, E. L. Harp, and G. F. Wieczorek. 1981. *Subsurface investigation of liquefaction, Imperial Valley earthquake, California, October 15, 1979. Open-File Rep.* U.S. Geological Survey,.

Beyzaei, C. Z. 2017. "Fine-Grained Soil Liquefaction Effects in Christchurch, New Zealand." UC Berkeley.

Bol, E., A. Önalp, E. Arel, S. Sert, and A. Özocak. 2010. "Liquefaction of silts: the Adapazari criteria." *Bull. Earthq. Eng.*, 8 (4): 859–873. https://doi.org/10.1007/s10518-010-9174-x.

Boore, D. M., J. P. Stewart, E. Seyhan, and G. M. Atkinson. 2014. "NGA-West2 Equations for Predicting PGA, PGV, and 5% Damped PSA for Shallow Crustal Earthquakes." *Earthq. Spectra*, 30 (3): 1057–1085. https://doi.org/10.1193/070113EQS184M.

Boulanger, R. W. 2003a. "Relating Kα to Relative State Parameter Index." *J. Geotech. Geoenvironmental Eng.*, 129 (8): 770–773. American Society of Civil Engineers. https://doi.org/10.1061/(ASCE)1090-0241(2003)129:8(770).

Boulanger, R. W. 2003b. "High Overburden Stress Effects in Liquefaction Analyses." *J. Geotech. Geoenvironmental Eng.*, 129 (12): 1071–1082. American Society of Civil Engineers. https://doi.org/10.1061/(ASCE)1090-0241(2003)129:12(1071).

Boulanger, R. W., and J. T. Dejong. 2018. "Inverse filtering procedure to correct cone penetration data for thin-layer and transition effects." *Cone Penetration Test. 2018*. Netherlands: CRC Press.

Boulanger, R. W., and I. M. Idriss. 2006. "Liquefaction Susceptibility Criteria for Silts and Clays." *J. Geotech. Geoenvironmental Eng.*, 132 (11): 1413–1426. https://doi.org/10.1061/(ASCE)1090-0241(2006)132:11(1413).

Boulanger, R. W., and I. M. Idriss. 2012. "Probabilistic Standard Penetration Test–Based Liquefaction–Triggering Procedure." *J. Geotech. Geoenvironmental Eng.*, 138 (10): 1185–1195. American Society of Civil Engineers. https://doi.org/10.1061/(ASCE)GT.1943-5606.0000700.

Boulanger, R. W., and I. M. Idriss. 2014. *CPT and SPT based liquefaction triggering procedures*. 259. Davis, California: University of California, Davis.

Boulanger, R. W., and I. M. Idriss. 2016. "CPT-Based Liquefaction Triggering Procedure." *J. Geotech. Geoenvironmental Eng.*, 142 (2): 04015065. https://doi.org/10.1061/(ASCE)GT.1943-5606.0001388.

Boulanger, R. W., I. M. Idriss, and L. H. Mejia. 1995. *Investigation and Evaluation of Liquefaction Related Ground Displacements at Moss Landing During the 1989 Loma Prieta Earthquake*. 118. UCD/CGM. Davis, California: University of California, Davis.

Boulanger, R. W., L. H. Mejia, and I. M. Idriss. 1997. "Liquefaction at Moss Landing during Loma Prieta Earthquake." *J. Geotech. Geoenvironmental Eng.*, 123 (5): 453–467. American Society of Civil Engineers. https://doi.org/10.1061/(ASCE)1090-0241(1997)123:5(453).

Box, G. E. P., and D. R. Cox. 1964. “An Analysis of Transformations.” *J. R. Stat. Soc. Ser. B Methodol.*, 26 (2): 211–252. [Royal Statistical Society, Wiley].

Bozorgnia, Y., and J. Stewart. 2020. *Data Resources for NGA-Subduction Project*. PEER Reports. PEER Reports. Pacific Earthquake Engineering Research Center, University of California, Berkeley, CA.

Brandenberg, S. J., D. Y. Kwak, P. Zimmaro, Y. Bozorgnia, S. L. Kramer, and J. P. Stewart. 2018. “Next-Generation Liquefaction (NGL) Case History Database Structure.” *5th Decenn. Geotech. Earthq. Eng. Soil Dyn. Conf.*, 426–433. Austin, Texas, USA: American Society of Civil Engineers.

Brandenberg, S. J., J. P. Stewart, K. S. Hudson, and P. Zimmaro. 2020a. *Cyclic Softening and Post Cyclic Volume Change of Fine-Grained Soil*. Final Report for USGS Award.

Brandenberg, S. J., J. P. Stewart, P. Wang, C. C. Nweke, K. Hudson, C. A. Goulet, X. Meng, C. A. Davis, S. K. Ahdi, M. B. Hudson, A. Donnellan, G. Lyzenga, M. Pierce, J. Wang, M. A. Winters, M.-P. Delisle, J. Lucey, Y. Kim, T. W. Gallien, A. Lyda, J. S. Yeung, O. Issa, T. Buckreis, and Z. Yi. 2020b. “Ground Deformation Data from GEER Investigations of Ridgecrest Earthquake Sequence.” *Seismol. Res. Lett.*, 91 (4): 2024–2034. https://doi.org/10.1785/0220190291.

Brandenberg, S. J., P. Zimmaro, J. P. Stewart, D. Y. Kwak, K. W. Franke, R. E. Moss, K. Ö. Çetin, G. Can, M. Ilgac, J. Stamatakos, T. Weaver, and S. L. Kramer. 2020c. “Next-generation liquefaction database.” *Earthq. Spectra*, 36 (2): 939–959. SAGE Publications Ltd STM. https://doi.org/10.1177/8755293020902477.

Bray, J. D., and R. B. Sancio. 2006. “Assessment of the Liquefaction Susceptibility of Fine-Grained Soils.” *J. Geotech. Geoenvironmental Eng.*, 132 (9): 1165–1177. https://doi.org/10.1061/(ASCE)1090-0241(2006)132:9(1165).

Bray, J. D., R. B. Sancio, T. Durgunoglu, A. Onalp, T. L. Youd, J. P. Stewart, R. B. Seed, O. K. Cetin, E. Bol, M. B. Baturay, C. Christensen, and T. Karadayilar. 2004a. “Subsurface Characterization at Ground Failure Sites in Adapazari, Turkey.” *J. Geotech. Geoenvironmental Eng.*, 130 (7): 673–685. https://doi.org/10.1061/(ASCE)1090-0241(2004)130:7(673).

Bray, J. D., R. B. Sancio, M. Riemer, and H. T. Durgunoglu. 2004b. “Liquefaction Susceptibility of Fine-Grained Soils.”

Carraro, J. a. H., P. Bandini, and R. Salgado. 2003. “Liquefaction Resistance of Clean and Nonplastic Silty Sands Based on Cone Penetration Resistance.” *J. Geotech. Geoenvironmental Eng.*, 129 (11): 965–976. American Society of Civil Engineers. https://doi.org/10.1061/(ASCE)1090-0241(2003)129:11(965).

Casagrande, A. 1936. *Characteristics of cohesionless soils affecting the stability of slopes and earth fills*. Harvard University.

Cauchy, A. L. 1847. “Methode generale pour la resolution des systemes d’equations simultanees.” *Comptes Rendus Acad. Sci.*, 25: 536–538.

Cetin, K. O., and H. T. Bilge. 2014. “Unified Assessment of Stress Scaling Factors for Liquefaction Engineering Problems.” 4293–4302. American Society of Civil Engineers. https://doi.org/10.1061/9780784413272.415.

Cetin, K. O., H. T. Bilge, J. Wu, A. M. Kammerer, and R. B. Seed. 2009. “Probabilistic Model for the Assessment of Cyclically Induced Reconsolidation (Volumetric) Settlements.” *J. Geotech. Geoenvironmental Eng.*, 135 (3): 387–398. https://doi.org/10.1061/(ASCE)1090-0241(2009)135:3(387).

Cetin, K. O., and C. Ozan. 2009. “CPT-Based Probabilistic Soil Characterization and Classification.” *J. Geotech. Geoenvironmental Eng.*, 135 (1): 84–107. https://doi.org/10.1061/(ASCE)1090-0241(2009)135:1(84).

Cetin, K. O., R. B. Seed, A. Der Kiureghian, K. Tokimatsu, L. F. Harder, R. E. Kayen, and R. E. S. Moss. 2004. “Standard Penetration Test-Based Probabilistic and Deterministic Assessment of Seismic Soil Liquefaction Potential.” *J. Geotech. Geoenvironmental Eng.*, 130 (12): 1314–1340. American Society of Civil Engineers. https://doi.org/10.1061/(ASCE)1090-0241(2004)130:12(1314).

Cetin, K. O., R. B. Seed, R. E. Kayen, R. E. S. Moss, H. T. Bilge, M. Ilgac, and K. Chowdhury. 2018. “SPT-based probabilistic and deterministic assessment of seismic soil liquefaction triggering hazard.” *Soil Dyn. Earthq. Eng.*, 115: 698–709. https://doi.org/10.1016/j.soildyn.2018.09.012.

Cetin, K., R. Seed, R. Moss, A. Kiureghian, K. Tokimatsu, L. Jr, R. Kayen, and I. Idriss. 2000. *Field performance case histories for SPT-based evaluation of soil liquefaction triggering hazard*. Geotechnical Research Report. Berkeley, California: University of California, Berkeley.

Chiba City. 2012. “Field investigation data for liquefaction countermeasures.”

Ching, J., J.-S. Wang, C. H. Juang, and C.-S. Ku. 2015. “Cone penetration test (CPT)-based stratigraphic profiling using the wavelet transform modulus maxima method.” *Can. Geotech. J.*, 52 (12): 1993–2007. NRC Research Press. https://doi.org/10.1139/cgj-2015-0027.

Chu, D. B., J. P. Stewart, R. W. Boulanger, and P. S. Lin. 2008. “Cyclic Softening of Low-Plasticity Clay and Its Effect on Seismic Foundation Performance.” *J. Geotech. Geoenvironmental Eng.*, 134 (11): 1595–1608. https://doi.org/10.1061/(ASCE)1090-0241(2008)134:11(1595).

Chu, D. B., J. P. Stewart, S. Lee, J. S. Tsai, P. S. Lin, B. L. Chu, R. B. Seed, S. C. Hsu, M. S. Yu, and M. C. H. Wang. 2004. “Documentation of soil conditions at liquefaction and non-liquefaction sites from 1999 Chi–Chi (Taiwan) earthquake.” *Soil Dyn. Earthq. Eng.*, 24 (9–10): 647–657. https://doi.org/10.1016/j.soildyn.2004.06.005.

Contreras, V., J. P. Stewart, T. Kishida, R. B. Darragh, B. S. Chiou, S. Mazzoni, R. R. Youngs, N. M. Kuehn, S. K. Ahdi, K. Wooddell, R. Boroschek, F. Rojas, and J. Órdenes. 2022. “NGA-

Sub source and path database." *Earthq. Spectra*, 38 (2): 799–840. SAGE Publications Ltd STM. https://doi.org/10.1177/87552930211065054.

Cressie, N. A. C. 2015. *Statistics for spatial data*. Hoboken, NJ: John Wiley & Sons, Inc.

Cubrinovski, M., and K. Ishihara. 2002. "Maximum and Minimum Void Ratio Characteristics of Sands." *Soils Found.*, 42 (6): 65–78. https://doi.org/10.3208/sandf.42.6_65.

Cubrinovski, M., A. Rhodes, N. Ntritsos, and S. Van Ballegooy. 2019. "System response of liquefiable deposits." *Soil Dyn. Earthq. Eng.*, 124: 212–229. https://doi.org/10.1016/j.soildyn.2018.05.013.

Dobry, R., R. S. Ladd, F. Y. Yokel, R. M. Chung, and D. Powell. 1982. *Prediction of Pore Water Pressure Buildup and Liquefaction of Sands during Earthquakes by the Cyclic Strain Method.* 176. National Bureau of Standards, Washington, DC. National Engineering Lab.

Duputel, Z., L. Rivera, H. Kanamori, and G. Hayes. 2012. "W phase source inversion for moderate to large earthquakes (1990-2010): W phase inversion for Mw≥ 6.0 earthquakes." *Geophys. J. Int.*, 189 (2): 1125–1147. https://doi.org/10.1111/j.1365-246X.2012.05419.x.

Ecemis, N., and M. Karaman. 2014. "Influence of non-/low plastic fines on cone penetration and liquefaction resistance." *Eng. Geol.*, 181: 48–57. https://doi.org/10.1016/j.enggeo.2014.08.012.

Eslami, M. 2017. *Experimental mapping of elastoplastic surfaces for sand and cyclic failure of low-plasticity fine-grained soils.* University of California, Los Angeles.

Gagniuc, P. A. 2017. *Markov chains: from theory to implementation and experimentation*. Hoboken, NJ: John Wiley & Sons.

Gelman, A. 2006. "Prior distributions for variance parameters in hierarchical models (comment on article by Browne and Draper)." *Bayesian Anal.*, 1 (3). https://doi.org/10.1214/06-BA117A.

Gelman, A., J. B. Carlin, H. S. Stern, D. B. Dunson, A. Vehtari, and D. B. Rubin. 2014. *Bayesian data analysis*. Texts in statistical science series. Boca Raton London New York: CRC Press, Taylor and Francis Group.

Geyin, M., A. J. Baird, and B. W. Maurer. 2020a. "Field assessment of liquefaction prediction models based on geotechnical versus geospatial data, with lessons for each." *Earthq. Spectra*, 36 (3): 1386–1411. https://doi.org/10.1177/8755293019899951.

Geyin, M., B. Maurer, B. Bradley, R. Green, and S. van Ballegooy. 2020b. "CPT-Based Liquefaction Case Histories Resulting from the 2010-2016 Canterbury, New Zealand, Earthquakes: A Curated Digital Dataset (Version 2)." Designsafe-CI.

Goulet, C. A., Y. Wang, C. C. Nweke, B. Tang, P. Wang, K. S. Hudson, S. K. Ahdi, X. Meng, M. B. Hudson, A. Donnellan, G. A. Lyzenga, S. J. Brandenberg, J. P. Stewart, T. Gallien, and M. A. Winters. 2021. "Comparison of Near-Fault Displacement Interpretations from Field and Aerial Data for the **M** 6.5 and 7.1 Ridgecrest Earthquake Sequence Ruptures." *Bull. Seismol. Soc. Am.*, 111 (5): 2317–2333. https://doi.org/10.1785/0120200222.

Green, R. A., and S. Olson. 2015. “Interpretation of Liquefaction Field Case Histories for Use in Developing Liquefaction Triggering Curves.”

Green, R. A., C. Wood, B. Cox, M. Cubrinovski, L. Wotherspoon, B. Bradley, T. Algie, J. Allen, A. Bradshaw, and G. Rix. 2011. “Use of DCP and SASW Tests to Evaluate Liquefaction Potential: Predictions vs. Observations during the Recent New Zealand Earthquakes.” *Seismol. Res. Lett.*, 82 (6): 927–938. https://doi.org/10.1785/gssrl.82.6.927.

Haselton, M. G., D. Nettle, and D. R. Murray. 2015. “The Evolution of Cognitive Bias.” *Handb. Evol. Psychol.*, D. M. Buss, ed., 1–20. Wiley.

Hirschhorn, R., and T. Schonberg. 2024. “Replication.” *Ref. Module Neurosci. Biobehav. Psychol.*, B9780128204801000140. Elsevier.

Hoffman, M. D., and A. Gelman. 2011. “The No-U-Turn Sampler: Adaptively Setting Path Lengths in Hamiltonian Monte Carlo.” arXiv. https://doi.org/10.48550/ARXIV.1111.4246.

Hoffman, M. D., and A. Gelman. 2014. “The No-U-Turn Sampler: Adaptively Setting Path Lengths in Hamiltonian Monte Carlo.” *J. Mach. Learn. Res.*, 15 (47): 1593–1623.

Holzer, T. L., and T. L. Youd. 2007. “Liquefaction, Ground Oscillation, and Soil Deformation at the Wildlife Array, California.” *Bull. Seismol. Soc. Am.*, 97 (3): 961–976. https://doi.org/10.1785/0120060156.

Huang, Y.-M. 2008. “Performance-based design and evaluation for liquefaction-related seismic hazards.” *PhD Thesis*. Seattle, Washington, USA: University of Washington.

Hudson, K. S., S. J. Brandenberg, P. Zimmaro, K. J. Ulmer, S. L. Kramer, and J. P. Stewart. 2023a. “Relationship Between Fines Content and Soil Behavior Type Index at Liquefaction Sites.” *J. Geotech. Geoenvironmental Eng.*, Submitted for Review.

Hudson, K. S., S. J. Brandenberg, P. Zimmaro, K. Ulmer, S. L. Kramer, and J. P. Stewart. 2023b. “Kriging Interpolation of Ground Motion Residuals at Liquefaction Case History Sites.” *Geo-Congr. 2023*, 365–372. Los Angeles, California: American Society of Civil Engineers.

Hudson, K. S., K. J. Ulmer, P. Zimmaro, S. L. Kramer, J. P. Stewart, and S. J. Brandenberg. 2023c. “Relationship between fines content (FC) and soil behavior type index (Ic).” Designsafe-CI.

Hudson, K. S., K. J. Ulmer, P. Zimmaro, S. L. Kramer, J. P. Stewart, and S. J. Brandenberg. 2023d. “Unsupervised machine learning for detecting soil layer boundaries from cone penetration test data.” *Earthq. Eng. Struct. Dyn.*, 52 (11): 3201–3215. https://doi.org/10.1002/eqe.3961.

Hudson, K. S., P. Zimmaro, K. Ulmer, B. Carlton, A. Stuedlein, A. Jana, A. Dadashiserej, S. J. Brandenberg, J. Stamatakos, S. L. Kramer, and J. P. Stewart. 2022. “Laboratory Component of Next-Generation Liquefaction Project Database.” *Proc. 4th Int. Conf. Perform. Based Des. Earthq. Geotech. Eng. Beijing 2022*, Geotechnical, Geological and Earthquake Engineering, L. Wang, J.-M. Zhang, and R. Wang, eds., 1865–1874. Cham: Springer International Publishing.

Hutabarat, D., and J. D. Bray. 2021. “Effective Stress Analysis of Liquefiable Sites to Estimate the Severity of Sediment Ejecta.” *J. Geotech. Geoenvironmental Eng.*, 147 (5): 04021024. American Society of Civil Engineers. https://doi.org/10.1061/(ASCE)GT.1943-5606.0002503.

Hutabarat, D., and J. D. Bray. 2022. “Estimating the Severity of Liquefaction Ejecta Using the Cone Penetration Test.” *J. Geotech. Geoenvironmental Eng.*, 148 (3): 04021195. American Society of Civil Engineers. https://doi.org/10.1061/(ASCE)GT.1943-5606.0002744.

Idriss, I. M., and R. W. Boulanger. 2006. “Semi-empirical procedures for evaluating liquefaction potential during earthquakes.” *Soil Dyn. Earthq. Eng.*, 11th International Conference on Soil Dynamics and Earthquake Engineering (ICSDEE): Part II, 26 (2): 115–130. https://doi.org/10.1016/j.soildyn.2004.11.023.

Idriss, I. M., and R. W. Boulanger. 2008. *Soil Liquefaction During Earthquakes*. Oakland, CA: Earthquake Engineering Research Institute.

Ishihara, K. 1985. “Stability of Natural Deposits during Earthquakes.” *Proc. Elev. Int. Conf. Soil Mech. Found. Eng.* San Francisco, California, USA.

Ishihara, K., and M. Yoshimine. 1992. “Evaluation of Settlements in Sand Deposits Following Liquefaction During Earthquakes.” *Soils Found.*, 32 (1): 173–188. https://doi.org/10.3208/sandf1972.32.173.

Iwasaki, T., T. Arakawa, and K.-I. Tokida. 1984. “Simplified procedures for assessing soil liquefaction during earthquakes.” *Int. J. Soil Dyn. Earthq. Eng.*, 3 (1): 49–58. https://doi.org/10.1016/0261-7277(84)90027-5.

Iwasaki, T. F., K. Tatsuoka, and S. T. Yasuda. 1978. “A Practical Method For Assessing Soil Liquefaction Potential Based On Case Studies At Various Sites In Japan.” *Proc. 2nd Int. Conf. Microzonat. Safer Constr. Res. Appl.*, 885–896. San Francisco, California, USA.

Iwasaki, T., K.-I. Tokida, F. Tatsuoka, S. Watanabe, S. T. Yasuda, and H. Sato. 1982. “Microzonation for soil liquefaction potential using simplified methods.” *Proc. 3rd Int. Earthq. Microzonat. Conf.*, 1319–1330. Seattle, Washington, USA.

Jayaram, N., and J. W. Baker. 2009. “Correlation model for spatially distributed ground-motion intensities.” *Earthq. Eng. Struct. Dyn.*, 38 (15): 1687–1708. https://doi.org/10.1002/eqe.922.

Jefferies, M., and K. Been. 2015. *Soil Liquefaction: A Critical State Approach, Second Edition*. London: CRC Press.

Johnson, N. L. 1949. “Systems of Frequency Curves Generated by Methods of Translation.” *Biometrika*, 36 (1/2): 149. https://doi.org/10.2307/2332539.

Kayen, R. E., and J. K. Mitchell. 1997. “Assessment of Liquefaction Potential during Earthquakes by Arias Intensity.” *J. Geotech. Geoenvironmental Eng.*, 123 (12): 1162–1174. American Society of Civil Engineers. https://doi.org/10.1061/(ASCE)1090-0241(1997)123:12(1162).

Kayen, R., R. E. S. Moss, E. M. Thompson, R. B. Seed, K. O. Cetin, A. D. Kiureghian, Y. Tanaka, and K. Tokimatsu. 2013. "Shear-Wave Velocity–Based Probabilistic and Deterministic Assessment of Seismic Soil Liquefaction Potential." *J. Geotech. Geoenvironmental Eng.*, 139 (3): 407–419. American Society of Civil Engineers. https://doi.org/10.1061/(ASCE)GT.1943-5606.0000743.

Kishida, T., and C.-C. Tsai. 2014. "Seismic Demand of the Liquefaction Potential with Equivalent Number of Cycles for Probabilistic Seismic Hazard Analysis." *J. Geotech. Geoenvironmental Eng.*, 140 (3): 04013023. American Society of Civil Engineers. https://doi.org/10.1061/(ASCE)GT.1943-5606.0001033.

Kramer, S. L. 1996. *Geotechnical earthquake engineering*. Prentice-Hall international series in civil engineering and engineering mechanics. Upper Saddle River, NJ: Prentice Hall.

Kramer, S. L., S. S. Sideras, and M. W. Greenfield. 2016. "The timing of liquefaction and its utility in liquefaction hazard evaluation." *Soil Dyn. Earthq. Eng.*, 6ICEGE – Earthquake Geotechincal Engineeering, 91: 133–146. https://doi.org/10.1016/j.soildyn.2016.07.025.

Kwak, D. Y., P. Zimmaro, S. N. Nakai, T. Sekiguchi, and J. P. Stewart. 2018. "Case study of liquefaction susceptibility from field performance of hydraulic fills."

Lange, N. A., and G. M. Forker. 1967. *Handbook of chemistry*. New York: McGraw-Hill.

Lasley, S. J., R. A. Green, and A. Rodriguez-Marek. 2016. "New Stress Reduction Coefficient Relationship for Liquefaction Triggering Analyses." *J. Geotech. Geoenvironmental Eng.*, 142 (11): 06016013. https://doi.org/10.1061/(ASCE)GT.1943-5606.0001530.

Lasley, S. J., R. A. Green, and A. Rodriguez-Marek. 2017. "Number of Equivalent Stress Cycles for Liquefaction Evaluations in Active Tectonic and Stable Continental Regimes." *J. Geotech. Geoenvironmental Eng.*, 143 (4): 04016116. https://doi.org/10.1061/(ASCE)GT.1943-5606.0001629.

Liao, S. S. C., D. Veneziano, and R. V. Whitman. 1988. "Regression Models For Evaluating Liquefaction Probability." *J. Geotech. Eng.*, 114 (4): 389–411. American Society of Civil Engineers. https://doi.org/10.1061/(ASCE)0733-9410(1988)114:4(389).

Liao, S. S. C., and R. V. Whitman. 1986. "Overburden Correction Factors for SPT in Sand." *J. Geotech. Eng.*, 112 (3): 373–377. https://doi.org/10.1061/(ASCE)0733-9410(1986)112:3(373).

Markov, A. A. 2006. "An Example of Statistical Investigation of the Text *Eugene Onegin* Concerning the Connection of Samples in Chains." *Sci. Context*, 19 (4): 591–600. https://doi.org/10.1017/S0269889706001074.

Martin, G., M. Lew, K. Arulmoli, J. Baez, T. Blake, J. Earnest, F. Gharib, J. Goldhammer, D. Hsu, S. Kupferman, J. O'Tousa, C. Real, W. Reeder, A. Simantob, and T. L. Youd. 1999. *Recommended Procedures For Implementation of DMG Special Publication 117 Guidelines for Analyzing and Mitigating Liquefaction Hazard in California*. SCEC Contribution. Los Angeles, California: Southern California Earthquake Center.

Matsuo, O. 2004. “Simplified Procedure for Assessing Liquefaction Potential of Soils in the Specifications for Highway Bridges.” *Proc. Jpn. Soc. Civ. Eng.*, 1–20.

Maurer, B. W., R. A. Green, S. Ballegooy, and L. Wotherspoon. 2017. “Assessing Liquefaction Susceptibility Using the CPT Soil Behavior Type Index.” *3rd Int. Conf. Perform.-Based Des. Earthq. Geotech. Eng.* Vancouver, Canada.

Maurer, B. W., R. A. Green, M. Cubrinovski, and B. A. Bradley. 2015a. “Assessment of CPT-based methods for liquefaction evaluation in a liquefaction potential index framework.” *Géotechnique*, 65 (5): 328–336. https://doi.org/10.1680/geot.SIP.15.P.007.

Maurer, B. W., R. A. Green, and O.-D. S. Taylor. 2015b. “Moving towards an improved index for assessing liquefaction hazard: Lessons from historical data.” *Soils Found.*, 55 (4): 778–787. https://doi.org/10.1016/j.sandf.2015.06.010.

Molina-Gómez, F., D. Cordeiro, C. Ferreira, and A. Viana Da Fonseca. 2022. “Soil stratigraphy from seismic piezocone data and multivariate clustering in alluvial soil deposits: Experience in the Lower Tagus Valley region.” *Cone Penetration Test. 2022*, 584–590. London: CRC Press.

Moss, R. E. S. 2003. “CPT-Based Probabilistic Assessment of Seismic Soil Liquefaction Initiation.” Berkeley, California: University of California, Berkeley.

Moss, R. E. S., B. D. Collins, and D. H. Whang. 2005. “Retesting of Liquefaction/Nonliquefaction Case Histories in the Imperial Valley.” *Earthq. Spectra*, 21 (1): 179–196. https://doi.org/10.1193/1.1852562.

Moss, R. E., R. B. Seed, R. E. Kayen, J. P. Stewart, A. Der Kiureghian, and K. O. Cetin. 2006. “CPT-Based Probabilistic and Deterministic Assessment of In Situ Seismic Soil Liquefaction Potential.” *J. Geotech. Geoenvironmental Eng.*, 132 (8): 1032–1051. https://doi.org/10.1061/(ASCE)1090-0241(2006)132:8(1032).

Müller, S., L. Schüler, A. Zech, and F. Heße. 2022. “GSTools v1.3: a toolbox for geostatistical modelling in Python.” *Geosci. Model Dev.*, 15 (7): 3161–3182. https://doi.org/10.5194/gmd-15-3161-2022.

Nakai, S., and T. Sekiguchi. 2013. “Analysis of liquefaction damage in Mihama-ku of Chiba city due to 2011 Tohoku earthquake.” *BUTSURI-TANSAGeophysical Explor.*, 66 (1): 37–43. https://doi.org/10.3124/segj.66.37.

NASEM. 2021. *State of the Art and Practice in the Assessment of Earthquake-Induced Soil Liquefaction and Its Consequences*. Washington, D.C.: National Academies Press.

Nickerson, R. S. 1998. “Confirmation Bias: A Ubiquitous Phenomenon in Many Guises.” *Rev. Gen. Psychol.*, 2 (2): 175–220. https://doi.org/10.1037/1089-2680.2.2.175.

Nielsen, F. 2016. “Hierarchical Clustering.” *Introd. HPC MPI Data Sci.*, Undergraduate Topics in Computer Science, 195–211. Cham: Springer International Publishing.

Ntritsos, N., and M. Cubrinovski. 2020. “A CPT-based effective stress analysis procedure for liquefaction assessment.” *Soil Dyn. Earthq. Eng.*, 131: 106063. https://doi.org/10.1016/j.soildyn.2020.106063.

Nweke, C. C., C. A. Davis, K. S. Hudson, K. W. Hudnut, S. J. Brandenberg, and J. P. Stewart. 2022. “Performance of Water Pipelines at Fault Crossings from the 2019 Ridgecrest Earthquakes.” *Lifelines 2022*, 343–355. Virtual Conference: American Society of Civil Engineers.

NZGD. 2016. “New Zealand Geotechnical Database.” https://www.nzgd.org.nz/: New Zealand Earthquake Commission.

O’Donnell, S. T., B. E. Rittmann, and E. Kavazanjian. 2017. “MIDP: Liquefaction Mitigation via Microbial Denitrification as a Two-Stage Process. I: Desaturation.” *J. Geotech. Geoenvironmental Eng.*, 143 (12): 04017094. American Society of Civil Engineers. https://doi.org/10.1061/(ASCE)GT.1943-5606.0001818.

Okamura, M., and Y. Soga. 2006. “Effects of Pore Fluid Compressibility on Liquefaction Resistance of Partially Saturated Sand.” *Soils Found.*, 46 (5): 695–700. https://doi.org/10.3208/sandf.46.695.

Oxford Dictionary of English. 2010. Oxford University Press.

Park, S.-S., and Y.-S. Kim. 2013. “Liquefaction Resistance of Sands Containing Plastic Fines with Different Plasticity.” *J. Geotech. Geoenvironmental Eng.*, 139 (5): 825–830. American Society of Civil Engineers. https://doi.org/10.1061/(ASCE)GT.1943-5606.0000806.

Pedregosa, F., G. Varoquaux, A. Gramfort, V. Michel, B. Thirion, O. Grisel, M. Blondel, P. Prettenhofer, R. Weiss, V. Dubourg, J. Vanderplas, A. Passos, D. Cournapeau, M. Brucher, M. Perrot, and É. Duchesnay. 2011. “Scikit-learn: Machine Learning in Python.” *J. Mach. Learn. Res.*, 12 (null): 2825–2830.

PEER. 2000a. “Documenting Incidents of Ground Failure Resulting from the Kocaeli, Turkey Earthquake.” Accessed October 18, 2023. https://apps.peer.berkeley.edu/publications/turkey/adapazari/index.html.

PEER. 2000b. “Documentation of Soil Conditions at Liquefaction Sites from 1999 Chi- Chi, Taiwan Earthquake.” https://apps.peer.berkeley.edu/lifelines/research_projects/3A02/index.html: PEER.

Phoon, K.-K., and F. H. Kulhawy. 1999. “Characterization of geotechnical variability.” *Can. Geotech. J.*, 36 (4): 612–624. NRC Research Press. https://doi.org/10.1139/t99-038.

Polito, C. 2001. “Plasticity Based Liquefaction Criteria.” *Int. Conf. Recent Adv. Geotech. Earthq. Eng. Soil Dyn.* San Diego, California, United States.

Polito, C. P. 1999. “The Effects Of Non-Plastic and Plastic Fines On The Liquefaction Of Sandy Soils.” Virginia Tech.

Polito, C. P., and J. R. Martin. 2001. “Effects of Nonplastic Fines on the Liquefaction Resistance of Sands.” *J. Geotech. Geoenvironmental Eng.*, 127 (5): 408–415. https://doi.org/10.1061/(ASCE)1090-0241(2001)127:5(408).

PWRI. 2016. *Re-examination of Evaluation Method of Liquefaction Strength of Sand Containing Fine Particles*. Public Works Research Institute, National Research and Development Corporation.

Rateria, G., and B. W. Maurer. 2022. “Evaluation and updating of Ishihara’s (1985) model for liquefaction surface expression, with insights from machine and deep learning.” *Soils Found.*, 62 (3): 101131. https://doi.org/10.1016/j.sandf.2022.101131.

Robertson, P. K. 1990. “Soil classification using the cone penetration test.” *Can. Geotech. J.*, 27 (1): 151–158. https://doi.org/10.1139/t90-014.

Robertson, P. K., and K. L. Cabal. 2015. *Guide to Cone Penetration Testing for Geotechnical Engineering*. Gregg Drilling & Testing, Inc.

Robertson, P. K., and C. (Fear) Wride. 1998. “Evaluating cyclic liquefaction potential using the cone penetration test.” *Can. Geotech. J.*, 35 (3): 442–459. NRC Research Press. https://doi.org/10.1139/t98-017.

Robinson, K., M. Cubrinovski, and B. Bradley. 2013. “Sensitivity of predicted liquefaction-induced lateral displacements from the 2010 Darfield and 2011 Christchurch earthquakes.” *Proc. N. Z. Soc. Earthq. Eng. Annu. Conf.*, 8. Wellington, New Zealand: University of Canterbury. Civil and Natural Resources Engineering.

Sancio, R. B. 2003. *Ground failure and building performance in Adapazari, Turkey*.

Seed, H. B. 1979. “Soil Liquefaction and Cyclic Mobility Evaluation for Level Ground during Earthquakes.” *J. Geotech. Eng. Div.*, 105 (2): 201–255. American Society of Civil Engineers. https://doi.org/10.1061/AJGEB6.0000768.

Seed, H. B., and I. M. Idriss. 1970. *Soil Moduli and Damping Factors for Dynamic Response Analyses.* California Univ., Berkeley. Earthquake Engineering Research Center.

Seed, H. B., and I. M. Idriss. 1971. “Simplified Procedure for Evaluating Soil Liquefaction Potential.” *J. Soil Mech. Found. Div.*, 97 (9): 1249–1273. American Society of Civil Engineers. https://doi.org/10.1061/JSFEAQ.0001662.

Seed, H. B., and I. M. Idriss. 1982. *Ground Motions and Soil Liquefaction During Earthquakes*. Earthquake Engineering Research Institute.

Seed, H. B., and K. L. Lee. 1966. “Liquefaction of Saturated Sands During Cyclic Loading.” *J. Soil Mech. Found. Div.*, 92 (6): 105–134. https://doi.org/10.1061/JSFEAQ.0000913.

Seed, H. B., and W. H. Peacock. 1970. *Applicability of Laboratory Test Procedures for Measuring Soil Liquefaction Characteristics Under Cyclic Loading*. College of Engineering, University of California.

Seed, H. B., K. Tokimatsu, L. F. Harder, and R. M. Chung. 1984. *The influence of SPT procedures in soil liquefaction resistance evaluations: Berkeley, University of California*. Earthquake

Engineering Research Center. EERC. Berkeley, California: University of California, Berkeley.

Seed, H. B., K. Tokimatsu, L. F. Harder, and R. M. Chung. 1985. “Influence of SPT Procedures in Soil Liquefaction Resistance Evaluations.” *J. Geotech. Eng.*, 111 (12): 1425–1445. American Society of Civil Engineers. https://doi.org/10.1061/(ASCE)0733-9410(1985)111:12(1425).

Seed, R. B., K. O. Cetin, R. E. S. Moss, A. M. Kammerer, J. Wu, J. M. Pestana, and M. F. Reimer. 2003. *Recent Advances in Soil Liquefaction Engineering and Seismic Site Response Evaluation*. EERC. Long Beach, California: University of California, Berkeley.

Sekiguchi, T., and S. Nakai. 2012. “Effects of Local Site Conditions on Liquefaction Damage in Mihama Ward of Chiba City.” *Proc. Int. Symp. Eng. Lessons Learn. 2011 Gt. East Jpn. Earthq.* Tokyo, Japan.

Steudlein, A., B. Alemu, T. M. Evans, S. Kramer, J. Stewart, K. Ulmer, and K. Ziotopoulou. 2023. *PEER Workshop on Liquefaction Susceptibility*. PEER Reports. PEER Reports. Pacific Earthquake Engineering Research Center, University of California, Berkeley, CA.

Stewart, J. P., S. J. Brandenberg, P. Wang, C. C. Nweke, K. S. Hudson, S. Mazzoni, Y. Bozorgnia, K. W. Hudnut, C. A. Davis, S. K. Ahdi, C. A. Goulet, F. Zareian, J. Fayaz, R. Koehler, C. Chupik, I. Pierce, A. Williams, S. Akciz, M. B. Hudson, and T. Kishida. 2019. *Preliminary Report on Engineering and Geological Effects of the July 2019 Ridgecrest Earthquake Sequence*. GEER. GEER Associtation (Report - 64).

Stewart, J. P., S. L. Kramer, D. Y. Kwak, M. W. Greenfield, R. E. Kayen, K. Tokimatsu, J. D. Bray, C. Z. Beyzaei, M. Cubrinovski, T. Sekiguchi, S. Nakai, and Y. Bozorgnia. 2016. “PEER-NGL project: Open source global database and model development for the next-generation of liquefaction assessment procedures.” *Soil Dyn. Earthq. Eng.*, 6ICEGE – Earthquake Geotechincal Engineeering, 91: 317–328. https://doi.org/10.1016/j.soildyn.2016.07.009.

Stuedlein, A. W., A. Dadashiserej, A. Jana, and T. M. Evans. 2023. “Liquefaction Susceptibility and Cyclic Response of Intact Nonplastic and Plastic Silts.” *J. Geotech. Geoenvironmental Eng.*, 149 (1): 04022125. American Society of Civil Engineers. https://doi.org/10.1061/(ASCE)GT.1943-5606.0002935.

Suzuki, Y., T. Sanematsu, and K. Tokimatsu. 1998. “Correlation between SPT and seismic CPT.” *Geotech. Site Charact.*, 1375–1380. Atlanta, Georgia: A.A. Balkema, Brookfield.

Terzaghi, K., R. B. Peck, and G. Mesri. 1996. “Soil mechanics in engineering practice. Third edition.” John Wiley, New York, NY (United States).

Thevanayagam, S. 1998. “Effect of Fines and Confining Stress on Undrained Shear Strength of Silty Sands.” *J. Geotech. Geoenvironmental Eng.*, 124 (6): 479–491. American Society of Civil Engineers. https://doi.org/10.1061/(ASCE)1090-0241(1998)124:6(479).

Tokimatsu, K., S. Tamura, H. Suzuki, and K. Katsumata. 2012. “Building damage associated with geotechnical problems in the 2011 Tohoku Pacific Earthquake.” *Soils Found.*, Special

Issue on Geotechnical Aspects of the 2011 off the Pacific Coast of Tohoku Earthquake, 52 (5): 956–974. https://doi.org/10.1016/j.sandf.2012.11.014.

Tokimatsu, K., and Y. Yoshimi. 1983. "Empirical Correlation of Soil Liquefaction Based on SPT N-Value and Fines Content." *Soils Found.*, 23 (4): 56–74. https://doi.org/10.3208/sandf1972.23.4_56.

Toprak, S., and T. L. Holzer. 2003. "Liquefaction Potential Index: Field Assessment." *J. Geotech. Geoenvironmental Eng.*, 129 (4): 315–322. American Society of Civil Engineers. https://doi.org/10.1061/(ASCE)1090-0241(2003)129:4(315).

Tsukamoto, Y., K. Ishihara, H. Nakazawa, K. Kamada, and Y. Huang. 2002. "Resistance of Partly Saturated Sand to Liquefaction with Reference to Longitudinal and Shear Wave Velocities." *Soils Found.*, 42 (6): 93–104. https://doi.org/10.3208/sandf.42.6_93.

Turner, B., S. J. Brandenberg, and J. P. Stewart. 2015. "Analysis of Drilled Shaft Settlement Caused by Liquefaction." *IFCEE 2015*, 1176–1188. San Antonio, Texas: American Society of Civil Engineers.

Turner, B. J., S. J. Brandenberg, and J. P. Stewart. 2016. "Case Study of Parallel Bridges Affected by Liquefaction and Lateral Spreading." *J. Geotech. Geoenvironmental Eng.*, 142 (7): 05016001. https://doi.org/10.1061/(ASCE)GT.1943-5606.0001480.

Ulmer, K. J. 2019. "Development of an Energy-based Liquefaction Evaluation Procedure." Blacksburg, Virginia, USA: Virginia Tech.

Ulmer, K. J., B. Carlton, T. Nguyen, and Q. Parker. 2023a. "An Expanded Data Set of Overburden (Kσ) and Initial Static Shear Stress (Kα) Correction Factors from Published Cyclic Laboratory Tests for Liquefaction Triggering Analyses." *Proc. Geo-Congr. 2023*, 197–206. Los Angeles, California.

Ulmer, K. J., B. Carlton, and J. Stamatakos. 2022. *Task 5b: Focused Study on the Effects of Overburden and Initial Static Shear Stresses*. Washington, D.C.: Nuclear Regulatory Commission.

Ulmer, K. J., R. A. Green, A. Rodriguez-Marek, and J. K. Mitchell. 2023b. "Energy-Based Liquefaction Triggering Model." *J. Geotech. Geoenvironmental Eng.*, 149 (11): 04023105. American Society of Civil Engineers. https://doi.org/10.1061/JGGEFK.GTENG-11402.

Ulmer, K. J., K. S. Hudson, S. J. Brandenberg, P. Zimmaro, R. Pretell, B. Carlton, S. L. Kramer, and J. P. Stewart. 2023c. *Task 7b: Draft Final Report Documenting Probabilistic Liquefaction Models*. U.S. Nuclear Regulatory Commission.

Ulmer, K. J., S. Upadhyaya, R. A. Green, A. Rodriguez-Marek, P. J. Stafford, J. J. Bommer, and J. van Elk. 2018. "A Critique of b-Values Used for Computing Magnitude Scaling Factors." 112–121. American Society of Civil Engineers. https://doi.org/10.1061/9780784481486.012.

Vaid, Y. P., and J. C. Chern. 1983. "Effect of Static Shear on Resistance to Liquefaction." *Soils Found.*, 23 (1): 47–60. https://doi.org/10.3208/sandf1972.23.47.

Vaid, Y. P., and J. C. Chern. 1985. “Cyclic and monotonic undrained response of saturated sands.”

Van Ballegooy, S., P. Malan, V. Lacrosse, M. E. Jacka, M. Cubrinovski, J. D. Bray, T. D. O’Rourke, S. A. Crawford, and H. Cowan. 2014. “Assessment of Liquefaction-Induced Land Damage for Residential Christchurch.” *Earthq. Spectra*, 30 (1): 31–55. https://doi.org/10.1193/031813EQS070M.

Virtanen, P., R. Gommers, T. E. Oliphant, M. Haberland, T. Reddy, D. Cournapeau, E. Burovski, P. Peterson, W. Weckesser, J. Bright, S. J. Van Der Walt, M. Brett, J. Wilson, K. J. Millman, N. Mayorov, A. R. J. Nelson, E. Jones, R. Kern, E. Larson, C. J. Carey, İ. Polat, Y. Feng, E. W. Moore, J. VanderPlas, D. Laxalde, J. Perktold, R. Cimrman, I. Henriksen, E. A. Quintero, C. R. Harris, A. M. Archibald, A. H. Ribeiro, F. Pedregosa, P. Van Mulbregt, SciPy 1.0 Contributors, A. Vijaykumar, A. P. Bardelli, A. Rothberg, A. Hilboll, A. Kloeckner, A. Scopatz, A. Lee, A. Rokem, C. N. Woods, C. Fulton, C. Masson, C. Häggström, C. Fitzgerald, D. A. Nicholson, D. R. Hagen, D. V. Pasechnik, E. Olivetti, E. Martin, E. Wieser, F. Silva, F. Lenders, F. Wilhelm, G. Young, G. A. Price, G.-L. Ingold, G. E. Allen, G. R. Lee, H. Audren, I. Probst, J. P. Dietrich, J. Silterra, J. T. Webber, J. Slavič, J. Nothman, J. Buchner, J. Kulick, J. L. Schönberger, J. V. De Miranda Cardoso, J. Reimer, J. Harrington, J. L. C. Rodríguez, J. Nunez-Iglesias, J. Kuczynski, K. Tritz, M. Thoma, M. Newville, M. Kümmerer, M. Bolingbroke, M. Tartre, M. Pak, N. J. Smith, N. Nowaczyk, N. Shebanov, O. Pavlyk, P. A. Brodtkorb, P. Lee, R. T. McGibbon, R. Feldbauer, S. Lewis, S. Tygier, S. Sievert, S. Vigna, S. Peterson, S. More, T. Pudlik, T. Oshima, T. J. Pingel, T. P. Robitaille, T. Spura, T. R. Jones, T. Cera, T. Leslie, T. Zito, T. Krauss, U. Upadhyay, Y. O. Halchenko, and Y. Vázquez-Baeza. 2020. “SciPy 1.0: fundamental algorithms for scientific computing in Python.” *Nat. Methods*, 17 (3): 261–272. https://doi.org/10.1038/s41592-019-0686-2.

Wang, W. 1979. *Some Findings in Soil Liquefaction*. Earthquake Engineering Department, Water Conservancy and Hydroelectric Power Scientific Research Institute.

Wang, Y., K. Huang, and Z. Cao. 2013. “Probabilistic identification of underground soil stratification using cone penetration tests.” *Can. Geotech. J.*, 50 (7): 766–776. NRC Research Press. https://doi.org/10.1139/cgj-2013-0004.

Whitman, R. V. 1971. “Resistance of Soil to Liquefaction and Settlement.” *Soils Found.*, 11 (4): 59–68. https://doi.org/10.3208/sandf1960.11.4_59.

Wiecki, T., J. Salvatier, R. Vieira, M. Kochurov, A. Patil, M. Osthege, B. T. Willard, B. Engels, C. Carroll, O. A. Martin, A. Seyboldt, A. Rochford, L. Paz, R. Goldman, K. Meyer, P. Coyle, M. E. Gorelli, O. Abril-Pla, J. Lao, R. Kumar, V. Andreani, T. Yoshioka, G. Ho, T. Kluyver, K. Beauchamp, A. Andorra, D. Pananos, E. Spaak, B. Edwards, and E. Ma. 2023. “pymc-devs/pymc: v5.9.1.” Zenodo.

Yang, J., S. Savidis, and M. Roemer. 2004. “Evaluating Liquefaction Strength of Partially Saturated Sand.” *J. Geotech. Geoenvironmental Eng.*, 130 (9): 975–979. American Society of Civil Engineers. https://doi.org/10.1061/(ASCE)1090-0241(2004)130:9(975).

Youd, T. L. 1973. *Liquefaction, flow, and associated ground failure*. Circular. Report.

Youd, T. L. 1998. *Screening guide for rapid assessment of liquefaction hazard at highway bridge sites*.

Youd, T. L., and M. J. Bennett. 1983. “Liquefaction sites, Imperial Valley, California.” *J. Geotech. Eng.*, 109 (3): 440–457. https://doi.org/10.1061/(ASCE)0733-9410(1983)109:3(440).

Youd, T. L., I. M. Idriss, R. D. Andrus, I. Arango, G. Castro, J. T. Christian, R. Dobry, W. D. L. Finn, L. F. Harder, M. E. Hynes, K. Ishihara, J. P. Koester, S. S. C. Liao, W. F. Marcuson, G. R. Martin, J. K. Mitchell, Y. Moriwaki, M. S. Power, P. K. Robertson, R. B. Seed, and K. H. Stokoe. 2001. “Liquefaction Resistance of Soils: Summary Report from the 1996 NCEER and 1998 NCEER/NSF Workshops on Evaluation of Liquefaction Resistance of Soils.” *J. Geotech. Geoenvironmental Eng.*, 127 (10): 817–833. https://doi.org/10.1061/(ASCE)1090-0241(2001)127:10(817).

Youd, T. L., and S. K. Noble. 1997. “Liquefaction Criteria Based on Statistical and Probabilistic Analyses.” *Natl. Cent. Earthq. Eng. Res.* Salt Lake City, Utah.

Zhang, B., K. K. Muraleetharan, and C. Liu. 2016. “Liquefaction of Unsaturated Sands.” *Int. J. Geomech.*, 16 (6): D4015002. American Society of Civil Engineers. https://doi.org/10.1061/(ASCE)GM.1943-5622.0000605.

Zhang, G., P. K. Robertson, and R. W. I. Brachman. 2004. “Estimating Liquefaction-Induced Lateral Displacements Using the Standard Penetration Test or Cone Penetration Test.” *J. Geotech. Geoenvironmental Eng.*, 130 (8): 861–871. https://doi.org/10.1061/(ASCE)1090-0241(2004)130:8(861).

Zimmaro, P., and K. Hudson. 2021. “Searles Lake Liquefaction.” Designsafe-CI.

Zimmaro, P., D. Y. Kwak, Y. T. Tsai, J. P. Stewart, S. J. Brandenberg, A. Mikami, and S. Kataoka. 2020a. “Database on seismic response of instrumented flood control levees.” *Earthq. Spectra*, 36 (2): 924–938. https://doi.org/10.1177/8755293019891712.

Zimmaro, P., C. C. Nweke, J. L. Hernandez, K. S. Hudson, M. B. Hudson, S. K. Ahdi, M. L. Boggs, C. A. Davis, C. A. Goulet, S. J. Brandenberg, K. W. Hudnut, and J. P. Stewart. 2020b. “Liquefaction and Related Ground Failure from July 2019 Ridgecrest Earthquake Sequence.” *Bull. Seismol. Soc. Am.*, 110 (4): 1549–1566. https://doi.org/10.1785/0120200025.